Surface and sub-surface hydrographic variability at the Prince Edward Islands: Perspectives from the high-resolution GLORYS model.

Bianca Soares
SRSBIA001

Supervisors: Dr Tarron Lamont
Dr Issufo Halo
Ms Cristina Russo

Submitted in fulfilment of the requirements for the degree of Master of Science (Physical Oceanography)

Department of Oceanography
Faculty of Science
University of Cape Town
Rondebosch
Cape Town
7701
May 2023

Plagiarism Declaration

I, Bianca Soares, know that plagiarism is wrong. Plagiarism is to use another's work and pretend that it is one's own.

I have used the Harvard formatting for citation and referencing. Each contribution to, and quotation in, this project from the work(s) of other people has been attributed, and has been cited and referenced.

This project is my own work.

I have not allowed, and will not allow, anyone to copy my work with the intention of passing it off as his or her own work.

Signature: Signed by candidate

Date: 26.05.2023

Acknowledgements

I would like to express my most sincere gratitude towards the following people for helping me produce this research project.

To Dr Tarron Lamont, words could not describe how grateful I am to be completing another project under your guidance. You never fail to amaze me with your incredible work ethic and ability to push me beyond my limits. Thank you for helping me throughout every step of this process and for your unwavering faith and patience in me, I am truly blessed to have had you as my supervisor throughout my postgraduate journey.

To Dr Issufo Halo, your gentle approach and constant reassurance throughout this project did more for me than you would ever know. Thank you for all your input and patience when it came to topics that were unfamiliar to me.

To Gloria, I know I won't have enough words to express how grateful I am for you and your constant support. The late nights, constant snack provisions and just your general presence are truly what helped me most to get across the finish line. You are going to be an incredible supervisor one of these days, but for now thank you for being such a special friend.

To the entire oceanography team on the Marion Relief Voyage of 2023, thank you for the spontaneous snack deliveries (Maurice), the wonderful games of splendor and the general feeling of support throughout it all.

To my incredible parents, thank you for never doubting my abilities and for always being in my corner. Thank you for providing me with a safe space to just be and for always being there at the drop of a hat when I needed it most.

To Monique, a constant joke that exists between us is that God knew we needed to be sisters because just being friends would not have sufficed. This is truer than ever, thank you for being my very best friend, sister, counselor and constant cheerleader all in one. You are quite possibly the best person I know, and I would not have been able to accomplish this without you.

To Cassidy Marshall, you are a very rare find in this world and I am just so grateful I get to experience a life with you in it. Thank you for all your support, warmth and interest throughout this process, even though I know you probably still have absolutely no idea what it is that I study.

Lastly but not least, to my incredible church family for all the love, comfort and support you have each shown me in such a short space of time has been remarkable to witness and has left me feeling more whole than ever before. A special thanks to Andri Claassen and Keiman Govender, although neither of you may realise, the words and prayers you spoke over me played a huge role in helping me get to where I am now. I am truly grateful for both of you.

All the glory of this project goes to my heavenly Father.

List of Figures

List of Tables

Glossary

Acronyms, Abbreviations and Terms	Explanation
PEIs	Prince Edward Islands
SSH	Sea Surface Height
SO	Southern Ocean
ACC	Antarctic Circumpolar Current
SAF	Sub-Antarctic Front
APF	Antarctic Polar Front
APFZ	Antarctic Polar Frontal Zone
SWIR	Southwest Indian Ridge
MPA	Marine Protected Area
MOC	Meridional Overturning Circulation
PFZ	Polar Frontal Zone
SACCF	Southern Antarctic Circumpolar Current Front
STF	Subtropical Front
SST	Sea Surface Temperature
SAMW	Sub-Antarctic Mode Water
AAIW	Antarctic Intermediate Water
NADW	North Atlantic Deep Water
AABW	Antarctic Bottom Water
CDW	Circumpolar Deep Water
AASW	Antarctic Surface Water
SASW	Sub-Antarctic Surface Water
CPT	Circumpolar Pressure Trough
ENSO	El Niño Southern Oscillation
SAM	Southern Annular Mode
SAO	Semi-Annual Oscillation
ACW	Antarctic Circumpolar Wave
ADP	Antarctic Dipole
SLP	Sea Level Pressure
ABFZ	Andrew Bain Fracture Zone
IME	Island Mass Effect
WOA18	World Ocean Atlas 2018
CARS09	CSIRO Atlas of Regional Seas 2009
SAWS	South African Weather Services
CTD	Conductivity, Temperature and Depth
NetCDF	Network Common Data Format
ADT	Absolute Dynamic Topography
SSS	Sea Surface Salinity
OI	Optimal Interpolation
MSS	Mean Sea Surface
SLA	Sea Level Anomaly
MDT	Mean Dynamic Topography
OSTIA	Operational SST and Sea Ice Analysis
GEBCO	General Bathymetric Chart of the Oceans
ETOPO	Earth TOPOgraph
T/S	Temperature-Salinity

Ro	Rossby number
Re	Reynolds number
Lrt	Rossby radius of deformation for a barotropic ocean
Lrc	Rossby radius of deformation for a baroclinic ocean
Bl	Blocking parameter
MLD	Mixed Layer Depth
CNR	COnsiglio Nazionale delle Ricerche

Table of Contents

Abstract

The Prince Edward Islands (PEI), comprising of Marion and Prince Edward Island, are located in the direct path of the eastward flowing Antarctic Circumpolar Current, nestled within the Antarctic Polar Frontal Zone of the Southern Ocean. The islands are home to a multitude of species which are supported by a sensitive and complex oceanic environment. Understanding the mechanisms at work, which sustain this rich ecosystem is therefore imperative for both the ecological management of the PEIs, and for the possible prediction of future climate change-driven environmental impacts. The presence of a possible Taylor column has been suggested as a main driver in supporting and maintaining the PEI ecosystem. However, due to the remote and hostile environment in which the islands are located, *in situ* data collection has proven to be a challenging task, which is necessary to study the Taylor column and to understand the island's general hydrographic variability. This study thus makes use of available *in situ*, satellite, reanalysis and modelled bathymetry data, to compare against the GLORYSV12 model output. This was to determine how accurately the model could reproduce surface and sub-surface variability of temperature, salinity, Sea Surface Height (SSH) and surface circulation at the PEIs, and to identify whether *in situ*, satellite and model conditions are suitable for the existence and evolution of a possible Taylor column at the islands. A clear overestimation of the geostrophic currents (up to 0.2 m s^{-1}) and underestimation of SSH (up to 0.6 m) by GLORYS was observed. The spatial and temporal variability of temperature and salinity was captured by GLORYS throughout the entire water column, despite the differences between temperature (biases from -2 to 2 ^{o}C) and salinity (biases from -0.4 to 0.4 PSU). Additionally, GLORYS was also able to simulate all five water masses, known to occur within the PEI region, throughout time. When GLORYS was compared to single point *in situ* SST time series data, a seasonal bias was observed with GLORYS overestimating SST in late summer (January to March) and underestimating SST for the remainder of the year (May to December). However, statistically significant strong, positive correlations ($r > 0.80$, $p < 0.001$) and relatively low biases (-0.50 to 0.10 ^{o}C) were still observed between GLORYS and the this *in situ* SST time series. Overall, this suggested that GLORYS reasonably captures temperature and salinity variability on a climatological-scale. However, when it comes to event-scale, the model fails to accurately reproduce specific mesoscale events, as observed in 2013, 2014 and 2015 when cyclonic and anticyclonic eddies, simulated by the model were not of the same size,

intensity nor in the same location as observed by *in situ* CTD data. GLORYS and satellite data both successfully proved that conditions are suitable for the formation and persistence of a possible Taylor column/Taylor cone at the PEIs. This was concluded with the relatively low Rossby numbers (< 0.07), high Reynolds numbers (> 2000), Blocking parameters which did not exceed 0.2, appropriate Rossby radius of deformation values (< 1000 km for a barotropic ocean and < 24 km for a baroclinic ocean) and an anticyclonic flow pattern around the PEI plateau, all indicative of the fact that conditions, which are typical for the formation of Taylor columns/Taylor cones, occur at the PEIs.

Chapter 1. Introduction

1.1 Background

The Southern Ocean (SO) has an essential role to play in regulating the global climate system and is therefore recognised as Earth's life-support system (Cunningham, 2005). A unique oceanographic environment free of land barriers and a strong westerly wind belt gives the SO the ability to circulate climate signals and water masses across the different ocean basins. The circulation dynamics of the cold water in this region contributes to its capacity in taking up anthropogenic heat and carbon, aiding to reduce the rate of global warming, while supporting global marine productivity (Cunningham, 2005; Rintoul et al. 2018).

The Prince Edward Islands (PEIs) archipelago consists of Marion and Prince Edward Islands (Ansorge and Lutjeharms, 2002). The islands are positioned in the direct path of the eastward flowing Antarctic Circumpolar Current (ACC), between the northern (sub-Antarctic Front) and the southern (Antarctic Polar Front) boundaries of the Antarctic Polar Frontal Zone (APFZ) of the SO. The unique bathymetry, characterised by the Southwest Indian Ridge (SWIR) toward the southwestern side of the PEIs and its several fracture zones, including the Andrew Bain Fracture Zone, contributes to the high levels of mesoscale variability observed in the region (Sokolov and Rintoul, 2009; Froneman et al. 2002; Toolsee et al. 2021). Ansorge et al. (2010) described a region of high mesoscale variability, resulting from the interaction between the ACC and the SWIR that extends towards and across the PEI region. Additionally, Lamont et al. (2019) described the generation of eddies along the sub-Antarctic front (SAF) and Antarctic Polar Front (APF), which impact the hydrographic conditions around the islands and function as a feeding ground for top predators.

The islands were declared a Marine Protected Area (MPA) in 2013 due to the multitude of ecosystems supported by the islands, and with climate change posing a huge threat to this environment, they are in an ideal location to identify and monitor any perturbations to the ecosystem functioning resulting from climate change (RSA, 2013; Ansorge et al. 2017). Analyses done by Perissinotto and Duncombe Rae (1990) and Lamont et al. (2019) have suggested the existence of a Taylor column within the PEIs water column. The existence of such a feature would enhance water retention and develop local scale upwelling events and

would play a crucial role in preserving the dynamic ecosystems of the PEIs by retaining nutrients and enhancing productivity within the inter-island region (Lamont et al. 2019).

1.2 Rationale, Aim and Key questions

Collecting *in situ* data in the Southern Ocean is a challenging task due to the remoteness and hostility of the environment. While there is a good record of data at Marion Island, which has been ongoing since 1949, these data are either single point observations affected by human error (Mélice et al. 2003) or are only snapshots of specific oceanographic conditions (Ansorge et al. 2010). These datasets cannot adequately provide the long-term, regional-scale coverage required for a detailed study of the environmental conditions around the PEIs. Satellite data is extensively used for scientific research in the SO but has also been shown to lack a high spatial and temporal resolution (Toolsee and Lamont, 2022). In many cases their coverage is limited to the sea surface. Lamont et al. (2019) explained that coarse resolution of altimetry data and limited existing *in situ* data could not provide a complete description of the extent and variability of the possible Taylor column existing at the PEIs. To attempt to overcome the above-mentioned limitations, this study aims at using output from a three-dimensional high-resolution hydrodynamic ocean model simulation in the PEIs region to fully capture and understand the surface and sub-surface oceanographic variability around the PEIs.

To achieve the aim set out by this study, the following three key questions were investigated:

1. What is the suitability and accuracy of the GLORYS12V1 model output compared to existing *in situ* and satellite data around the PEIs?
2. What is the surface and sub-surface hydrographic variability surrounding the PEIs, using the GLORYS12V1 model, and what are the drivers thereof?
3. Are the *in situ*, satellite and model conditions suitable for the formation and existence of a Taylor column at the PEIs?

Understanding the mechanisms that sustain the persistence of the rich ecosystem, which is able to support high population densities of marine life at the PEIs, could enhance the ecological management of the PEI MPA, and possibly contribute to potential predictions of future environmental impacts on biological communities. From a global perspective, this study could enhance both our understanding and ability to predict the impacts of climate change on similar vulnerable ecosystems. The lack of previous long-term *in situ* data, within the Southern Ocean,

is the main reason for the uncertainty faced when predicting ecosystem responses to climate change at the PEIs. The results from the current study, along with continued monitoring could provide important measurements and the understanding required for the identification and interpretation of oceanographic variability and its impacts on ecosystem functioning within the PEIs region. Should this study demonstrate that the GLORYS model can be reliably used, it would introduce a new tool for more detailed investigations into a variety of research questions. Additionally, GLORYS could aid in routine monitoring due to the daily available output provided by Copernicus Marine Environment Monitoring Service (CMEMS), which has not been possible in the past since such near real-time model output has only become available in recent years.

Chapter 2. Literature Review

2.1 Significance of the Southern Ocean

The Southern Ocean (SO) encloses the most remote region on Earth, Antarctica, and is defined as the general global ocean south of 35°S (Chapman et al. 2020). Due to the lack of continental barriers, an uninterrupted zonal current exists around Antarctica, known as the Antarctic Circumpolar Current (ACC), which connects and allows for the exchange of heat, gases, moisture, salt and freshwater between the Atlantic, Indian and Pacific Ocean basins (described in greater detail in *Section 2.2*) (*Figure 2.1*) (Cunningham, 2005; Chapman et al. 2020; Rintoul and Naveira Garabato, 2013). The world's climate system includes the ocean, the atmosphere and especially the interaction between them. The SO plays a crucial role in linking this climate system with the ocean's overturning circulation, creating a three-dimensional global ocean circulation that regulates Earth's climate (Cunningham, 2005; Rintoul and Naveira Garabato, 2013).

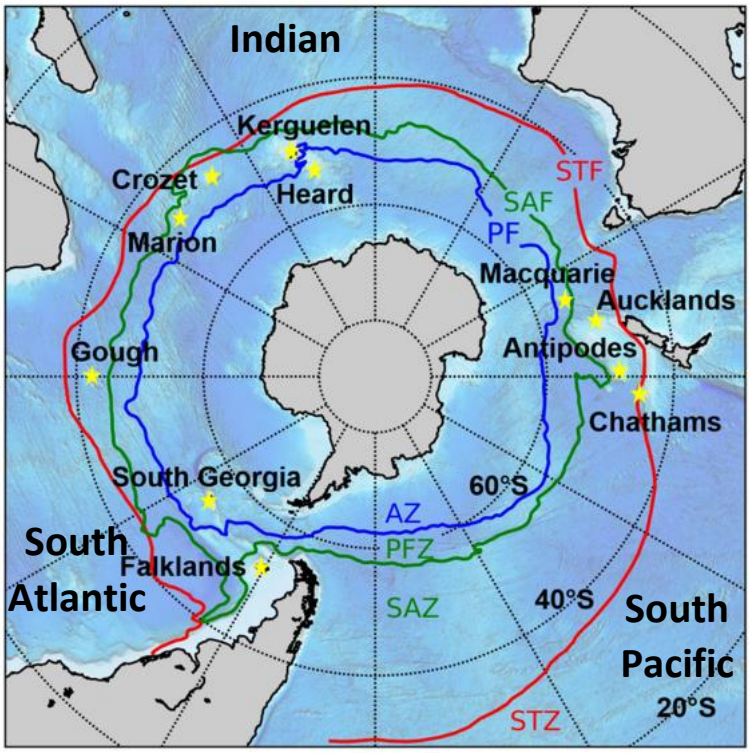

Figure 2.1: Schematic adapted from Cherel (2020) showing the Southern Ocean and its interbasin connection to subtropical waters. The yellow stars denote the main islands. The oceanic fronts and zones are displayed with the circling-coloured lines. Abbreviations are as follows: AZ, Antarctic Zone; PF, Polar Front; PFZ, Polar Frontal Zone; SAZ, sub-Antarctic Zone; STF, Subtropical Front; STZ, Subtropical Zone.

The complex ocean-atmospheric circulation of the SO drives its main role of distributing heat from lower latitudes to the poles (Cunningham, 2005). The ocean and atmosphere transport similar quantities of heat, but the critical difference lies in the timescales at which the heat is distributed. The atmosphere can circulate the heat on a timescale of approximately a month, while the deep waters of the SO can store it at depth for tens to thousands of years before outcropping at the surface. Wind-driven upwelling and the exposure of dense, deep waters at the surface caused by the characteristic steeply sloped density surfaces of the ACC, enables nutrients and carbon to be brought to the upper ocean, while sinking transports heat and gases northwards and downward into the thermocline for extensive periods of time, providing a significant mechanism that stabilises the climate (Rintoul and Naveira Garabato, 2013; Cunningham, 2005; Shi et al. 2018).

The robust overturning circulation allows the SO to take up more anthropogenic carbon dioxide (CO_2) than any of the other oceans, where 40% of the globe's total anthropogenic CO_2 uptake occurs south of 40°S (Rintoul et al. 2018; Rintoul and Naveira Garabato, 2013). Previous studies have revealed strong correlations between atmospheric CO_2 levels and Antarctic temperatures, suggesting that the SO is the source for climate-related changes in atmospheric CO_2 (Anderson et al. 2002; Sigman and Boyle, 2000). Two processes within the SO contribute to it being a region that is believed to regulate atmospheric CO_2 over time periods that are relevant to climate change. The first is the uptake of atmospheric CO_2 via wind-driven upwelling, where cold, deep waters are exposed at the surface and because CO_2 is more soluble in colder water, the invasion of CO_2 occurs within these surface waters (Anderson et al. 2002). The biological pump is also introduced through upwelled waters whereby reintroduced CO_2 and dissolved inorganic nutrients, from the deep, are consumed by phytoplankton through photosynthesis and converted into organic material which settles into the deep ocean (Anderson et al. 2002; Sigman and Boyle, 2000). This process of photosynthesis lowers the in-water partial pressure of CO_2 resulting in the flux of atmospheric CO_2 into the ocean surface (Sigman and Boyle, 2000). Secondly, the overturning circulation within the SO causes surface waters to be drawn down to around 1000 m, forming Intermediate Waters, and then further into the ocean, as Bottom Water, which trapand sequester CO_2, aiding in the mitigation of global warming (Cunningham, 2005; Anderson et al. 2002; Rintoul et al. 2018).

Studies have shown that greenhouse gas induced warming and depletion of ozone in the stratospheric layer of the polar vortex are primary contributors to the intensification and southward shift of the westerly winds which encircle Antarctica and influence CO_2 uptake and

sea ice extent (Mayewski et al. 2015). The accelerated rate of melting ice shelves, ice sheet collapse and sea-level rise are among some of the major consequences expected due to these changes in strength and mean position of the westerlies (Mayewski et al. 2015). Implications may already be underway, whereby the glacier retreat in West Antarctica has been referred to as being 'irreversible'. These changes have a significant influence on the rate of ice sheet response and climate change within the Southern Hemisphere (Mayewski et al. 2015).

The SO's overturning circulation and continuous upwelling has made it the ocean basin with the highest known nutrient levels, sustaining global marine productivity by exporting the upwelled, nutrient-rich waters to the lower latitudes (Perissinotto et al. 1990; Rintoul et al. 2018). The transition from subtropical to Antarctic waters occurs across a series of sharp meridional gradients in salinity, temperature, oxygen and other variables (described in greater detail in *Section 2.2*) (Chapman et al. 2020). These transition zones are known as fronts, and it is within and along these fronts that previous studies have recorded marine mammals and seabirds assembling and foraging (Chapman et al. 2020). Given these significant influences that the SO has on sea level, marine ecosystems, global climate systems and ocean circulation, any changes occurring within this region could have massive ramifications for the world's oceans and climate system (Chapman et al. 2020; Rintoul et al. 2018; Rintoul and Naveira Garabato, 2013).

2.2 Antarctic Circumpolar Current System

The SO is dominated by two major circulations: a zonal (west-east) circumpolar circulation (ACC) and a meridional (north-south) overturning circulation (MOC). These oceanic circulation systems are driven by air-sea fluxes of heat and freshwater, coupled with the strong westerly winds that dominate the region (Cunningham, 2005; Morrow et al. 2010). The ACC connects each of the oceanic basins, facilitating exchanges of multiple properties as well as the blending of water masses. The MOC circulates water from depth to the surface across the ACC and it is this intimate connection between the two main circulation systems which regulates Earth's climate (Cunningham, 2005; Rintoul et al. 2001). This section will review the 'ACC system' which comprises of the ACC and its associated fronts, the water masses and MOC of the SO. The ACC itself, its fronts and the water masses of the SO have a stronger significance to this study and will be described in greater detail than the MOC.

2.2.1 Antarctic Circumpolar Current and the fronts

The ACC is the largest oceanic current, transporting between 140 to 144 Sv of water in an eastward flowing band, approximately 25 000 km in length, around Antarctica (Cunningham, 2005; Hughes, 2005; Rintoul and Naveira Garabato, 2013). The shoaling of isopycnals towards the south is what causes the eastward geostrophic flow of the ACC, resulting from wind and buoyancy forcing, including ocean-ice interactions (Rintoul and Naveira Garabato, 2013). The ACC is positioned within the Polar Frontal Zone (PFZ) of the Southern Ocean, approximately between 40°S and 60°S (*Figure 2.2*) (Hughes, 2005; Ansorge and Lutjeharms,2002).

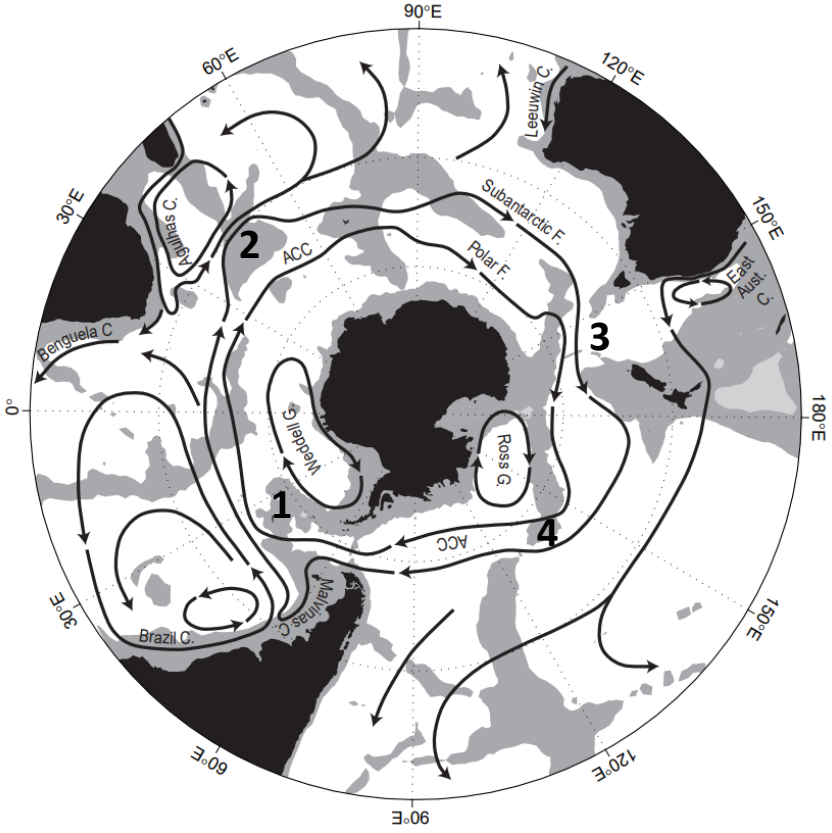

Figure 2.2: Adapted schematic from Rintoul et al. (2001) of the major oceanic currents south of 20 °S. Shaded areas denote depths shallower than 3500 m. Abbreviations are as follows: ACC, Antarctic Circumpolar Current; F, front; C, current; G, gyre. Numbers represent the submarine topography which impacts the meandering of the ACC: 1 - Scotia Arc; 2 – Kerguelen Plateau; 3 - Macquarie Ridge complex; 4 - Pacific Antarctic Ridge.

The ACC's flow is dominated by a system of intense circumpolar currents known as 'fronts', as first noted by Deacon (1937). Fronts in the ocean are defined as distinct boundaries where the water holds different temperature, salinity, density and gradient properties (Sokolov and Rintoul, 2002). Between the fronts, the water properties are relatively homogenous, producing water masses with unique environmental characteristics (Chapman et al. 2020). The density differences across the fronts form deep, eastward flowing jets which are responsible for most of the ACC transport (Rintoul and Naveira Garabato, 2013; Rintoul et al. 2001; Chapman et

al. 2020). The ACC comprises of three main fronts from north to south these are: the sub-Antarctic Front (SAF), the Antarctic Polar Front (APF) and the Southern ACC Front (SACCF) (*Figure 2.2 and 2.3*) (Sokolov and Rintoul, 2002). The Subtropical Front (STF), north of the ACC, and the Southern Boundary Front, near Antarctica, have dynamics which are different to that of the ACC and as a result are not considered to be part of the ACC (Chapman et al. 2020).

The uninterrupted flow of the ACC, due to the lack of land barriers, promotes the inter-basin connection allowing for the global overturning circulation (Rintoul et al. 2001). This zonal current is however not a stable flow. Gille (1994) used altimeter data to map the full path of the ACC and observed the northward and southward meandering of the ACC inferring that the fronts are topographically steered by the submarine topography (*Figure 2.2*) (Cunningham, 2005; Rintoul et al. 2001). The meandering of the SAF and APF act to catalyse the formation of mesoscale eddies and submesoscale filaments which are believed to have a greater influence on the dynamical and thermodynamical balances in the SO than in any other region of the ocean (Chapman et al. 2020; Cunningham, 2005; Rintoul et al. 2001).

Researchers have built what was is referred to as the 'traditional' view of the SO fronts comprising, the SAF, APF and SACCF, however with increased availability of high-resolution satellite data, it has become clear that the SO and specifically the ACC is far more complex than the traditional view would imply. The ACC does not consist of a set number of circumpolar fronts but rather of temporally and spatially varying filaments that form, disappear, spilt, merge, drift and meander (Chapman et al. 2020). Sokolov and Rintoul (2009) described the SAF and APF as having multiple branches namely, the northern (N-SAF; N-APF), middle (M-SAF; M-APF) and southern (S-SAF; S-APF) branches that join and diverge.

While the conceptual idea of a front being a water mass boundary is universally accepted, the definition for the position of a front is still a subject of debate. Two broad definitions have been suggested according to previous studies, the first being local definitions which makes use of gradient thresholds, typically of Sea Surface Temperature (SST) or Sea Surface Height (SSH), to detect a front. However, this definition fails to include the variabilty in time and space of the fronts (Chapman et al. 2020). Secondly, the global frontal definition seeks to identify a specific value, of temperature or SSH, that can be used to locate the fronts and by using this method a front can be found that both varies in time and is spatially continuous (Chapman et al. 2020). As part of this global definition, the contour based method by Sokolov and Rintoul

(2009) has been shown to produce accurate findings when compared to *in situ* data in the PEI region (Lamont et al. 2019).

Long-term warming and freshening of the SO is underway and given the significant influence the ACC and its fronts have within the SO, there is a concerted effort to understand the projected changes the fronts could encounter. The contour based method of locating the fronts has suggested, over a period of approximately 15 years, the main fronts of the ACC have shifted between 0.5^{o} to 1.5^{o} (about 60 km) southwards and warming within the SO has emerged as the result of this southward shift (Chapman et al. 2020; Sokolov and Rintoul, 2009; Marshall and Speer, 2012; Ansorge et al. 2017). More recent work, using the local definition for identifying fronts, has not observed a southward shift of the fronts and the warming has instead been described as the accumulation of heat in the ACC as the result of changes in the wind-driven overturning circulation (Chapman et al. 2020; Gille, 2014).

2.2.2 Overturning Circulation in the Southern Ocean

A significant circulation exists in the SO along the meridional vertical plane known as the MOC (Rintoul et al. 2001). Westerly winds around Antarctica and the prevailing westerly wind belt drive divergent Ekman transport, south of the ACC, which upwells deep water to the surface, forming sub-Antarctic Mode Water (SAMW) and Antarctic Intermediate Water (AAIW) which then flow equatorward (*Figure 2.3*) (Rintoul et al. 2001; Morrison et al. 2015). North of the westerly wind belt, convergent Ekman transport occurs and surface waters are downwelled to the deep ocean and transported poleward and upward across the ACC to balance the equatorward flow (Rintoul et al. 2001; Cunningham, 2005).

Cold, salty, deep water, known as North Atlantic Deep Water (NADW), forms in the Arctic and flows southward into the SO, where between 9 and 12 Sv are upwelled south of 50^{o}S, due to the divergence in the Ekman transport (*Figure 2.3*) (Cunningham, 2005). This upwelling results in the tilting of isopycnals, producing increased potential energy which is extracted by eddies, flattening them out. Mesoscale eddies therefore form part of the deep water upwelling branch and contribute to transporting NADW into the mixed layer around Antarctica (Marshall and Speer, 2012; Cunningham, 2005).

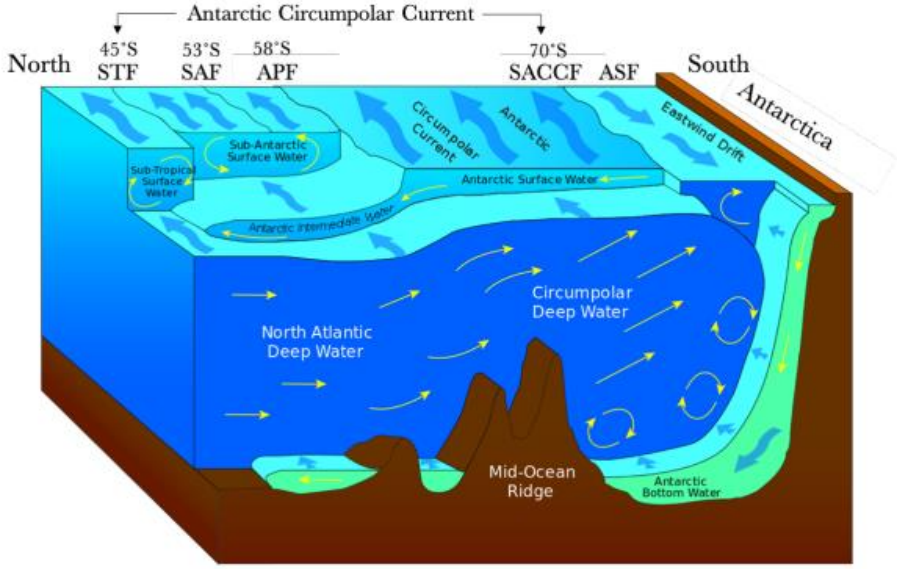

Figure 2.3: Image adapted from Rintoul and Naveira Garabato (2013) showing the Southern Ocean circulation. This vertical view displays the different water masses present, with the deepest one being the Antarctic Bottom Water (AABW), followed by the Circumpolar Deep Water (CDW) and the North Atlantic Deep Water (NADW) which is upwelled south of 50°S creating surface divergence. The upwelled water then flows northward as the Antarctic Surface Water (AASW) and Antarctic Intermediate Water (AAIW). At the surface, the illustration shows the flow of the Antarctic Circumpolar Current and its associated fronts, the Sub-tropical Front (STF), the sub-Antarctic Front (SAF), the Antarctic Polar Front (APF) and the Southern ACC Front (SACCF).

Of the 75% of NADW that enters into the bottom overturning cell, only some is transformed into Antarctic Bottom Water (AABW) through air-sea exchange, where the NADW is cooled, and by brine rejection, increases its salinity making it denser. AABW then flows equatorward, completing the overturning circulation and the remaining NADW flows into the Indian and Pacific Oceans as Circumpolar Deep Water (Marshall and Speer, 2012; Cunningham, 2005).

2.2.3 Atmospheric forcing in the Southern Ocean

The SO is dominated by westerly winds often termed, “roaring forties”, “furious fifties” and “screaming sixties” due to their intensity. These winds can create the strongest waves, which act as the interface between the upper ocean and lower atmospheric layer driving the air-sea flux of momentum, heat, moisture and gases (Derkani et al. 2021). The large-scale atmospheric pattern over the SO is driven by the circumpolar trough of low pressure, known as the Circumpolar Pressure Trough (CPT), at approximately 60°S, whereby the ACC’s transport is dependent on the force exerted by this trough’s zonal (east-west) wind stress. The wind stress is greatest between 50°S and 55°S, with a wind stress maximum near the axis of the ACC (Cunningham, 2005; Rintoul et al. 2001). Previous studies have suggested that energy input

from the wind into the ACC is balanced by bottom form stress (bathymetry drag). Calculations done across four main submarine ridges namely, Kerguelen, Macquarie, the Scotia Arc and South Pacific Ridges (*Figure 2.2*), showed that the total bottom pressure drop across the ridges was able to balance the zonal momentum imparted by the wind (Cunningham, 2005).

As the ACC encounters a ridge, SSH decreases which develops a high-pressure barotropic form stress on the upstream slope of the ridge, while downstream low-pressure forms, and as a result the ACC exerts energy across the ridge, removing energy from the flow by overcoming the pressure difference (*Figure 2.4*) (Cunningham, 2005). While this balance in energy has not yet been proven using observational data, numerical models have shown the energy lost by bottom form stress over the four ridges is sufficient to balance the energy obtained by the ACC through wind stress.

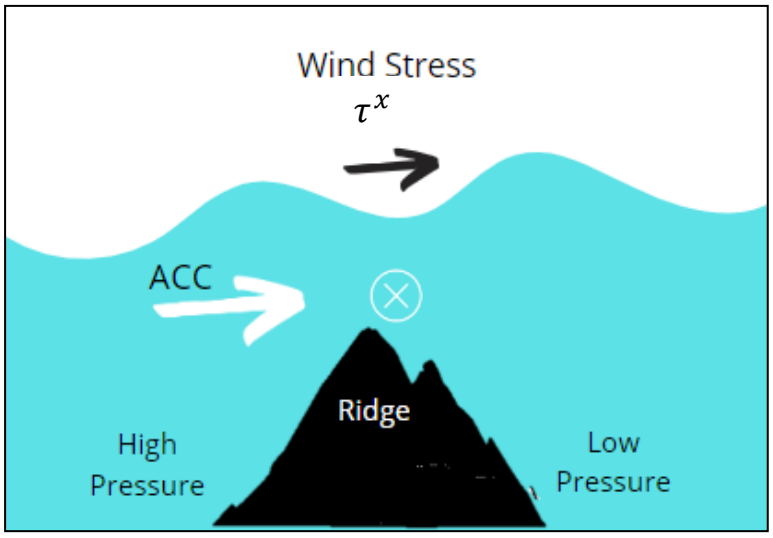

Figure 2.4: Schematic representing the process which facilitates the balance between bottom form stress (bathymetry drag) and zonal wind stress (τ^x). Equatorward flow (⊗) exists across the ridge as a result of the geostrophic pressure balance.

Eddies produced by the ACC are what balance the zonal wind stress by transmitting it through the water column, where it can be balanced by the bottom from stress. This is obtained in a similar way to the barotropic form stress and is called interfacial form stress, where the eddies disturb the density field producing the respective high and low pressures on either end of the ridge (Cunningham, 2005). This stress is then passed down into the water column until it reaches the bottom topography where the bottom form stress will then act to balance the wind input energy within the ACC. Using model output, the ACC's transport is proportional to the square root of wind stress however, this neglects other forcing processes that are likely to influence the ACC's transport (Cunningham, 2005).

Teleconnections are used to describe the climate links between regions that are geographically separate (Nigam and Baxter, 2015). Previous studies have shown three teleconnections to have the most significant influence on atmospheric variability within the SO; namely El Niño-Southern Oscillation (ENSO), Southern Annular Mode (SAM) and the Semi-Annual Oscillation (SAO) (Rouault et al. 2005; McKenna et al. 2020; van den Broeke, 2000). The ENSO phenomena is characterised by anomolous warming (El Niño) or cooling (La Niña) events occurring along the equator in the Pacifc Ocean (McKenna et al. 2020). Two Southern Hemisphere subpolar teleconnections are suggested to be linked and driven by ENSO; the Antarctic Circumpolar Wave (ACW) and the Antarctic Dipole (ADP) (Yuan, 2004).

The ADP is the main driver of surface air temperture and sea ice anomalies in the SO (Li et al. 2021). These anomalies are observed as SST and Sea Level Pressure (SLP) anomalies which propagate poleward in the Pacific and Atlantic sector of the SO and interact with the ACC resulting in the circulation throughout the entire SO (White et al. 2002). The ADP presents a seesaw-like connection between the Pacific and Atlantic sector of the SO and prevails due to the influence of ENSO which changes the intensity and shape of the Hadley cell, and alters the position of the polar jet stream. During an El Niño event, in the Pacific centre of the ADP, the Hadley cell contracts and strengthens, strengthening the jet stream which generates an equatorward shift of the storm tracks (Yuan, 2004). This results in fewer storms, positive (warm) SST anomalies and negative (reduced) sea ice anomalies. By contrast, in the Atlantic centre of the ADP, the Hadley cell expands and relaxes, weakening the jet stream and shifts the storm tracks poleward resulting in a higher frequency of storms, negative (cold) SST anomalies and positive (increased) sea ice anomalies. The La Niña event presents the reversed signals in the Pacific and Atlantic sectors of the SO (Yuan, 2004).

Analysis of atmospheric and oceanic variables have revealed the eastward propogation of anomalies in SST, precipitation, sea ice extent, SLP and winds around the SO as a wave called the ACW (Mélice et al. 2005). As recorded by White and Peterson (1996) the inititation of the ACW most likely occurs due to the presence of El Niño events in the equatorial Pacific, with the direct effects thereof, within the PEIs region being related with SST anomalies (Mélice et al. 2005). The influence of the varying ENSO phases on rainfall patterns have not been recorded at the PEIs (Rouault et al. 2005).

The SAM describes the shift in strength and position of the westerly wind belt throughout its various phases (Rouault et al. 2005; Lenton and Matear, 2007). The positive phase includes the

poleward shift and intensification of the westerly winds over the SO, while conversely the negative phase is characterised by the equatorward shift and weakening of the jet stream. Therefore during the positive phase of SAM, as the wind belt shifts southwards, the resulting winds speeds at the PEIs are reduced, while the negative phase of SAM presents the reversed conditions with increased wind speeds at the PEIs (Rouault et al. 2005). SAM is described as the main driver of atmospheric variability within the SO, where the shifting in strength of the westerly winds concurrently induces changes in the SO circulation. These include changes to the strength of the ACC, impacting the depth of the mixed layer and amount of oceanic heat transport. Northward flowing Ekman transport is also influenced by the phase changes of SAM, contributing to the increased upwelling along Antarctica's coastline (Lenton and Matear, 2007).

The characteristic CPT, over the SO, varies over a seasonal time scale, both in position and intensity, giving rise to the SAO as a result of the differences in heat budgets and energy uptake between Antarctica and its surrounding SO. A half-yearly cycle is created whereby in austral winter and spring the trough moves southwards (shrinking) and intensifies. Austral autumn and summer presents the northwards movement (expanding) and weakening of the CPT (Rouault et al. 2005; Van den Broeke, 2000). Annual temperature cycles arise, between Antarctica and the surrounding ocean, as a result of changes to the CPT, and it is these temperature cycles which reflect as varying SLP (Taschetto and Wainer, 2006). SAO has a seasonal impact on the PEIs climate, which was evident in the PEIs seasonal wind speeds (Rouault et al. 2005).

2.3 Prince Edward Islands

The Prince Edward Islands (PEIs) archipelago is made up of Marion and Prince Edward Islands (Ansorge and Lutjeharms, 2000). The islands were declared a Marine Protected Area (MPA) in 2013 and represent 80% of South Africa's Southern Ocean ecosystem diversity (RSA, 2013). Multiple terrestrial and marine ecosystems are supported by these islands and due to their extreme vulnerability to perturbations brought on by climate change, they are particularly useful for identifying and monitoring responses to such changes (Ansorge et al. 2017). This section will review the PEIs oceanographic setting and past variability and climate change observations.

2.3.1 Prince Edward Islands oceanographic setting

Marion Island (46º 54'S; 37º 45'E), the larger of the two sub-Antarctic islands, measures over 270 km^2 and is located approximately 19 km southwest of the smaller Prince Edward Island (46º 38'S; 37º 57'E) with an area of 45 km^2 (*Figure 2.5*). The PEIs, together with South Georgia, Bouvet, Crozet, Kerguelen, Heard, Auckland and Campbell Islands, represent the only land in the SO (Chown and Froneman, 2008; Ansorge and Lutjeharms, 2000).

The bottom topography from which the PEIs rise is intricate, with steep escarpments and a shallow plateau between 40-200 m that separates them. The islands are relatively isolated in a deep and vast SO (> 3000 m), with the closest landmasses being the Crozet Island group situated 950 km to the east and South Africa over 2000 km to the northwest (Chown and Froneman, 2008; Ansorge and Lutjeharms, 2000). The islands are of volcanic origin and are considered young in geological terms, with the oldest recorded date of lava on Marion Island being 450 000 years ago, inferring the islands to be less than a million years old (Chown and Froneman, 2008; Quilty, 2007).

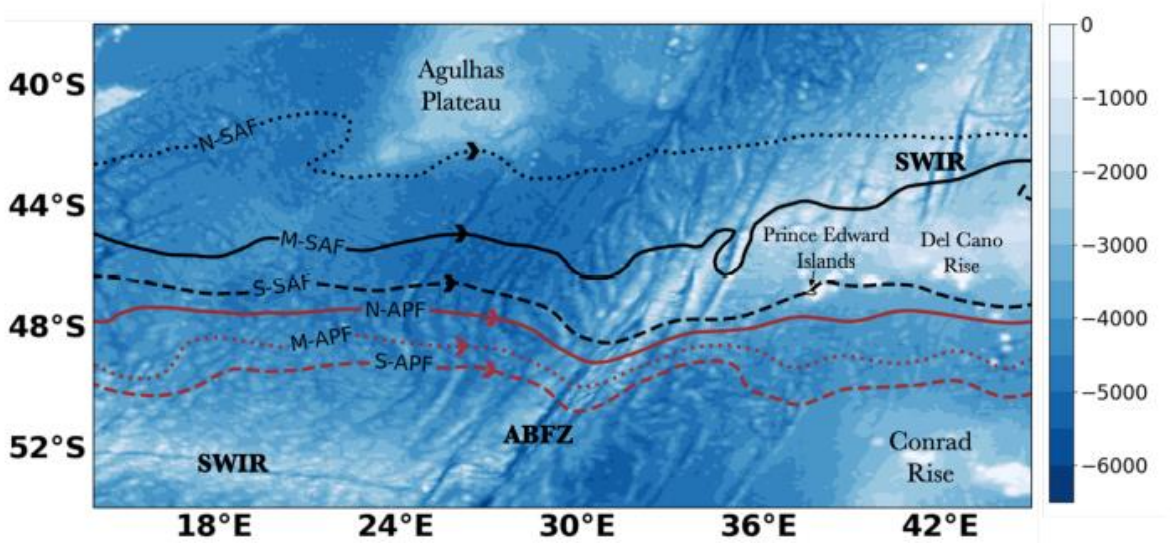

Figure 2.5: Map taken from Toolsee (2022) showing the bathymetry of the Southern Ocean surrounding the Prince Edward Islands. The mean positions of the three branches for the sub-Antarctic Front (N-SAF, M-SAF, S-SAF) and for the Antarctic Polar Front (N-APF, M-APF, S-APF) have been identified according to the method outlined by (Sokolov and Rintoul, 2009). Other abbreviations include the South-West Indian Ridge (SWIR) and the Andrew Bain Fracture Zone (ABFZ).

The shallow Del Cano Rise lies northeast of the PEIs and the Southwest Indian Ridge (SWIR) is located on the western side of the PEIs. The SWIR is a mid-ocean ridge that spans across the ocean floor from the south-west Indian Ocean basin to the south-east Atlantic Ocean, passing through the SO. It includes multiple fracture zones, with the Andrew Bain Fracture Zone (ABFZ), at 50°S; 30°E, being the largest and closest to the PEIs (*Figure 2.5*). Using

hydrographic data, the ABFZ has been shown to influence the flow of the ACC, contributing to the high level of mesoscale variability observed in the region (Sokolov and Rintoul, 2009; Froneman et al. 2002; Toolsee et al. 2021).

The PEIs are positioned in the direct path of the ACC, within the Antarctic Polar Frontal Zone (APFZ) of the SO (Sokolov and Rintoul, 2009; Ansorge and Lutjeharms, 2002). Previous studies have shown the northern (sub-Antarctic Front) and the southern (Antarctic Polar Front) boundaries of the APFZ concentrate the ACC's transport and the SWIR acts as a choke point to the ACC's flow. Upon approaching the ridge, part of the ACC is forced to diverge, while a substantial portion of the ACC is funneled through the ABFZ (Ansorge et al. 2010; Sokolov and Rintoul, 2009; Froneman et al. 2002; Ansorge and Lutjeharms, 2005). Froneman et al. (2002) observed the merging of the APF with a northern frontal band but the sub-surface temperature conditions of the band, being 3.5 ^{o}C, did not coincide with the expected sub-surface signature of the SAF which is typically 6 ^{o}C. Upon further investigation it was concluded that the ABFZ funnels and merges the APF with the S-SAF, while the M-SAF and N-SAF diverge and continue flowing north-eastwards (Froneman et al. 2002). Further east of the ABFZ, the APF and S-SAF separate once again, resulting in the APF diverting south of the PEIs and the SAF north of the PEIs (Ansorge et al. 2010; Sokolov and Rintoul, 2009; Froneman et al. 2002; Ansorge and Lutjeharms, 2005).

When the SAF is positioned far to the north of the PEIs, the APFZ widens up to 5^{o} of latitude and the advective forces decrease in strength, contributing to the production of eddies within the shelf region between the two islands. The eddies assist in prolonging the residence time of water masses within the region as opposed to their usual rapid movement downstream of the islands. Conversely, when the SAF is closer to the PEIs, the strong jets associated with the fontal branches prohibit the formation of eddies within the inter-island region (Ansorge and Lutjeharms, 2002). The SWIR also results in the enhanced generation of cyclonic and anticyclonic eddies (Ansorge et al. 2010). From these findings, it has been deduced that the SWIR and the positioning of the PEIs results in the distortion of the ACC's flow, contributing to the intense spatial and temporal variability of this region (Froneman et al. 2002).

While extensive hydrographic surveys had been done within the inter-island region of the PEIs, the large-scale circulation and influences of the SAF and APF on the islands were severely understudied. To resolve this, the first extensive cruise was conducted in 1989, called the Marion Offshore Ecological Study 2 (MOES 2). A replicate cruise was required thereafter to

validate the results and in 1997 the Marion Island Oceanographic Survey 2 (MIOS 2) was orchestrated (Ansorge and Lutjeharms, 2000). The major findings from these voyages included that the SAF position recorded during the MIOS 2 cruise was much father south of the PEIs than that recorded in MOES 2. Eddies were observed during both cruises, where MOES 2 observed a cold core eddy, originating from the APF, south of the islands and a warm core eddy north of the islands, believed to have been spawned from farther north. Downstream of the islands two counter-rotating eddies were observed during MIOS 2, a northen cyclonic eddy was recorded, retaining properties similar to those of Antartic Surface Water (AASW) inferring that it would have originated from the APF and been advected to the north where it was trapped within the APFZ. The anticyclonic eddy located further south displayed density and temperataure characteristics resembling those of sub-Antarctic Surface Water (SASW) origin suggesting this eddy was shed from the SAF. These results concluded that the leeward side of the PEIs is a region of considerable meridional exchange of both physical and chemical properties and that the mesoscale varaibility and frontal movements in the surrounding oceanic area strongly impact the surface and sub-surface hydrographic conditions at the islands (Ansorge and Lutjeharms, 2000).

Despite the high nutrient levels across the wider SO, the PEI surroundings is considered a low chlorophyll region with the exceptions of increased concentrations of chlorophyll *a* at frontal boundaries. Studies have shown the enhanced primary productivity at the Subtropical Convergence is evident through distinct algal bloom events (Chown and Froneman, 2008). The same is true along the SAF and APF, whereby localised upwelling resulting from the meandering of the fronts and eddy shedding brings nutrient-rich water to the surface (Chapman et al. 2020). These upwelling processes are not only of immense importance to the lower trophic level ecosystems surrounding the fronts themselves but are also important for many seabirds and marine mammals feeding both far from and near the PEIs. Correlations between high concentrations of seabirds and frontal systems have been recorded, and thus the dynamics of the fronts therefore have a direct impact on the PEIs ecosystem (Chown and Froneman, 2008). Meridional transport of heat, salt, nutrients and other water properties can be carried across frontal bands by eddies (Volkov et al. 2010). Eddies and the meandering of the fronts within the PEI region therefore have a direct impact on primary productivity in the region. When the SAF is located further north of the islands, eddies and various water masses are retained within the inter-island region supporting algae blooms. Studies have shown that not only phytopankton species originating from the sub-Antarctic region are found at the PEIs but

that subtropical, tropical and Antarctic species have been recorded, indicative of the various water masses entering into this region from which these species originate (Chown and Froneman, 2008; Ansorge et al. 2017; Ansorge et al. 2010).

2.3.2 Variability and climate change at the PEIs

The remoteness that the PEIs possess makes them the ideal location for studying responses to climate change. Mélice et al. (2003) performed statistical analysis using nearshore daily SST values, recorded from Marion Island, from 1949 to 1998 and recorded an increase of 1.4 ^{o}C over the 49 year period, or a 0.03 ^{o}C rise per year. In addition to this, total annual precipitation has decreased by 25%, and an increase in extreme events and in winds from the northwest have been recorded (Rouault et al. 2005; Ansorge et al. 2017). Air temperatures at Marion Island have increased by 1.2^{o}C, between 1969 and 1999, as documented by Smith (2002) and yearly sunshine hours have increased by 3.3 hours since the 1950's (Ansorge et al. 2017). These variations in the climate systems surrounding the islands directly influence the ecoystem with studies showing that the Antarctic species inhabiting this region have small tolerances to environmental changes, suggesting that immense consequences could ensue with climate change (Rouault et al. 2005).

Shangheta (2021) performed an updated study to Mélice et al. (2003) by analysing the daily SST data from 1949 to 2018, finding that while the trend of increasing SST and air temperature still persists, the rate of increase was smaller than previously recorded with a rise of 0.022^{o}C per year. This study further corroborated the decrease in rainfall, wind speed and surface air pressure that was previously observed in other studies, however, no change in the hours of sunshine was observed.

Increased temperatures across the sub-Antarctic are consistent with changes in the large-scale atmospheric circulation. The changes observed at Marion Island are believed to be brought on specifically by changes in regional atmospheric circulation (Chown and Froneman, 2008). Rouault et al. (2005), using meterological and SST data from Marion Island along with NCEP reanalysis data, recorded that since the 1960s the most significant changes in the local climate system of this region occurred from October to May and that these changes and the warming of Marion Island are consistent with the increased influence of the atmospheric South Indian Ocean anticyclone. The position and intensity of the South Indian Ocean anticyclone has not changed but rather its influence on the local climate system of Marion Island has increased

which was linked to the phase change of the semiannual oscillation in the SO (Chown and Froneman, 2008; Rouault et al. 2005). Increased amounts of warmer water are being advected into the mid-latitudes of the sub-Antarctic due to variations in the South Indian Ocean anticyclone, which in turn could be linked to the suggested poleward shift of the SAF. Changes in the latitudinal position of the SAF could result in the island's ocean temperature being dominated by warmer sub-Antarctic waters. Subsequently, the close proximity of the fronts to the islands would allow for the strong associated currents to prevail in the inter-island region, reducing the retention of water masses and resulting in the decline of phytoplankton blooms within the region (Chown and Froneman, 2008; Ansorge et al. 2010; Louise Allan et al. 2013). Drastic changes in the distribution of species and in the total productivity of the SO are expected to be seen with climate change and suggested positional changes of fronts at the PEIs (Ansorge et al. 2017).

2.4 Taylor Column Theory at the Prince Edward Islands

Over 5 million breeding pairs of top predators have been estimated to occupy the islands during the peak breeding season. The energy required to sustain these populations comes from the intimate interconnection between the oceanic environment and the PEIs themselves (Ansorge and Lutjeharms, 2000; Ansorge et al. 2017). This, however, poses the question of what mechanism is at work, in the first place, to produce the energy that supports this complex and diverse ecosystems?

One possible theory put forward was the ability of the islands to locally enhance chlorophyll *a* (chl *a*) concentrations and support phytoplankton production, termed the Island Mass Effect (IME) (Ansorge et al. 2017). Lamont and Toolsee (2022) presented the first local-scale investigation, highlighting seasonal and spatial variation of chl *a* in support of the IME at the PEIs. The main findings from this study included the increase of chl *a* during austral autumn and summer, which correlated with warmer surface waters, higher light levels and a shallow mixed layer depth (± 80 m). While these observations coincided with previous findings and support the IME theory, mention of several other processes were made to account for the increased primary production. Such processes included frontal variations carrying water masses with increased nutrients and biota into the PEIs vicinity, the bifurcation of the ACC, wake effects, turbulent mixing and isopycnal shoaling caused by eddies in the lee of the islands,

all of which could be major drivers of enhanced vertical exchange of nutrients and contribute to the retention and accumulation of nutrients at the islands, stimulating phytoplankton growth.

Similarly, hydrographic and biological studies done in the inter-island region revealed Antarctic planktonic species to be dominating a sub-Antarctic environment and higher concentrations of zooplankton northeast of the islands were suggested to be the result of phytoplankton production at the islands (Ansorge and Lutjeharms, 2000). Studies thereafter, however, argued against this hypothesis based on the low silica concentrations found in surface waters, which is required for phytoplankton production, and it was suggested once again that the shifting of fronts could cause the introduction of foreign zooplankton through water masses intruding into the APFZ (Ansorge and Lutjeharms, 2000).

A second theory was therefore proposed, the Von Kármán Vortex Street theory which explains that when there is strong enough wind shear together with the PEIs interacting with the ACC, Von Kármán Street vortex fields form on the leeward side of the islands. This feature includes cyclonic and anticyclonic eddies resulting in upwelling and downwelling respectively. Once again, while these findings held truth, such patterns could also be attributed to vagrant eddy formation and frontal meandering (Ansorge and Lutjeharms, 2000).

Perissinotto and Duncombe Rae (1990) performed a dimensional analysis and showed the eddies being observed at the PEIs were not the result of wake vortex shedding and that the dominant flow was geostrophic rather than frictional. They proposed that a Taylor column could exist for majority of the flow conditions at the islands (Ansorge and Lutjeharms, 2000; Lamont et al. 2019). A Taylor column is an enclosed anticyclonic vortex, with an inverted cone shape which would enhance water retention and develop local scale upwelling events (Figure 2.6) (Ma et al. 2021; Ansorge and Lutjeharms, 2000; Lamont et al. 2019).

The stationary anticyclonic eddy associated with the Taylor column is believed to be situated in the inter-island region over the shallow plateau of the PEIs, while the cyclonic eddy is proposed to be advected downstream of the islands (Perissinotto and Duncombe Rae, 1990; Ansorge and Lutjeharms, 2000). Lamont et al. (2019) supported the existence of a Taylor cloumn at the PEIs using two mooring deployments which recorded westward flow within the bottom layers of the water column. It was noted that while the westward flow could have been attributed to mesoscale eddies and meandering fronts in the region, many of the observations appeared to be unrelated to such processes. Additionally, the findings revealed that the Taylor column may be a more permanent structure than previously thought and that depending on their

orientation to the PEIs, deep-sea eddies and frontal movements may either enhance the Taylor column, resulting in decreased bottom temperatures or dissipate it, resulting in warmer bottom waters on the shelf.

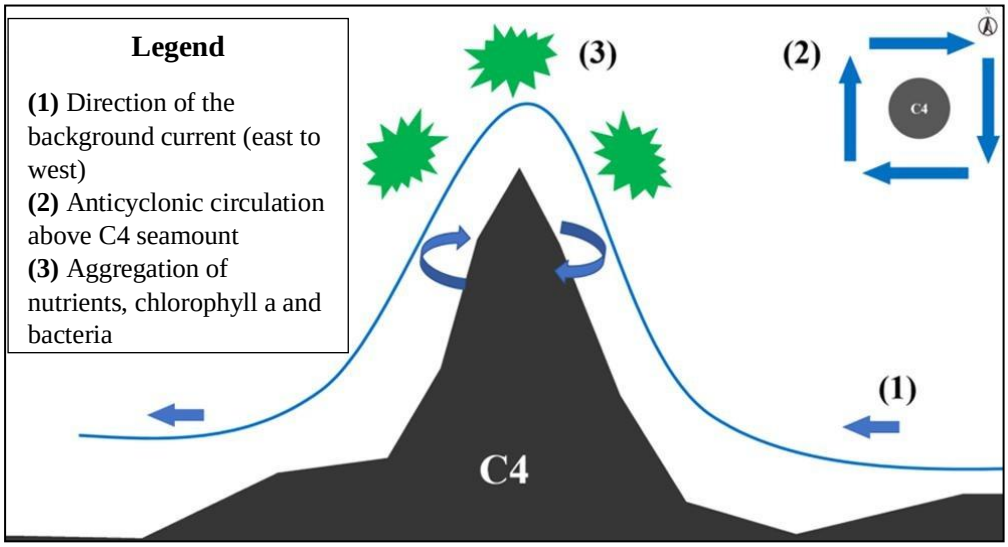

Figure 2.6: Schematic taken from Ma et al. (2021) demonstrating the flow structure, for the Northern Hemisphere, of a Taylor column around a seamount, called C4, in the Tropical Western Pacific Ocean. Labelling corresponds to the legend. The schematic labelled (2) displays the top view of the seamount.

CTD data from the 1980s revealed similar findings where anitcyclonic motion was observed on the shelf of Marion Island during four separate occurrences and the low-salinity signals recorded in this region were described at the result of freshwater run-off from the islands which could have been retained due to the posible Taylor column feature (Ansorge and Lutjeharms, 2000). This theory has been criticized because the horizontal scales of the PEIs are thought to be less than those required, in theory, for the formation of a Taylor column (Ansorge and Lutjeharms, 2000). Taylor columns have also only been proven to exist over shallow isolated seamounts, whereas the PEIs protrude above the sea surface. However, all previous studies have lacked the high spatial resolution data within the PEI region necessary to compile a comprehensive description on whether a Taylor column persists in this region and where exactly it persists, as it is still unclear if the feature encircles the entire inter-island plateau or if it soley resides around Marion Island (Ansorge and Lutjeharms, 2000; Lamont et al. 2019). The presence of such a feature would play a crucial role in preserving the dynamic ecosystems of the PEIs by retaining nutrients and enhancing productivity within the inter-island region (Lamont et al. 2019; Perissinotto and Duncombe Rae, 1990).

Thus, the aim of the present study is to use the high spatial and temporal resolution of the GLORYS model output to identify the surface and sub-surface oceanographic variability around the PEIs and the drivers thereof. This will include examining the suitability and accuracy of the GLORYS model within the PEI region and whether the *in situ*, satellite and model conditions are suitable to observe the existence of a Taylor Column at the islands.

Chapter 3. Data and Methods

This chapter details the various datasets and analysis methods used to best address the aim of this study. As mentioned in *Chapter 1*, the main aim of this study is to increase the knowledge of surface and sub-surface oceanographic variability and its drivers at the Prince Edward Islands (PEIs).

To achieve the aim set out by this study, the following three key questions were investigated:

1. What is the suitability and accuracy of the GLORYS12V1 model output compared to existing *in situ* and satellite data around the PEIs?
2. What is the surface and sub-surface hydrographic variability surrounding the PEIs, observed from the GLORYS12V1 model, and what are the drivers thereof?
3. Are the *in situ*, satellite and model conditions suitable for the formation and existence of a Taylor column at the PEIs?

To answer these key questions, a combination of *in situ*, satellite data and model output, was obtained and analysed using a variety of figures produced using Python Software, Python version 3.8 available at https://www.python.org/downloads/release/python-380/.

3.1 *In situ* Data

The *in situ* data used included data obtained from various hydrographic cruises, climatological *in situ* data from WOA18 (World Ocean Atlas 2018) and CARS09 (CSIRO Atlas of Regional Seas 2009), as well as sea surface temperature from SAWS (South African Weather Services).

3.1.1 Cruise Data

Annual hydrographic sampling is now done at the PEI region, aboard the SA Agulhas *II*. The first survey conducted in 2013, covered an extensive grid within the surrounding PEI region. Thereafter, since 2014, only two transects have been routinely sampled, one being a north-south (N-S) transect upstream of the islands and the other an east-west (E-W) transect crossing over the inter-island region (*Figure 3.1*). The N-S transect, comprised of between seven and nine stations (*Table 3.1*), is located at the mean longitudinal position of 37.3^{o} E and was the focus for this study (*Figure 3.1*). Frontal movement is the reason for the variation in number

of stations between April 2013 and April 2018 whereby water properties of the sub-Antarctic Front and Antarctic Polar Front were able to be captured through the addition of CTD stations to the N-S transect for certain years.

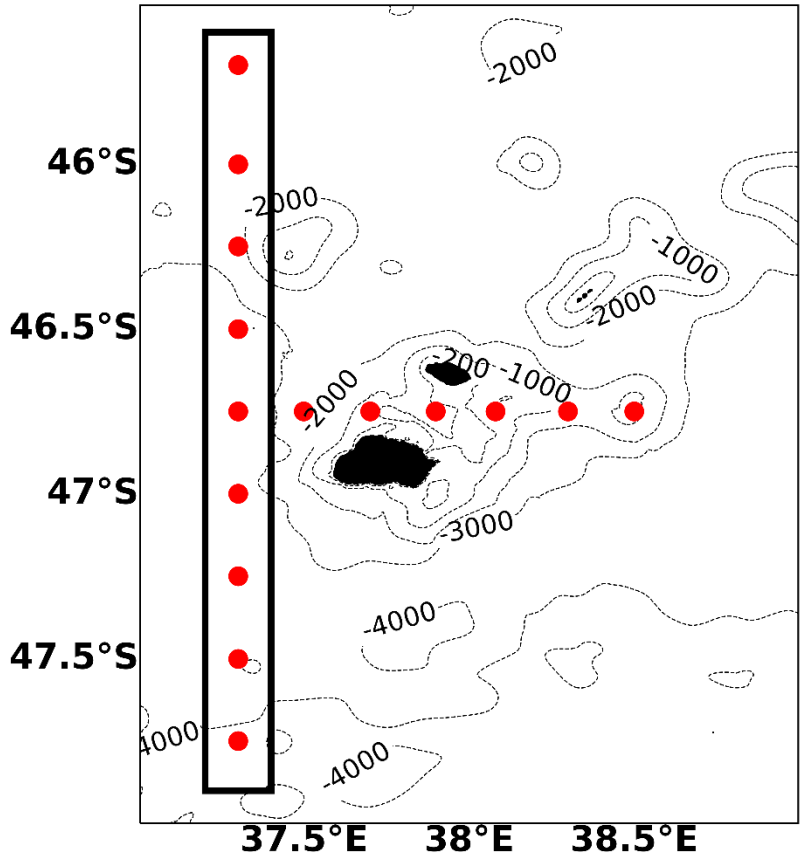

Figure 3.1: GEBCO2022 bathymetry in the vicinity of the Prince Edward Islands. Red dots represent the CTD station positions for both the north-south (N-S) and east-west (E-W) transects between April 2013 and April 2018. A black box highlights the N-S transect.

The aim of these annual transects is to obtain data on the vertical structure of the hydrographic patterns upstream of the PEIs, which can be used for event-scale and future long-term analyses (Lamont et al. 2019). In order to obtain this data, multiple different Sea-Bird Electronics (SBE) 911 Plus Conductivity, Temperature and Depth (CTD) instruments were used. CTD casts were performed at each of the routine stations, producing vertical profiles of temperature and salinity, which were used to calculate Conservative temperature (^{o}C) and Absolute salinity (g kg^{-1}), similar to Lamont et al. (2019). Individual seawater samples were collected at specific depths and the salinity was analysed either onboard or in the laboratory post-cruise using a Guildline Portasal salinometer, for calibration of the CTD conductivity sensors (Lamont et al. 2019).

Table 3.1: Dates, number (#) of CTD stations and latitudinal extent of the N-S transect conducted annually, upstream of the Prince Edward Islands at a mean longitudinal position of 37.3 °E.

Cruise	Date	# CTD Stations	Latitudinal Extent
PEI_2013	20-22 April 2013	7	45.9 – 47.5° S
PEI_2014	10-12 April 2014	8	45.8 – 47.5° S
PEI_2015	23-25 April 2015	8	45.7 – 47.5° S
PEI_2016	17-19 April 2016	8	45.7 – 47.5° S
PEI_2017	17-19 April 2017	8	45.7 – 47.5° S
PEI_2018	24-26 April 2018	9	45.7 – 47.7° S

The CTD data was processed using SeaBird data processing software called "SBE Data Processing" (versions 7.22.4; 7.23.1; 7.23.2 and 7.23.5), organised according to the dates of transects and only the N-S transects for the full available depth profiles were extracted and imported into Python. The E-W transect was not used because the spatial resolution resulting from the CTD station spacing (8 nm) was not able to capture the full extent or complexity of the hydrographic variability throughout the water column across the island shelf.

3.1.2 World Ocean Atlas 2018 Data

WOA18 (World Ocean Atlas 2018) is a set of climatological *in situ* data, objectively analysed on 0.25°, 1° and 5° grids at 57 standard depth levels from the surface to 1500 m. The focus of this study required the highest resolution available and thus the quarter degree grid was selected which only includes climatological *in situ* temperature (°C) and salinity (PSU) fields (Locarnini et al. 2019). The monthly climatologies of temperature and salinity are available as an average of six 'decadal' time periods: 1955-1964, 1965-1974, 1975-1984, 1985-1994, 1995-2004 and 2005-2017, as well as a thirty year "climate normal" period between 1981-2010 (Locarnini et al. 2019).

The data sources on which this atlas is based is a combination of surface and sub-surface historical *in situ* data and surface only data obtained from the Global Oceanographic Data Archaeology and Rescue (GODAR) project, and the World Ocean Database project (WOD). The historical *in situ* temperature and salinity profile data were compiled from bottle samples (Reversing thermometers), Mechanical Bathythermographs (MBT), ship-deployed Conductivity-Temperature-Depth (CTD) instruments, Digital Bathythermographs (DBT),

Expendable Bathythermographs (XBT), profiling floats, moored and drifting buoys, gliders, undulating oceanographic recorders (UOR), and pinniped mounted CTD sensors (Locarnini et al. 2019; Zweng et al. 2019). Additionally, ship mounted thermosalinograph (TSG) data was included as part of the surface salinity profiles dataset (Zweng et al. 2019).

Quality control procedures of the temperature and salinity data were a complex task due to the lack of data and metadata, in both time and space. As a result, several statistical checks were applied, and subjective judgement was used. These analyses are described in detail by Locarnini et al. (2019) and Zweng et al. (2019) for temperature and salinity, respectively.

The WOA18 data is made freely available via the National Centers for Environmental Information (NCEI) archives at https://www.ncei.noaa.gov/access/world-ocean-atlas-2018/. Temperature and salinity quarter-degree monthly fields were downloaded, along with the respective number of observations, as Climate and Forecast (CF) compliant Network Common Data Format (NetCDF) files.

3.1.3 CSIRO Atlas of Regional Seas 2009 Data

CARS2009 (CSIRO Atlas of Regional Seas 2009) is a compilation of both gridded mean ocean water properties, from modern day measurements, and of average seasonal cycles. CARS2009, hereafter referred to as CARS09, used in this study, covers the globe's oceans on a 0.5^{o} grid, in comparison to its prior version CARS2006 which only had tropical Northern and Southern Hemisphere coverage (Dunn, 2014).

CARS09 data is derived mainly from historical sub-surface oceanographic measurements such as, ship-based CTD and hydrology casts from CSIRO Marine archives, the World Ocean Circulation Experiment (WOCE) Global Hydrographic Program (GHP) and from the July 2008 update of the World Ocean Database (WOD). A smaller portion of data is acquired from research vessel instrument profiles and autonomous profiling buoys namely Argo and Tao (Dunn, 2014).

The observational data was interpolated to 79 standard depth levels (0–5500 m) and an adaptive-length scale loess mapper was used to optimise the resolution in data-rich areas, producing the 0.5^{o} grid (Dunn, 2014).

CARS09 data is freely available in multiple formats at http://www.marine.csiro.au/atlas/ spanning between 1 January 1985 to 31 April 2009. The purpose of this study required monthly

climatological fields of temperature (°C) and salinity (PSU) to be downloaded, for the entire timespan, in NetCDF format.

3.1.4 South African Weather Service Data

Daily sea surface temperature (SST) has been measured at Marion Island from 1949 to the present. The meteorological station is positioned on the north-eastern coastline of Marion Island (*Figure 3.2*). The parameter was previously measured by using a specialised bucket, with a mercury bulb thermometer attached, to scoop up ocean water from a jetty. The temperature was recorded while the thermometer was still immersed in the water (Mélice et al. 2003). More recently, a similar method has been implemented, with the difference of the mercury thermometer being housed in white tubing and the temperature being read immediately after emerging from the water (Shangheta, 2021).

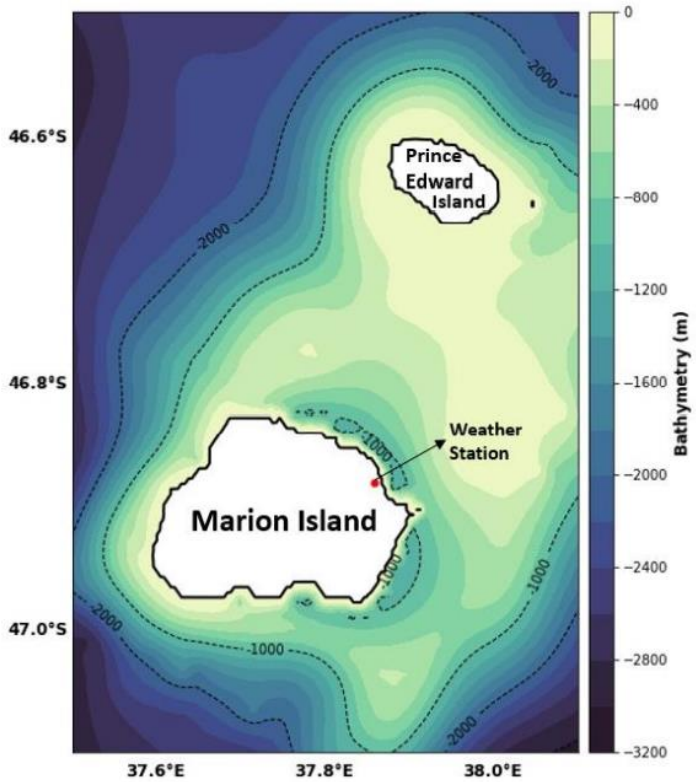

Figure 3.2: Map taken from Shangheta (2021) showing the location of the meteorological station at Marion Island.

This daily *in situ* data, acquired from the South African Weather Service (SAWS), covers the period from 1 January 1949 to 31 December 2021, of which only data between 16 January 1993 and 16 May 2020 was used to match the available model output period. The data was

then imported and arranged by date in an Excel spreadsheet and the data affected by instrumental errors (Mélice et al. 2003) over the period November 1998 to November 2000, was manually removed. Although Melice et al. (2003) suggested that any potential incorrect observations on a daily scale would be removed by the process of averaging over a full month, we used the procedures outlined by Shangheta (2021) for the detection and removal of remaining outliers. The outliers were removed as a function of the daily climatological mean (the average for each day of the year) and the daily climatological standard deviation, under the assumption that the data followed a normal distribution. This was calculated for the period between January 1949 to December 2018, where every data point that fell 4 standard deviations above and below the daily climatological mean were removed (Shangheta, 2021).

3.2 Satellite Data

The satellite data used in this study comprised of absolute dynamic topography (ADT) data, sea surface temperature (SST) data and sea surface salinity (SSS) data which were obtained from various online platforms.

3.2.1 Absolute Dynamic Topography Data

Sea level datasets used to be distributed on the Archiving, Validation and Interpretation of Satellite Oceanographic data (AVISO) altimetry portal until it was taken over by Copernicus Marine Environment Monitoring Service (CMEMS), in 2015, and by the Copernicus Climate Change Service (C3S) in 2016 (Taburet et al. 2021). For this investigation, the dataset used was provided by C3S and generated by the Data Unification and Altimeter Combination System (DUACS) which collates measurements from two satellite altimeters. C3S primarily focuses on long-term variability of the ocean's sea level, therefore requiring stable and homogenous sea level data. This is achieved through the implementation of a two-satellite constellation throughout the entire production period (Taburet et al. 2021).

The DUACS reprocessed delayed-time sea level product undergoes a processing sequence to produce the final product. The first step is the acquisition of Level 2 altimetry data. Thereafter, pre-processing of this data occurs where corrections are applied. Input data quality control is then done to ensure that the most accurate altimeter data is being used and algorithms are applied for the detection and resolution of more subtle errors (Legeais, 2021). The multi-

mission cross calibration procedure follows to certify accurate and consistent data flow from all satellites. Along-track Level 3 product generation occurs by projecting the Level 2 data onto theoretical co-located track positions, where final quality controls can occur. Using optimal interpolation (OI), the Level 4 gridded merged maps of all the measurements are made from all altimeter missions (Legeais, 2021). Lastly, output checks and final quality controls are done to produce the product of Level 4 gridded, daily sea level data which is freely available from CMEMS at https://marine.copernicus.eu/.

The Earth's shape is described as an ellipsoid, rather than a sphere due to the Earth's width, height and length parameters being unequal. The reference ellipsoid is a smoothed, mathematical idealisation of Earth's surface. While the reference ellipsoid is accurate in capturing Earth's shape, it fails to account for Earth's topography, therefore introducing the geoid model. The Earth's Geoid is the average shape that the ocean's surface would be if it were under the influence of gravity and rotation alone. The ocean is influenced by a variety of factors such as wind, tides, precipitation, differential heating, among others which impact and change the Geoid from its average shape (*Figure 3.3*). The shape of the Geoid is higher than the reference ellipsoid when there is an excess in mass, and it is then lower when a mass deficit is experienced. The difference in height between the average Geoid and Earth's true Geoid, caused by ocean and atmosphere perturbations, is the Absolute Dynamic Topography (ADT, m).

Sea Surface Height (SSH) above the reference ellipsoid (*Figure 3.3*) is obtained from Equation 1.

$$SSH = Orbit - Altimetric\ range \quad \textbf{(1)}$$

Using SSH we can obtain Mean Sea Surface (MSS), which is the surface above the reference ellipsoid but includes the Geoid. The MSS is obtained by calculating the temporal mean SSH over a period N (Taburet et al. 2021) using Equation 2.

$$MSS_N = \langle SSH \rangle_N \quad \textbf{(2)}$$

Sea Level Anomaly (SLA) is therefore the anomaly of the SSH signal around the mean according to Equation 3.

$$SLA = SSH - MSS_N \quad \textbf{(3)}$$

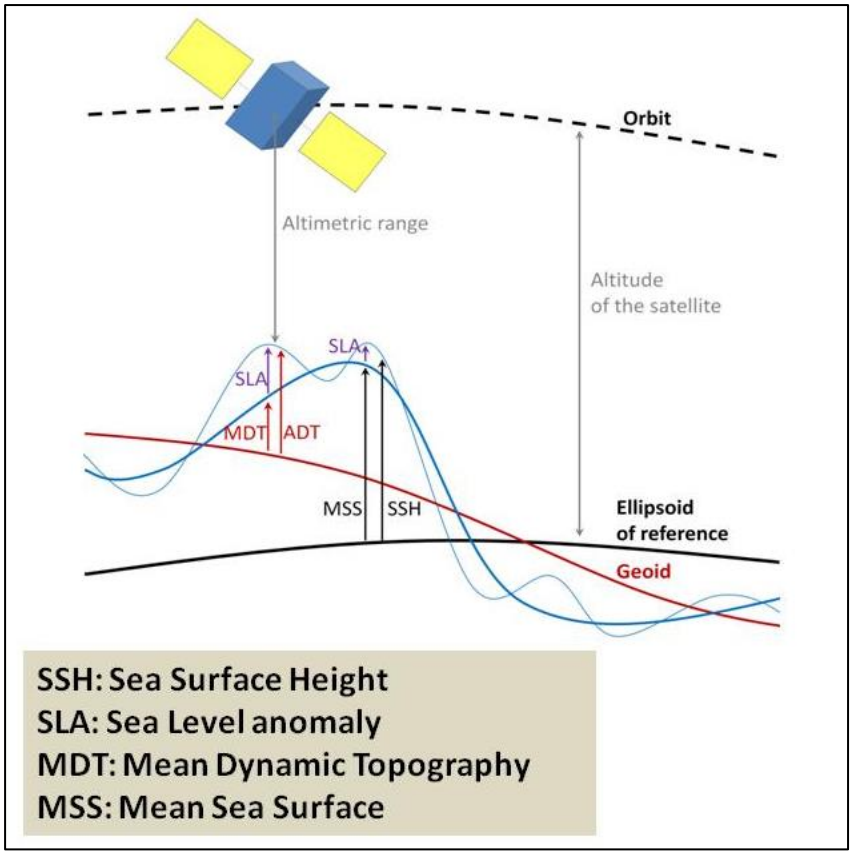

Figure 3.3: Schematic taken from Taburet et al. (2021) to explain the concept of Sea Surface Height using altimetry data.

Mean Dynamic Topography (MDT) is the surface above the Geoid and is obtained by taking the temporal mean SSH over period N and subtracting the Geoid height using Equation 4.

$$MDT = \langle SSH \rangle_N - Geoid \quad \textbf{(4)}$$

$$MDT = MSS_N - Geoid$$

The ADT is therefore the SSH corrected for the Geoid height and can be calculated using Equation 5 (Taburet et al. 2021).

$$ADT = SLA + MDT \quad \textbf{(5)}$$

$$ADT = SSH - MSS_N + MDT$$

This Level 4 reprocessed daily ADT product is called SEALEVEL_GLO_PHY_CLIMATE_L4_MY_008_057 and has a 0.25° (Latitude) x 0.25° (Longitude) spatial resolution with global coverage. The data spans between 1 January 1993 and 9 February 2022 and the variables used in this study were 'adt' (Absolute Dynamic

Topography, m), 'ugos' (Absolute geostrophic velocity: eastward zonal component, m s^{-1}) and 'vgos' (Absolute geostrophic velocity: northward meridian component, m s^{-1}).

3.2.2 Sea Surface Temperature Data

To investigate Sea Surface Temperature (SST) surrounding the Prince Edward Island (PEIs), a satellite product was selected due to the lack of high spatial and temporal resolution *in situ* data in the Southern Ocean (SO), owing to the remoteness and hostility of this environment (Gille, 2008). A gridded reprocessed, Level 4, SST product known as SST-GLO-SST-L4-REP-OBSERVATIONS-010-011 was used (Worsfold et al. 2022). This dataset is produced by the Operational SST and Sea Ice Analysis (OSTIA) system at the Meteorological (Met) Office, which makes use of re-processed European Space Agency Sea Surface Temperature Climate Change Initiative (ESA SST CCI), C3S (Merchant et al. 2019) European Organisation for the Exploitation of Meteorological Satellites (EUMETSAT), Remote Sensing Systems (REMSS) satellite data and *in situ* SST data from the HadIOD dataset (Atkinson et al. 2014; Worsfold et al. 2022).

The dataset was obtained from the CMEMS platform at https://marine.copernicus.eu/ on a 0.05° (Latitude) x 0.05° (Longitude) global coverage grid, with a monthly temporal resolution from 1 October 1981 to 31 December 2021. The variable 'analysed_sst' (analysed sea surface temperature, K) was selected and downloaded in NetCDF format and was converted from Kelvin (K) to degrees Celsius (°C) using the equation (Helmenstine, 2019):

$$°C = K - 273.15$$

3.2.3 Sea Surface Salinity Data

Similar to SST, satellite Sea Surface Salinity (SSS) was selected due to the lack of high spatial and temporal resolution *in situ* data. This product makes use of a multivariate OI algorithm to combine four different input data types to produce a global, gap-free Level 4 reprocessed SSS and Sea Surface Density (SSD) product known as MULTIOBS_GLO_PHY_S_SURFACE_MYNRT_015_013, developed by the COnsiglio Nazionale delle Ricerche (CNR) (Nardelli and Pisano, 2021) and includes four datasets, of which the multi-year reprocessed monthly data (dataset-sss-ssd-rep-monthly) was selected.

The OI algorithm combines background field data, *in situ* salinity measurements, Soil Moisture Ocean Salinity (SMOS) satellite images and satellite SST information to produce the final reprocessed SSS and SSD product (Nardelli and Pisano, 2021). The background field data was previously based on the Coriolis Ocean database ReAnalysis (CORA) analyses but is now being taken from the older version of the monthly reprocessed dataset MULTIOBS_GLO_PHY_REP_015_002. The *in situ* salinity measurements are obtained from CTD and Argo profiles, found in two internal CMEMS datasets known as INSITU_GLO_TS_ASSIM_NRT_OBSERVATIONS_013_047 (near real-time) and INSITU_GLO_TS_ASSIM_REP_OBSERVATIONS_013_051 (reprocessed observations) (Nardelli and Pisano, 2021). The SMOS satellite data provides daily ocean salinity values that are used to produce the dataset, which has been corrected for land-sea corruption and latitudinal bias by the Centre Aval de Traitement des Données SMOS (CATDS). Finally, the satellite SST information used is the near real-time and multi-year Level 4 reprocessed OSTIA SST dataset (SST_GLO_SST_L4_NRT_OBSERVATIONS_010_001/SST_GLO_SST_L4_REP_OBSERVATIONS_010_011) (Nardelli and Pisano, 2021).

In this investigation, the SSS product was obtained from the CMEMS portal at https://marine.copernicus.eu/, with a spatial resolution of 0.25° (Latitude) x 0.25° (Longitude) and a monthly temporal resolution from 15 January 1993 to 15 December 2021. The variable 'sos' (analysed sea surface salinity, PSU) was selected and downloaded in NetCDF 4.0 CF1.7 format (Nardelli and Pisano, 2021).

3.3 Model Data

The model data comprised of a global ocean eddy-resolving model referred to as the GLORYS model and two bathymetric models: General Bathymetric Chart of the Oceans (GEBCO) and Earth TOPOgraphy (ETOPO).

3.3.1 Bathymetry Data

Bathymetry maps are typically compiled from measurements made using multibeam echo sounders, mounted either below or over the side of vessels. Unfortunately, such data are not widely available in remote regions of the world's ocean, particularly at the PEIs in the SO (Gille, 2008). As such, most studies use satellite-derived bathymetry products to illustrate and examine variations in bottom depth across the PEI shelf. However, an investigation into this

for the purpose of this study demonstrated that different bathymetric products and different versions of the same product yielded distinct differences among themselves as well as in comparison to *in situ* data (*Figure 3.4 and 3.5*).

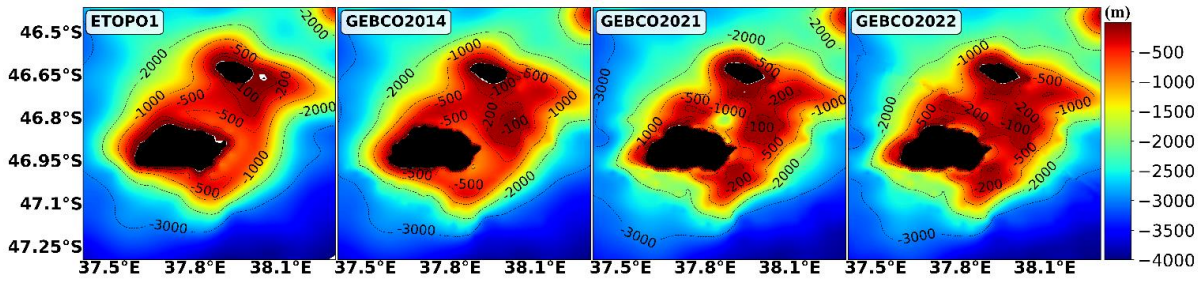

Figure 3.4: Model-derived bathymetry (m) around the PEIs. Earth TOPOgraphy (ETOPO1) (1 Arc-minute; 2 km resolution Global Relief Model) was produced in 2009, while the General Bathymetric Chart of the Oceans (GEBCO) datasets were produced in 2014 (GEBCO2014; 1 km resolution), 2021 (GEBCO2021; 0.5 km resolution) and 2022 (GEBCO2022; 0.5 km resolution), respectively. Areas shaded black denote land above sea level.

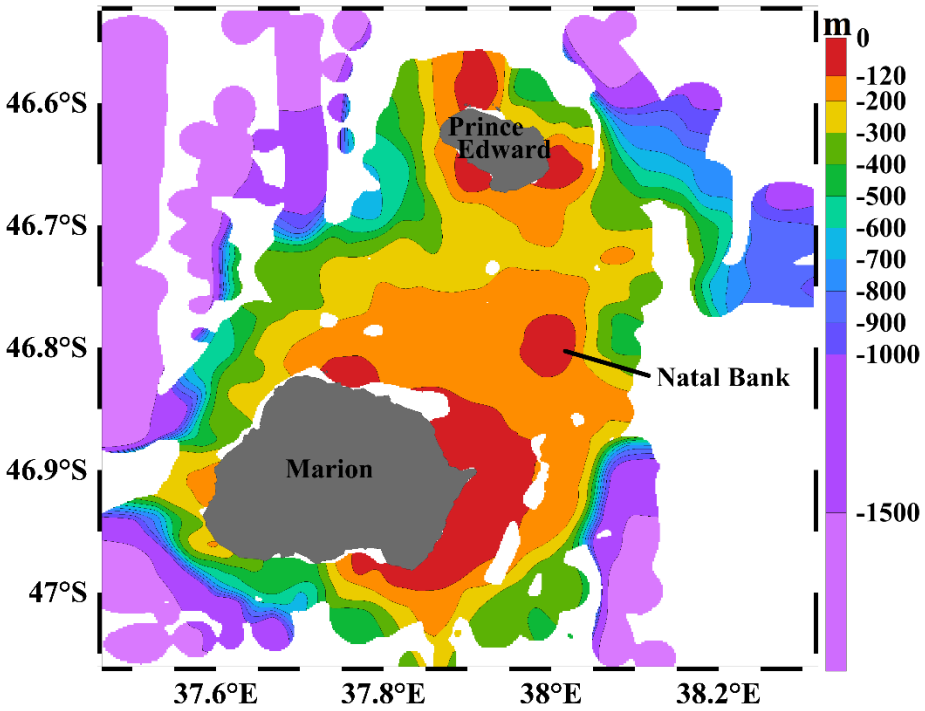

Figure 3.5: Map showing in situ bathymetry, produced by the Department of Forestry, Fisheries and the Environment (DFFE) around the PEIs, using a combination of available single-beam echo sounder data (Rudolph et al. 2022), and additional bottom depth estimates obtained from CTD-mounted altimeters and ship-mounted Acoustic Doppler Current Profiler (S-ADCP) data, used to improve the spatial resolution of bottom depth data. White shading indicates area of no data.

Two bathymetric models were selected and used in this study, GEBCO and ETOPO. GEBCO provides global gridded bathymetric datasets for ocean and land terrain, using elevation data (m). The GEBCO datasets used in this study were developed in 2014 (GEBCO_2014; 1 km

resolution), 2021 (GEBCO_2021; 0.5 km resolution) and 2022 (GEBCO_2022; 0.5 km resolution), by the Nippon Foundation-GEBCO Seabed 2030 Project.

The GEBCO_2022 Grid was compiled by producing a 'base' grid and a number of regional data grids were then included onto it (Grid, 2022). The base grid makes use of the Version 2.4 SRTM15+ dataset (Tozer et al. 2019) between the latitudes 50° S and 60° N and was then expanded to include the polar regions by using bathymetric datasets, mainly based on multibeam data, developed by the four Seabed 2030 Regional Centers. A detailed description of the development of the grid can be found at https://www.gebco.net/data_and_products/gridded_bathymetry_data/gebco_2022/documents/GEBCO_2022_Grid.pdf.

The GEBCO_2021 Grid was built from multiple regional and global grids just as described for the GEBCO_2022 Grid. The main difference however is that GEBCO_2021 utilised Version 2.2 of the SRTM15+ dataset to produce the base grid. Further information regarding the development of this grid can be found at https://www.gebco.net/data_and_products/gridded_bathymetry_data/gebco_2021/documents/GEBCO_2021_Grid.pdf.

The GEBCO_2014 Grid was produced by updating the base grid with a compilation of gridded bathymetry datasets such as the Baltic Sea Bathymetry Database, multibeam and single beam bathymetry data, to name a few. A comprehensive list of the additional datasets and development of the GEBCO_2014 grid is available at https://www.bodc.ac.uk/data/documents/nodb/301801/. The base grid used for this GEBCO product was the same as that used in the GEBCO_2008 Grid which employed Version 5 of the SRTM30+ dataset.

ETOPO1 is a Global Relief Model developed in 2008 by the National Geophysical Data Center (NGDC), an office of the National Oceanic and Atmospheric Administration (NOAA), with a 1 Arc-Minute spatial resolution (2 km) (Amante and Eakins, 2009). This model collated shoreline, bathymetric, topographic, integrated bathymetric-topographic and bedrock digital datasets and, using the 'Feature Manipulation Engine' (FME) data translation tool package, the data were then shifted to World Geodetic System 1984 (WGS 84) horizontal datum and sea level vertical datum datasets and converted into ESRI (http://www.esri.com/) ArcGIS shape files (Amante and Eakins, 2009). The files were edited, assessed and the data was gridded using 'Generic Mapping Tools' (GMT) version 4.3 (http://gmt.soest.hawaii.edu) and Caress and

Chayes' [1995] 'MB-System' version 5.1.0 (http://www.ldeo.columbia.edu/res/pi/MB-System/) to produce the final global relief model (Amante and Eakins, 2009).

Bathymetric data are most commonly used to produce nautical charts for safe maritime navigation. Marine scientists use such data to map ocean currents; create ocean models for researching, monitoring and forecasting the properties of the ocean; determine oceanographic mooring deployment locations; map habitats of benthic biota; and monitoring climate change/variability impacts, including beach erosion, sea level rise and subsidence, among others (NOAA, 2021). With so many operations and procedures relying on bathymetry, it is essential that the bathymetric products being used are accurate and reliable and it is expected that by using higher spatial resolution model data, more accurate spatial variations will be yielded but this was not observed (*Figure 3.4; Figure 3.5*).

ETOPO1 shows a small island east of Prince Edward Island and GEBCO2021 shows a "hole" just north of Marion Island, deeper than 1500 m (*Figure 3.4*). These features are confirmed as errors when compared to the *in situ* data (*Figure 3.5*) and field experience in this region. The Natal Bank, confirmed by the *in situ* data, (*Figure 3.5*) is not captured by ETOPO1 but is observed in the three versions of GEBCO. *In situ* data displays a narrow channel, >200 m deep, incising the shelf from west to east, which the satellite products fail to capture. The satellite products show a channel, >500 m deep, along the north-eastern edge of Marion Island, while in contrast the *in situ* data shows a broad, shallow bank <120 m depth.

Ultimately, bathymetry model product inaccuracies arise due to erroneous interpolation of minimal data with overall poor quality and coarse spatial resolution. Since bathymetry is a key input into numerical model simulations, and to define locations for long-term mooring deployments of oceanographic instruments among many other uses, it is of the utmost importance to have accurate bathymetry data.

3.3.2 GLORYS Data

GLORYS12V1, hereafter referred to as GLORYS, is a global ocean eddy-resolving model with a monthly temporal resolution that spans from 1 January 1993 to 31 May 2020 and a 1/12^{o} (8 km) spatial resolution with 50 vertical depth layers (Drévillon et al. 2021a). The GLORYS model input is the Nucleus for European Modelling of the Ocean (NEMO) version 3.1 platform, which is driven at the surface by the European Centre for Medium-Range Weather Forecasts' (ECMWF) ERA-Interim reanalysis, then by ERA5 reanalyses for the more recent

years since 1 January 2019 (Russo et al. 2022; Drévillon et al. 2021a). A reduced-order Kalman Filter scheme was used to assimilate the observational data and includes an adaptive-error estimate and a localisation algorithm (Drévillon et al. 2021a). The observational data includes along-track SLA, satellite SST, Centre ERS d'Archivage et de Traitement (CERSAT) Sea Ice Concentration and *in situ* temperature and salinity vertical profiles from CORA (Russo et al. 2022; Drévillon et al. 2021a). An expansion on the model input, atmospheric forcing and observational data assimilated into GLORYS can be found in *Table 3.2*.

Table 3.2: Table adapted from Russo et al. (2022) Supplementary Material, showing the expanded information regarding the GLORYS model. SST Data acronyms are Advanced Very High Resolution Radiometer (AVHRR). Altimetry Data acronyms include Topography Experiment (TOPEX), European Remote Sensing (ERS) satellites, Geosat Follow-On (GFO) satellite, Joint Altimetry Satellite Oceanography Network (JASON) satellites, Environmental Satellite (Envisat), Cyrosphere Satellite-2 (Cryosat-2), Ka-band Altimeter (Altika) Satellite with Argos and Altika (SARAL), Sentinel satellites, Geodetic Satellite (GEOSAT) and the Hai Yang 2A satellite (HY-2A). Sea ice concentrations acronyms include Centre ERS d'Archivage et de Traitement (CERSAT) and Institut Francais de Recherche pour l'Exploitation de la mer (Ifremer). In situ Data acronyms are Coriolis Ocean database ReAnalysis (CORA).

Model	**NEMO 3.1**
Atmospheric Forcing	ECMWF ERA-Interim reanalysis (79 km) ERA5 (31 km)
Assimilation System	3D Multivariate reduced-order Kalman filter
SST Data	AVHRR
Altimetry Data	TOPEX Poseidon ERS-1, -2 GFO Jason-1, -2, -3 Envisat CryoSat-2 SARAL Sentinel-3A, -3B Geosat HY-2A
Sea Ice Concentration Data	Ifremer/CERSAT
***In situ* Data**	CORA version 4.1, 5.0, 5.1

Three GLORYS datasets were obtained from the CMEMS platform at https://marine.copernicus.eu/. The first is known as 'cmems_mod_glo_phy_my_0.083_P1M-m' containing the monthly mean fields, between 1 January 1993 to 31 December 2020, for the following variables selected for the purpose of this study, 'thetao' (seawater potential temperature, ^{o}C), 'so' (seawater salinity, PSU), 'uo' (eastward ocean current velocity, m.s^{-1}),

'vo' (northward ocean current velocity, $m.s^{-1}$) and 'zos' (sea surface height above geoid, m) (Drévillon et al. 2021b). Daily mean fields from the dataset, 'cmems_mod_glo_phy_my_0.083_P1D-m', for specific dates between April 2013 and April 2017, were downloaded to match the dates of the vertical CTD profiles collected during the cruises listed in *Table 3.1*. The last was the bathymetric dataset 'cmems_mod_glo_phy_my_0.083_static' containing the static field for 'deptho' (sea floor depth below geoid, m). The bathymetric product compiles ETOPO1 for the deep ocean and GEBCO_2008 for the coastal and continental shelf region, to produce the complete product (Drévillon et al. 2021b).

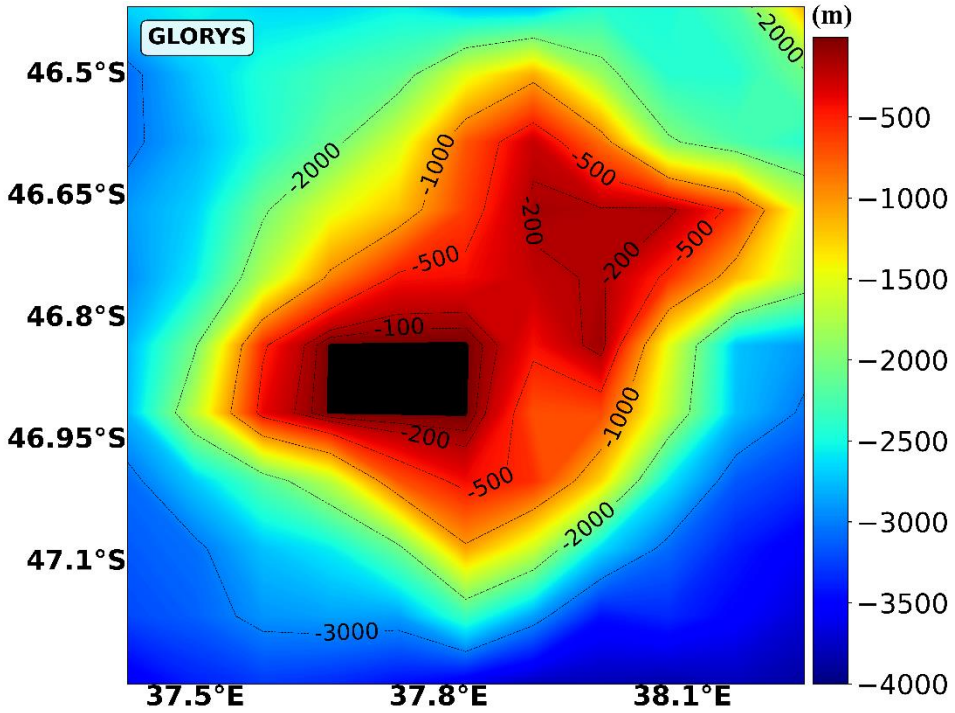

Figure 3.6: GLORYS bathymetry (m) around the PEIs. Areas shaded black denote land above sea level.

Comparing the GLORYS model bathymetric output (*Figure 3.6*) to the *in situ* (*Figure 3.5*) and satellite (*Figure 3.4*) bathymetry products, it is evident that the model produces an overall smoother bathymetry surrounding the PEIs. It captures neither the presence of Prince Edward Island nor the Natal Bank and fails to depict the correct shape and extent of Marion Island. GLORYS does however manage to simulate the broad shallow bank along the north-eastern edge of Marion Island as suggested by the *in situ* data also captures the general structure and shape of the bathymetry between 200 m and 500 m reasonably well. Given the differences between the model bathymetry and the ETOPO and GEBCO products and *in situ* bathymetry, it can be expected that the model will likely fail to correctly represent some of the dynamics

associated with the interactions of the bathymetric structure of the islands with the surrounding flow.

3.4 Data Analysis

Analysis of all parameters in this study was done using Python Software Foundation, Python Language Reference version 3.8. The study grid spans the region from 35.5°E to 43°E and 43.5°S to 49°S. Data within the 5° x 5° region outlined by the black box in *Figure 3.7*, was averaged and used for the time series analysis.

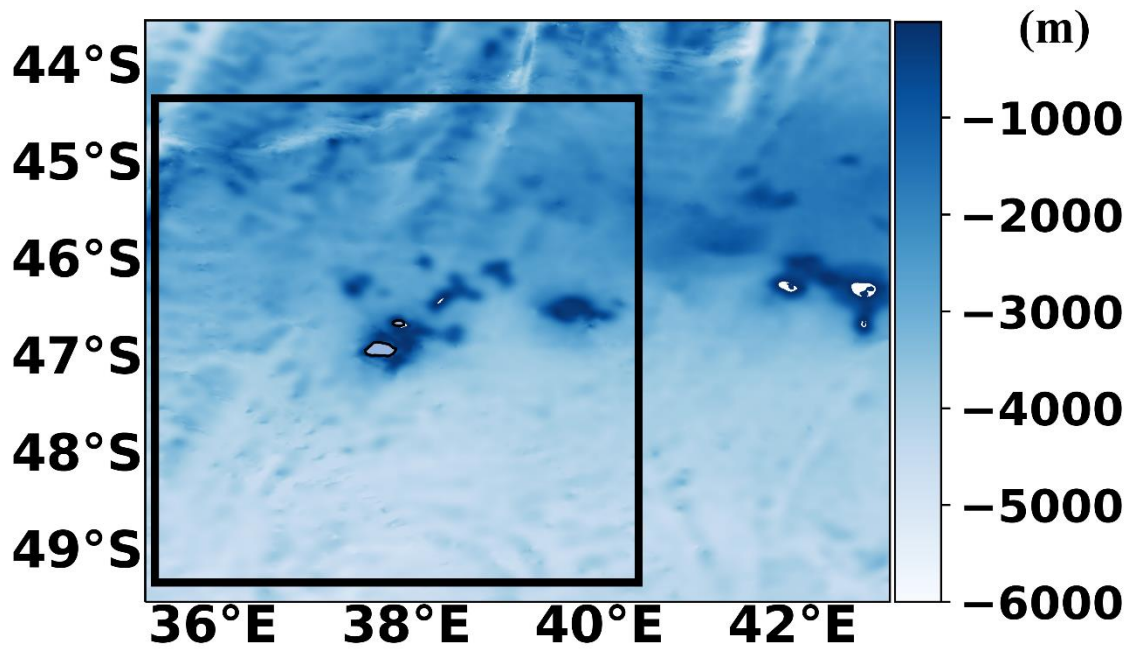

Figure 3.7: GEBCO_2022 bathymetry (m) depicting the study grid (35.5°E – 43°E; 43.5°S - 49°S). The black box denotes the 5° x 5° zoomed region (35.4°E – 40.4°E; 44.3°S – 49.3°S).

3.4.1 Bathymetry Analysis

Bathymetry maps for ETOPO1, GEBCO_2014, GEBCO_2021, GEBCO_2022 and GLORYS were produced for a region spanning 37.4 to 38.3 °E and 46.4 to 47.3 °S. This was done to compare and validate the modelled bathymetry from GLORYS, and to comment on the degree to which GLORYS' bathymetry is smoothed. The comparison was described above in Section 3.3.

3.4.2 Calculation of monthly climatologies and bias

To compare and understand the surface and sub-surface oceanographic spatial variability around the PEIs, monthly climatology surface maps were plotted for SST (°C), temperature at 200 m (°C), SSS, salinity at 200 m, SSH (m), ADT (m) and surface geostrophic current speed ($m.s^{-1}$). These climatologies were constructed using the respective data products (WOA18, CARS09, OSTIA, CNR, GLORYS and ADT altimetry). A monthly climatology is understood

to be a mean value, of a variable, for each calendar month calculated over a long period of time (Wilks, 1995). The datasets used to produce these climatology plots were downloaded using a monthly timescale, and the monthly climatologies were calculated by averaging each of the months over the respective full time series of each dataset. Figures illustrating the monthly climatologies were then plotted over the study grid.

Bias is a means of comparing an average parameter with an observed parameter to obtain a statistical difference between the two (Wilks, 1995). Biases were calculated using all the monthly climatologies (WOA18, CARS09, OSTIA, CNR, GLORYS and ADT altimetry), with the main purpose of comparing and observing where GLORYS was over or underestimating the various parameters. The first step in calculating these biases was to re-grid GLORYS to match the lower resolution datasets. This excluded OSTIA, which was re-gridded to the resolution of GLORYS. Finally, the parameters from the other datasets were subtracted from GLORYS and the newly produced arrays were plotted as the biases.

3.4.3 Time series of monthly means

A time series is a collection of singular data points, chronologically ordered and arranged over intervals in time (Wilks, 1995). Within the main study grid, SST (^{o}C), temperature at 200 m (^{o}C), SSS and salinity at 200 m were obtained and averaged over the 5^{o} x 5^{o} region outlined in *Figure 3.7*, centered around Marion and Prince Edward Islands. A mean value was produced, per month for the WOA18, CARS09, OSTIA, CNR and GLORYS datasets. Additionally, monthly means were calculated using the SAWS SST data, but were limited to the single collection location as illustrated in *Figure 3.8*. Line graphs were produced using these values, allowing for comparisons to be made between datasets and for the analysis of seasonal cycles between the surface and sub-surface environments.

3.4.4 Temperature-Salinity profiles

Temperature-Salinity (T/S) profiles were created primarily to observe to what degree of accuracy the GLORYS model output captures the water masses when compared to the WOA18, CARS09 datasets and to the *in situ* CTD cruise data. Density (σ_t, kg.m^{-3}) is defined by the Thermodynamic Equation of Seawater-2010 (TEOS-10) as the density using *in situ* temperature and salinity and where pressure = 0, according to the following equation.

$$\sigma_t = \sigma_{S,T,0} = \rho_{S,T,0} - 1000\ kg/m^3$$

The Gibbs-SeaWater (GSW) Oceanographic Toolbox was used in Python, which contains the TEOS-10 equations for the evaluation of thermodynamic properties of seawater and was used to calculate σ_t for the T/S plots.

3.4.5 Correlations

Correlation tests are a powerful tool in analysing the relationship between variables. Obtaining the correlation between two variables can be done in multiple ways. This study employed the most common, the Pearson correlation, established by Karl Pearson (Pearson, 1895). The Pearson correlation coefficient (R) offers how strong the linear association is between two variables and is calculated according to Equation 6 (Toolsee, 2021; Hogg et al. 2014).

$$\boldsymbol{R} = \frac{\boldsymbol{n}(\sum \boldsymbol{xy}) - (\sum \boldsymbol{x})(\sum \boldsymbol{y})}{\sqrt{\left[\boldsymbol{n}\sum \boldsymbol{x^2} - (\sum \boldsymbol{x})^2\right] - \left[\boldsymbol{n}\sum \boldsymbol{y^2} - (\sum \boldsymbol{y})^2\right]}}$$

where n is the number of ordered pairs in the time series, x is the values for the first variable and y the values for the second variable. The output values for R from the above equation are explained in Table 3.3 that follows.

Table 3.3: Evaluation of the Pearson Correlation Coefficient (R), adapted from Toolsee (2022).

R values	Correlation	Relationship Interpretation
-1	Perfect Correlation	As the one variable increase, the corresponding variable decreases.
-1 < R ≤ -0.8	Strong Correlation	
-0.8 < R ≤ -0.5	Moderate Correlation	
-0.5 < R ≤ -0.3	Low Correlation	
-0.3 < R ≤ 0	Negligible Correlation	
0	No Correlation	No relationship
0 < R ≤ 0.3	Negligible Correlation	As the one variable increases (decreases), the corresponding variable also increases (decreases).
0.3 < R ≤ 0.5	Low Correlation	
0.5 < R ≤ 0.8	Moderate Correlation	
0.8 < R ≤ 1	Strong Correlation	
1	Perfect Correlation	

In accordance with the correlation, a t-test can be performed to evaluate the accuracy of the correlation between the two variables, by returning the statistical significance of the correlation coefficient in the form of a p-value. At the 95% significance level, if the p-value is less than 0.05, the null hypothesis, which states that there is no difference between the two variables means, can be rejected inferring that the correlation is statistically significant. Conversely, if the p-value is greater than 0.05, the null hypothesis cannot be rejected indicating that the correlation between the two variables holds no statistical significance (Hogg et al. 2014).

In this study, two Pearson Correlations were performed between the monthly SAWS SST data and the corresponding monthly GLORYS SST, over the time span 16 January 1993 to 16 May 2020. The daily SAWS data were averaged into monthly climatological means and imported into Python to produce scatter plots fitted with linear regression lines presenting the Pearson relationship between the SAWS and GLORYS datasets. An additional Pearson Correlation was performed between the monthly climatological means of the two. Two points of equal distance were identified in the GLORYS data as being the closest to the SAWS point. As a result, both points, and an average between, them were used in the correlations for this study (*Figure 3.8)*.

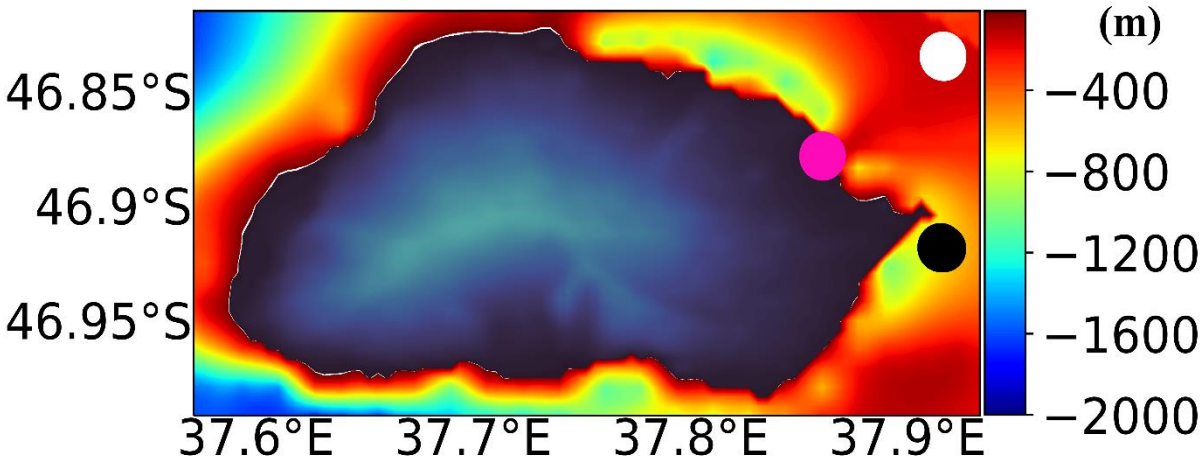

Figure 3.8: GEBCO_2022 bathymetry map showing the location points where data was extracted to perform the correlations. The pink marker denotes the location of the jetty on Marion Island where the SAWS data is sampled. The white and black markers denote the closest GLORYS data points, to the jetty, being the northern and southern points respectively.

3.4.6 Vertical section plots

Vertical sections were produced using the CTD cruise data and GLORYS model output along the N-S transect described in Section 3.1.1. This transect is located at 37.3°E and spans the latitudinal range from 45.7°S to 47.5°S. Along this transect, temperature and salinity data were extracted from both the CTD and GLORYS data, throughout the water column (0-4000 m), and co-located in both time and space.

An additional set of vertical climatology plots were produced using the northward and eastward ocean current velocities ($m.s^{-1}$) from GLORYS data along a N-S orientated transect spanning the same latitudinal range but at two separate longitudinal locations of 37.83°E and 37.92°E, for the upper 2000 m. This was done in order to gain a detailed understanding of the observed conditions upstream of the islands and in the inter-island region, as well as to compare how accurately the observed conditions are simulated and described by GLORYS.

3.4.7 Theoretical calculations for the existence of the Taylor Column

Owens and Hogg (1980) provided the first set of non-dimensional parameters with set threshold values to evaluate whether a Taylor column could exist in a seamount area. While previous studies have investigated Taylor columns over seamounts and not within island systems, the PEIs bathymetry mimics that of a seamount as previously described by Perissinotto and Duncombe Rae (1990). Therefore, this study followed the same approach as Owens and Hogg (1980) and included the Rossby number (Ro), Reynolds number (Re), Rossby radius of deformation for a barotropic (Lrt) and baroclinic ocean (Lrc) and the blocking parameter (Bl) (Owens and Hogg, 1980; Ma et al. 2021). GLORYS, GEBCO_2022, altimetry data and ATLAS gridded data as described by (Chelton et al. 1998) were used to compute and plot the following calculations:

Rossby Number

The Rossby number (Ro) describes the flow of a fluid by providing the ratio between inertial and Coriolis forces (Mininni et al. 2009). It was calculated according to Equation 7.

$$Ro = U / f L \quad \textbf{(7)}$$

where U is the horizontal current velocity ($m.s^{-1}$), f is the Coriolis parameter (f = 2 ω sin(latitude)), ω is the angular velocity of the Earth around its axis [7.2921159 × 10^{-5} radians/second] and L is the horizontal length scale (m) of the island plateau (Owens and Hogg, 1980; Ma et al. 2021) measuring 50 km (Perissinotto and Duncombe Rae, 1990).

Reynolds Number

The Reynolds number (Re) is the ratio between inertial and viscous forces (Mininni et al. 2009). It was calculated according to Equation 8.

$$Re = U\ L\ /\ \upsilon \quad \textbf{(8)}$$

where U is the horizontal current velocity ($m.s^{-1}$), L is the horizontal length scale (m) of the island plateau measuring 50 km and υ is the vertical eddy viscosity (0.00012 $m^2.s^{-1}$) (Madec and NEMO team, 2016).

Barotropic Rossby radius of deformation

The Rossby radius of deformation is the length scale at which Coriolis forces become as important as buoyancy forces (Chelton et al. 1998). It was calculated according to Equation 9 for barotropic flow (oceanic flow that changes only by a few percent with temperature and salinity is referred to as barotropic flow. It is therefore a flow whose density depends solely on pressure, resulting in the flow's density being approximately steady throughout the water column (Marghany, 2021).

$$Lr = \sqrt{g\ D}\ /\ f \quad \textbf{(9)}$$

where g is the gravitational acceleration (9.81 $m.s^{-2}$), D is the ocean depth (m) and f is the Coriolis parameter (f = 2 ω sin(latitude)), ω is the angular velocity of the earth around its axis [7.2921159 × 10^{-5} radians/second].

Baroclinic Rossby radius of deformation

To calculate the Rossby radius for a baroclinic flow, the Brunt–Väisälä frequency or buoyancy force (N(z)) has to be calculated according to Equation 10 described by Chelton et al. (1998).

$$N^2(z) = -\frac{g}{\rho 0}\left[\frac{\rho(Z_k)-\rho(Z_{k+1})}{Z_k - Z_{k+1}}\right] \quad \textbf{(10)}$$

where g is gravitational acceleration (9.81 m.s^{-2}) and $\rho 0$ is the mean density of seawater (1000 kg.m^{-3}). These are then multiplied by the vertical gradient of seawater density (Figure 3.7).

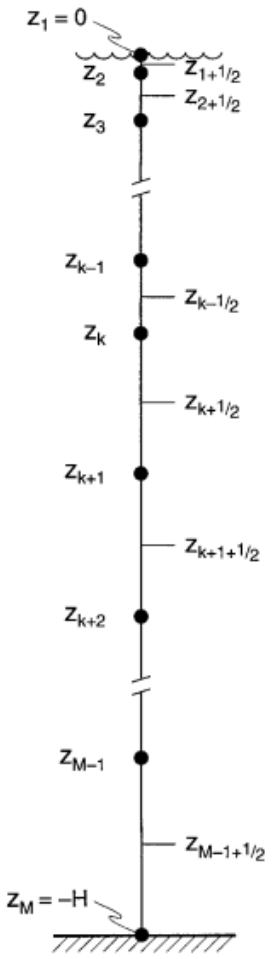

Figure 3.7: A schematic taken from Chelton et al. (1998) to describe the vertical profile of depth, from which the buoyancy frequency (N(z)) is calculated.

The Wentzel-Kramers-Brillouin (WKB) approximation of the Rossby radius of deformation (λ) can then be solved for a region outside of the equatorial band and where mode m is greater than or equal to 1, according to Equation 11 presented by Chelton et al. (1998). While these calculations were not performed in this study, they were used in a similar manner by Chelton et al. (1998) to create the 1-degree gridded global ATLAS of the baroclinic gravity-wave phase speed (c) and the baroclinic Rossby radius of deformation, which was used in this study.

$$\lambda_m \approx \lambda_m^{WKB} = \frac{1}{|f\ (\theta)|\ m\ \pi}\int_{-H}^{0} N(z)\ dz, \quad \begin{array}{l} if\ |\theta| \geq 5^o \\ and\ m \geq 1 \end{array} \quad \textbf{(11)}$$

where f is the Coriolis parameter ($f = 2\,\omega \sin(\theta)$, ω is the angular velocity of the earth around its axis [7.2921159×10^{-5} radians/second], θ is the latitude, m is the baroclinic mode number and N(z) is the Brunt–Väisälä frequency or buoyancy force integrated with depth (m).

Blocking parameter

The blocking parameter (Bl) is a combination of Ro and α (alpha), where α is the relative height of the bathymetric feature to the water depth. The Bl controls and describes the Taylor Column formation and flow behaviour (White et al. 2007). It was calculated according to Equation 13 (Owens and Hogg, 1980; Ma et al. 2021).

$$\alpha = h / H \quad \textbf{(12)}$$

$$Bl = \alpha / Ro \quad \textbf{(13)}$$

where h is the island plateau (m), H is the water depth (m) and Ro is the Rossby number.

3.4.8 Identification of front positions

The contour-based method, described by Sokolov and Rintoul (2002), was used in this study to identify the positions of the fronts within the region surrounding the PEIs. The sub-Antarctic Front (SAF) and the Antarctic Polar Front (APF) were identified according to their distinct temperature and salinity gradients by Sokolov and Rintoul (2002) and was recorded as each consisting of three branches, namely the Northern sub-Antarctic Front (N-SAF), Middle sub-Antarctic Front (M-SAF), Southern sub-Antarctic Front (S-SAF), Northern Antarctic Polar Front (N-APF), Middle Antarctic Polar Front (M-APF) and Southern Antarctic Polar Front (S-APF). Optimised ADT (m) measurements obtained from satellite altimetry data were used to overlay the positions of the fronts, in this study.

Table 3.4: Absolute Dynamic Topography (m) of the three distinct branches, sub-Antarctic Front (SAF) and Antarctic Polar Front (APF) as described by Sokolov and Rintoul (2002).

Frontal Branch Name	Sea Surface Height (m)
N-SAF	0.240
M-SAF	0.030
S-SAF	-0.170
N-APF	-0.300
M-APF	-0.480
S-APF	-0.630

Chapter 4. Results and Discussion

The PEIs are situated in a remote and hostile environment within the SO. With no adequate *in situ* datasets able to provide comprehensive long-term, regional-scale coverage necessary to study the environmental conditions around the PEIs in detail, this study used the high spatial and temporal resolution of the GLORYS model output to identify the surface and sub-surface oceanographic variability around the PEIs and the drivers thereof.

To achieve the aim set out by this study, the following three key questions were investigated:

1. What is the suitability and accuracy of the GLORYS12V1 model output compared to existing *in situ* and satellite data around the PEIs?
2. What is the surface and sub-surface hydrographic variability surrounding the PEIs, shown by the GLORYS12V1 model output, and what are the drivers thereof?
3. Are the *in situ*, satellite and model conditions suitable for the formation and existence of a Taylor column at the PEIs?

This chapter details and assesses the findings from the various datasets to address the aim of this study by answering the three key questions.

4.1 Horizontal spatial variability of hydrographic conditions

This section addresses the first two key questions by applying an approach that uses the combination of coarse resolution *in situ* data, slightly higher resolution satellite data, and high resolution model output in order to firstly, evaluate and discuss the validity and accuracy of the GLORYS model when compared to the *in situ* and satellite data. Secondly, this section identifies and assesses both the larger and smaller scale surface and sub-surface physical oceanographic processes, and the drivers thereof, within the PEIs region.

4.1.1 Circulation

In this study, the seasonal cycle at the PEIs is defined for the Southern Hemisphere as, austral summer (December to February, DJF), autumn (March to May, MAM), winter (June to August, JJA) and spring (September to November, SON) (Alpert et al. 2004). A study done by Armitage

et al. (2018) using traditional altimeter estimates of SSH for the open ocean and height estimates for the ice-covered regions, was able to compile the first complete picture of sea level across the SO. The results revealed that in the deeper open SO, sea level was lowest in autumn (AMJ) and highest in spring and summer (OND and JFM), while the reverse was true along Antarctica's coastline. This seasonal cycle of SSH/ADT, described by Armitage et al. (2018), was not observed in the study region at the PEIs (*Figure 4.1 to 4.4*) nor was it evident in the large-scale overview of satellite ADT (*Figure A1*) or GLORYS SSH (*Figure A2*). The lack of seasonal variability observed in the Antarctic region could be due to the absence of height estimates for the regions covered by ice Armitage et al. (2018). Ice-coverage obscures the large-scale satellite ADT (*Figure A1*) over the winter and spring period (JJA and SON). Over the larger SO region, GLORYS SSH (*Figure A2*) does not display any sea ice-cover because the sea ice area fraction variable was not overlaid in this study's results as it was beyond the scope of this study. GLORYS does, however, receive assimilated CERSAT sea ice concentration data and could be studied when investigating the suitability of the GLORYS model output for regions closer to Antarctica, where ice cover should be considered. Additionally, around the PEIs, no clear localised seasonal cycle was observed for altimetry ADT nor for GLORYS SSH (*Figures 4.1; 4.2*).

Total surface current (R_{total}) in the ocean is made up of geostrophic currents (R_{geos}) and Ekman currents (R_{ek}) (Toolsee et al. 2021). Toolsee et al. (2021) demonstrated that R_{geos} was such a large proportion of R_{total} such that the geostrophic currents, in the PEIs surroundings, were approximately four times larger than the Ekman currents, concluding that the main driver of surface circulation within this region was geostrophic currents rather than wind forcing. The current study, however, used the total ocean current velocities from the GLORYS dataset to calculate geostrohpic velocities, therefore allowing for the direct comparison to be made between the satellite (*Figure 4.1; 4.3*) and GLORYS (*Figure 4.2; 4.3*) geostrophic ocean current velocities.

As described in section 3.2.1 of Chapter 3 the ADT is the SSH corrected for the Geoid height and can thus be referred to as the instantaneous height above the geoid (Taburet et al. 2021). GLORYS makes use of a variable called SSH but is in fact the SSH above the geoid, making it ADT (Drévillon et al. 2021a) and therefore allows this study to directly compare satellite ADT and GLORYS SSH (*Figure 4.1; 4.2; 4.4*). While both satellite ADT (*Figure 4.1*) and GLORYS SSH (*Figure 4.2*) have similar ranges (-0.550 to 0.106 m for satellite ADT and -0.988 to -0.290 m for GLORYS SSH), it was immediately evident that the GLORYS SSH

consisted entirely of negative values, while the satellite ADT had a larger spread of positive values. Additionally, *Figure 4.4* illustrates this difference in spread with an underestimation of between 0.2 to 0.6 m in SSH by GLORYS with respect to the satellite altimetry ADT.

According to the equation, ADT is calculated using SLA and MDT (ADT = SLA + MDT). Both GLORYS and the satellite data made use of delayed time SLA from all altimetric satellites (Drévillon et al. 2021a; Taburet et al. 2021). The MDT assimilated into GLORYS was a hybrid based on CNES-CLS13 and a new glacial isostatic adjustment file (Drévillon et al. 2021b). The satellite altimetry product, however, made use of a MDT product which combines CNES_CLS18 (Taburet et al. 2021) with CMEMS_2020 (Jousset and Mulet, 2020) for the Black Sea and Mediterranean Sea. The MDT being assimilated into GLORYS is therefore smaller than the MDT used in the satellite data, resulting in the lower and more negative SSH observed for GLORYS (*Figures 4.2*) than for the ADT from satellite alimetry (*Figures 4.1*).

The monthly climatological means of the ocean surface currents for the satellite data and GLORYS output (*Figure 4.1; Figure 4.2*) provided a good representation of the known mean eastward flow in the region surrounding the PEIs, throughout the year. The ACC bifurcates upon approaching the shallowing bathymetry of the PEIs, where part of the current veers northward, rejoining the main flow downstream of the islands (Ansorge et al. 2010). While this deflection of the current was clearly evident in GLORYS (*Figure 4.2*), it was visible to a lesser extent in the satellite data (*Figure 4.1*), the current speed was overestimated by approximately 0.2 m s^{-1} by GLORYS (*Figure 4.3*). Additionally, a near constant underestimation of GLORYS current speed, by 0.2 m s^{-1}, was observed along the northern branch of the APF (N-APF) (*Figure 4.3*).

The satellite current speed significantly decreases downstream of the PEIs (*Figure 4.1*), in agreement with the findings by Toolsee et al. (2021). The opposite was observed for GLORYS (*Figure 4.2*), where the current speed was faster in the lee of the islands (current vectors for GLORYS are much larger than those for the altimetry data). Overall, GLORYS overestimated these current speeds by approximately 0.4 m s^{-1} (*Figure 4.3*) which could be explained by the intensified bifurcation of the ACC, upstream of the PEIs, simulated by GLORYS, combined with the absence of Prince Edward Island in the smoothed GLORYS bathymetry (see section 3.3.2 for a more detailed description of GLORYS bathymetry). An increased overestimation of approximately 0.4 m s^{-1} between January and March was observed at the southeastern edge of the islands. It appears that a singular data point bordering the white shaded region

surrounding the islands, could be the cause of this overestimation and can therefore be inferred as an artefact related to the smoothed bathymetry in GLORYS. Anomalous anticlockwise flow patterns were evident in the lee of the PEIs (*Figure 4.2*), likely due to the fact that at 200 m the GLORYS model output appeared to simulate shallow bathymetric features that possibly resulted in this anticlockwise flow, better depicted and described in section 4.1.2 (*Figure 4.15*).

Sea level anomalies (SLAs) are primarily driven by horizontal pressure-gradient forces, Coriolis force, frictional forces, gravity and the effects of the Earth's geoid. These SLAs affects the state of the sea surface by giving rise to the "mounds" in the subtropics and the "valleys" in the high latitudes, resulting in the global surface circulation (Marshall and Plumb, 2007). Both the satellite ADT and GLORYS SSH received SLAs from the same altimetric sources, therefore ruling out SLAs as the primary source causing the discrepancies observed between the satellite and GLORYS current speeds. Instead, a multitude of factors are suggested here as potential causes for the discrepancies between GLORYS and satellite altimetry; (1) the application of varying interpolation methods, where satellite altimetry made use of optimal interpolation (OI) to fill in the gaps between the data (Taburet et al. 2021), while GLORYS used a reduced-order Kalman Filter scheme (Drévillon et al. 2021a); (2) as described in the section 3.3.1 of Chapter 3, the relatively smoother bathymetry used in GLORYS could be a factor contributing to some of the current speed discrepancies; (3) the different spatial resolutions, with GLORYS having a higher resolution of 8 km and the satellite data measuring at an approximate resolution of 28 km (Drévillon et al. 2021a; Taburet et al. 2021); and (4) as discussed above, the different MDT products used to calculate ADT in GLORYS and the satellite altimetry would have contributed to the differences observed.

A meridional pattern of the current velocities was apparent in both the satellite data and GLORYS model output, with lower R_{geos} values recorded north of the PEIs and higher velocities evident to the south of the Islands. The bifurcation of the ACC, resulting in a smaller portion of the current being deflected to the north of the PEIs, coupled with the close proximity of the S-SAF and N-APF to the south of the Islands, could be the drivers for the observed north-south pattern of R_{geos}. This observed meridional variation in current speed is in agreement with the findings by Toolsee et al. (2021). The reverse meridional pattern was observed for SSH/ADT, with higher values in the northern part of the study area, and lower to the south, (*Figure 4.1; Figure 4.2*), concurring with the meridional variations observed by Armitage et al. (2018). This SSH/ADT pattern can be explained by the large-scale meridional gradient in SSH/ADT, whereby south of the ACC deep water is upwelled to the surface driven by Ekman

transport which creates depressions in mean sea level as a result of the cyclonic circulation (Rintoul et al. 2001; Morrison et al. 2015). In contrast, north of the westerly wind belt (30 to 55° S), surface waters are downwelled by the converging Ekman transport creating an elevated mean sea surface, brought on by the resulting anticyclonic flow (Rintoul et al. 2001; Cunningham, 2005).

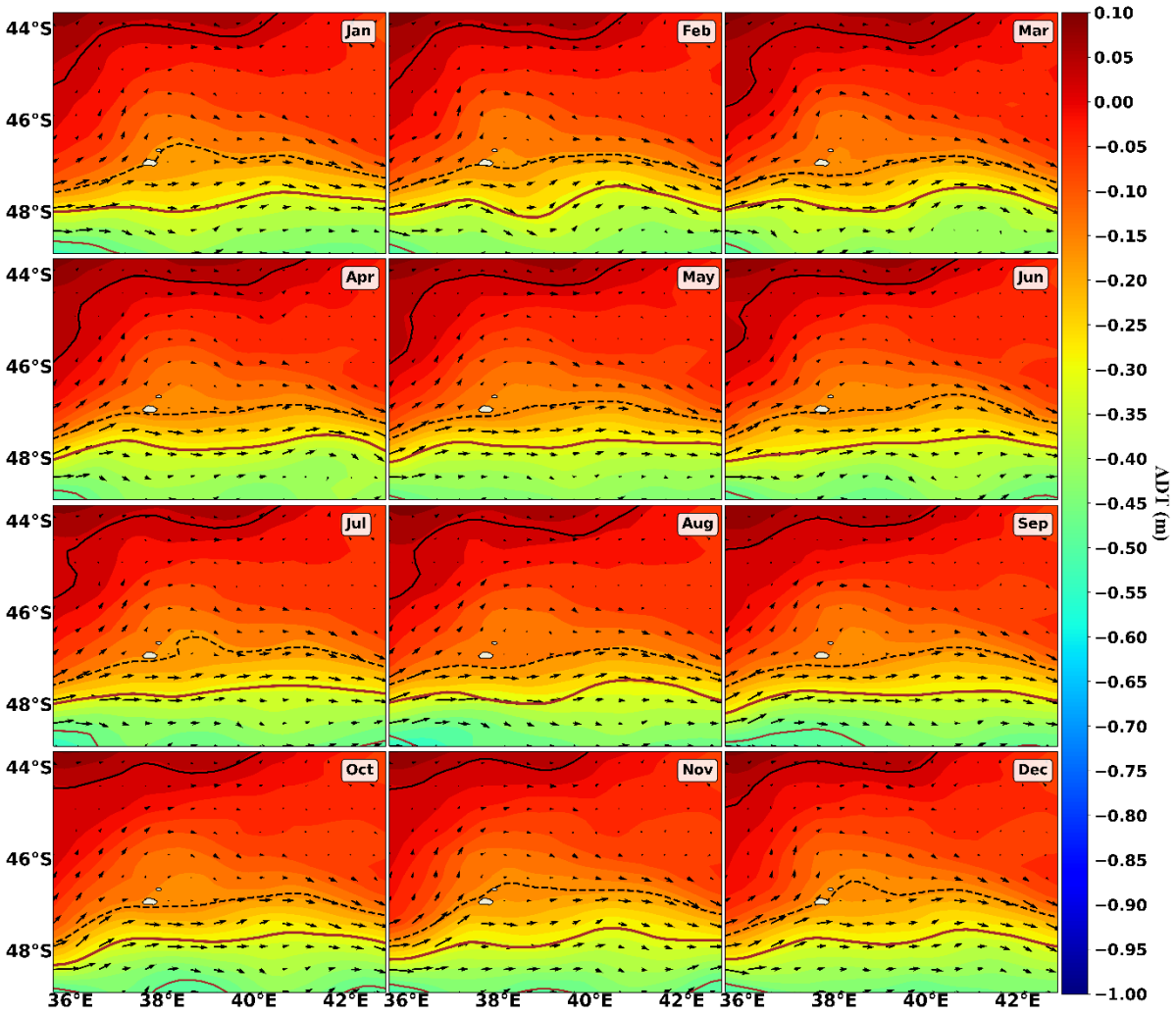

Figure 4.1: The monthly climatology of absolute dynamic topography (ADT) (m) with vectors showing geostrophic current (R_{geos}) direction, from January (Jan) to December (Dec) around the Prince Edward Islands from 1993 to 2022 using the daily reprocessed satellite ADT data. The black solid and dashed lines represent the M-SAF and S-SAF, respectively. The solid thick and thinner brown lines represent the N-APF and M-APF, respectively. These front positions were identified from satellite altimetry using ADT according to the process described by Sokolov and Rintoul (2002).

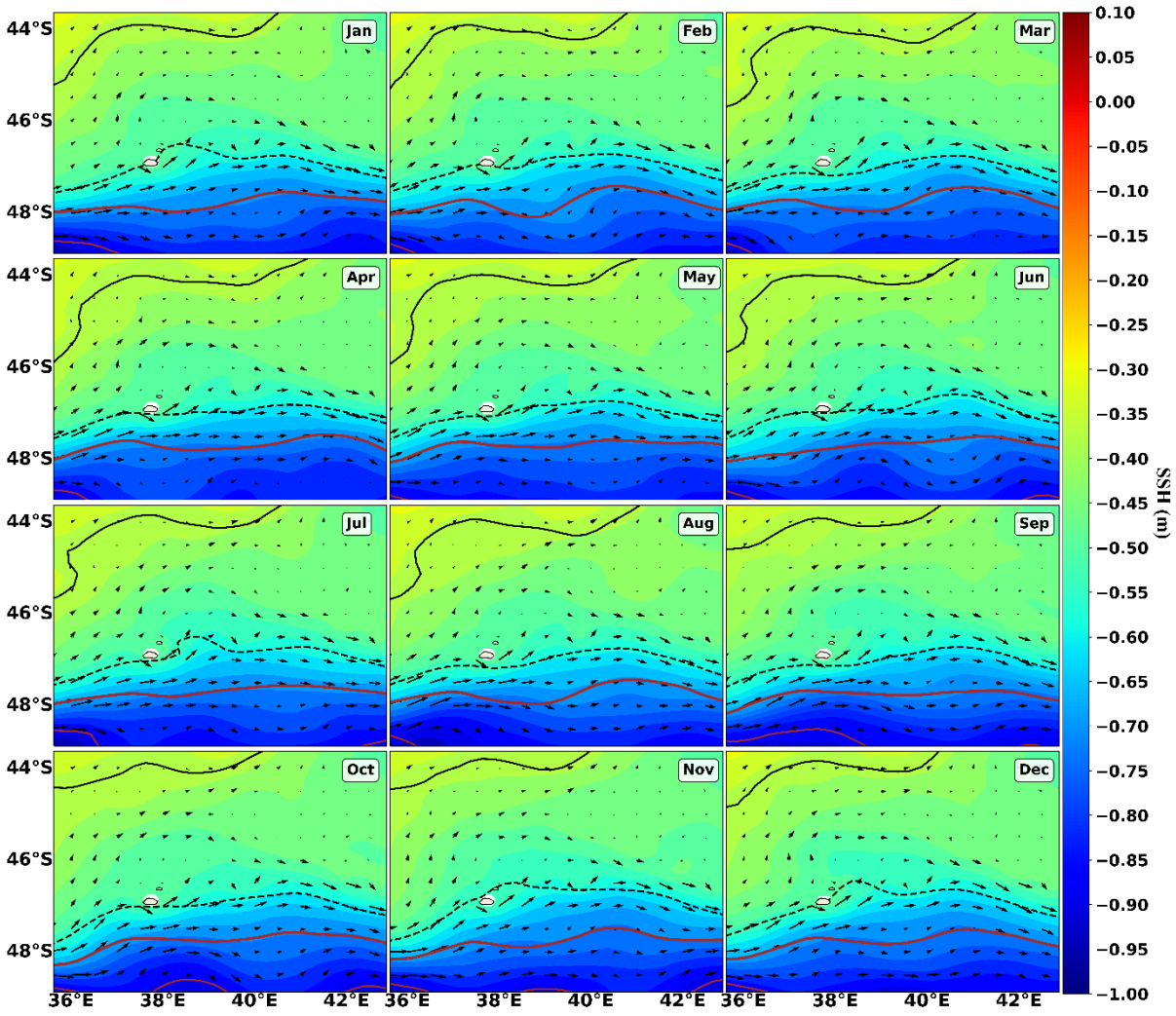

Figure 4.2: The monthly climatology of sea surface height (SSH) (m) with vectors showing geostrophic current (R_{geos}) direction, between January (Jan) and December (Dec) around the Prince Edward Islands from 1993 to 2020 using the GLORYS model output. The black solid and dashed lines represent the M-SAF and S-SAF, respectively. The solid thick and thinner brown lines represent the N-APF and M-APF, respectively. White shading denotes regions of no data. These front positions were identified from satellite altimetry using ADT according to the process described by Sokolov and Rintoul (2002).

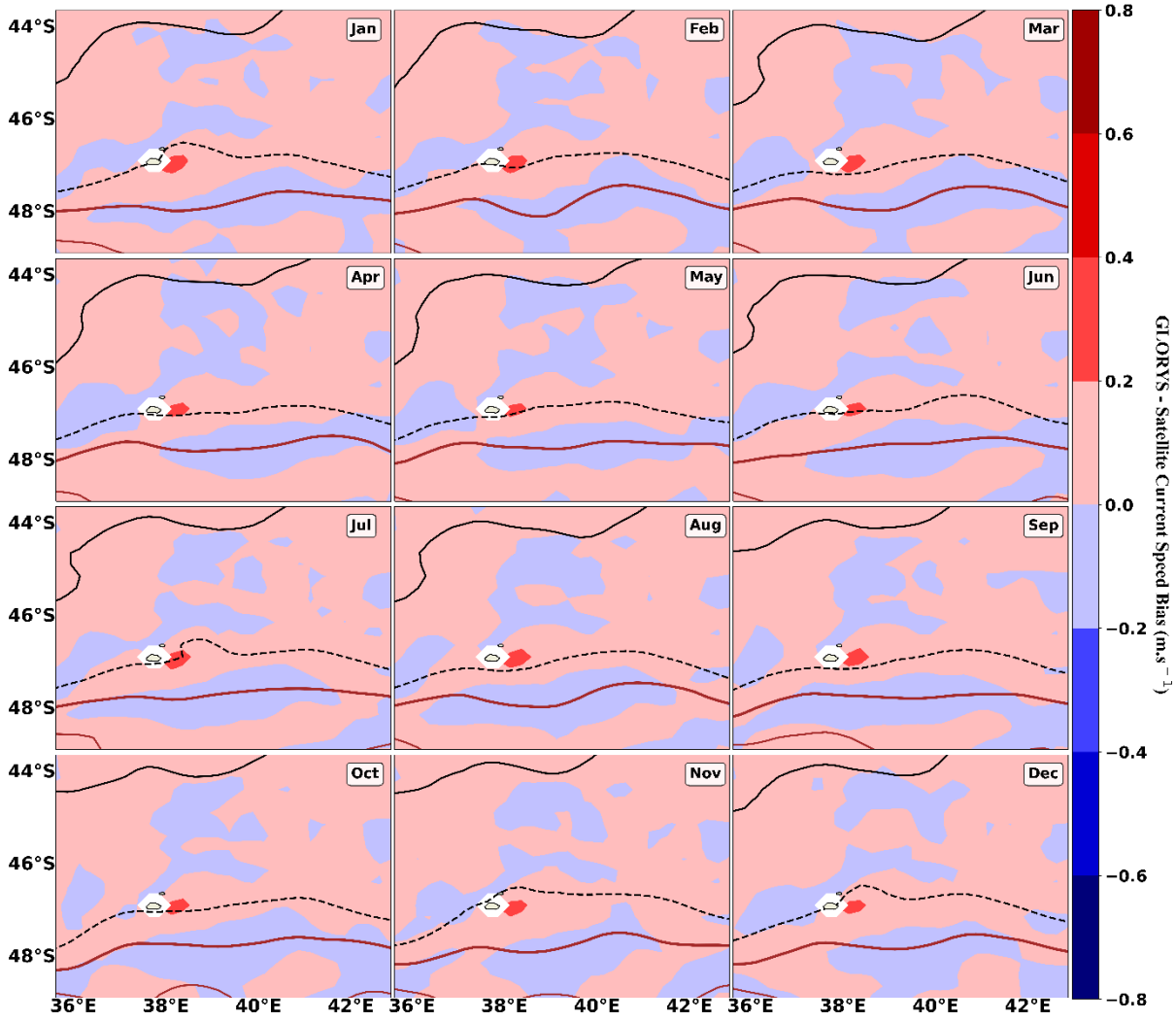

Figure 4.3: The monthly climatology of current speed bias (m s^{-1}) (GLORYS R_{geos} – Satellite R_{geos}), from January (Jan) to December (Dec) around the Prince Edward Islands. The black solid and dashed lines represent the M-SAF and S-SAF, respectively. The solid thick and thinner brown lines represent the N-APF and M-APF, respectively. White shading denotes regions of no data. These front positions were identified from satellite altimetry using ADT according to the process described by Sokolov and Rintoul (2002).

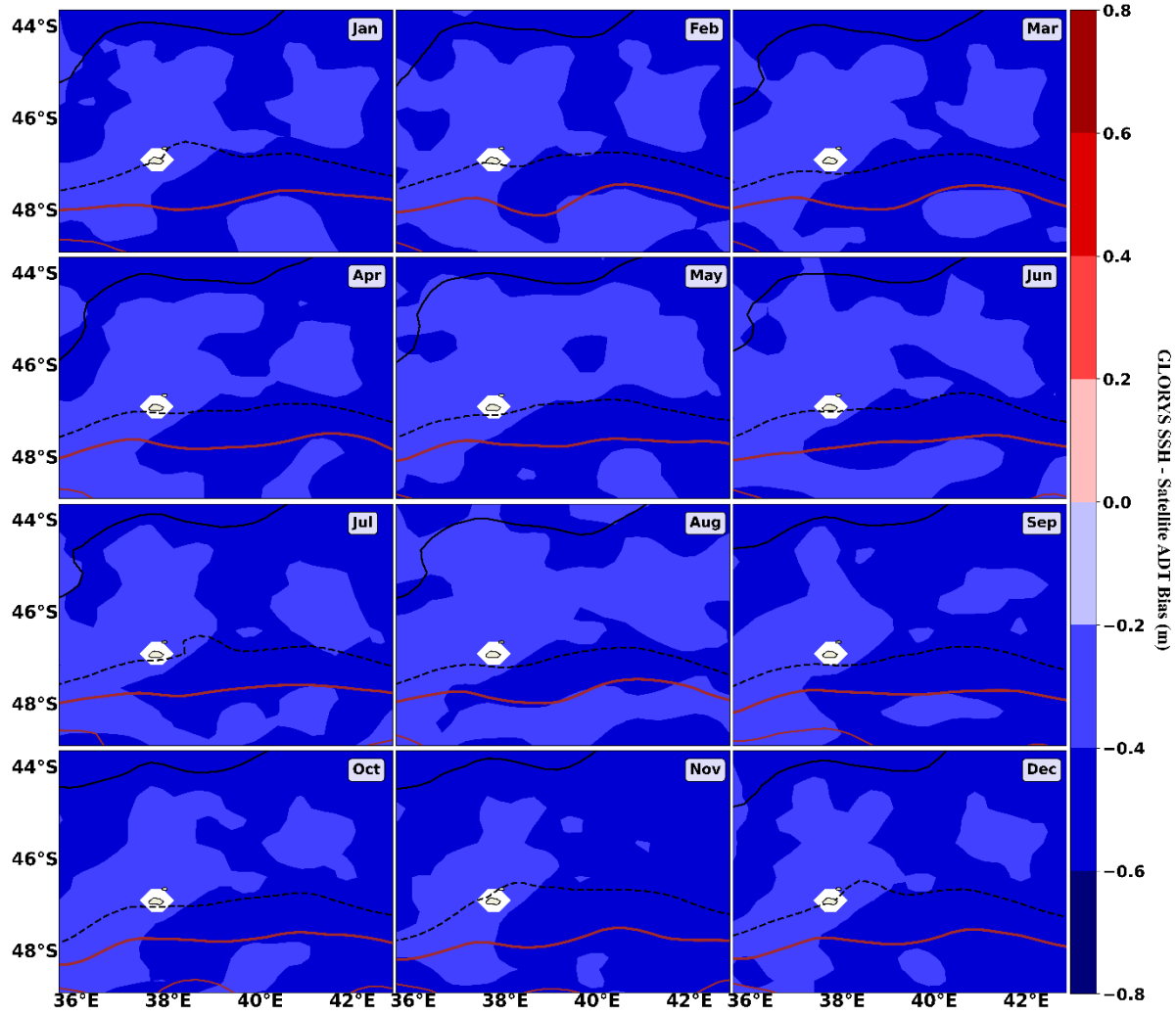

Figure 4.4: The monthly climatology of sea surface height (SSH) bias (m) (GLORYS SSH – Satellite ADT), from January (Jan) to December (Dec) around the Prince Edward Islands. The black solid and dashed lines represent the M-SAF and S-SAF, respectively. The solid thick and thinner brown lines represent the N-APF and M-APF, respectively. Areas shaded white denote regions of no data. These front positions were identified from satellite altimetry using ADT according to the process described by Sokolov and Rintoul (2002).

4.1.2 Temperature

Temperature at the surface

In order to assess the validity and suitability of the GLORYS model at reproducing SST variability in the PEIs region, it was necessary to initially investigate the known degree of variability and drivers of SST in the region using *in situ* (WOA18 and CARS09) and reanalysis (OSTIA) products.

The same meridional SST gradient was observed across the *in situ* (WOA18 and CARS09), satellite (OSTIA) and model (GLORYS) outputs evaluated in this study, where higher SST (>6 ^{o}C) was observed to the north of the PEIs and lower SST (<5 ^{o}C) to the south, agreeing with

Toolsee et al. (2021). This north-south gradient can be explained as the result of the Earth's tilt which decreases the amount of available solar radiation with increasing latitude (Marshall and Plumb, 2007).

WOA18 and OSTIA SST monthly climatologies (*Figure 4.5; Figure 4.7*) displayed comparable seasonal cycles. Warmer waters had a greater southward extension, into the study region, in summer and early autumn (March and April). During the end of autumn (May), through winter and spring, there was a greater northward extension of cooler waters (*Figure 4.5; Figure 4.7*). An explanation for this potentially lies in the interactions between the islands and the associated fronts. As described in section 2.3.1 of Chapter 2, the PEIs straddles the northern SAF and southern APF. These frontal systems separate the warmer sub-Antarctic Surface Water (SASW), north of the SAF, from the cooler Antarctic surface water, south of the APF. As far as is known, no previous studies have been conducted of the seasonal cycle for the frontal positions in the vicinity of the PEIs using satellite data over a long period of time (> 25 years). While a high degree of latitudinal variability of the fronts has been observed, it has been suggested that the latitudinal movement of the fronts is responsible for the presence of the predominant water masses at the islands (Lamont et al. 2019; Ansorge et al. 2010). When the SAF lies farther to the north of the PEIs, the associated warmer SASW is pushed further north and eddies on the shelf region at this time have been observed to contain water with properties belonging to AASW (Ansorge and Lutjeharms, 2002). The reverse is true when the SAF is closer to the PEIs, bringing with it the warmer SASW over the PEIs and pushing the cooler AASW further south (Ansorge and Lutjeharms, 2002).

While the seasonal cycle of SST is more closely linked to the available solar radiation variations resulting from Earth's tilt, the frontal movements may be an additional contributing factor to SST seasonality (Toolsee et al. 2021). In comparison to the WOA18 and OSTIA datasets, the CARS09 (*Figure 4.6*) dataset displayed a one month lag in the seasonal pattern, with the southward extension of warmer waters occurring in late summer through autumn, and the northward extension of cooler waters, occurred from the beginning of winter, through spring and persisted into early summer (December) (*Figure 4.6*). Reasoning for this may come from the fact that the CARS09 dataset is derived mainly from historical sub-surface oceanographic measurements, leading to the misinterpretation of temperature variability at the surface (Dunn, 2014). Additionally, both the WOA18 and CARS09 datasets were the results

of limited interpolated *in situ* data, which was collected during specific cruises, and thus the interpolations may be biased to conditions observed during those cruise periods.

At the PEIs, the highest SST for WOA18 (11.4 °C) and for OSTIA (11.7°C) was observed in February. The lowest SST for WOA18 (2.7 °C) and for OSTIA (2.7 °C) was observed in September (*Figure 4.5; Figure 4.7* respectively). CARS09 (*Figure 4.6*) presented an expected delay of highest SST (11.2°C) in March, but the lowest SST (2.6 °C) agreed with WOA18 and OSTIA, occurring in September. While the exact SST values in this study were slightly higher than those recorded by both Toolsee et al. (2021) and Lamont and Toolsee (2022), the months in which they occurred coincided exactly. Although it was expected that the SST maximum would have been in December or January and the minimum in June or July, resulting from the respective maximum and minimum amounts of available solar radiation during the winter and summer, the delay can be explained by the immense capacity to which the SO stores heat (Zanna et al. 2018). A lag between the heat input into the ocean and the output of observed SST is created due to this large heat-storage capacity. The response time of the SO surrounding the PEIs is observed to be between 1 and 2 months, supporting the SST maxima in February, which would follow the increased solar radiation experienced over December and January. Similarly, the SST minima observed in September follows the lowest shortwave radiation period in June and July (Toolsee et al. 2021).

To investigate the seasonal cycle further and the variability of SST around the PEIs, data were extracted from the 5° x 5° study box around the PEIs (*Figure 4.9a*) and averaged to plot a monthly climatology (*Figure 4.9b*). As expected, the long-term mean SST in the 5° x 5° study box (*Figure 4.9b*) showed the same seasonal patterns observed in WOA18, CARS09 and OSTIA SST (*Figure 4.5 to Figure 4.7*), but with a smaller range of values (4.5 to 8 °C), resulting from averaging over the smaller area.

The GLORYS SST monthly climatology (*Figure 4.8*) captures the general seasonal cycle observed across WOA18 (*Figure 4.5*), CARS09 (*Figure 4.6*) and OSTIA (*Figure 4.7*), where warm waters had the greatest southward extension throughout summer and early autumn with a peak (12.1 ^{o}C) in February. Cooler waters had the most northward extension across late autumn, winter and spring with a minimum SST (2.6 ^{o}C) in September. Comparatively, GLORYS is most similar to the OSTIA dataset, capturing the near exact same seasonal cycle (*Figure 4.9b*). This close resemblance is supported by the overall weakest bias (*Figure 4.12*), where a general positive (warm) bias is observed southwest, upstream and north of the PEIs,

resulting from an overestimation of SST between 0 to 0.6 ºC by GLORYS. Directly downstream of the islands, however, an underestimation of between 0 to 0.4 ºC in SST is presented by GLORYS, which could be explained by the overestimation of current speeds which were recorded in section 4.1.1 (*Figure 4.2)* suggesting that the smoothed simulation of the islands bathymetry by GLORYS has a significant impact on the flow of the ACC and the resultant cooling observed.

GLORYS presented the largest difference when compared to CARS09, evident by the varying monthly SST means (*Figure 4.9b*) and with the strongest bias produced (*Figure 4.11*). The bias between GLORYS and CARS09 presented a clear seasonal pattern, with a positive (warm) bias in spring and summer, and negative (cold) bias in autumn and winter. The driver behind this is suggested to be the underestimation of SST by CARS09 in summer and spring and the overestimating in autumn and winter (*Figure 4.9 displays lower (underestimated) SST values in summer and spring and higher (overestimated) SST values in autumn and winter*), resulting from the lack of surface temperature data, as previously mentioned. The CARS09 dataset was interpolated from limited *in situ* data, which was collected during specific cruises, and thus the interpolations could be biased to the mesoscale events which could have occurred during those cruise periods. The same would be true for the WOA18 dataset.

While the GLORYS SST around the PEIs is similar to the SST of WOA18, it is apparent that GLORYS overestimates SST north of the islands by up to 2 ºC in the summer (*Figure 4.10*). Based on the distribution of data collection points, evident as the scatter of black dots in Figure 4.5, it is clear that during the summer months there are less points north of the PEIs. It is suggested that this decrease in data points, along with erroneous interpolation could be misconstruing the true representation of SST for the northern region, thus producing WOA18 data with lower SST values in comparison to GLORYS in the summer.

A model evaluation done by Veitch et al. (2009) investigated the ability of the Regional Ocean Modeling System at simulating the Benguela system in its entirety, concluding that the model underestimated SST along the coast of the order of 1.5 ºC. A similar study done by Russo et al. (2022) which compared the GLORYS model against OSTIA SST for the Agulhas system, recorded an overestimation (> 1 ºC) of SST in the Agulhas Current by GLORYS. In comparison to these previous studies, a maximum SST overestimation of 2 ºC was observed in comparison to coarse resolution *in situ* (WOA18 and CARS09) datasets. However, when GLORYS was compared to the OSTIA product, a higher resolution, overall, more spatially

consistent dataset, a maximum SST overestimation of only 0.6 °C was observed. From this it can be inferred that the GLORYS SST overestimation, in this study, was not extreme and ultimately suggests that the GLORYS model output accurately captures both the seasonal variability as well as the spatial variability of SST within the PEI surrounding region.

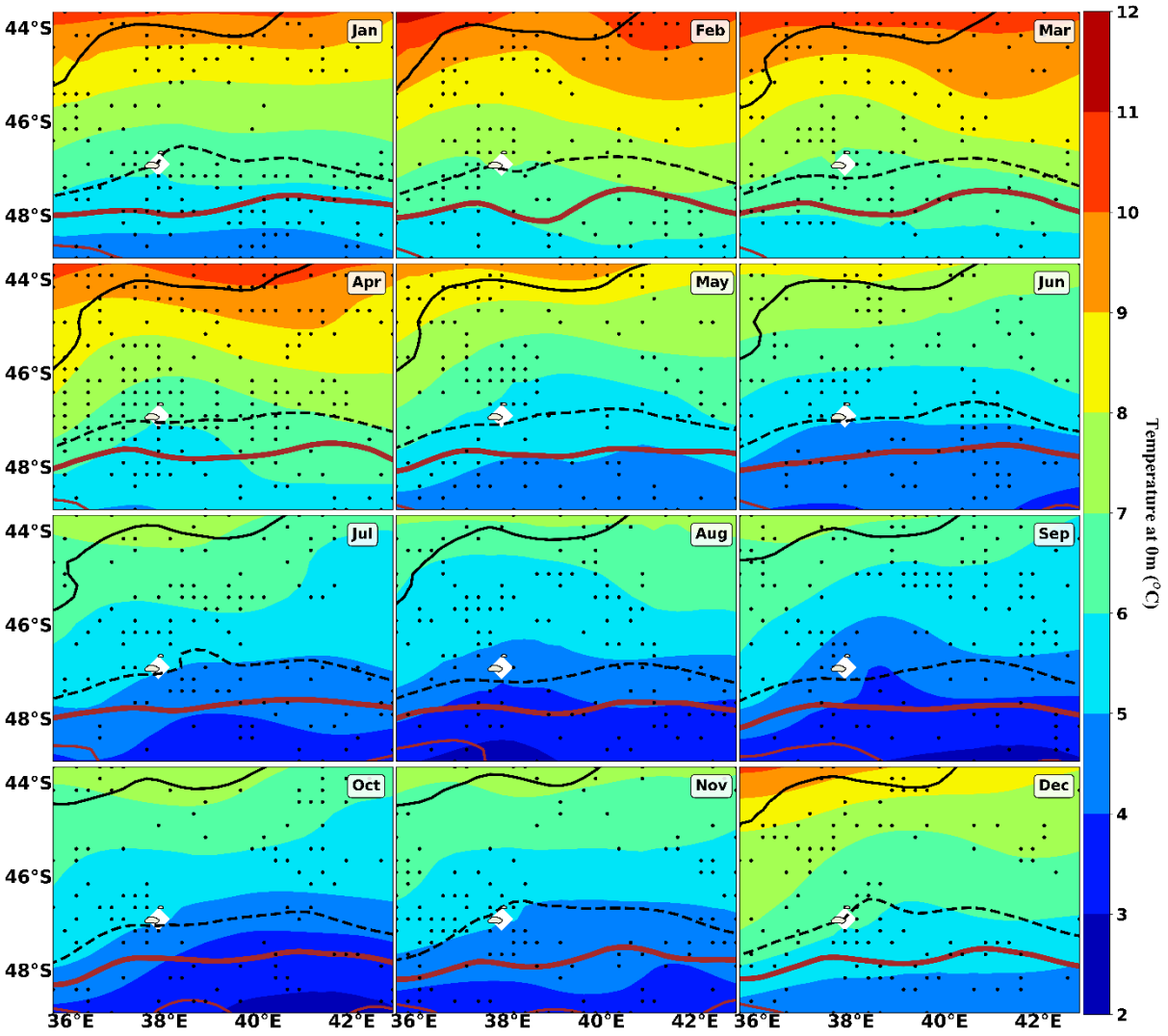

Figure 4.5: The monthly climatology of sea surface temperature (SST) (°C) from January (Jan) to December (Dec) around the Prince Edward Islands from 1955 to 2017 using the WOA18 data. The black solid and dashed lines represent the M-SAF and S-SAF, respectively. The solid thick and thinner brown lines represent the N-APF and M-APF, respectively. Areas shaded white denote regions of no data. Black filled dots illustrate the distribution of data collection points used to produce the map. These front positions were identified from satellite altimetry using ADT according to the process described by Sokolov and Rintoul (2002).

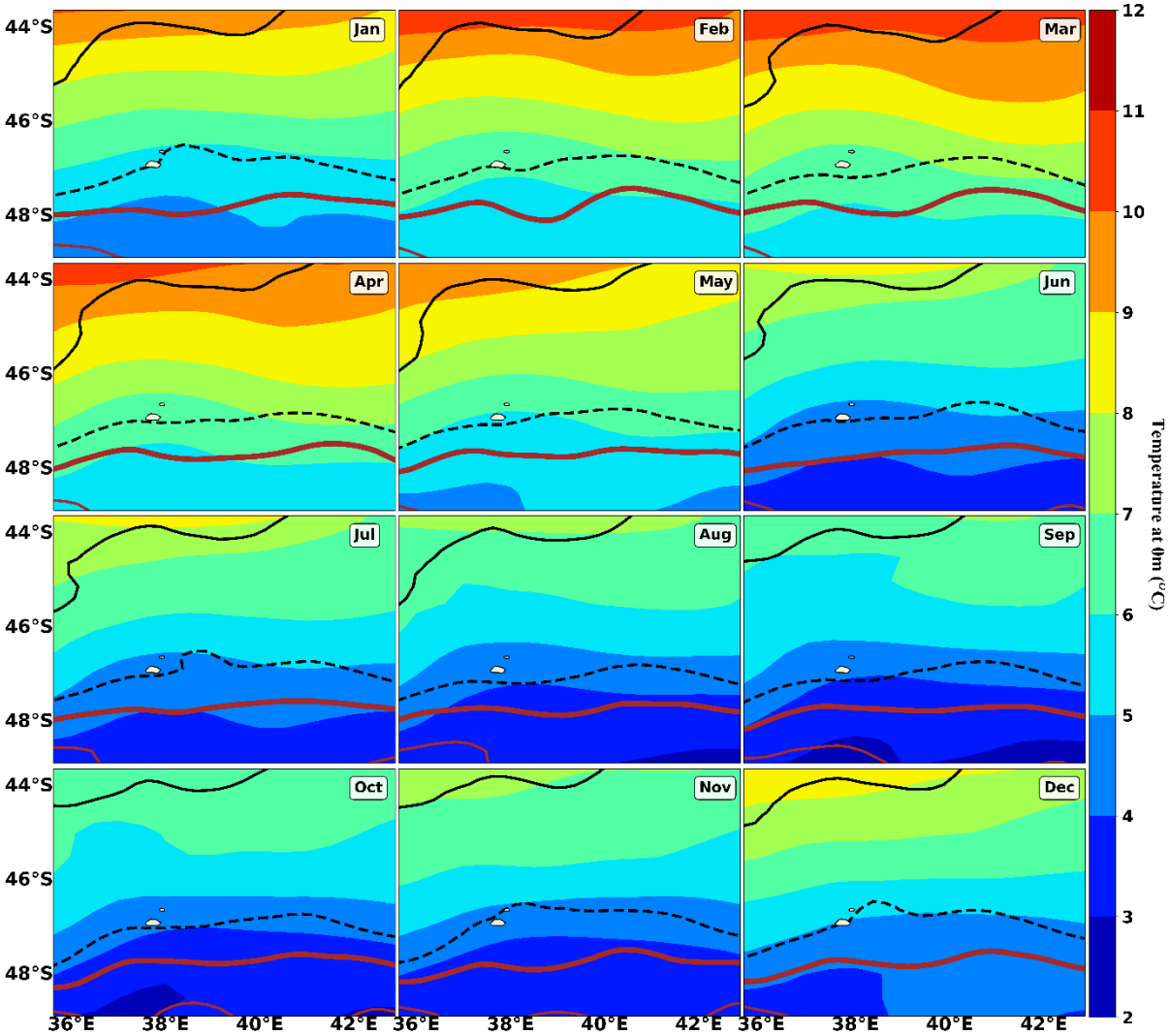

Figure 4.6: The monthly climatology of sea surface temperature (SST) (°C) from January (Jan) to December (Dec) around the Prince Edward Islands from 1985 to 2009 using the CARS09 data. The black solid and dashed lines represent the M-SAF and S-SAF, respectively. The solid thick and thinner brown lines represent the N-APF and M-APF, respectively. These front positions were identified from satellite altimetry using ADT according to the process described by Sokolov and Rintoul (2002).

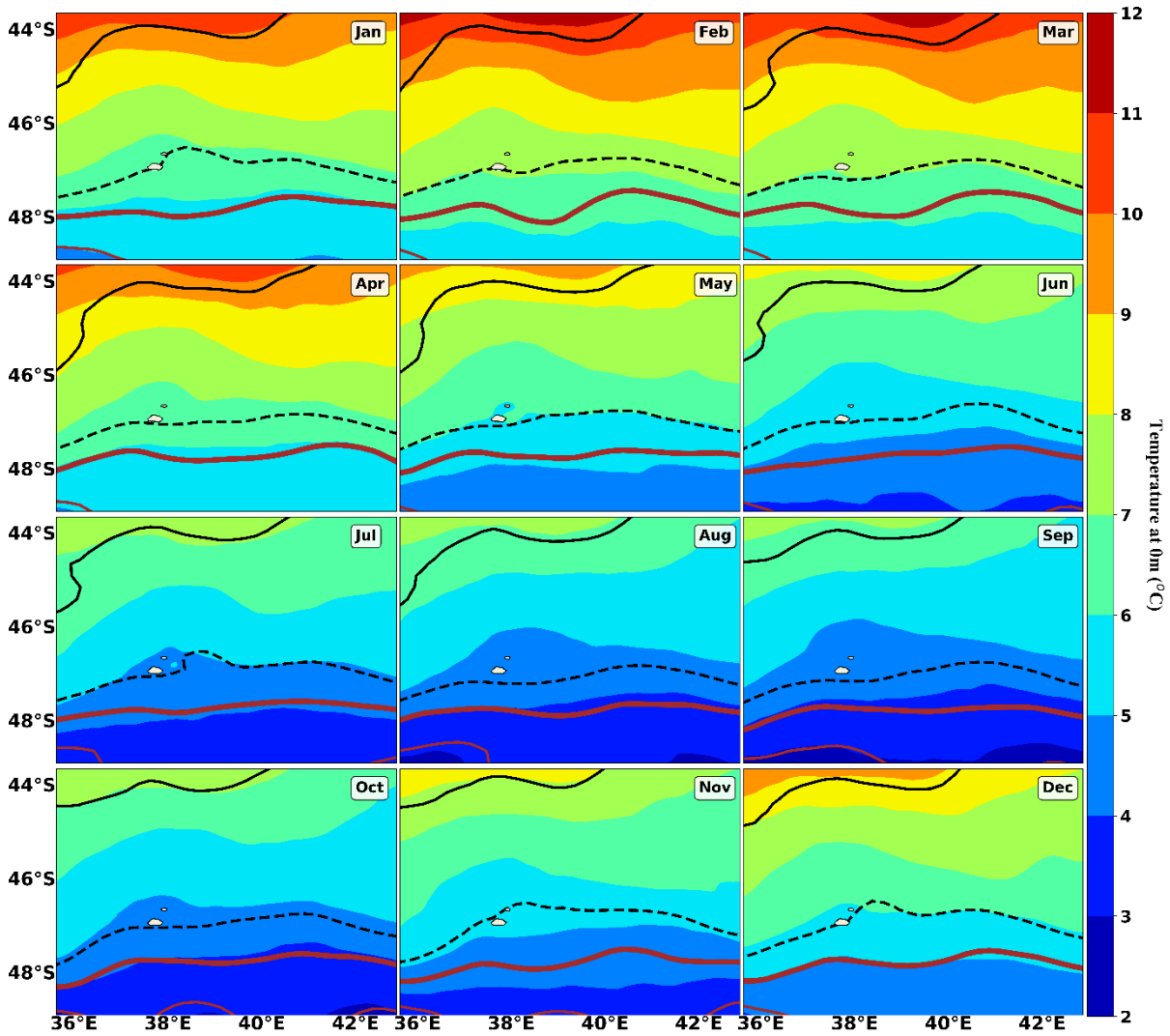

Figure 4.7: The monthly climatology of sea surface temperature (SST) (°C) from January (Jan) to December (Dec) around the Prince Edward Islands from 1981 to 2021 using the OSTIA dataset. The black solid and dashed lines represent the M-SAF and S-SAF, respectively. The solid thick and thinner brown lines represent the N-APF and M-APF, respectively. These front positions were identified from satellite altimetry using ADT according to the process described by Sokolov and Rintoul (2002).

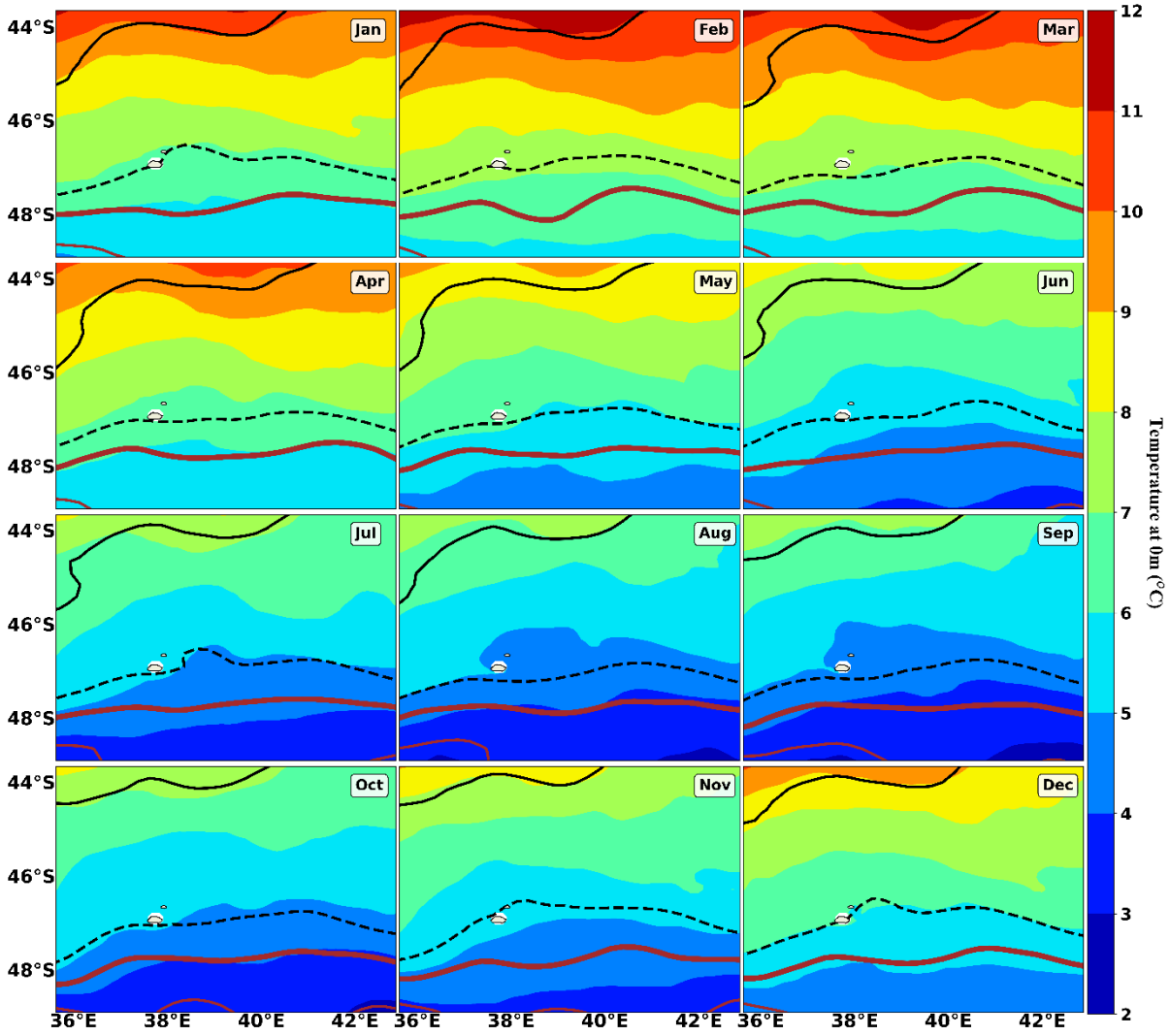

Figure 4.8: The monthly climatology of sea surface temperature (SST) (°C) from January (Jan) to December (Dec) around the Prince Edward Islands from 1993 to 2020 using the GLORYS model output. The black solid and dashed lines represent the M-SAF and S-SAF, respectively. The solid thick and thinner brown lines represent the N-APF and M-APF, respectively. Areas shaded white denote regions of no data. These front positions were identified from satellite altimetry using ADT according to the process described by Sokolov and Rintoul (2002).

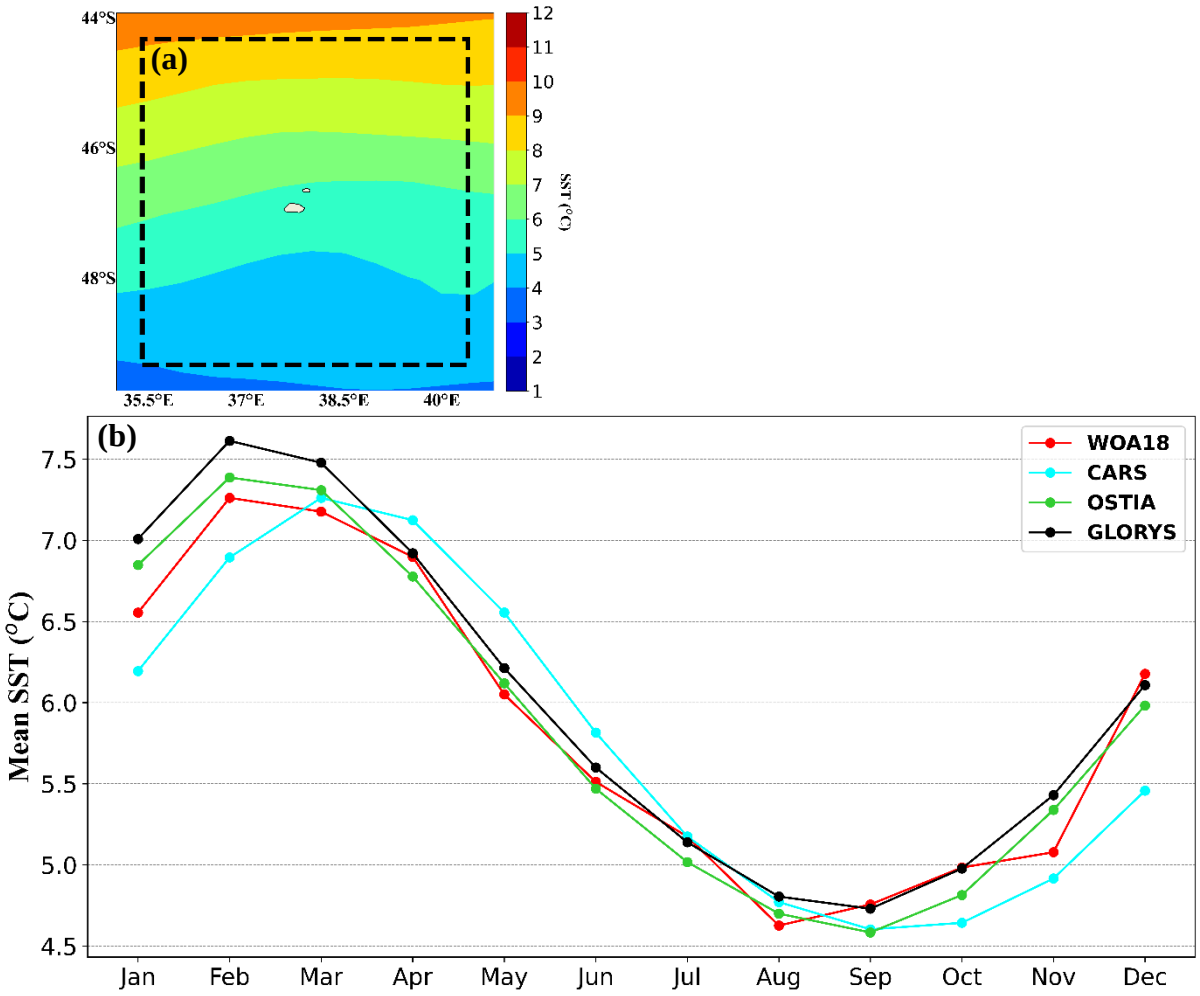

*Figure 4.9: (**a**) The 5° x 5° study box around the Prince Edward Islands from which sea surface temperature (SST) (°C) data was extracted and averaged to produce the long-term mean SST. (**b**) Monthly climatology of the averaged SST (°C) data in the study box from the three datasets; WOA18, CARS09, OSTIA and from the GLORYS model output.*

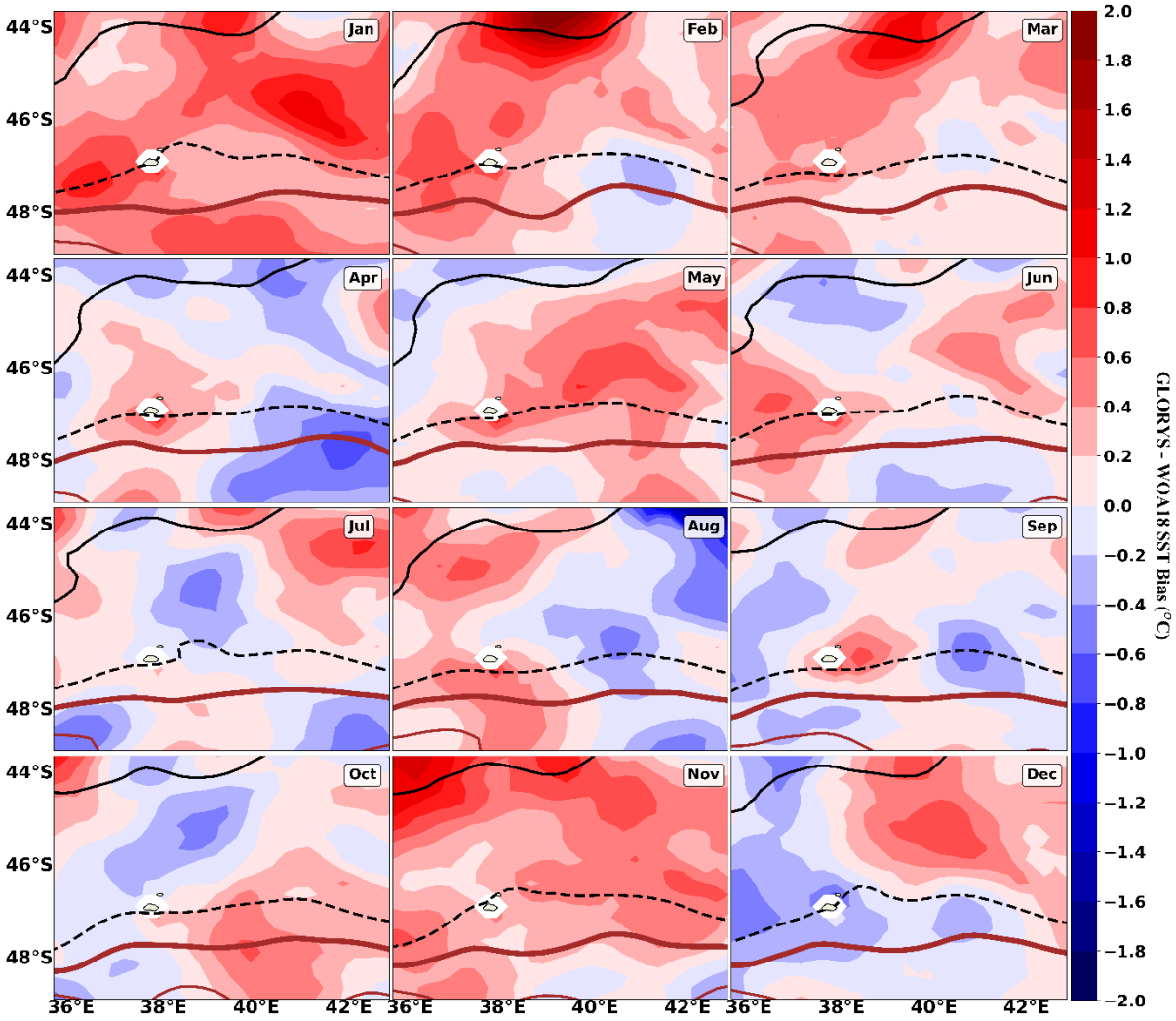

Figure 4.10: The monthly climatology of sea surface temperature (SST) bias (°C) (GLORYS SST – WAO18 SST) from January (Jan) to December (Dec) around the Prince Edward Islands. The black solid and dashed lines represent the M-SAF and S-SAF, respectively. The solid thick and thinner brown lines represent the N-APF and M-APF, respectively. White shading denotes regions of no data. These front positions were identified from satellite altimetry using ADT according to the process described by Sokolov and Rintoul (2002).

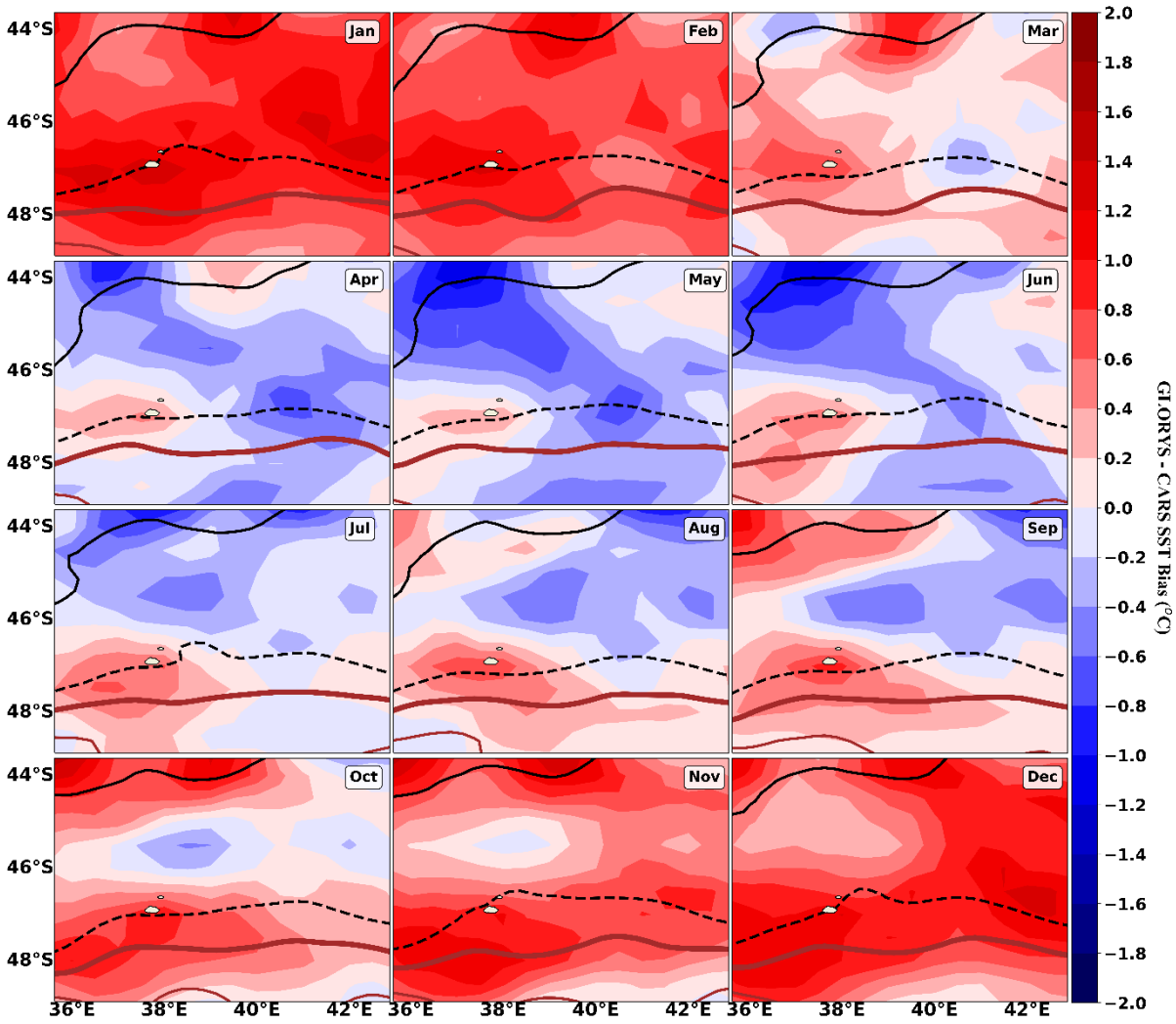

Figure 4.11: The monthly climatology of sea surface temperature (SST) bias (°C) (GLORYS SST – CARS09 SST) from January (Jan) to December (Dec) around the Prince Edward Islands. The black solid and dashed lines represent the M-SAF and S-SAF, respectively. The solid thick and thinner brown lines represent the N-APF and M-APF, respectively. White shading denotes regions of no data. These front positions were identified from satellite altimetry using ADT according to the process described by Sokolov and Rintoul (2002).

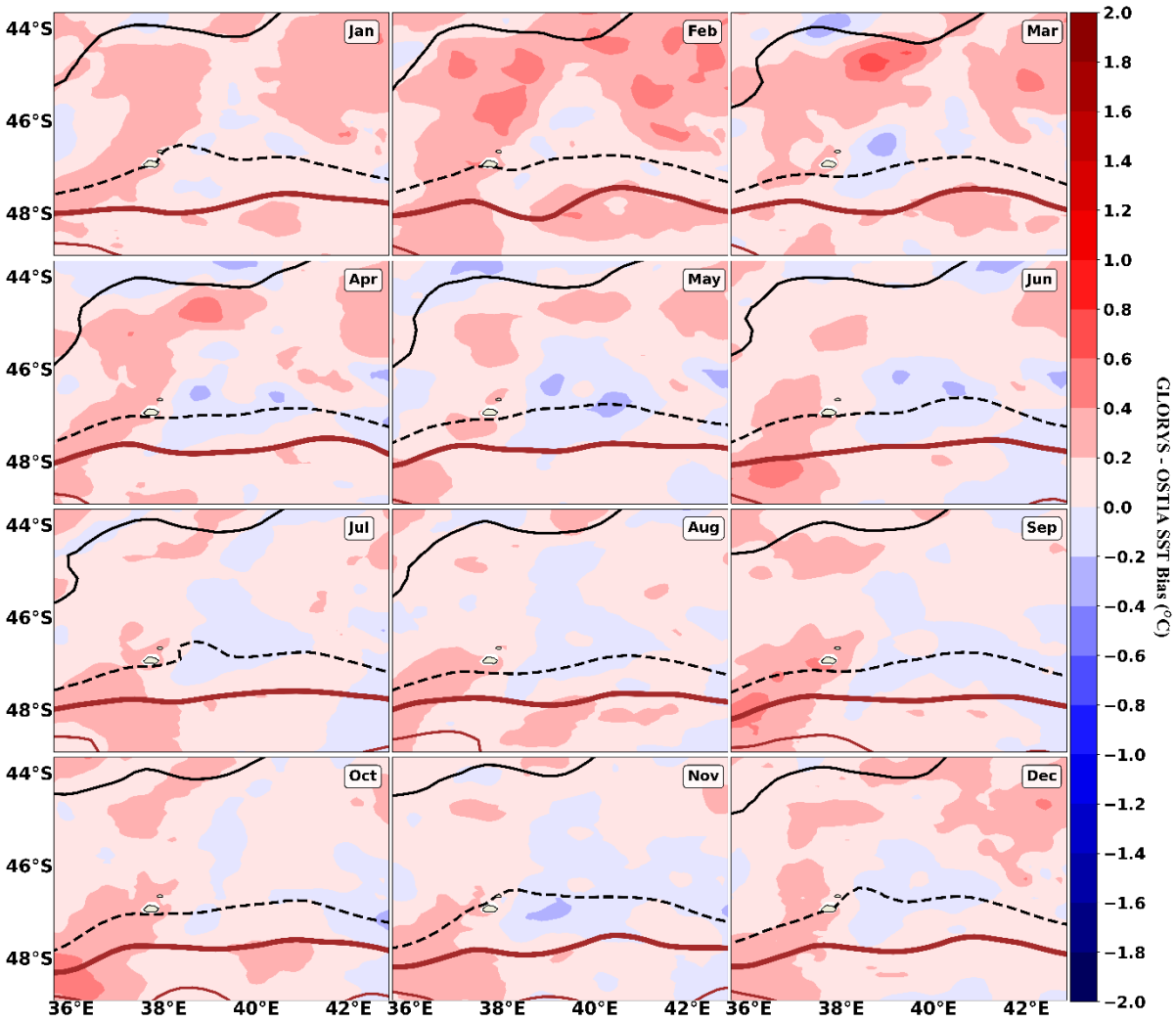

Figure 4.12: The monthly climatology of sea surface temperature (SST) bias (°C) (GLORYS SST – OSTIA SST) from January (Jan) to December (Dec) around the Prince Edward Islands. The black solid and dashed lines represent the M-SAF and S-SAF, respectively. The solid thick and thinner brown lines represent the N-APF and M-APF, respectively. White shading denotes regions of no data. These front positions were identified from satellite altimetry using ADT according to the process described by Sokolov and Rintoul (2002).

Temperature at 200 m

Similar, to SST, the temperature at 200 m and the variability thereof was first assessed at the PEIs using *in situ* (WOA18 and CARS09) datasets. The GLORYS model output was then compared against these products to investigate the suitability and accuracy of the model at reproducing the subsurface temperature.

The meridional gradient of higher temperatures (>5 ^{o}C) to the north of the PEIs and lower temperatures (<4 ^{o}C) to the south were again observed across the *in situ* (WOA18 and CARS09) (*Figure 4.13; Figure 4.14*) and the model (GLORYS) (*Figure 4.15*) outputs. These findings agree with the north-south gradient observed over the region for SST (*Figure 4.5 to 4.8*), therefore suggesting that the decreasing amount of available solar radiation with latitude

has the same influence on temperature at the subsurface (200 m depth) (Marshall and Plumb, 2007).

WOA18 (*Figure 4.13*) and CARS09 (*Figure 4.14*) displayed similar seasonal patterns with higher temperatures at the PEIs in austral winter (JJA), observed as a greater southward extension of warmer water over the islands. Spring and summer (SON and DJF) presented lower temperatures, evident as a greater northward extension of colder waters surrounding the PEIs. This seasonal cycle of temperatures at 200 m opposes the SST seasonal variability over the same region for WOA18 (*Figure 4.5*) and CARS09 (*Figure 4.6*). At the PEIs, the highest temperature, at 200 m depth, for WOA18 (7.5 °C) and for CARS09 (8.3°C) was observed in September and July respectively. The lowest 200 m temperature for WOA18 and CARS09 (2.1 °C) was observed in November (*Figure 4.13; Figure 4.14*).

The opposing seasonality observed with temperature at 200 m is likely related to the strong seasonal cycle of the upper mixed layer depth (MLD) in the SO. The oceanic mixed layer is a layer that through turbulent mixing processes, has salinity, temperature and density readings almost completely homogenous throughout its vertical depth. A study done by de Boyer Montégut et al (2004) observed, between 45°S and 60°S in the SO, the MLD extends as deep as 300 m in the winter months and is as shallow as 70 m in the summer. This temporal variability can be linked to several contributing factors such as forcing by surface conditions like wind, interal waves and the lateral advection of atmospheric and oceanic properties, amonst many others. The deepened MLD, along with strong vertical convection in winter suggests that the warm surface waters are well mixed to a depth of 200 m. Whereas in summer the shallower MLD and associated relatively weaker winds, which lead to weaker convection process, the warmer surface waters are confined to the surface layer thus leaving the cooler water below it which is what was observed at 200 m. (*Figure 4.13; Figure 4.14*) Therefore at the surface, due to the available amount of solar radiation resulting from Earth's tilt, SST is higher in summer and lower in winter but in the subsurface this is reversed due to the depth at which the surface water is allowed to penetrate until based on the MLD. The lower water temperatures in the summer are supported by the findings in Lamont et al. (2019), whereby bottom temperatures recorded from mooring data illustrated similar differences in temperature which were attributed to the seasonality of the MLD within the SO.

As previously mentioned for SST, to further investigate the temperature seasonal cycle at 200 m around the PEIs, data were extracted from a 5° x 5° study box around the PEIs (*Figure 4.16a*)

and averaged to plot a time series (*Figure 4.16b*). As expected, the long-term mean temperature for WOA18 and CARS09 in the 5° x 5° (*Figure 4.16b*) showed the same seasonal pattern as observed in Figures 4.13 and 4.14, but with a smaller range of values (4 to 5.2 °C), resulting from averaging over the smaller area. The seasonal pattern produced using the WOA18 data displayed more variability (*Figure 4.16b*), in comparison to the smoother CARS09 seasonal cycle and is suggested to be the result of less available data at depth. The Lamont et al. (2019) study revealed a temperature range of 3 to 6 ^{o}C recorded from a mooring deployed at 174 m on the north-eastern shelf region of Marion island. While the Lamont et al. (2019) results are isolated to the shelf and thus are more influenced by the localised oceanographic variability, the similar ranges in temperature and seasonal patterns, for at least the spring and summer months, instills a confidence in the *in situ* results presented above, despite the disproportional distribution of collected data points.

The monthly temperature climatology by GLORYS (*Figure 4.15*) did not demonstrate as clear of a seasonal cycle as the *in situ* (*Figure 4.13; Figure 4.14*) data. Colder Antarctic waters maintained a position south of the PEIs and warmer more subtropical waters encompassed the northern extent of the islands, as well as around the islands themselves, whereby warmer waters (>5 ^{o}C) were sustained over the island's system throughout the entire year The highest temperature (8.2 ^{o}C) was recorded in August and the lowest temperature (2.5 ^{o}C) was in October, suggesting there was a delay of one month by GLORYS in simulating the same seasonal cycle as that of WOA18 and CARS09.

The GLORYS 200 m temperature climatology presented cooler bands of water that appeared to be wrapping around the PEIs in a clockwise direction (*Figure 4.15*), which matched the associated flow patterns highlighted by the overlaid total current vectors. This deviation in the flow pattern was also evident within the GLORYS SSH plot (*Figure 4.2*). The GLORYS model output appeared to simulate bathymetric features shallower than 200 m (*Figure 4.15*), evident as the areas shaded in white. It is therefore suggested that this bathymetry could be the driver of the anticyclonic flow observed around the PEIs, most noticeable between November and January. This anomalous temperature pattern was not observed in the WOA18 (*Figure 4.13*) and CARS09 (*Figure 4.14*) climatologies, owing to the fact that these bathymetric features do not exist within those datasets. It can be inferred that these bathymetric features are not accurate because, as examined in section 3.3.1 in Chapter 3, the ETOPO and GEBCO data did not display any shallow banks in the lee of the PEIs.

GLORYS was able to capture a weaker seasonal cycle, in the 5° x 5° study box (*Figure 4.16b*), compared to CARS09 and WOA18, where a maximum temperature of 5.10 °C was recorded in the winter and a minimum of 4.81 °C in the summer. Although GLORYS showed the same seasonal pattern, the overall monthly temperatures were on average 0.45 °C warmer than WOA18 and CARS09. This warm bias was evident in Figures 4.17 and 4.18, where the overall pattern observed was an overestimation of temperature by GLORYS.

Similar to the pattern described earlier for SST, the overall GLORYS bias for temperature at 200 m, with respect to WOA18 (*Figure 4.17*) can be described as a strong, warm (positive) bias resulting from the overestimation of temperature by GLORYS. The months of June and July, however, presented a weak, cool (negative) bias and coupled with the lack of a clear seasonal bias, this is suggested to be the result of an underestimation of temperature by GLORYS, specifically over the localised region around the PEIs (*Figure 4.17*). When compared with the CARS09 dataset, however, a clearer seasonal pattern is evident with a cool (negative) bias observed between April and September to the north of the PEIs and a warm (positive) bias between October and March, south of the islands (*Figure 4.18*). This seasonal bias is suggested to be linked to the overall warmer seasonal cycle simulated by GLORYS. Over the summer and spring months, GLORYS overestimated the temperatures south of the PEIs, simulating temperatures which were a 1.80 ^{o}C warmer than those observed by CARS09. The winter and autumn months presented an underestimation of temperature by GLORYS, suggesting the model was unable to capture the degree to which the water temperature increased, as was observed by WOA18 and CARS09 (Figure 4.13; Figure 4.14). Additionally, WOA18 and CARS09 displayed a clear southward migration of warmer waters over the PEIs, the model did not capture this southward extension, most evident by the strongest cool bias in June at the northern boundary of this study region (*Figure 4.18*). An explanation for the underestimation by GLORYS in the winter and autumn months is suggested to be the result of the anticyclonic flow simulated by the imitated bathymetric features in the lee of the PEIs. This flow pattern resulted in the encroaching of southern-originating, cold waters into the northern parts of the islands, opposing the warmer waters observed by WAO18 and CARS09.

While comprehensive long term (±27 years) investigations of subsurface temperatures, in the vicinity of the PEIs, have not yet been conducted, and because there are no previous publications to compare the current findings to, it can be assumed that the temperature at 200 m should resemble the observations produced by the WOA18 (*Figure 4.13*) and CARS09 (*Figure 4.14*) datasets. Therefore, the overall comparison of GLORYS to these *in situ* datasets

suggests that while the model captures the seasonal variability, albeit weak, it fails to accurately capture the spatial variability of temperature at 200 m, for the PEIs region. This suggestion however should be considered with discretion given that the *in situ* (WOA18 and CARS09) datasets were based on limited observations at depth, more so than at the surface, and that their end results are mainly achieved through interpolation, inferring that they themselves may be presenting a misconstrued perception of what the temperature variability at depth actually is.

On a climatological scale, GLORYS performs better at the surface (biases were smaller with SST) owing to the fact that more surface data, both *in situ* and satellite, is being assimilated into the model (Russo et al. 2022; Drévillon et al. 2021a). When it came to the subsurface, GLORYS overestimated temperature, resulting from; fewer *in situ* data points, the absence of satellite data being assimilated at these depths and the influence of inaccurate bathymetry. Overall, the large-scale patterns and biases captured by GLORYS are evident across the entire SO and not just observed at the PEIs (*see Appendix Figures A7 to A9*) supporting the validity of the GLORYS model output at simulating temperature within the surrounding PEI region.

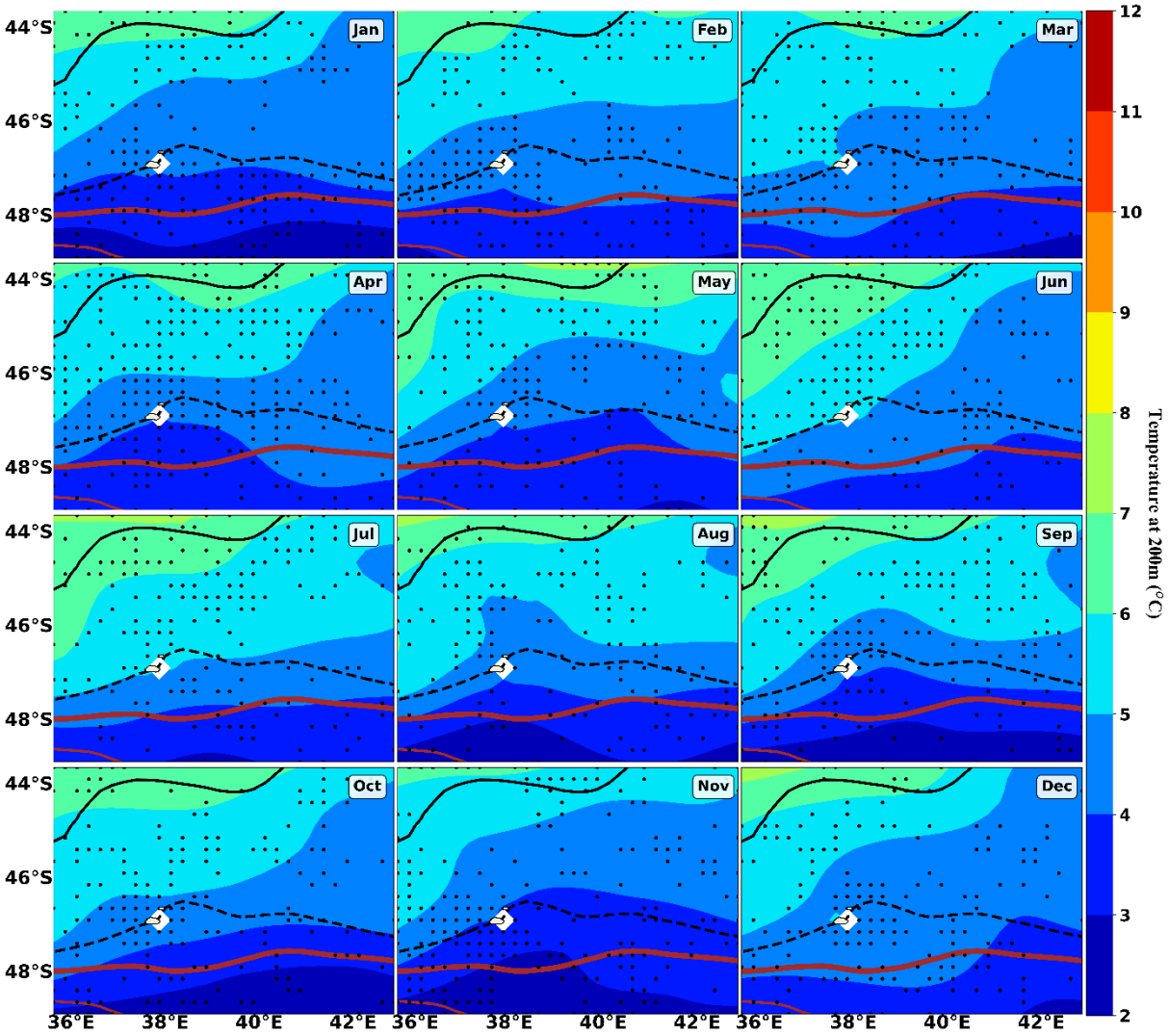

Figure 4.13: The monthly climatology of sea water temperature (°C) at a depth of 200 m, from January (Jan) to December (Dec) around the Prince Edward Islands from 1955 to 2017 using the WOA18 data. The black solid and dashed lines represent the M-SAF and S-SAF, respectively. The solid thick and thinner brown lines represent the N-APF and M-APF, respectively. Areas shaded white denote regions of no data. Black filled dots illustrate the distribution of data collection points used to produce the map. These front positions were identified from satellite altimetry using ADT according to the process described by Sokolov and Rintoul (2002).

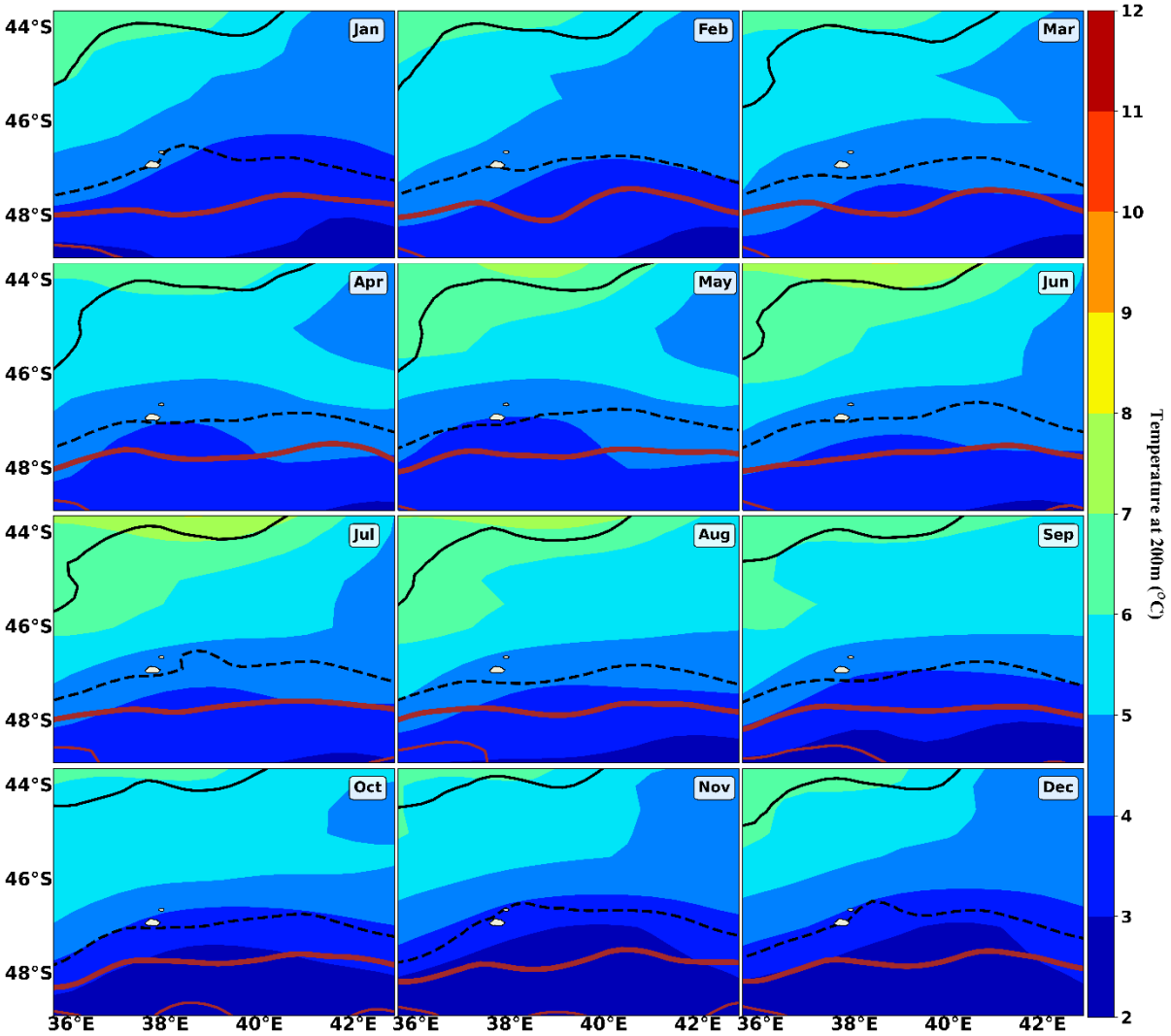

Figure 4.14: The monthly climatology of sea water temperature (°C) at a depth of 200 m, from January (Jan) to December (Dec) around the Prince Edward Islands from 1985 to 2009 using the CARS09 data. The black solid and dashed lines represent the M-SAF and S-SAF, respectively. The solid thick and thinner brown lines represent the N-APF and M-APF, respectively. These front positions were identified from satellite altimetry ADT according to the process described by Sokolov and Rintoul (2002).

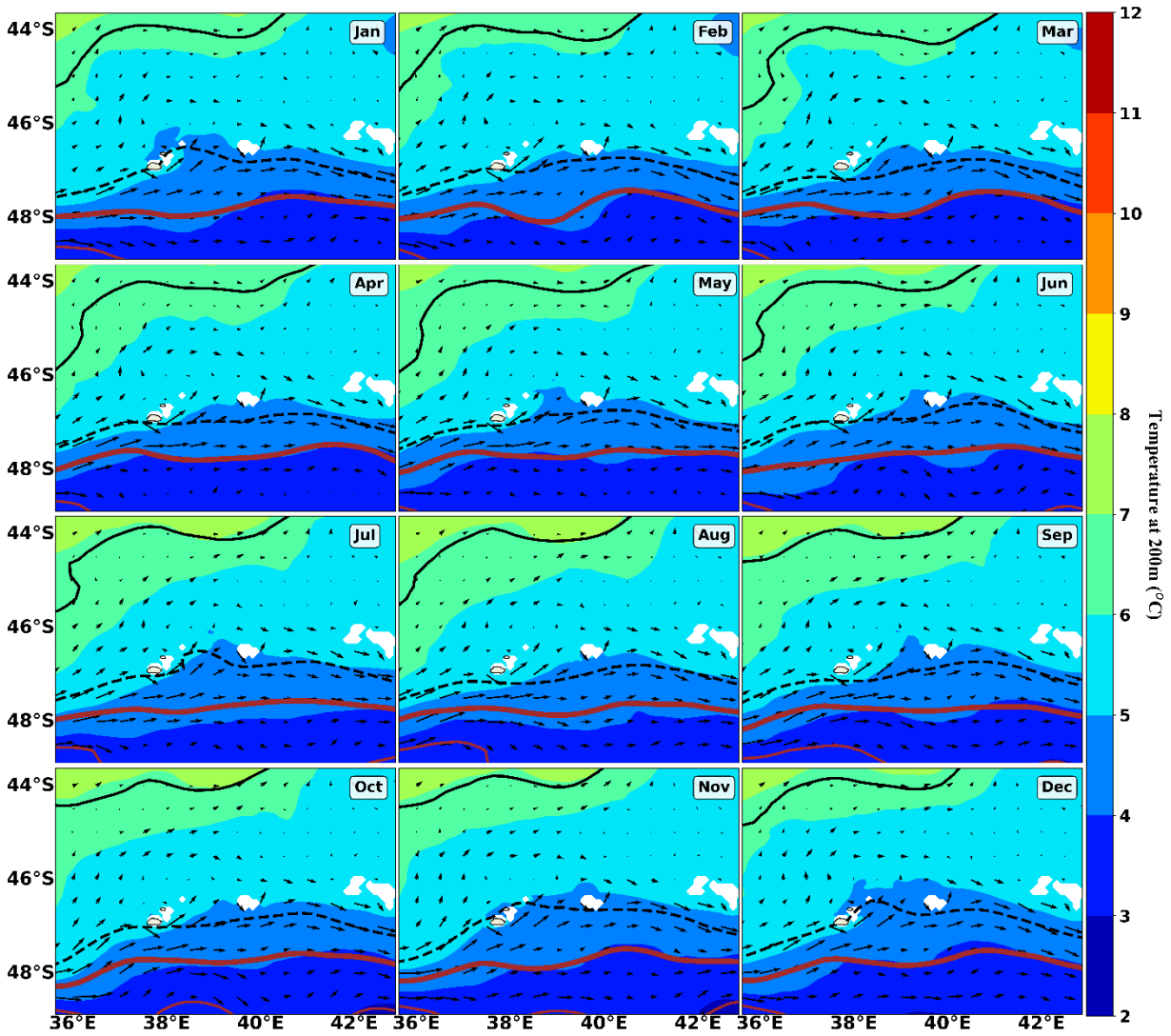

Figure 4.15: The monthly climatology of sea water temperature (°C) at a depth of 200 m, with vectors showing total current (R_{total}) direction around the Prince Edward Islands. Between January (Jan) and December (Dec) from 1993 to 2020 using the GLORYS model output. The black solid and dashed lines represent the M-SAF and S-SAF, respectively. The solid thick and thinner brown lines represent the N-APF and M-APF, respectively. Areas shaded white denote regions of no data. These front positions were identified from satellite altimetry using ADT according to the process described by Sokolov and Rintoul (2002).

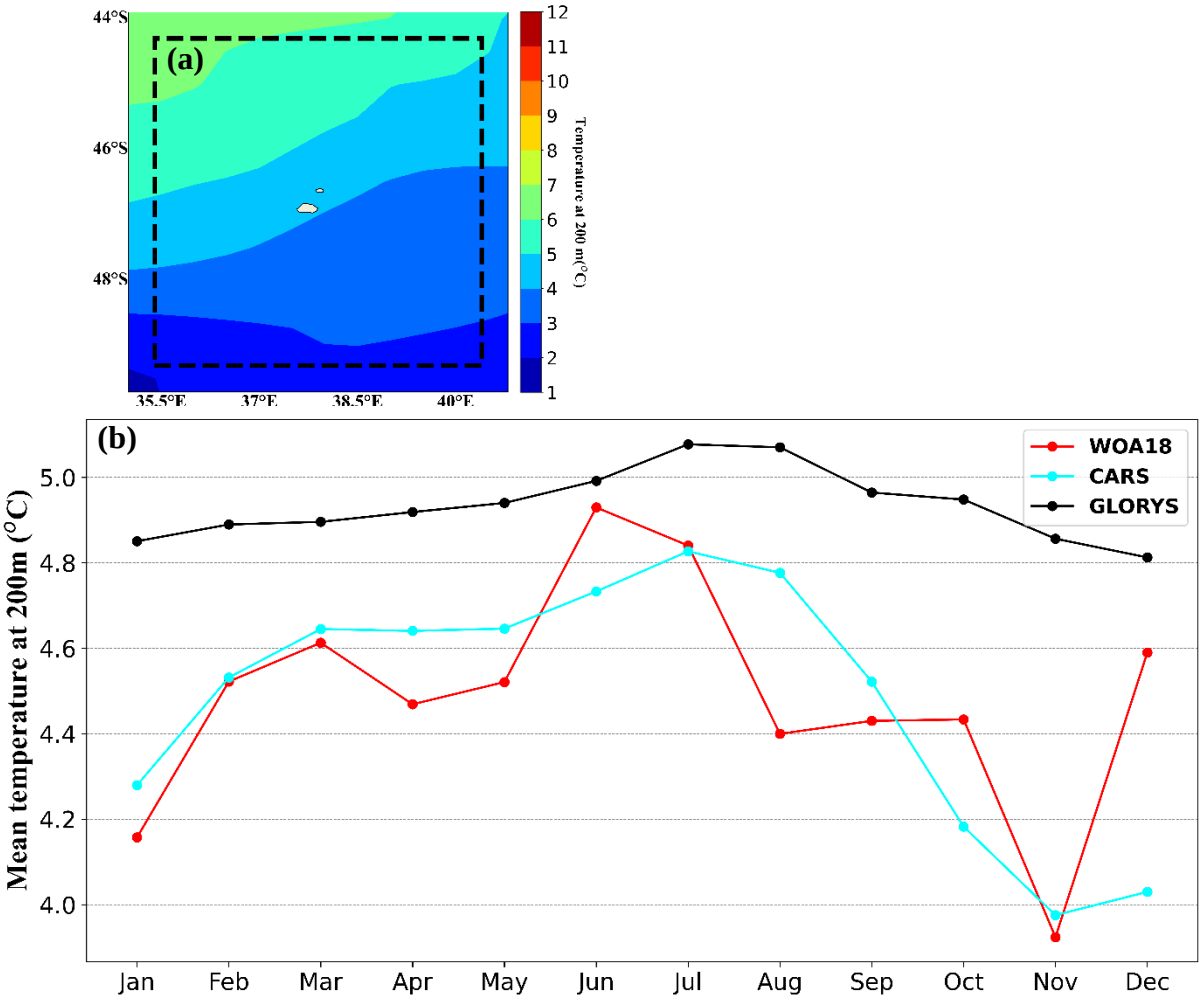

*Figure 4.16: (**a**) The 5° x 5° study box around the Prince Edward Islands from which temperature (°C) data at 200 m was extracted and averaged to produce the long-term mean SST. (**b**) Monthly climatology of the averaged temperature (°C) at 200 m in the study box from the two datasets; WOA18, CARS09, and from the GLORYS model output.*

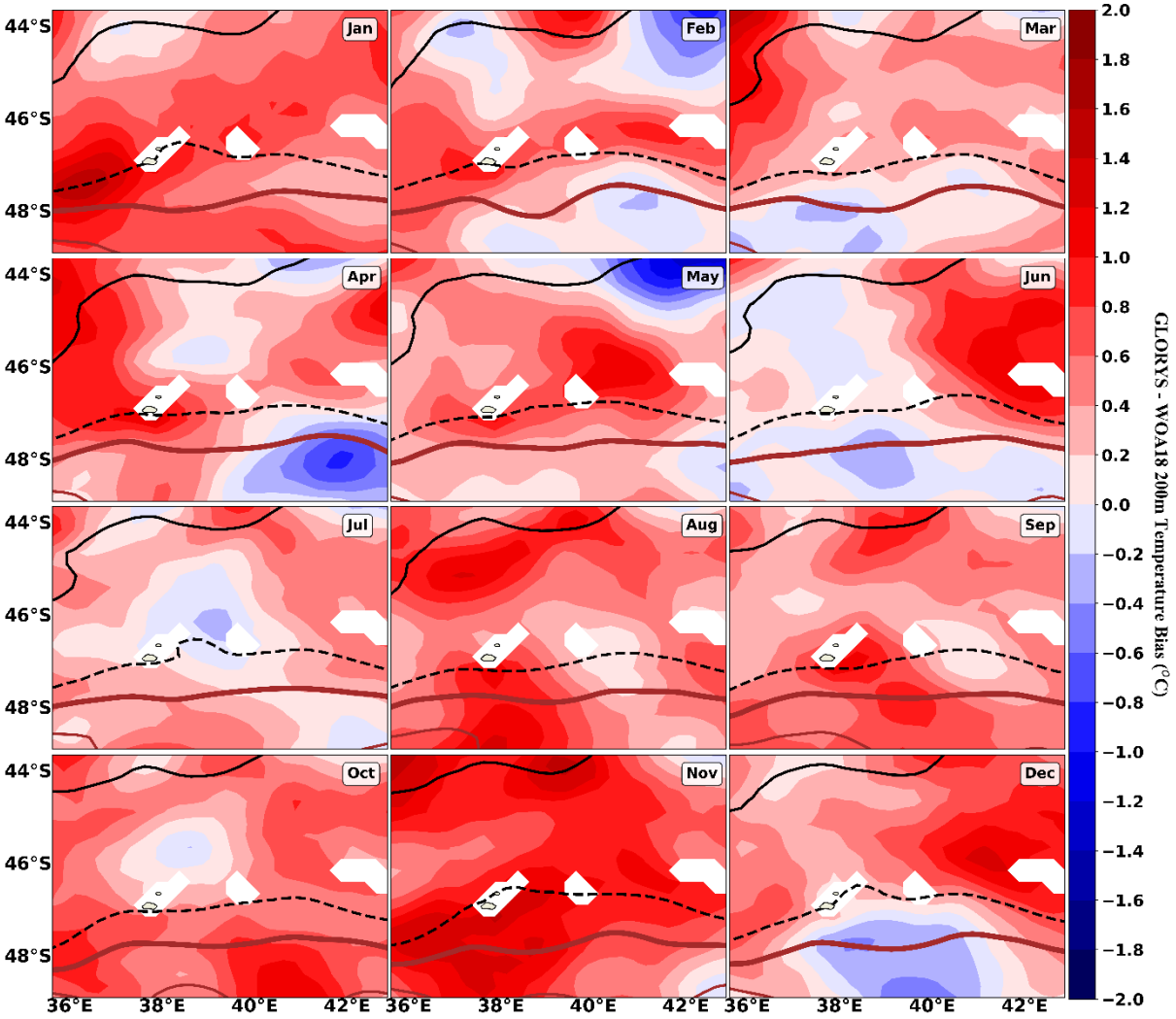

Figure 4.17: The monthly climatology of temperature (°C) at 200 m bias (GLORYS temp – WOA18 temp) from January (Jan) to December (Dec) around the Prince Edward Islands. The black solid and dashed lines represent the M-SAF and S-SAF, respectively. The solid thick and thinner brown lines represent the N-APF and M-APF, respectively. White shading denotes regions of no data. These front positions were identified from satellite altimetry using ADT according to the process described by Sokolov and Rintoul (2002).

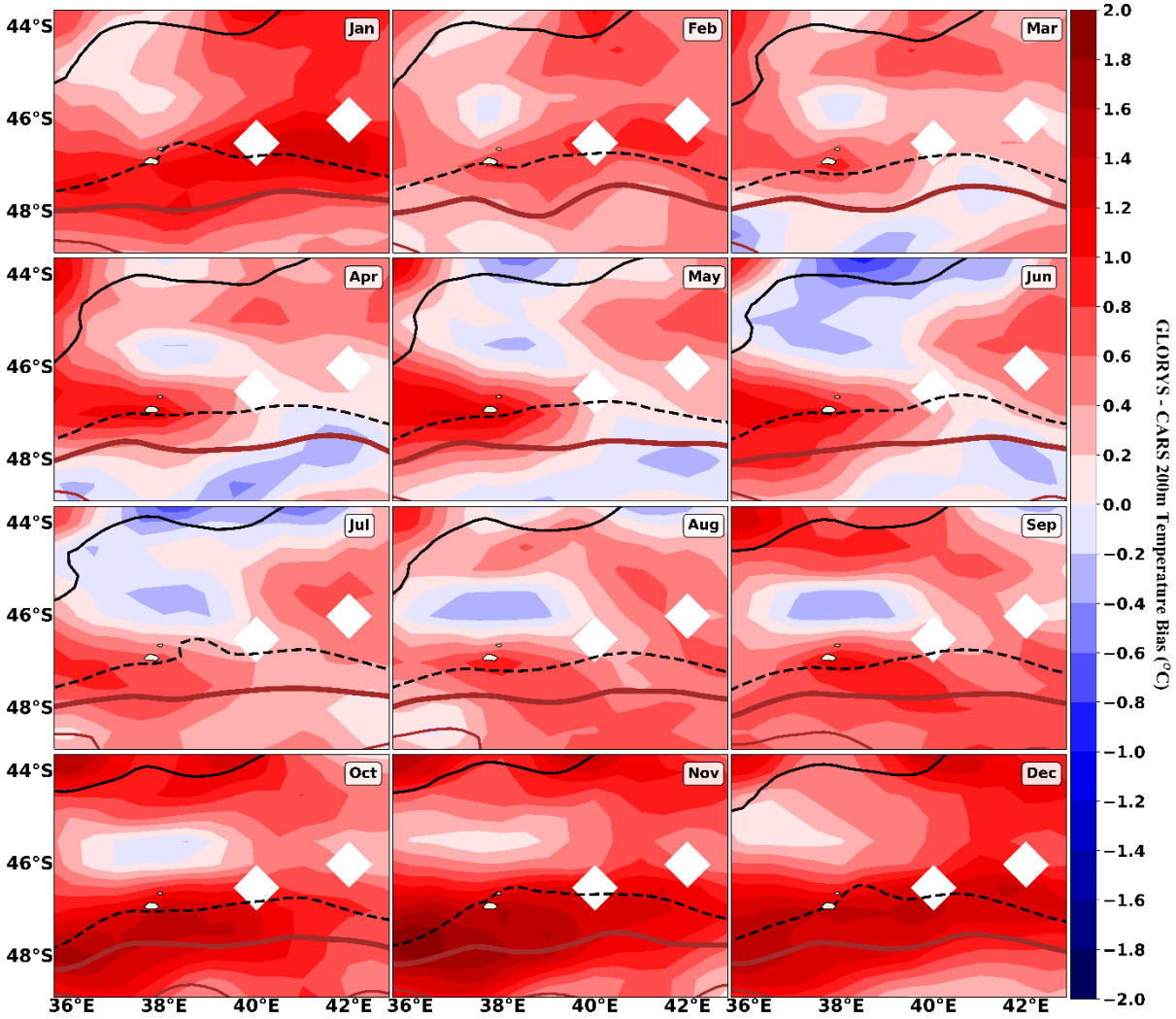

Figure 4.18: The monthly climatology of temperature (°C) at 200 m bias (GLORYS temp – CARS09 temp) from January (Jan) to December (Dec) around the Prince Edward Islands. The black solid and dashed lines represent the M-SAF and S-SAF, respectively. The solid thick and thinner brown lines represent the N-APF and M-APF, respectively. White shading denotes regions of no data. These front positions were identified from satellite altimetry using ADT according to the process described by Sokolov and Rintoul (2002).

4.1.3 Salinity

Salinity at the surface

The evaluation followed for SSS matched that which was described in section 4.1.2 for SST. In order to examine the suitability and accuracy of the GLORYS model at reproducing SSS spatial and temporal variability, within the PEI region, it was first required that the known varibility and drivers thereof be identified in the region. *In situ* (WOA18 and CARS09) and satellite (CNR) products were used to achieve this.

The same north-south gradient was observed in the *in situ* (WOA18 and CARS09), satellite (CNR) and model (GLORYS) climatologies produced in this study, with higher SSS (> 33.8 PSU) values to the north of the PEIs and lower SSS (< 33.8 PSU) values to the south. This

meridional pattern forms part of the larger SSS north-south gradient and can be more clearly seen within the large-scale overviews of the SO (see Appendix figures A10 to A13). SSS variability is driven by several factors, where over the equator consistently high levels of precipitation result in decreased salinity at the surface. Conversely towards the higher latitudes, over the open ocean the SSS increases due to decreased rainfall and increased evaporation. The polar regions present a decreased SSS owing to the freshwater input from melting ice, snow and glaciers (Klemas, 2011).

The monthly SSS climatologies by WOA18, CARS09 and CNR (*Figure 4.19; Figure 4.20; Figure 4.21, respectively*) each illustrated comparable seasonal cycles, observed as an extension of less saline water (< 33.8 PSU), from the southwest, into the study region, over late summer (February) and autumn (MAM). This lower SSS persisted into winter for WOA18 (JJA) (*Figure 4.19*), over the PEIs, and for CARS09 (*Figure 4.20*) into spring (September and October) in the lee of the islands. The slightly more saline (> 33.9 PSU) surface waters in the northeastern part of the study area extended further south during spring and summer (*Figure 4.19; Figure 4.20; Figure 4.21*). While the maximum SSS for WOA18 (34.2 PSU) and CNR (34.2 PSU) was observed in December, the maximum SSS for CARS09 (34.1 PSU) was observed in February. The SSS minimum for WOA18 (33.6 PSU) , CNR (33.8 PSU) and CARS09 (33.7 PSU) occurred in June, March and August, respectively.

Since precipitation impacts surface salinity, a possible explanation for this study's observed SSS seasonal cycle may correspond to the seasonality of rainfall over the region. This is described in a study done by Shangheta (2021) which investigated daily rainfall, amongst other parameters, from 1949 to 2018 at Marion Island. Shangheta (2021) observed peaks in rainfall in December/January and May, whereas minumum rainfall was observed in February/March and October. Only the May rainfall peak, observed by Shangheta (2021) corresponded with the decreased SSS observed in autumn in the current study. In addition, the October rainfall minimum, observed by Shangheta (2021), was found to mirror the increased SSS observed in spring within this study. A study done by Rouault et al. (2005) found similar findings to Shangheta (2021), where a decreased rainfall trend was observed in summer and corresponded to increased air pressure at Marion Island. Rouault et al. (2005) tentatively linked the increased air pressure to either decreased atmospheric cyclonic activity over the islands, or due to a hypothesised southward shift of the SO cyclonic storm tracks (Rouault et al. 2005). Surface salinity may also be influenced by snow and ice melt, although no long-term studies have undertaken this investigation yet within the localised PEI envionment (Klemas, 2011). Sumner

et al. (2004) detailed the extent of perennial ice and snow melt, along with the disappearance of a snowline and the 'Ice Plateau' on Marion Island as the result of climate change, confirming a significant amount of fresh water runoff to be entering into the surrounding oceanographic environment around the islands.

The GLORYS SSS monthly climatology (*Figure 4.22*) captured the general seasonal pattern observed across WOA18 (*Figure 4.19*), CARS09 (*Figure 4.20*) and CNR (*Figure 4.21*), where less saline waters protruded into the study region in the summer (January and February), autumn and winter months, with a minimum SSS (33.7 PSU) observed in May. More saline waters, originating from the northeast, had a greater southward extension over spring and summer, with a maximum SSS (34.3 PSU) in November.

The seasonal cycle was noticeably clearer in the SSS time series (*Figure 4.9b*), obtained by extracting and averaging the data from a 5° x 5° study box around the PEIs (*Figure 4.9a*). Although a smaller range was observed (33.78 to 33.92 PSU), resulting from averaging over the smaller area, the seasonal pattern matched those described in the climatologies (*Figures 4.19 to 4.21*). This salinity range matches the characteristic salinity signal from both Subantarctic Surface waters (SASW), which typically lie north of the SAF, and from Antarctic Surface waters (AASW), separated from SASW by the APF (Ansorge and Lutjeharms, 2002). These water masses are described in greater detail in section 4.1.4.

Comparatively, the GLORYS SSS variability most closely resembled that of the WOA18 and CNR SSS (*Figure 4.24; Figure 4.26, respectively*), evident with the overall weak SSS biases observed across the PEI surrounding region. The bias between GLORYS and CNR (*Figure 4.26*) presented a clear seasonal cycle with GLORYS generally overestimating SSS from midwinter (July and August) to summer, and underestimating SSS in autumn and early winter (June). The bias between GLORYS and WOA18 did not show clear seasonal variations (*Figure 4.24*), most likely due to the fact that WOA18 presented a higher degree of variability possibly resulting from erroneous interpolation of minimal data collection points. This variability was also observed in the area-averaged monthly climatology (*Figure 4.9b*), where WOA18 lacked the smooth seasonal pattern which was evident for the other datasets.

GLORYS presented the largest difference when compared to the CARS09 dataset (*Figure 4.25*), likely resulting from the muted seasonal cycle in CARS09. This is evident with the overestimation by GLORYS of surface salinity in summer and in spring, by 0.4 PSU. The autumn and early winter months presented an underestimation of up to 0.2 PSU by GLORYS.

The overall weak biases, supports the credibility of the model's output at simulating the seasonal cycles and spatial variability of SSS within the PEI region.

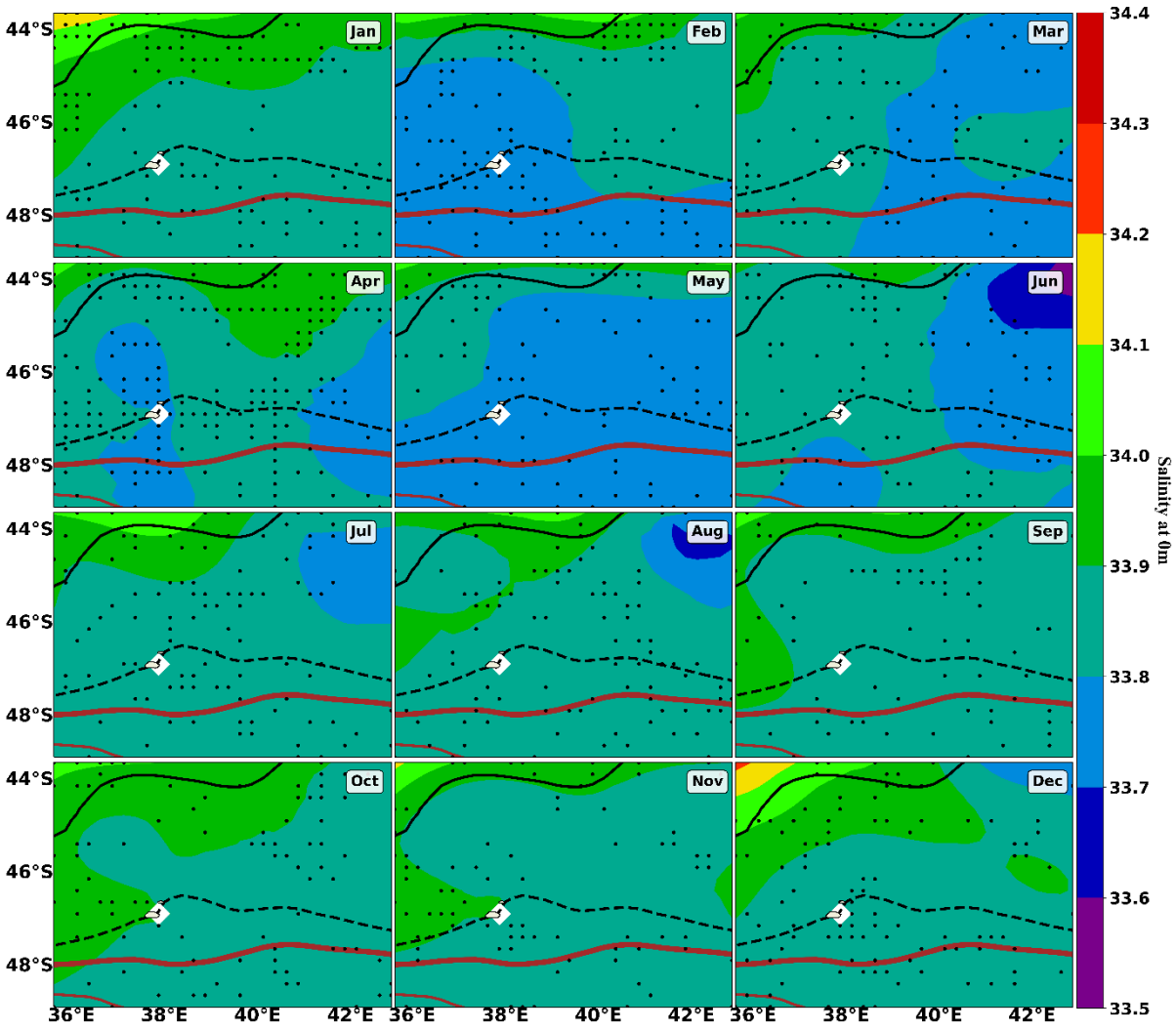

Figure 4.19: The monthly climatology of sea surface salinity (SSS) from January (Jan) to December (Dec) around the Prince Edward Islands from 1955 to 2017 using the WOA18 data. The black solid and dashed lines represent the M-SAF and S-SAF, respectively. The solid thick and thinner brown lines represent the N-APF and M-APF, respectively. Areas shaded white denote regions of no data. Black filled dots illustrate the distribution of data collection points used to produce the map. These front positions were identified from satellite altimetry using ADT according to the process described by Sokolov and Rintoul (2002).

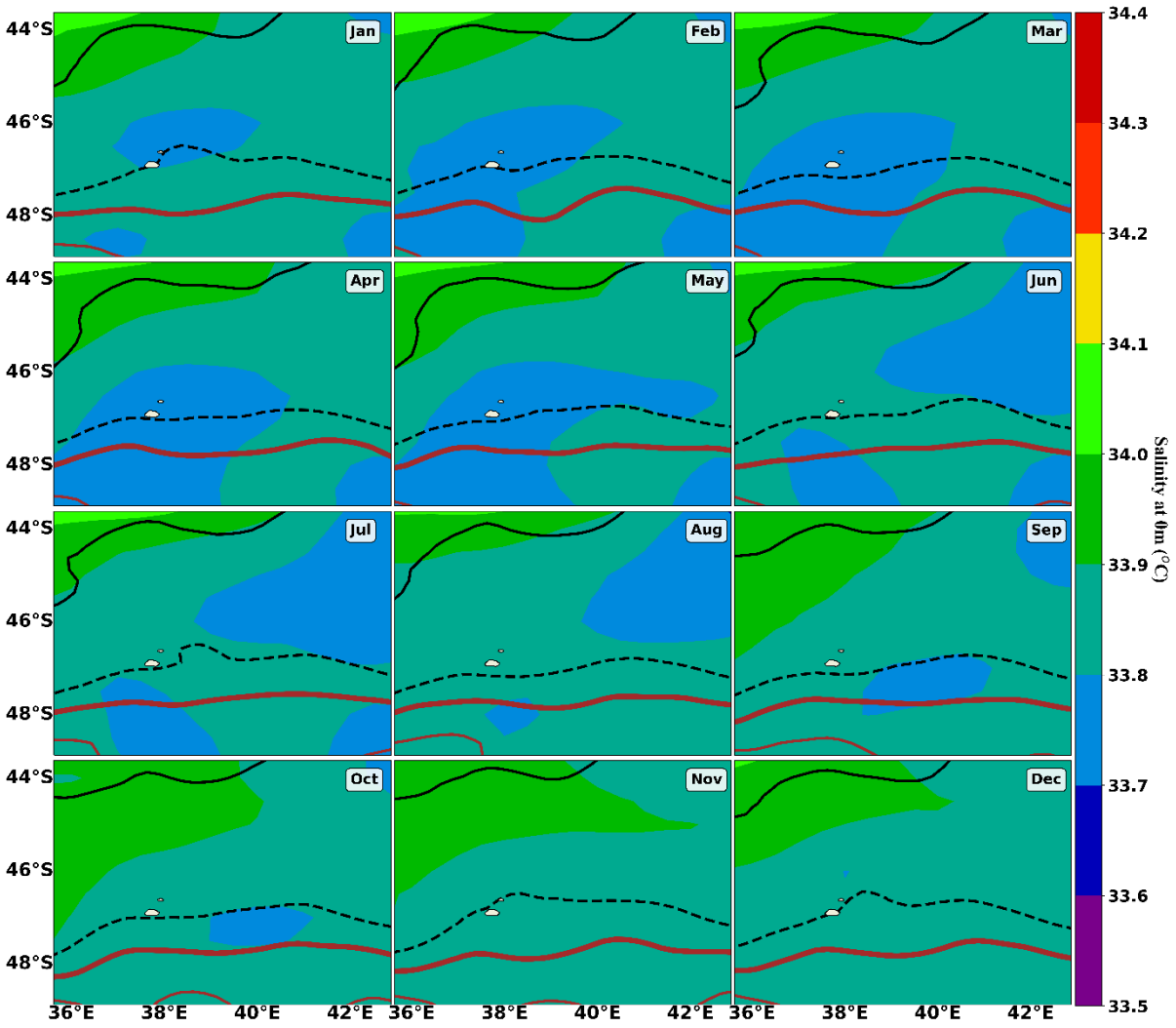

Figure 4.20: The monthly climatology of sea surface salinity (SSS) from January (Jan) to December (Dec) around the Prince Edward Islands from 1985 to 2009 using the CARS09 data. The black solid and dashed lines represent the M-SAF and S-SAF respectively. The solid thick and thinner brown lines represent the N-APF and M-APF respectively. These front positions were identified from satellite altimetry using ADT according to the process described by Sokolov and Rintoul (2002).

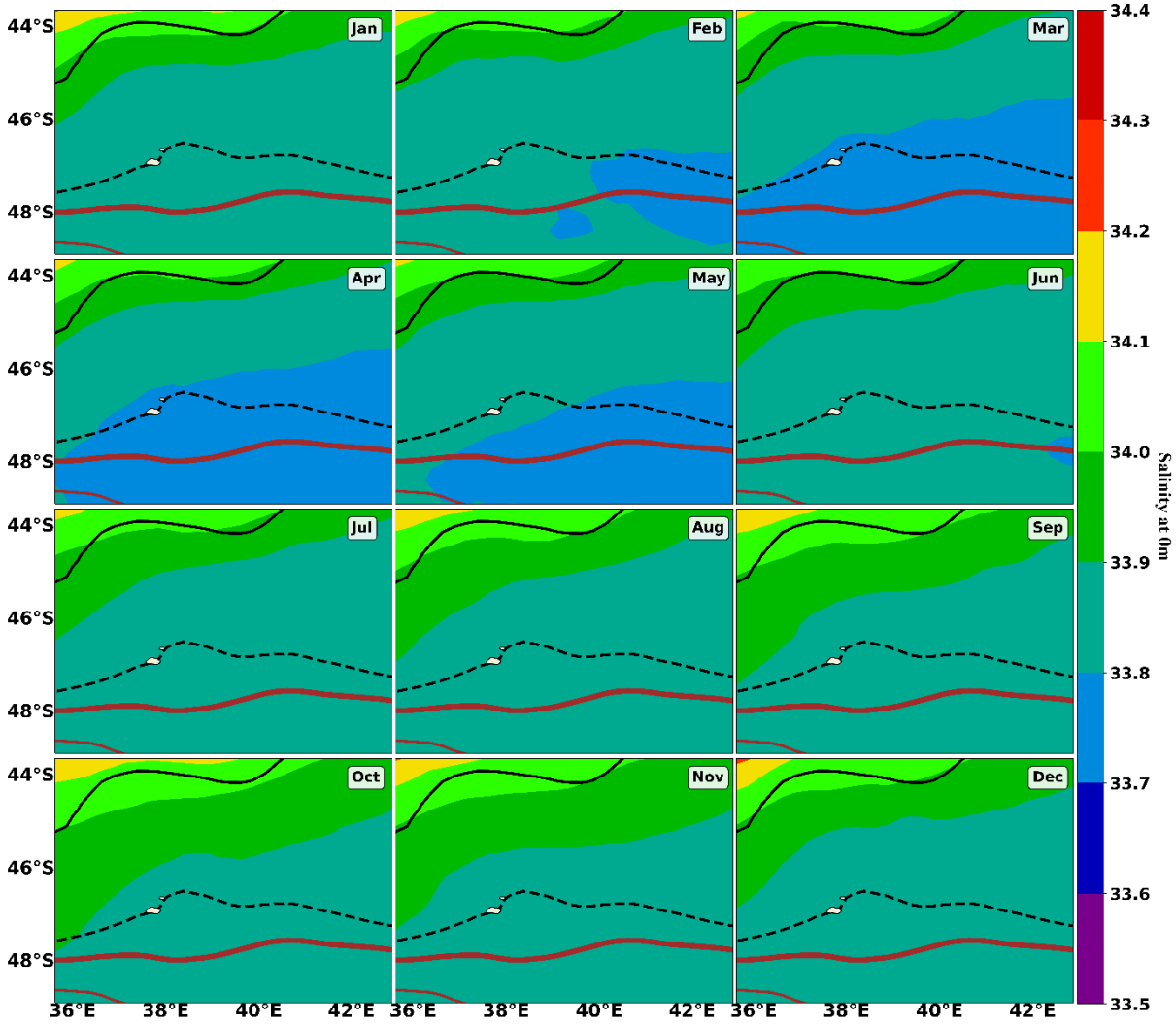

Figure 4.21: The monthly climatology of sea surface salinity (SSS) from January (Jan) to December (Dec) around the Prince Edward Islands from 1993 to 2021 using the CNR data. The black solid and dashed lines represent the M-SAF and S-SAF respectively. The solid thick and thinner brown lines represent the N-APF and M-APF respectively. Areas shaded white denote regions of no data. These front positions were identified from satellite altimetry using ADT according to the process described by Sokolov and Rintoul (2002).

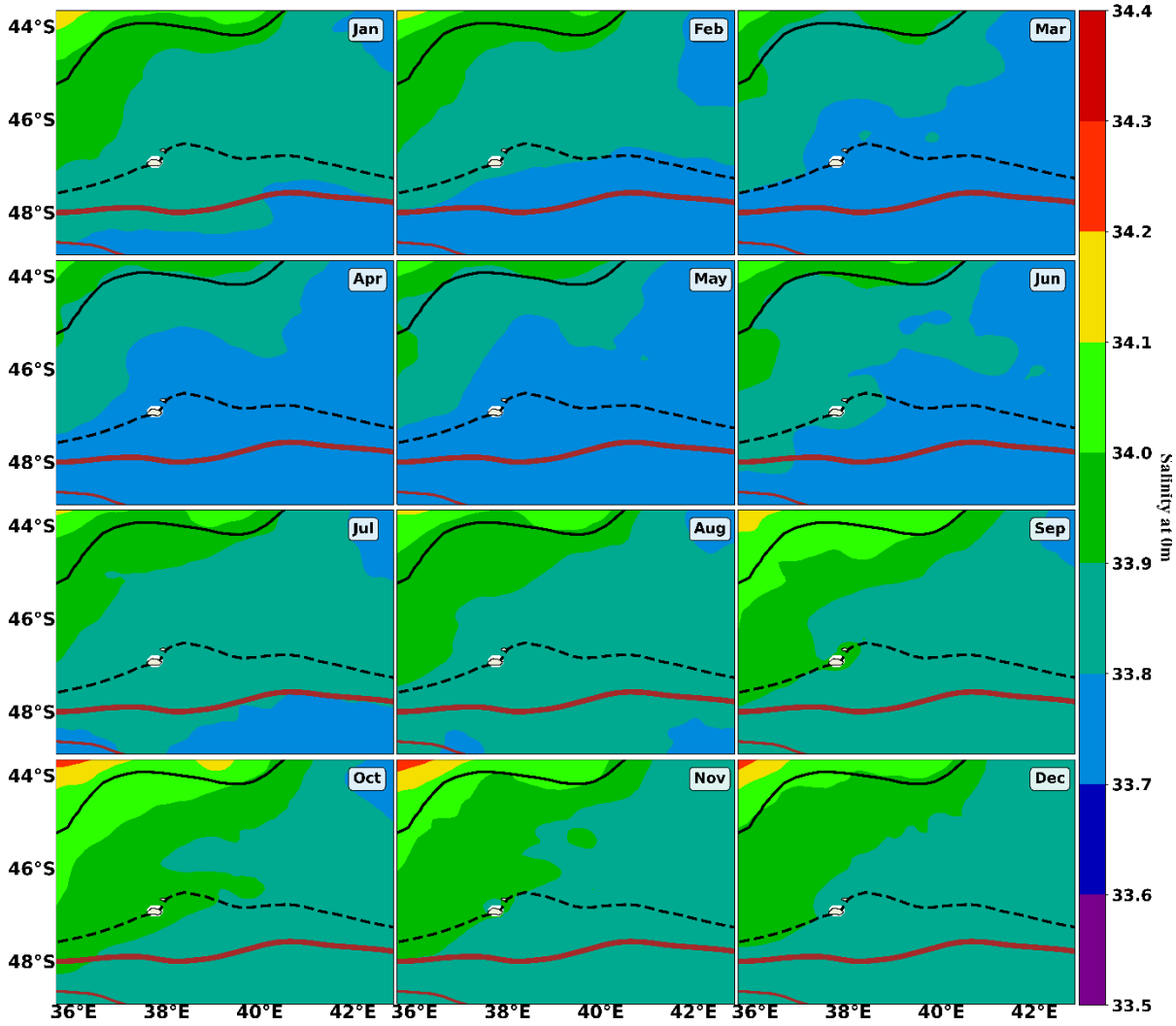

Figure 4.22: The monthly climatology of sea surface salinity (SSS) from January (Jan) to December (Dec) around the Prince Edward Islands from 1993 to 2020 using the GLORYS model output. The black solid and dashed lines represent the M-SAF and S-SAF respectively. The solid thick and thinner brown lines represent the N-APF and M-APF respectively. Areas shaded white denote regions of no data. These front positions were identified from satellite altimetry using ADT according to the process described by Sokolov and Rintoul (2002).

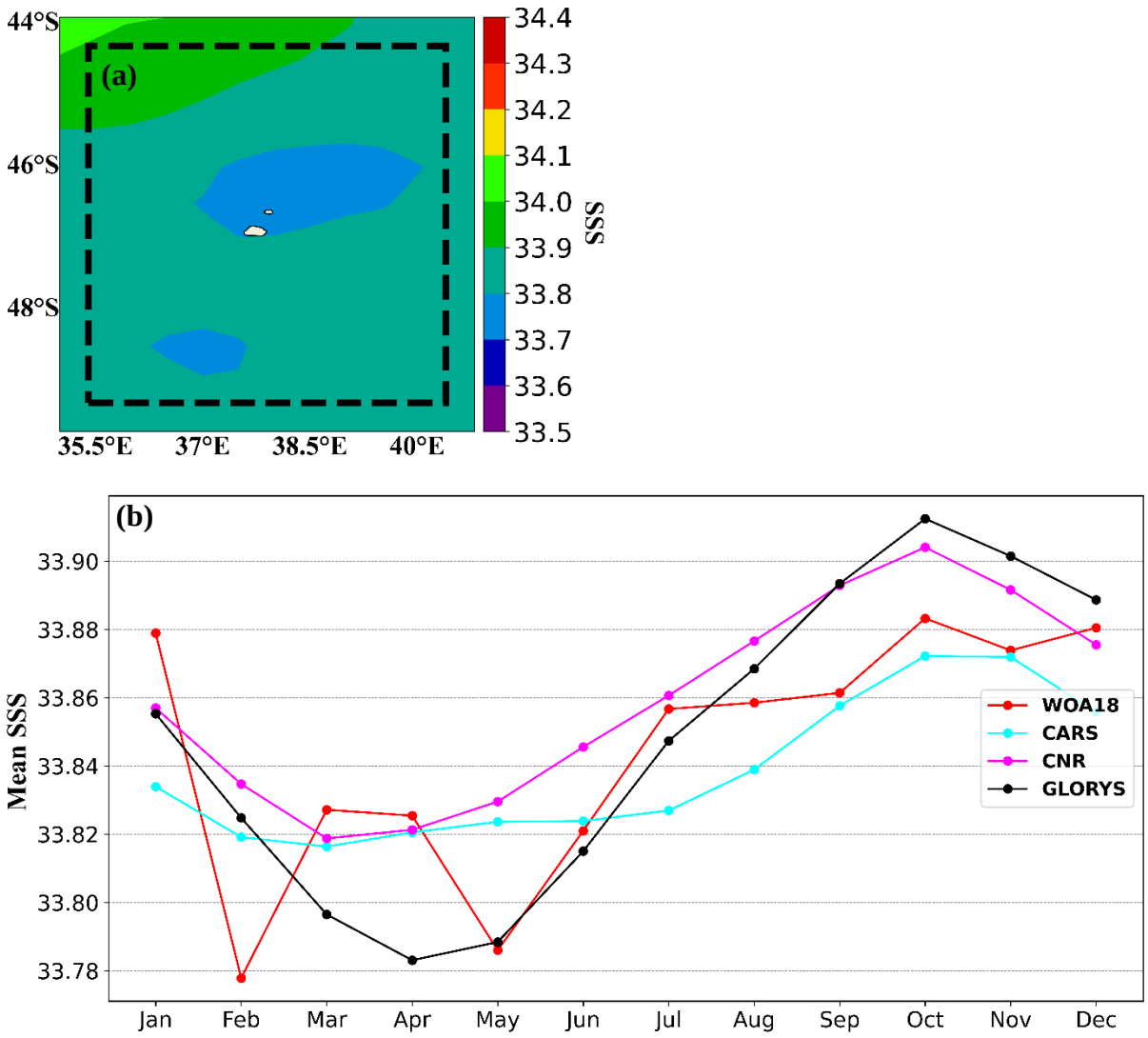

*Figure 4.23: (**a**) The 5° x 5° study box around the Prince Edward Islands from which sea surface salinity (SSS) was extracted and averaged to produce the long-term mean SSS. (**b**) Monthly climatology of the averaged SSS data in the study box from the three datasets; WOA18, CARS09, CNR and from the GLORYS model output.*

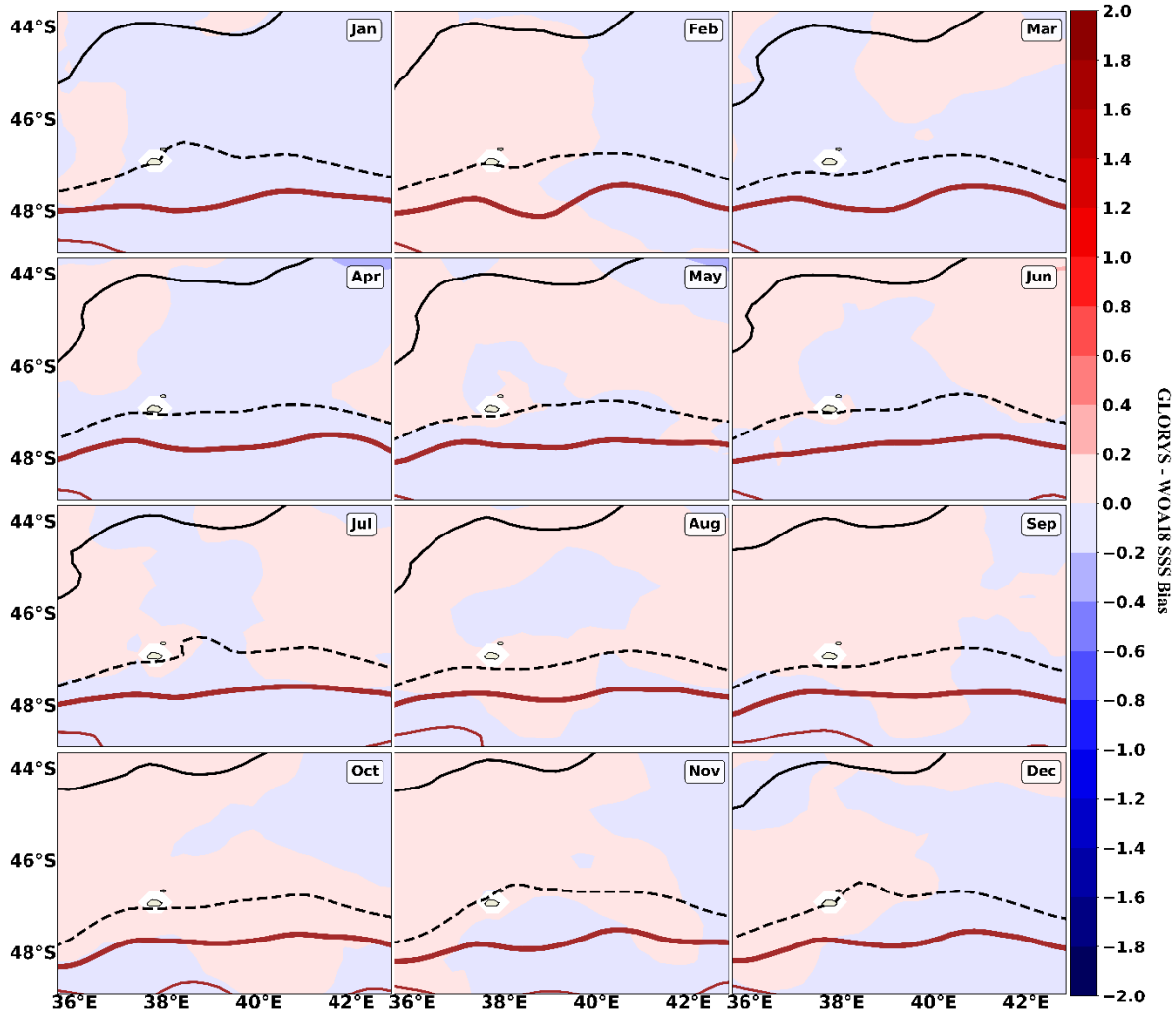

Figure 4.24: The monthly climatology of sea surface salinity (SSS) bias (GLORYS SSS – WAO18 SSS) from January (Jan) to December (Dec) around the Prince Edward Islands. The black solid and dashed lines represent the M-SAF and S-SAF respectively. The solid thick and thinner brown lines represent the N-APF and M-APF respectively. White shading denotes regions of no data. These front positions were identified from satellite altimetry using ADT according to the process described by Sokolov and Rintoul (2002).

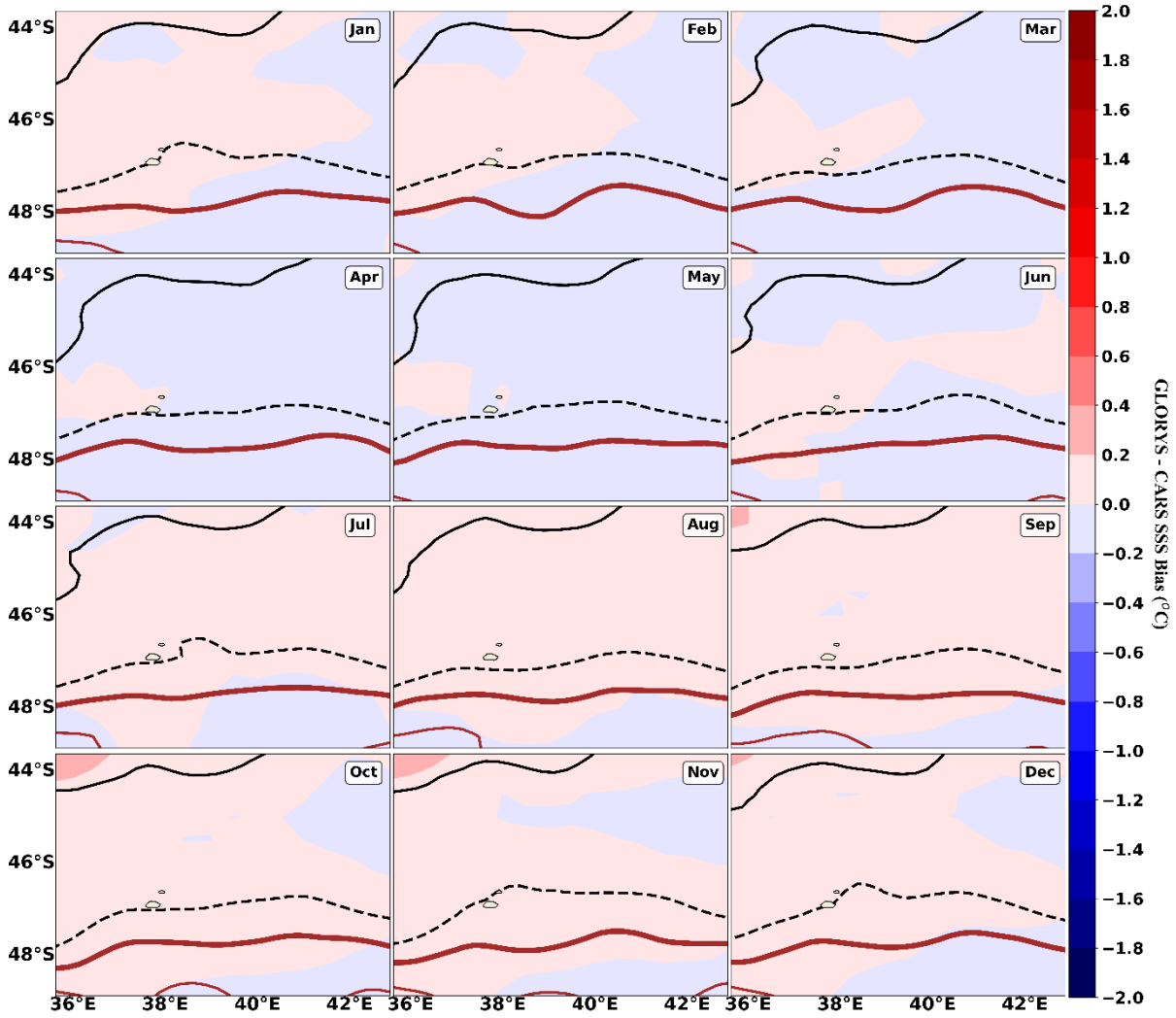

Figure 4.25: The monthly climatology of sea surface salinity (SSS) bias (GLORYS SSS – CARS09 SSS) from January (Jan) to December (Dec) around the Prince Edward Islands. The black solid and dashed lines represent the M-SAF and S-SAF respectively. The solid thick and thinner brown lines represent the N-APF and M-APF respectively. White shading denotes regions of no data. These front positions were identified from satellite altimetry using ADT according to the process described by Sokolov and Rintoul (2002).

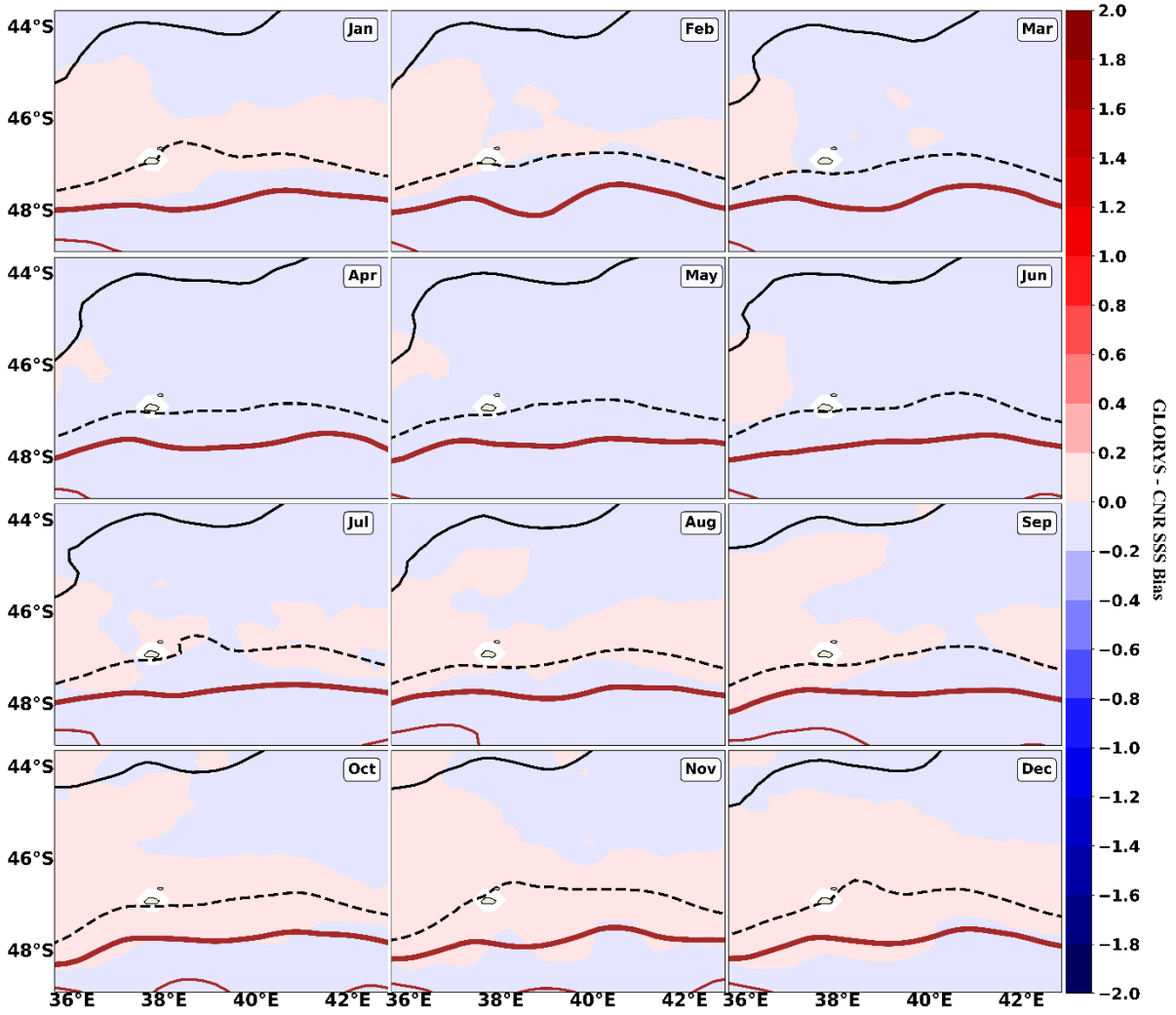

Figure 4.26: The monthly climatology of sea surface salinity (SSS) bias (GLORYS – CNR) from January (Jan) to December (Dec) around the Prince Edward Islands. The black solid and dashed lines represent the M-SAF and S-SAF respectively. The solid thick and thinner brown lines represent the N-APF and M-APF respectively. White shading denotes regions of no data. These front positions were identified from satellite altimetry using ADT according to the process described by Sokolov and Rintoul (2002).

Salinity at 200 m

The meridional gradient of higher salinity (> 34.1 PSU) values to the north of the PEIs and lower salinities (< 34.1 PSU) to the south, was also observed at 200 m in the *in situ* datasets (WOA18 and CARS09) (*Figure 4.27; Figure 4.28*) and model (GLORYS) output (*Figure 4.29*), owing to the larger north-south salinity gradient, across the SO, as described for SSS. Compared to surface waters, those at deeper depths are typically more saline and thus are of a higher density (Marshall and Plumb, 2007). This explains the overall observed higher salinity values, at 200 m (*Figure 4.27 to Figure 4.29*), in comparison to the lower SSS range (*Figure 4.19 to Figure 4.22*).

WOA18 (*Figure 4.27*) and CARS09 (*Figure 4.28*) displayed similar seasonal patterns with higher salinities, at 200 m depth, at the PEIs in autumn and winter, observed as a greater southward extension of more saline water towards the islands, from the northeast. It is worth noting that the seasonal cycle in WOA18 (*Figure 4.27*) was less evident as a result of the decreased available *in situ* data with depth, coupled with the erroneous interpolation arising from the fewer data collection points. Spring and summer presented extensions of less saline waters from the southwest. Within the study region, the highest salinity, at 200 m, for WOA18 (34.3 PSU) and for CARS09 (34.4 PSU) was observed in July and June, respectively. The lowest salinity for WOA18 (33.9 PSU) and CARS09 (33.9 PSU) was observed in February and August, respectively (*Figure 4.13; Figure 4.14*).

To investigate the seasonal cycle further, a monthly climatology, using the averaged salinity data at 200 m in the 5° x 5° study box (*Figure 4.30a*) from the two datasets (WOA18 and CARS09), was produced (*Figure 4.30b*). This revealed that while the seasonal cycles for SSS and SST were contrasting, the salinity and temperature seasonal cycles, at 200 m, correspond with each other (*Figure 4.30b; Figure 4.23b, respectively*). The increase in the 200 m salinity and temperature, over the winter and autumn period suggests that the seasonality of the MLD which drives the seasonal pattern of temperature, at 200 m (*Figure 4.23b*), may similarly impact subsurface salinity (*Figure 4.30b*) (de Boyer Montėgut et al. 2004). Additionally, water masses found within this region may contribute to the salinity seasonality observed at 200 m since SASW, to the north of the PEIs, is defined by a subsurface salinity maximum and Antarctic Surface Water (AASW), located to the south, is seasonally variable (Ansorge and Lutjeharms, 2002). In winter the AASW extends as a homogenous mixed layer to 250 m, while in summer the layer only extends between 50 and 100 m deep (Ansorge and Lutjeharms, 2002). The mixing of these water masses, therefore, could be producing the peak in salinity during winter when the MLD is at its deepest, while in summer the salinity maximum is contained within the shallow surface layers above 200 m.

The GLORYS climatology (*Figure 4.29*) does not capture the seasonal cycle as clearly as WOA18 and CARS09. The GLORYS model's maximum salinity (34.4 PSU) was observed in August and minimum salinity (34.0 PSU) in September. The model appears to simulate a greater southward extension of saline (> 34.1 PSU) water, throughout all the months, with slightly more saline water in winter. The distribution of less saline (< 34.1 PSU) water, while appearing to have a slight increase over the late spring and summer months seems to be continually restricted far south of the PEIs. The smaller range of salinities simulated by

GLORYS, along with the overall higher salinity values was evident with the overestimation of GLORYS salinity in both the biases (*Figure 4.31; Figure 4.32*) and the time series (*Figure 4.30b*). However, the maximum overestimation of GLORYS by only 0.4 PSU (*Figure 4.31; Figure 4.32*) suggests that, relatively the GLORYS model's performance at reproducing temporal and spatial salinity variability, at 200 m, was satisfactory.

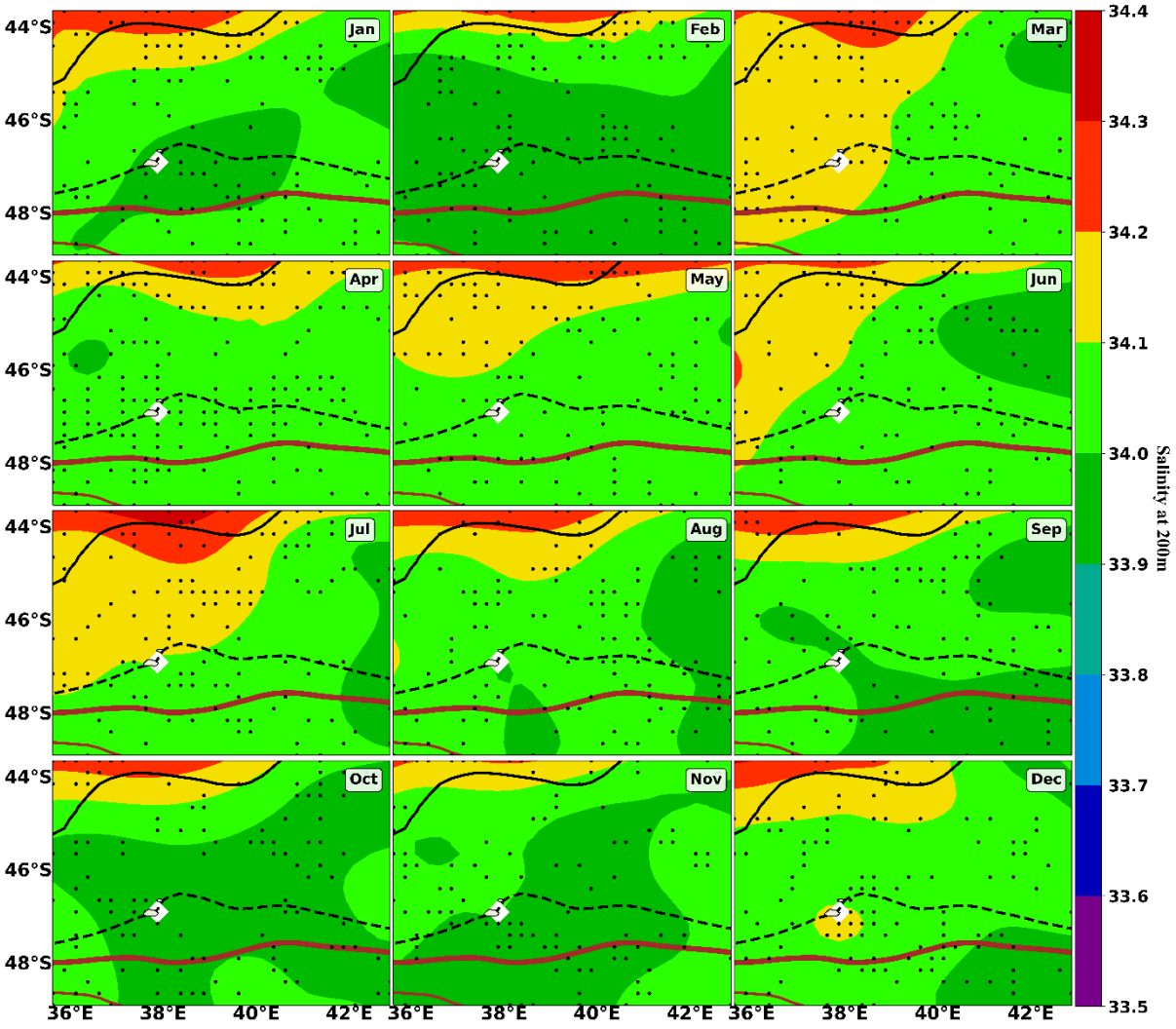

Figure 4.27: The monthly climatology of salinity at a depth of 200 m, from January (Jan) to December (Dec) around the Prince Edward Islands from 1955 to 2017 using the WOA18 data. The black solid and dashed lines represent the M-SAF and S-SAF, respectively. The solid thick and thinner brown lines represent the N-APF and M-APF, respectively. Areas shaded white denote regions of no data. Black filled dots illustrate the distribution of data collection points used to produce the map. These front positions were identified from satellite altimetry using ADT according to the process described by Sokolov and Rintoul (2002).

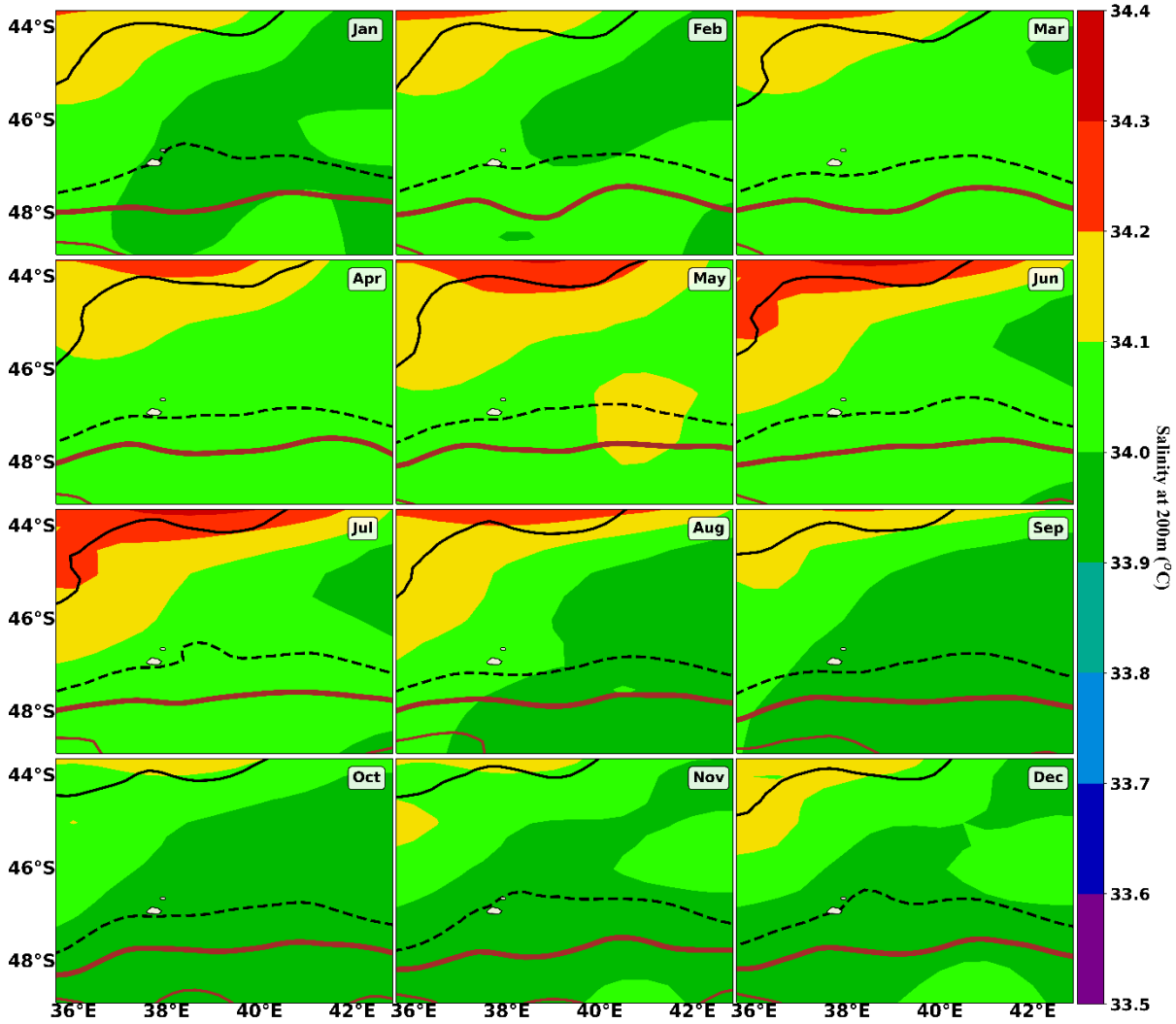

Figure 4.28: The monthly climatology of salinity at a depth of 200 m, from January (Jan) to December (Dec) around the Prince Edward Islands from 1985 to 2009 using the CARS09 data. The black solid and dashed lines represent the M-SAF and S-SAF respectively. The solid thick and thinner brown lines represent the N-APF and M-APF respectively. These front positions were identified from satellite altimetry using the ADT according to the process described by Sokolov and Rintoul (2002).

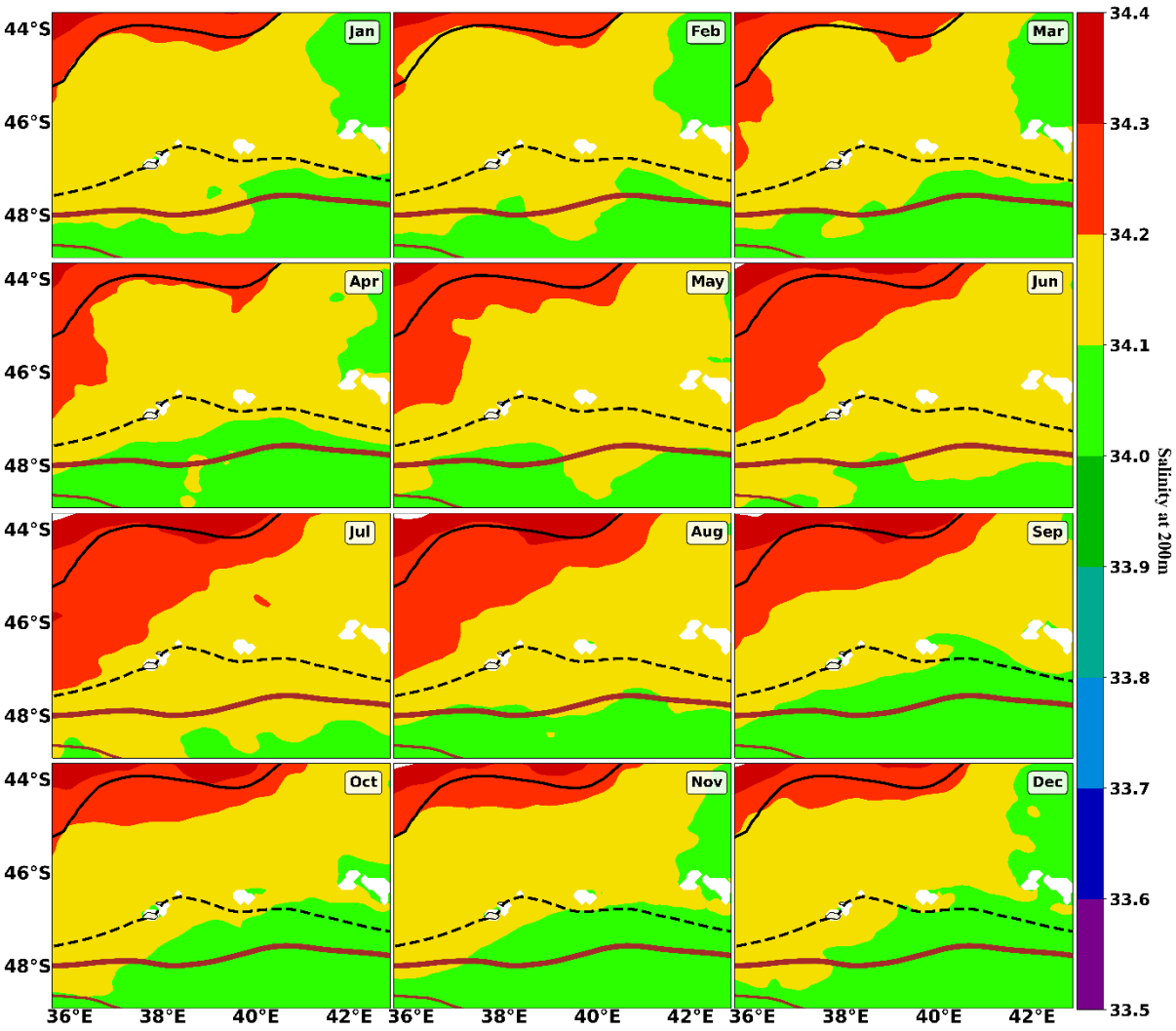

Figure 4.29: The monthly climatology of salinity at a depth of 200 m, from January (Jan) to December (Dec) around the Prince Edward Islands from 1993 to 2020 using the GLORYS model output. The black solid and dashed lines represent the M-SAF and S-SAF respectively. The solid thick and thinner brown lines represent the N-APF and M-APF respectively. Areas shaded white denote regions of no data. These front positions were identified from satellite altimetry using ADT according to the process described by Sokolov and Rintoul (2002).

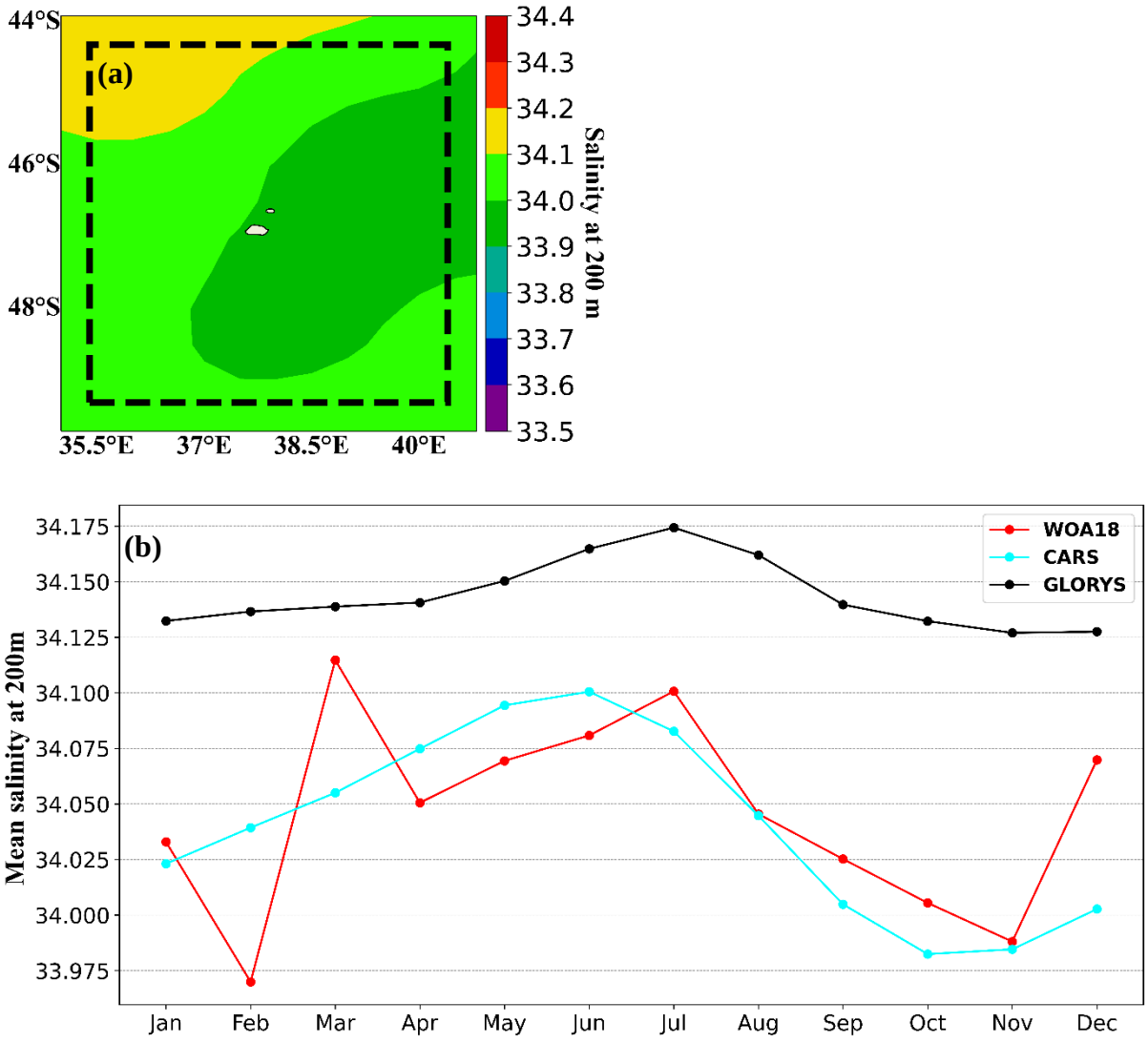

*Figure 4.30: (**a**) The 5° x 5° study box around the Prince Edward Islands from which salinity data at 200 m was extracted and averaged to produce the long-term mean salinity at 200 m. (**b**) Monthly climatology of the averaged salinity data at 200 m in the study box from the two datasets; WOA18 and CARS09, and from the GLORYS model output.*

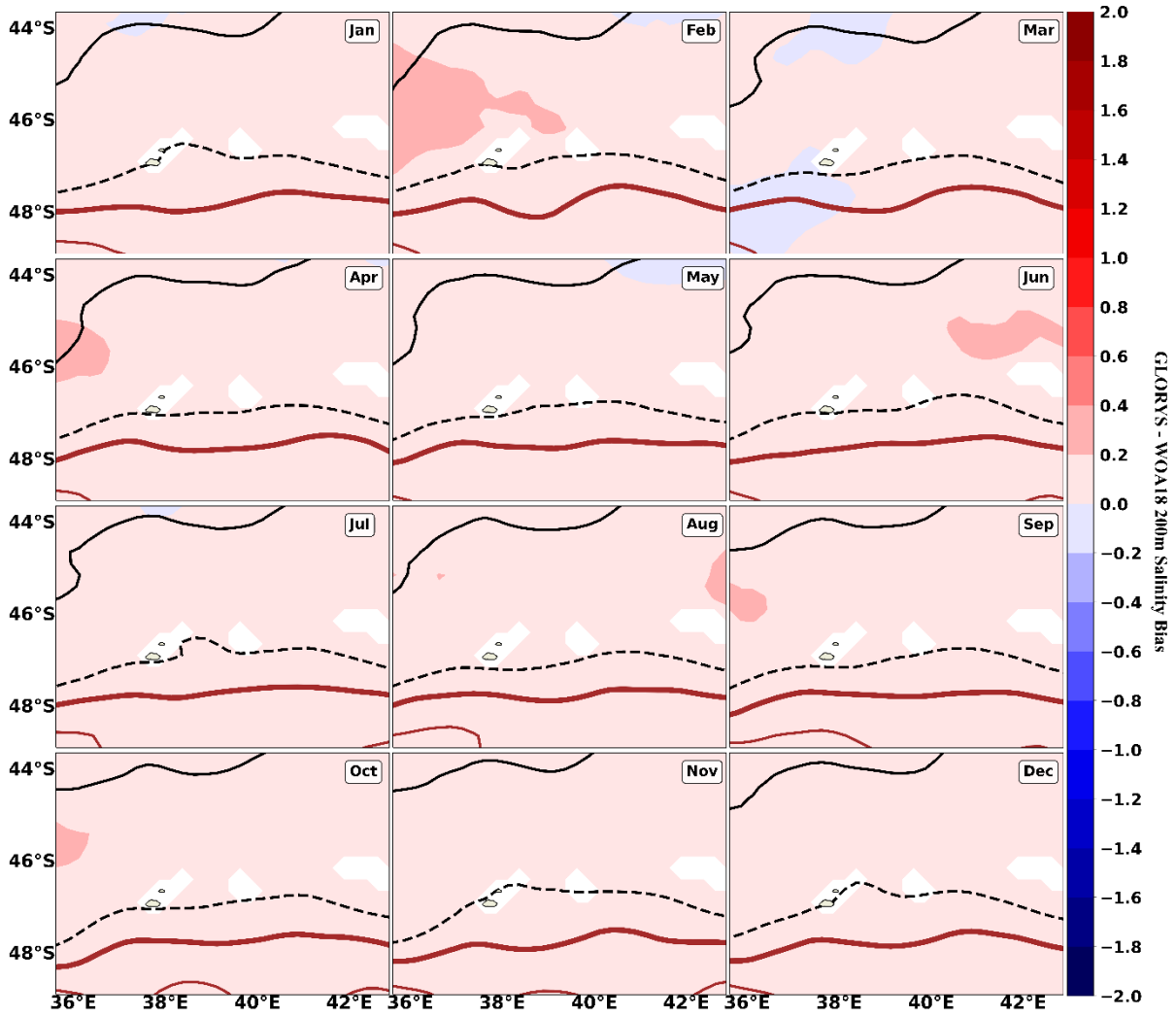

Figure 4.31: The monthly climatology of salinity at 200 m bias (GLORYS– WOA18) from January (Jan) to December (Dec) around the Prince Edward Islands. The black solid and dashed lines represent the M-SAF and S-SAF respectively. The solid thick and thinner brown lines represent the N-APF and M-APF respectively. White shading denotes regions of no data. These front positions were identified from satellite altimetry using the ADT according to the process described by Sokolov and Rintoul (2002).

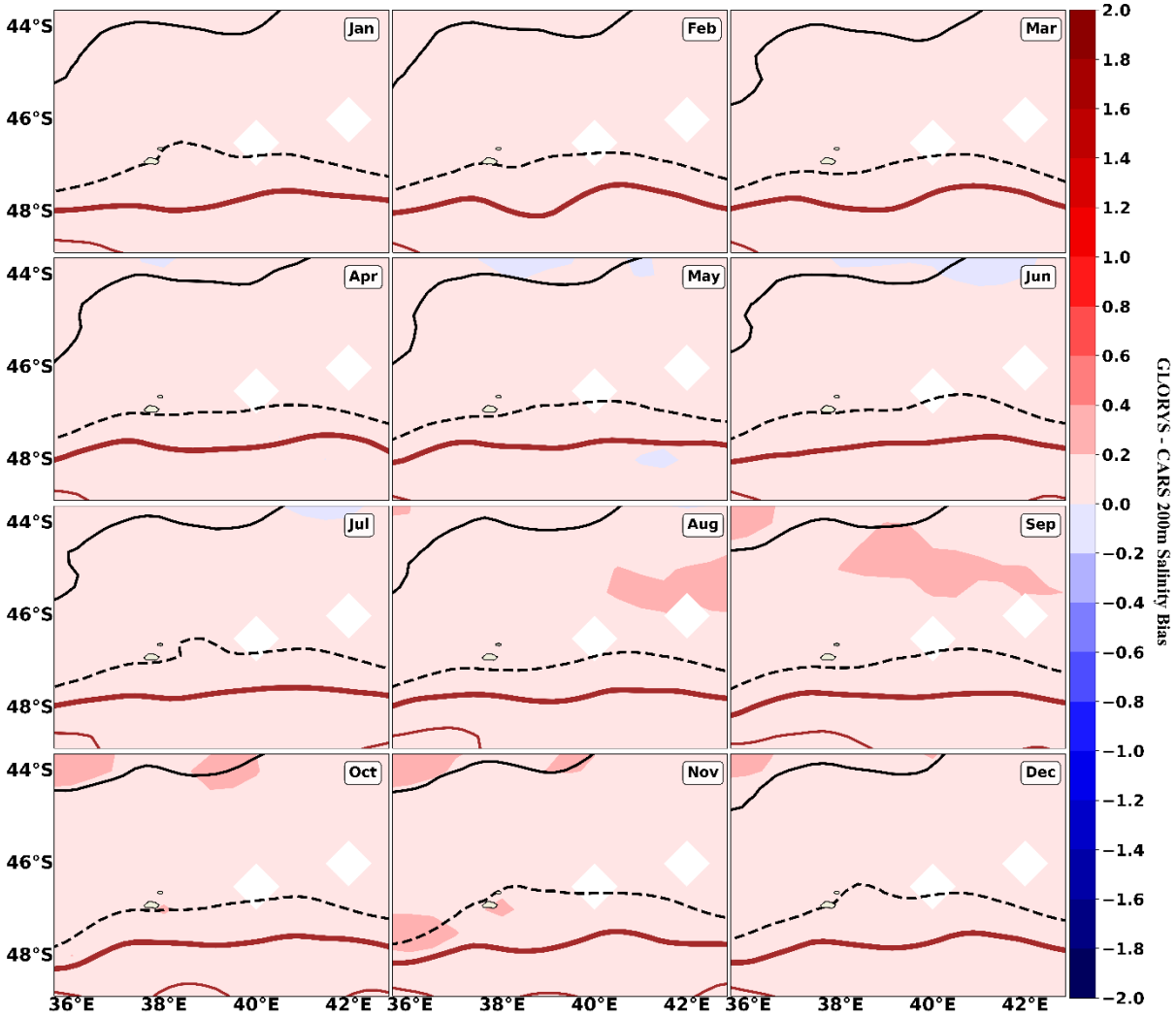

Figure 4.32: The monthly climatology of salinity at 200 m bias (GLORYS– CARS09) from January (Jan) to December (Dec) around the Prince Edward Islands. The black solid and dashed lines represent the M-SAF and S-SAF respectively. The solid thick and thinner brown lines represent the N-APF and M-APF respectively. White shading denotes regions of no data. These front positions were identified from satellite altimetry using ADT according to the process described by Sokolov and Rintoul (2002).

4.1.3 Water Masses

The monthly Temperature-Salinity (TS) plots (*Figure 4.33*) displayed a characteristic shape of broad salinity bands and narrow temperature ranges for the PEI region, indicative of the five main water masses which dominate the region. The five water masses can be described as sub-Antarctic Surface Water (SASW), Antarctic Surface Water (AASW), Antarctic Intermediate Water (AAIW), Circumpolar Deep Water (CDW) and Antarctic Bottom Water (AABW) (van den Berg et al. 2021; Lamont et al. 2019). The water masses were identified according to their unique temperature and salinity signatures, as outlined in Table 4.1.

Table 4.1: Water masses within the PEI surrounding region, their respective temperature and salinity ranges and the studies from which they were acquired.

Water Masses	Temperature Range (°C)	Salinity Range (PSU)	Reference
SASW	3 – 14	33.8 – 34.4	(Ansorge and Lutjeharms, 2002)
AASW	-1.85 – 6	33.4 – 34.2	(Ansorge and Lutjeharms, 2002)
AAIW	2 – 5	± 34.4	(Karas et al. 2019)
CDW	0.650 ± 0.005	34.707 ± 0.005	(Pardo et al. 2012)
AABW	-0.753 ± 0.005	34.660 ± 0.005	(Pardo et al. 2012)

Of those five water masses, only three were observed in WOA18 namely, SASW, AASW and AAIW due to the restricted depth level of 1500 m in the dataset. Similarly, CARS09 illustrated SASW and AASW, while the AAIW was partially captured owing to the limited three depth levels (50, 200 and 1000 m) at which the data was collected and interpolated. The GLORYS model, however, simulated all five water masses throughout time (*Figure 4.33*).

Comparatively, GLORYS simulated a broader temperature and salinity range of the SASW, for each of the months. The larger temperature and salinity ranges of SASW were most noticeable in summer (January/February), where the simulated temperature range by GLORYS extended from approximately 5 to 11.5 °C, while WOA18 and CARS09 only indicated temperature ranges from approximately 5 to 10 °C and 5 to 8 °C, respectively. SASW salinity simulated by GLORYS, in the summer, extended from approximately 33.7 to 34.5 PSU, whereas WOA18 and CARS09 illustrated smaller salinity ranges from 33.8 to 34.25 PSU and 33.7 to 34.3 PSU, respectively. The higher temperature range for SASW in GLORYS, can be explained by the overestimation of GLORYS SST with respect to WOA18 and CARS09 (*most evident in Figure 4.10; Figure 4.11, respectively*) specifically to the north of the PEIs where SASW is the dominant water mass (Ansorge and Lutjeharms, 2002). The SASW has a subsurface salinity maximum (Ansorge and Lutjeharms, 2002), which was overestimated by GLORYS salinity at 200m, with respect to WOA18 and CARS09 (*visible in Figure 4.31; Figure 4.32, respectively*) over the entire PEI region.

The evaluation of the seasonal cycle presented an approximate 3 °C difference in temperature maxima between summer (January/February) and winter (July/August), observed among *in*

situ (WOA18 and CARS09) products and the model (GLORYS) output. The higher temperatures (6 – 12 ^{o}C) and smaller salinity range (33.7- 34.4 PSU) in the T/S plots, indicative of the surface ocean, presented stronger seasonality than the deeper ocean, evident by the lower temperatures (-1 – 4 ^{o}C) and larger salinity range (33.4 – 34.8 PSU) in the deep ocean. This is due to the ocean's surface environment experiencing a greater influence by short-term fluctuations in salinity and temperature, driven by wind, waves, and tides among others (Marshall and Plumb, 2007). Overall, GLORYS compared fairly well in reproducing the water masses observed across the *in situ* (WOA18 and CARS09) products. This could be due to the model's 50 depth levels which extend from the near surface (~ 0.45 m) to 5727.92 m deep (Drévillon et al. 2021a), coupled with the model's numerical code which enables it to accurately solve processes such as diffusion and mixing, among others, at each depth level. The model appears to be able to accurately capture spatial and temporal variability of salinity and temperature throughout the entire water column for the PEI region.

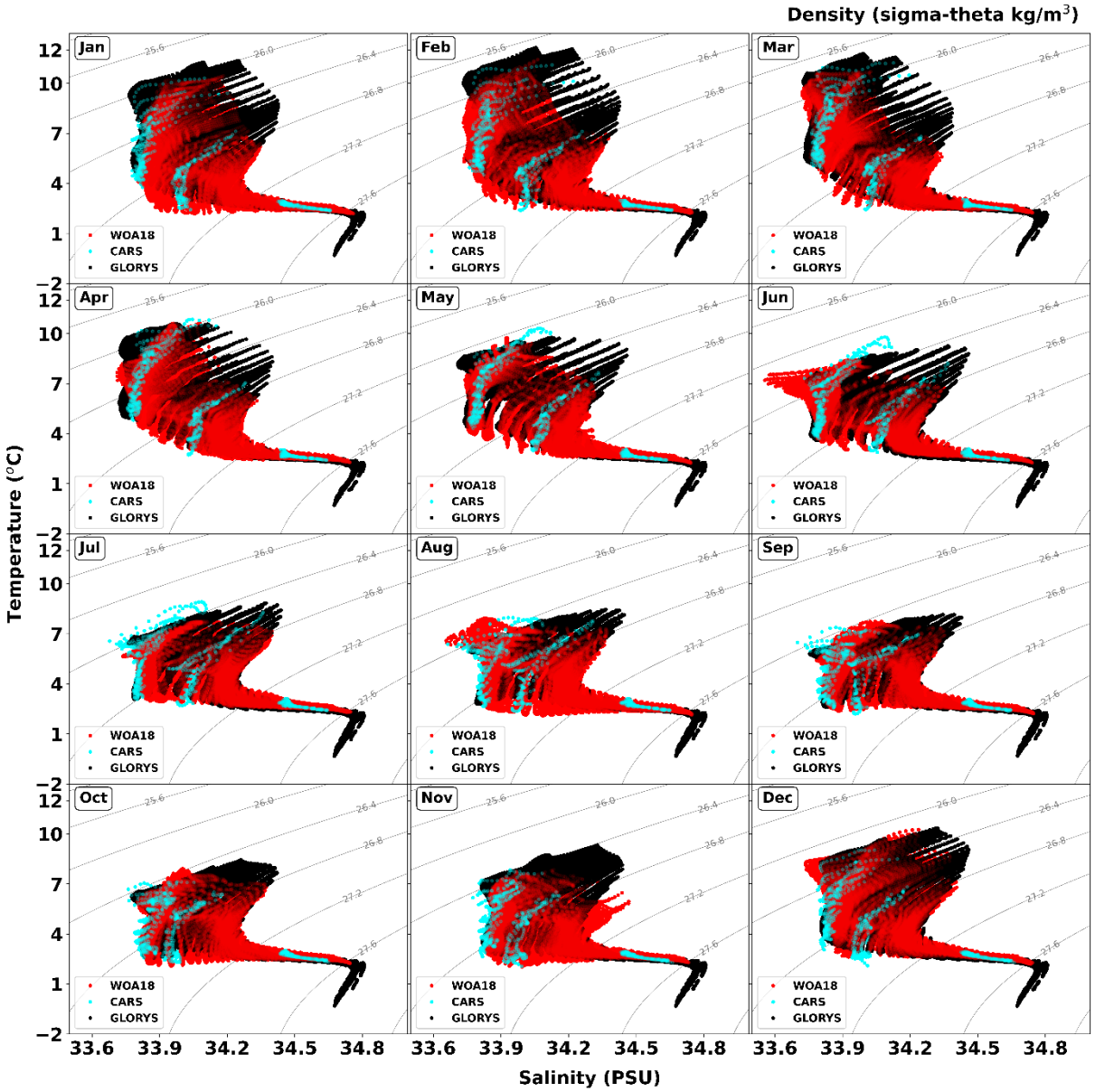

Figure 4.33: Monthly climatological T/S plots from January (Jan) to December (Dec) around the Prince Edward Islands in the study grid (35.5°E – 43°E; 43.5°S - 49°S) for the WOA18 (red), CARS09 (blue) and GLORYS (black) datasets. Grey curved lines indicate isopycnals for the respective density levels (sigma-theta kg/m^3).

4.1.5 GLORYS and SAWS SST comparisons

To better assess the validity of GLORYS at simulating SST variability around the PEIs, Pearson correlations were conducted from January 1993 to May 2020 between the monthly SAWS *in situ* SST, and three GLORYS monthly SST points (*Figure 4.34*). As explained in Section 3.4.5, the Pearson correlation coefficient (r) measures the strength of the linear relationship between two variables (Toolsee, 2021; Hogg et al. 2014). According to Table 3.3 a negative coefficient stipulates that as one variable increases (decreases), the corresponding variable decreases (increases). A positive coefficient stipulates that as the one variable

increases (decreases) so too does the other variable increase (decrease). Two points of equal distance were identified in the GLORYS output as being the closest to the SAWS *in situ* location. As a result, both points, and an average between them, were used in the correlations for this section (*Figure 4.34a)*.

Strong, positive, significant correlations were observed between GLORYS and the SAWS data. The strongest correlation (r = 0.8344, p<0.001) was observed at the northern GLORYS grid point (*Figure 4.34c*). This was closely followed by the correlation (r = 0.8336, p<0.001) of the average between the northern and southern GLORYS grid points (*Figure 4.34b*). Comparatively, the weakest correlation (r = 0.8326, p<0.001) was observed at the southern GLORYS grid point (*Figure 4.34d*). However, given the strong correlations at both the northern and southern grid points, the difference in correlation coefficients can be deemed negligible. While the model's grid points did not match the location of the *in situ* SAWS data, GLORYS was still able to simulate the SST variability within the vicinity of the *in situ* SAWS data location with reasonable accuracy.

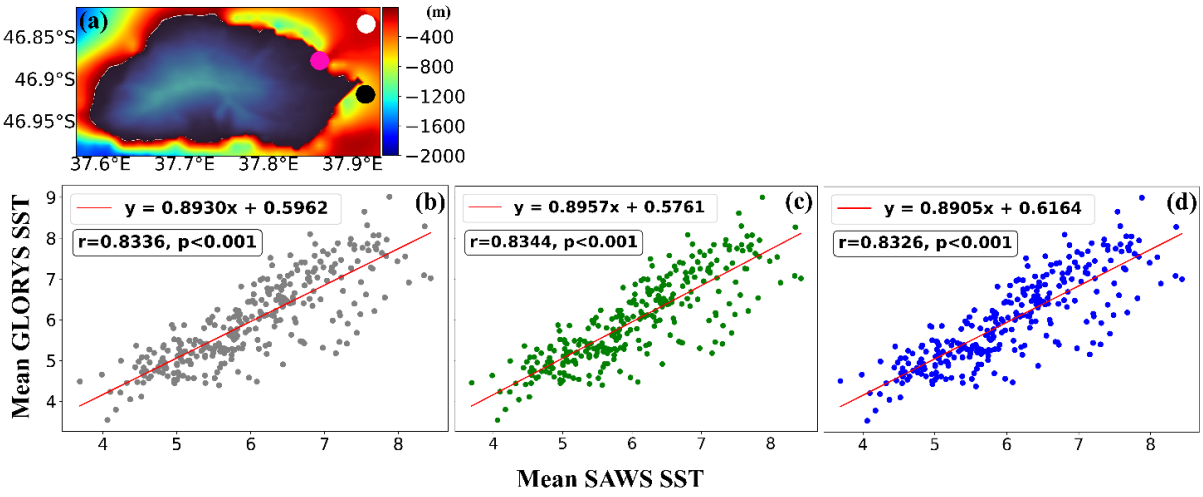

*Figure 4.34: (**a**) Map displaying the locations of the SAWS in situ data (pink), the northern GLORYS grid point (white) and the southern GLORYS grid point (black). Scatter plots showing the relationship and Pearson correlations between SAWS in situ SST and (**b**) the average between the northern and southern GLORYS (GLORYS Avg) grid points (**c**) the northern GLORYS (GLORYS N) grid point and (**d**) the southern GLORYS (GLORYS S) grid point. The solid red line indicates the line of best fit for each correlation and can be reproduced using the equations displayed in the top left of each respective correlation graphs.*

Monthly GLORYS SST simulated at the northern (GLORYS N), southern (GLORYS S) and the average between the northern and southern GLORYS points (GLORYS Avg), as described above, were used to calculate the bias compared to the monthly SAWS SST *in situ* data (*Figure 4.35*). There appeared to be a seasonality within the bias, where all three GLORYS data points slightly underestimated SST in autumn (April and May). This underestimation by the GLORYS

SST grid points then increased until it reached the largest negative bias in spring (October) with an average of -0.50 °C (*Figure 4.35*). Thereafter, the underestimation decreased until early summer (December). Summer (January) presented a slight overestimation of SST with the maximum positive bias, averaged at 0.10 °C, observed at the end of summer (February), followed by a sharp decrease in the overestimation (*Figure 4.35*). This seasonal signal in the bias observed between SAWS and GLORYS SST (*Figure 4.35*) was different from the biases observed in Section 4.1.2 with WOA18 (*Figure 4.10*), CARS09 (*Figure 4.11*) and OSTIA (*Figure 4.12*). This may be the result of the fact that the closest GLORYS grid points to the SAWS data point were approximately 6 km away, therefore suggesting that perhaps the offshore oceanographic environment simulated by GLORYS was in fact warmer towards the end of summer and colder throughout the remainder of the year. Another factor influencing the seasonal bias observed between SAWS and GLORYS (*Figure 4.35*) could be owed to the inaccurate simulation of Marion Island's coastline by GLORYS, which could be obscuring the smaller-scale dynamics occurring off the coastline. As previously reported by Russo et al. (2022), GLORYS was also unable to simulate the smaller-scale dynamics in the coastal regions of Southern Africa's oceans.

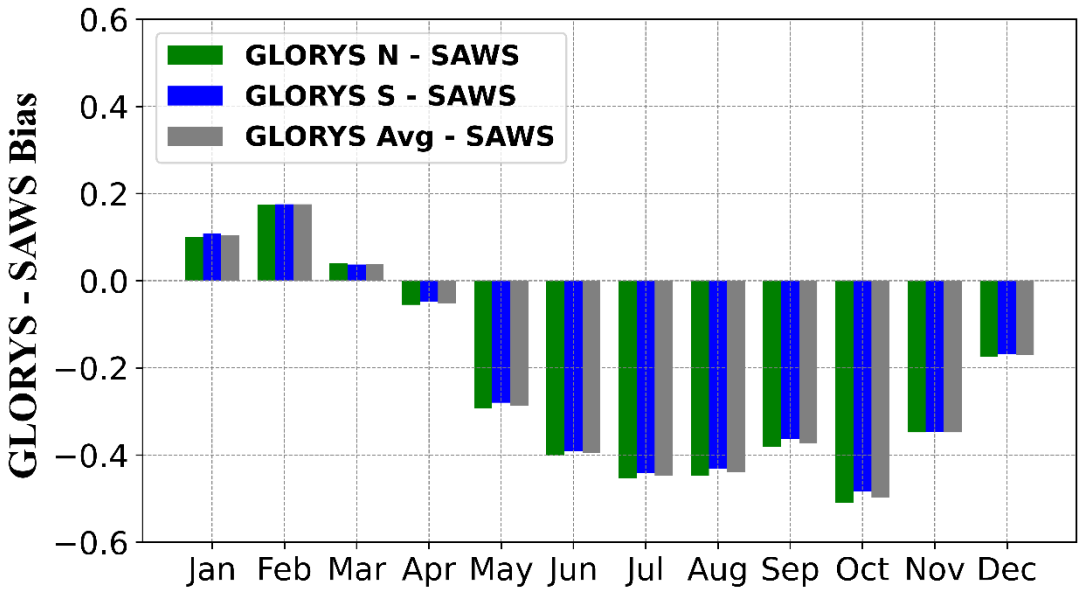

Figure 4.35 Bar graph showing the average monthly bias between GLORYS SST (°C) at the northern (GLORYS N), southern (GLORYS S), and averaged (GLORYS Avg) grid points and the SAWS in situ SST (°C) from 1993 to 2020.

Overall, the statistically significant strong, positive correlations ($r > 0.80$, $p < 0.001$) and relatively low biases (-0.50 to 0.10 °C) suggest that the GLORYS output is able to reproduce similar SST data in comparison to the *in situ* SAWS SST data. While the SAWS data may only be obtained at Marion Island, a study by Mélice et al. (2003) concluded that the data was

representative of the PEI region and thus, it can be inferred that GLORYS also accurately simulates the spatial variability of SST in the surrounding PEI environment.

4.1.6 GLORYS and CTD comparisons

Annual hydrographic CTD surveys have been ongoing since 2013 at the PEI region (Lamont et al. 2019). The focus for this study was the north-south (N-S) transect upstream of the islands, at the mean longitudinal position of 37.3 ^{o}E (described in greater detail in Section 3.1.1). *In situ* CTD data and corresponding (in time and space) GLORYS data were analysed between 2013 and 2018, to assess the degree of validity and accuracy of GLORYS in simulating event-scale hydrographic features, throughout the water column within the PEI region.

2013

The 2013 survey initially suggested the position of southern branch of the sub-Antarctic Front (S-SAF) to be south of the PEIs, according to Sokolov and Rintoul (2009), who concluded the location of the S-SAF to be at a temperature of 2.72 ^{o}C at 400 db. While this temperature was observed at ~ 47.25 ^{o}S (*Figure 4.36c and d*), it was evident that it resulted from significant doming of the 2.5 ^{o}C isotherm from approximately 1500 db to 300 db. Therefore, the temperature signal at 400 db was the result of a cyclonic eddy rather than the position of the S-SAF, agreeing with Lamont et al. (2019). GLORYS was able to simulate the cyclonic eddy, observed by the doming of the 2.5 ^{o}C isotherm from approximately 1400 db to 300 db, but GLORYS simulated weaker uplift than observed *in situ*. The model did, however, fail to produce the small-scale variations which were observed in the eddy by the *in situ* data, most likely due to the mixing at the boundary of the mesoscale feature (as seen in the CTD data), and suggested a more southward location (~ 47.5 ^{o}S) than the *in situ* data (*Figure 4.36c and d*).

With regards to the water masses, SASW and AASW are typically identifiable by their respective characteristic shallow subsurface salinity maxima and shallow temperature minima (Ansorge and Lutjeharms, 2002). A mixture of SASW and AASW was observed along this 2013 transect (*Figure 4.36b*). This could have been due to the S-SAF being located north of the PEIs, which was confirmed by Lamont et al. (2019), and because of the cyclonic eddy which would have induced greater surface and subsurface mixing. GLORYS clearly illustrated the signal of both SASW and AASW, where a higher salinity maximum (over 0.4 PSU difference) and a lower temperature minimum (over 1 ^{o}C difference) were respectively simulated (*Figure 4.36b*).

The *in situ* 34.7 PSU isohaline between 47.25 °S and 47.5 °S (*Figure 4.36d*) was observed to be flat and followed the bottom bathymetry, but the same isohaline simulated by GLORYS, however, appeared to be sloping upwards and away from the bathymetry. This may be attributed to the inaccurate bathymetry simulated by GLORYS (see Section 3.3.2 for more detail). Additionally, GLORYS appeared to simulate two smaller anti-cyclonic (cyclonic) features in temperatures (salinity) from 46 °S to 46.5 °S and between 46.75 °S and 47.25 °S (*Figure 4.36e and f*), which were not observed in the *in situ* vertical sections. Two possible explanations for this are, either GLORYS simulated a shallower bottom depth along the transect than shown by the *in situ* data or given the higher resolution of GLORYS it was able to simulate smaller features than could be observed by the *in situ* data with coarser station spacing.

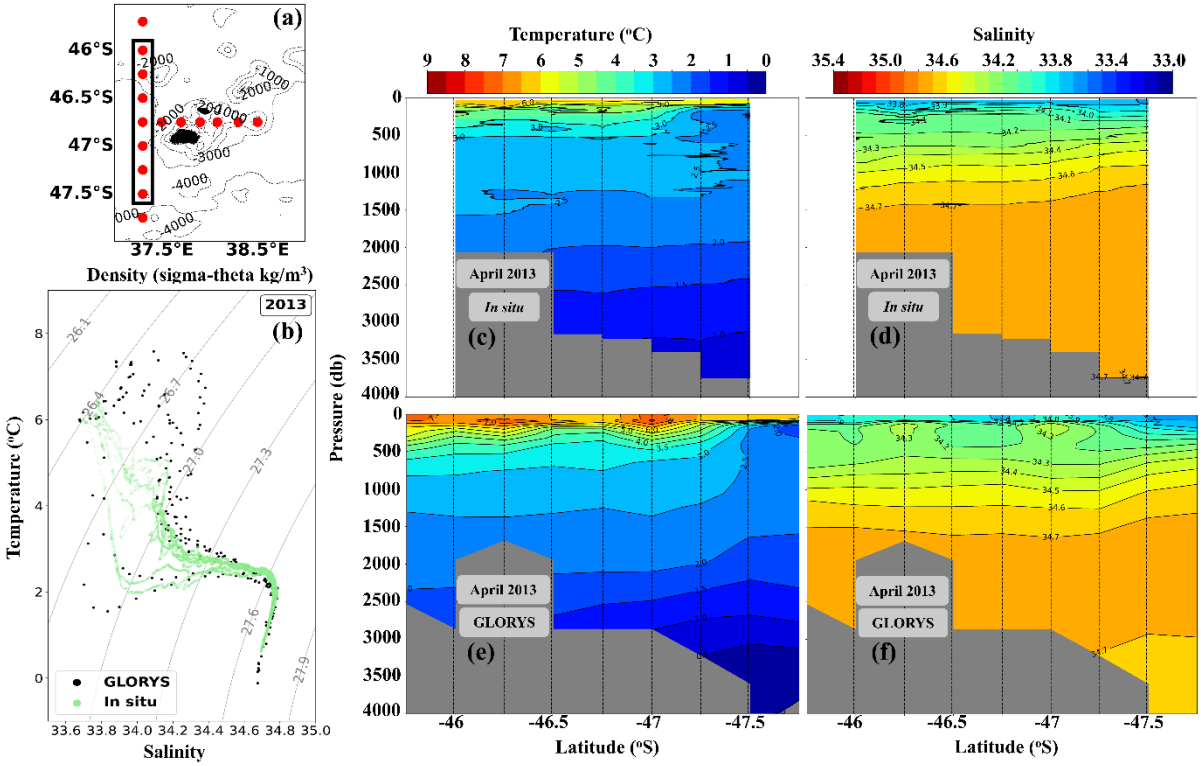

*Figure 4.36: (**a**) GEBCO 2022 bathymetry map of the surrounding PEI region, with red dots to denote the CTD station positions for the north-south (N-S) transect. The black box highlights the seven stations done in April 2013, used to produce plots (b) and (c). (**b**) Temperature/Salinity (T/S) relationship for the PEI 2013 survey, using the in situ CTD data (green) and GLORYS (black) output. Vertical section maps, using the in situ CTD data, of temperature (°C) (**c**) and salinity (**d**) during April 2013. White shading denotes the absence of data from the northern and southernmost CTD stations which were not sampled in April 2013. Vertical section maps, using GLORYS output, of temperature (°C) (**e**) and salinity (**f**) during April 2013. Dashed black vertical lines indicate the station positions along the transects, and the grey areas indicate ocean floor.*

2014

According to Lamont et al. (2019), the two northernmost stations (*Figure 4.37a*) were positioned north of the S-SAF in 2014. The warmer surface waters and subsurface salinity maxima at these stations resulted in the SASW being clearly evident in this survey (*Figure 4.37b*). GLORYS, however, illustrated SASW with a lower subsurface salinity maximum and with temperatures approximately 2 ^{o}C cooler than those observed by *in situ*. Additionally, the AASW simulated by GLORYS had a much lower (over 2 ^{o}C difference) surface temperature minimum (*Figure 4.37b*).

A cyclonic, cold-core eddy was observed along this transect, evident by the doming isotherms between 46.25 °S and 47 °S (*Figure 4.37c*), similarly identified by Lamont et al. (2019), with warmer waters (> 7 ^{o}C) to the north and south of the eddy's boundaries. The GLORYS model simulated the cyclonic eddy, but similar to the 2013 transect, it was simulated at a more southerly position between approximately 46.75 °S and 47.75 °S (*Figure 4.37e*). While the *in situ* data showed an uplift of the 2.5 ^{o}C isotherm from approximately 1600 db to 800 db (*Figure 4.37c*), GLORYS illustrated an uplift, of the same isotherm, from approximately 1500 db to 200 db (*Figure 4.37e*). Coupled with the cold (< 2 ^{o}C) closed isotherms above 1000 db, it can be inferred that GLORYS simulated a much stronger uplift in the core of the cyclonic eddy (*Figure 4.37e*). The *in situ* data observed the concaving of isohalines within the core of the eddy, above 500 db and the doming of isohalines, below 500 db (*Figure 4.37d*). This signature was the result of the cold-core eddy advecting and trapping warmer, more saline SASW around the eddy's boundaries. GLORYS, however, simulated the concaving isohalines beyond 500 db (*Figure 4.37f*), therefore suggesting GLORYS simulated stronger advection and retention of the eddy (*Figure 4.37d*).

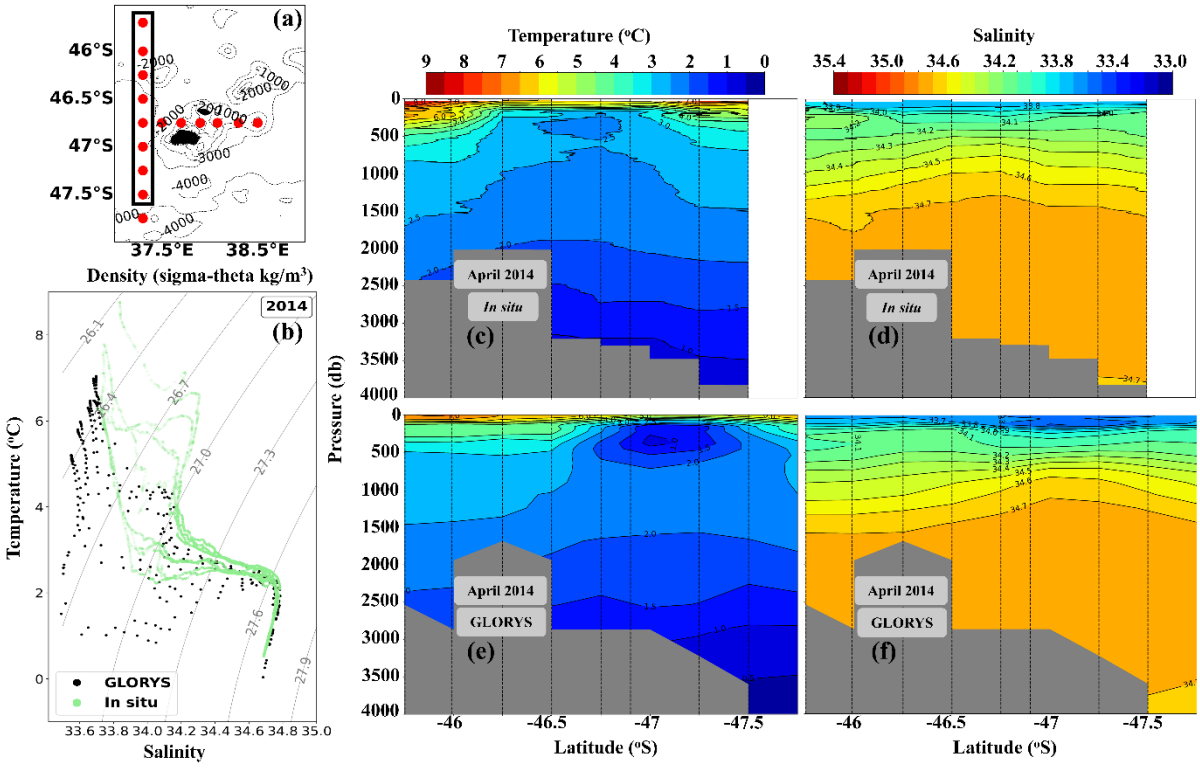

*Figure 4.37 (**a**) GEBCO 2022 bathymetry map of the surrounding PEI region, with red dots to denote the CTD station positions for the north-south (N-S) transect. The black box highlights the eight stations done in April 2014, used to produce plots (b) and (c). (**b**) Temperature/Salinity (T/S) relationship for the PEI 2014 survey, using the in situ CTD data (green) and GLORYS (black) output. Vertical section maps, using the in situ CTD data, of temperature (°C) (**c**) and salinity (**d**) during April 2014. White shading denotes the absence of data from the southernmost CTD station which was not sampled in April 2014. Vertical section maps, using GLORYS output, of temperature (°C) (**e**) and salinity (**f**) during April 2014. Dashed black vertical lines indicate the station positions along the transects, and the grey areas indicate ocean floor.*

2015

The 2015 transect illustrated the S-SAF to the south of the PEIs according to the SSH data analysed by Lamont et al. (2019), therefore the seven northernmost stations were north of the S-SAF resulting in the prevalent signal of the SASW in the T/S (green dots) plot (*Figure 4.38b*). The *in situ* data (green dots) (*Figure 4.38b*) which produced the singular T/S trace between approximately 5 and 3 °C was the result of only the southernmost station being located south of the S-SAF and thus being the only station to capture the AASW signature. GLORYS reproduced very similar results, simulating the clear separation between the distinct SASW (from 5.5 to 8 °C and 33.8 to 32.45 PSU) and AASW (from 2.5 to 6 °C and 33.8 to 34.18 PSU) (*Figure 4.38b*).

A warm-core anticyclonic eddy was observed in the *in situ* data and is in agreement with the findings of Lamont et al. (2019), whereby the core of the eddy was approximately between 46.25 °S and 46.75 °S (*Figure 4.38c*). It was illustrated by the depression of isotherms and by the presence of warmer water (>7 ^{o}C) within the core. The warm-core eddy was simulated at a more southerly location, between approximately 46.5 °S and 47.25 °S, by GLORYS (*Figure 4.38e*). The GLORYS isotherms around the core of the anticyclonic eddy were however much closer together than those observed by the *in situ* data, illustrating a stronger temperature gradient above 500 db, which was indicative of stronger downwelling (*Figure 4.38e*).

The downward sloping bathymetry simulated by GLORYS in the temperature (*Figure 4.38e*) and salinity (*Figure 4.38f*) vertical sections, between 47 ^{o}S and 47.5 ^{o}S, was absent at the corresponding *in situ* temperature and salinity vertical sections (*Figure 4.38c and Figure 4.38d, respectively*). The strong uplift of the 0.5 and 1 ^{o}C isotherms (*Figure 4.38e*) and the 34.4 isohaline (*Figure 4.38f*) in GLORYS may be an artefact resulting from the simulated bathymetry which was shallower and followed a different shape than the *in situ* data.

Less saline water (< 34.0 PSU) was observed to extend to approximately 300 db in the *in situ* data (*Figure 4.38d*) and slight dipping of the isohalines was evident until approximately 1000 db, indicative of the anticyclonic core. GLORYS instead simulated more saline waters (>34.1 PSU) doming near the surface and appeared to illustrate strong uplift of the isohalines south of 47 ^{o}S.

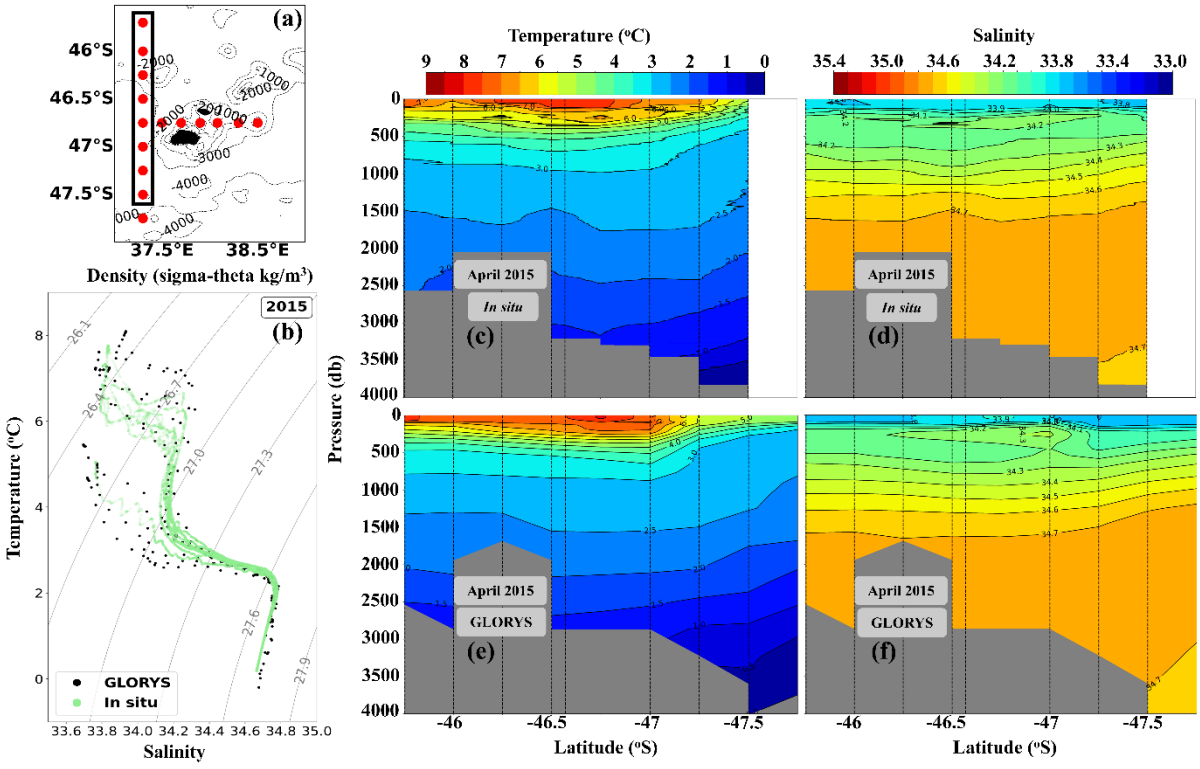

*Figure 4.38: (**a**) GEBCO 2022 bathymetry map of the surrounding PEI region, with red dots to denote the CTD station positions for the north-south (N-S) transect. The black box highlights the eight stations done in April 2015, used to produce plots (b) and (c). (**b**) Temperature/Salinity (T/S) relationship for the PEI 2014 survey, using the in situ CTD data (green) and GLORYS (black) output. Vertical section maps, using the in situ CTD data, of temperature (°C) (**c**) and salinity (**d**) during April 2015. White shading denotes the absence of data from the southernmost CTD station which was not sampled in April 2015. Vertical section maps, using GLORYS output, of temperature (°C) (**e**) and salinity (**f**) during April 2015. Dashed black vertical lines indicate the station positions along the transects, and the grey areas indicate ocean floor.*

2016

During the 2016 cruise, Lamont et al. (2019) observed a considerable amount of latitudinal movement of the S-SAF, where it meandered between a northward and southward position relative to the PEIs. The northernmost CTD station was located north of the middle branch of the sub-Antarctic Front (M-SAF) and as a result had the highest surface and intermediate temperatures, as well as the highest subsurface salinity maximum. This was evident in the *in situ* T/S plot (green dots) (*Figure 4.39a*), and in the *in situ* temperature (*Figure 4.39c*) and salinity (*Figure 4.39d*) vertical sections, between 45.75 °S and 46 °S, where higher surface temperatures (>7 °C) and a high subsurface salinity (34.2 PSU) was observed. GLORYS did not capture the presence of this water in the T/S plot (black dots) (*Figure 4.39a*) but instead did simulate higher proportions of the SASW and less AASW (*Figure 4.39a*), possibly due to GLORYS simulating the S-SAF much further south than the *in situ* data suggests. More saline waters (> 34.3 PSU) were simulated above 100 db by GLORYS (*Figure 4.39f*), which appeared

to narrow the surface layers of less saline water (< 33.9 PSU), in comparison to the *in situ* data which suggested a deeper surface layer comprising of less saline water (< 33.9 PSU) (*Figure 4.39d*).

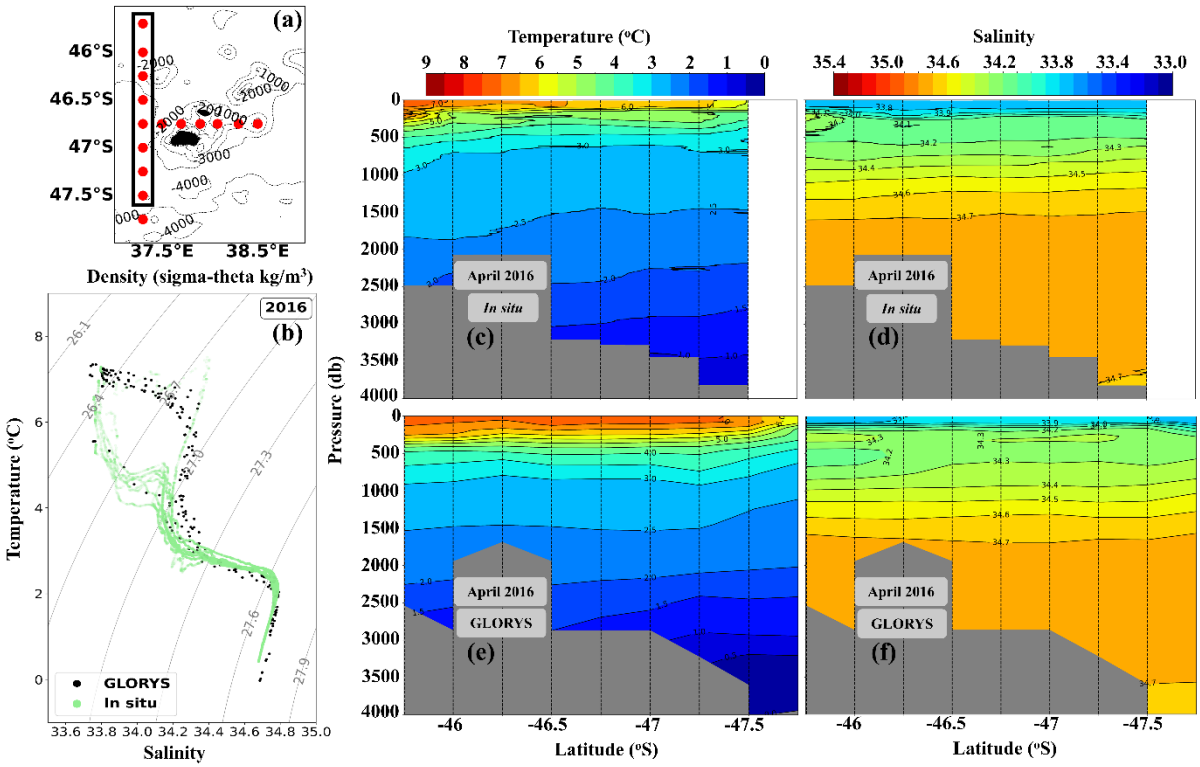

*Figure 4.39 (**a**) GEBCO 2022 bathymetry map of the surrounding PEI region, with red dots to denote the CTD station positions for the north-south (N-S) transect. The black box highlights the eight stations done in April 2016, used to produce plots (b) and (c). (**b**) Temperature/Salinity (T/S) relationship for the PEI 2016 survey, using the in situ CTD data (green) and GLORYS (black) output. Vertical section maps, using the in situ CTD data, of temperature (°C) (**c**) and salinity (**d**) during April 2016. White shading denotes the absence of data from the southernmost CTD station which was not sampled in April 2016. Vertical section maps, using GLORYS output, of temperature (°C) (**e**) and salinity (**f**) during April 2016. Dashed black vertical lines indicate the station positions along the transects, and the grey areas indicate ocean floor.*

2017

While the S-SAF was observed to have substantial latitudinal variation in the 2017 survey as described by Lamont et al. (2019), the *in situ* T/S plot (green dots) (*Figure 4.40b*) showed waters with characteristics of mainly SASW. This was most likely due to the four northernmost stations being located north of the S-SAF, confirmed by Lamont et al. (2019). GLORYS appeared to simulate a much clearer distinction between SASW and AASW, where warmer (> 7 °C) and more saline (> 34.1 PSU) surface and intermediate waters were illustrated by GLORYS in the T/S, temperature and salinity vertical section plots (*Figure 4.40b, e and f, respectively*), indicative of the SASW. This was most likely due to the M-SAF being within close proximity to the four northernmost stations, thus it is suggested that due to the higher

resolution of GLORYS, it was able to better capture the presence of the M-SAF, than what *in situ* was able to.

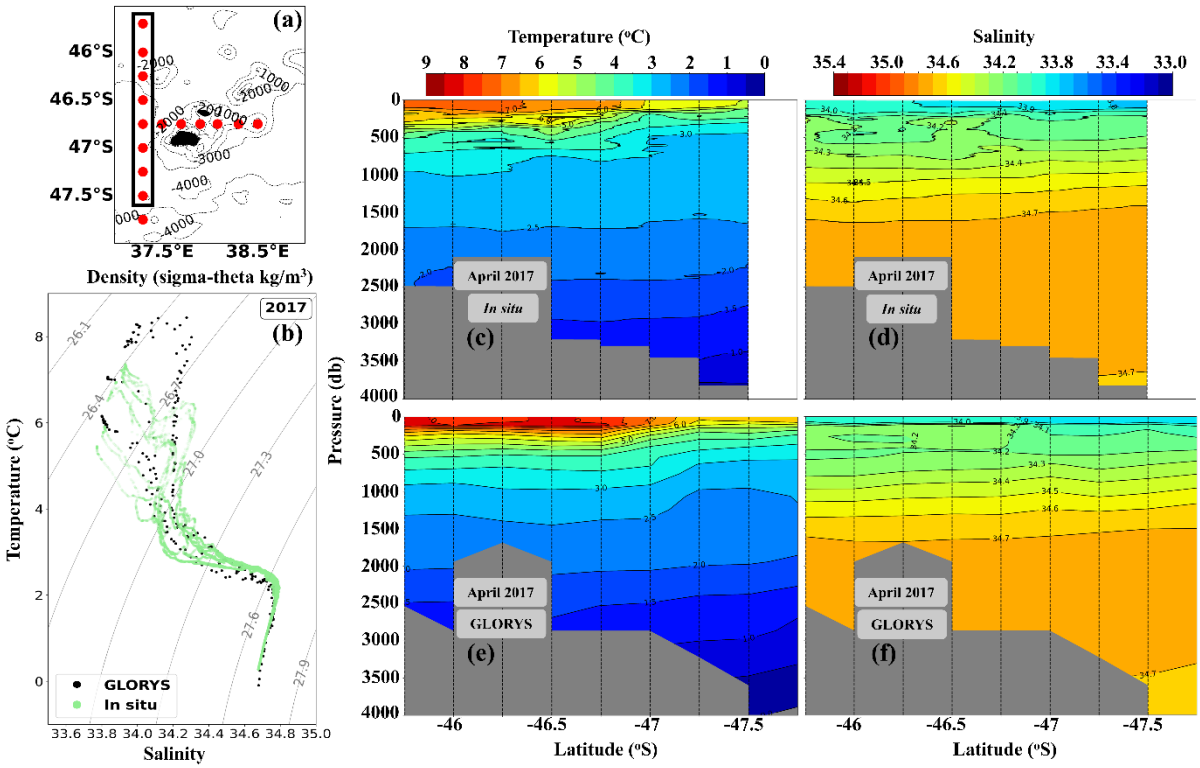

*Figure 4.40: (**a**) GEBCO 2022 bathymetry map of the surrounding PEI region, with red dots to denote the CTD station positions for the north-south (N-S) transect. The black box highlights the eight stations done in April 2017, used to produce plots (b) and (c). (**b**) Temperature/Salinity (T/S) relationship for the PEI 2017 survey, using the in situ CTD data (green) and GLORYS (black) output. Vertical section maps, using the in situ CTD data, of temperature (°C) (**c**) and salinity (**d**) during April 2017. White shading denotes the absence of data from the southernmost CTD station which was not sampled in April 2017. Vertical section maps, using GLORYS output, of temperature (°C) (**e**) and salinity (**f**) during April 2017. Dashed black vertical lines indicate the station positions along the transects, and the grey areas indicate ocean floor.*

2018

At 400 db, the 2.72 °C isotherm, characteristic of the S-SAF was observed by *in situ* at approximately 47.75 °S, agreeing with the findings by Lamont et al. (2019), and therefore confirmed the S-SAF was south of the islands for the 2018 survey. The majority of the *in situ* stations (*Figure4.41 b, c, and d*) along this transect were thus displaying warm (> 6 °C), saline (>34.1 PSU) waters typical of SASW. While GLORYS illustrated warmer surface waters (> 7 °C) (*Figure 4.41b*), it did not display the higher saline surface waters, nor did it simulate the uplift of the 2.72 °C isotherm to the same extent as *in situ* (*Figure 4.41e, f*). The model may have simulated the front further south because the beginnings of the uplift was evident by the 3 °C isotherm between 47 and 47.75 °S (*Figure 4.41e*).

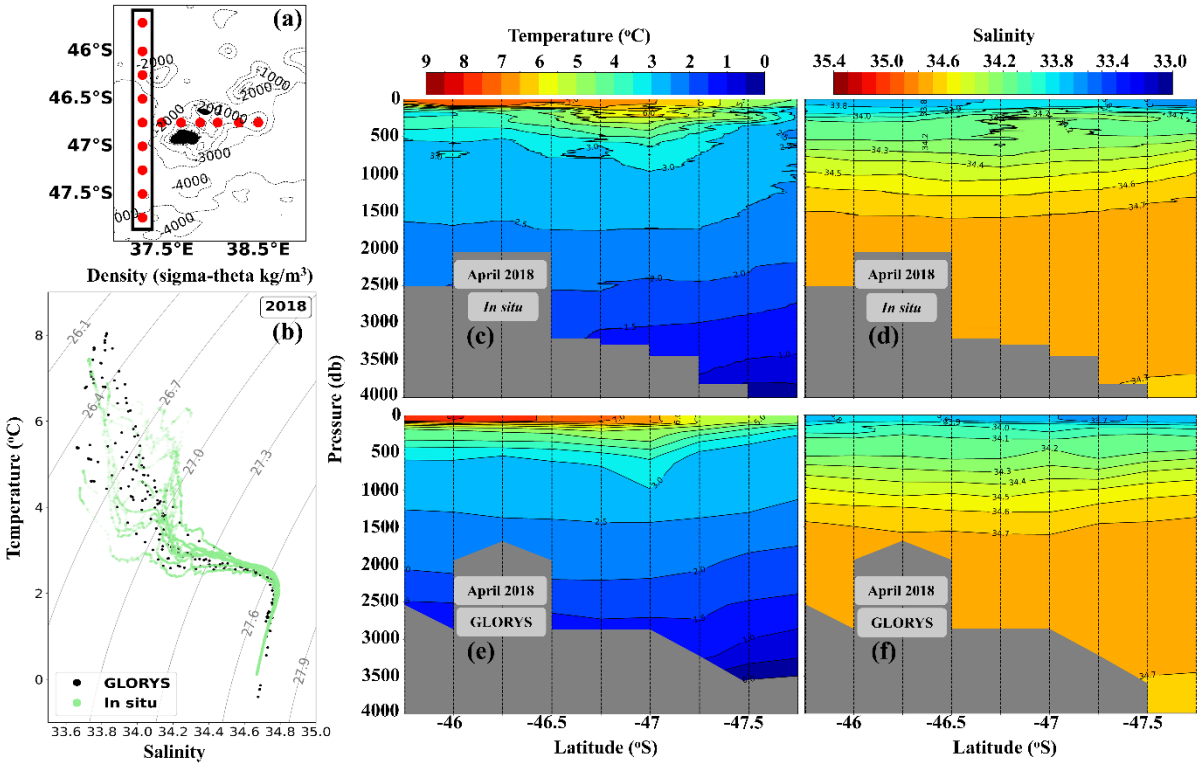

*Figure 4.41: (**a**) GEBCO 2022 bathymetry map of the surrounding PEI region, with red dots to denote the CTD station positions for the north-south (N-S) transect. The black box highlights the nine stations done in April 2018, used to produce plots (b) and (cf). (**b**) Temperature/Salinity (T/S) relationship for the PEI 2018 survey, using the in situ CTD data (green) and GLORYS (black) output. Vertical section maps, using the in situ CTD data, of temperature (°C) (**c**) and salinity (**d**) during April 2018. Vertical section maps, using GLORYS output, of temperature (°C) (**e**) and salinity (**f**) during April 2018. Dashed black vertical lines indicate the station positions along the transects, and the grey areas indicate ocean floor.*

Overall, the GLORYS model was able to capture the general temperature and salinity variability, throughout the water column. It does, however, struggle to simulate smaller scale variability, as similarly observed by Russo et al. (2022). At the surface, this is suggested to be due to the fact that while the ocean's surface is constantly interacting with the atmosphere, thus the surface in situ data will reflect these interactions, GLORYS however, may not have a feedback mechanism to consistently update and simulate this interaction, despite being atmospherically forced (ECMWF ERA-Interim reanalysis and ERA5, see Section 3.3.2). Additionally, the shallower and erroneous bathymetry simulated by GLORYS (as described in greater detail in Section 3.3.2) may be influencing the spatial variability of oceanographic parameters such as temperature and salinity, at a small scale.

4.2 Quantitative analysis for Taylor Column existence

The Taylor column was first observed by William Thomson (Kelvin) in 1868 (Fuentes, 2009) and later studied by Taylor (1917) and Proudman (1916) as a consequence of the Taylor-Proudman theorem. The theoretical concept illustrated that in a homogenous (constant density), uniformly flowing ocean, a body of water upon encountering an obstacle, such as a seamount, would form a column-like structure that moves perpendicular to the rotation axis (Taylor, 1923; Marshall and Plumb, 2007). Taylor columns have been observed as isolated anti-cyclonic circulations around seamounts but given that the ocean is stratified with variable currents, surface conditions and seamount shapes, the resulting flow patterns of Taylor columns, in the real ocean environment, are more complex (White et al. 2007).

Several non-dimensional numbers have been used to assist in identifying whether oceanic conditions are suitable for the development of Taylor columns. These are, the Rossby number, the Reynolds number, the Rossby radius of deformation and the blocking parameter. This section addresses the last key question of this study by using a combination of satellite data, modelled bathymetry data (GEBCO) and the high resolution GLORYS model output to calculate and assess these values. The purpose thereof is to identify and discuss the suitability of the model conditions for the formation and evolution of a possible Taylor column around the PEIs.

4.2.1 Rossby Number

The Rossby number (Ro) describes the importance of the Earth's rotation in governing the flow patterns observed by determining the ratio of inertial forces to Coriolis forces (Mininni et al. 2009; White et al. 2007). The comparison between the satellite derived Ro (*Figure 4.42*) and the model derived Ro (*Figure 4.43*) at the surface, showed good agreement. However, GLORYS produced higher values, for the entire PEI surrounding region, in comparison to satellite, this was most likely due to the higher current speeds simulated by the model (see Section 4.1.1). A similar meridional pattern was observed in both the satellite and model Ro (*Figure 4.42; Figure 4.43*), with a band of higher values at approximately 48 ^{o}S. This can be explained by the increased current speed due to the bifucation of the ACC upon approaching the shallowing bathymetry of the PEIs (Ansorge et al. 2010). This was clearly evident with both the satellite and GLORYS geostrophic vectors (see Section 4.1.1) where majority of the current veered southwards, rejoining the main flow downstream of the islands.

White et al. (2007) described a similar phenomena for the flow pattern around seamounts, whereby the flow spilts apon encountering an obstacle, resulting in the acceleration of the left-hand branch (when facing downstream in the northern hemisphere) around said obstacle. This results in the occurrence of an isolated anticyclonic circulation around the seamount (White et al. 2007). The opposite would be true for the southern hemisphere, where the majority of the flow would be diverted to the right of the obstacle (when facing downstream), therefore supporting the findings of the birfucation observed in this study, along with the band of higher Ro (*Figure 4.42; Figure 4.43*). A similar north-south pattern was observed at 200 m (see Appendix *Figure A16*), however slighly lower Ro values were observed than those captured by GLORYS at the surface. This is suggested to be due to the stronger surface currents which are primarily driven by wind stress, as opposed to the slighlty weaker thermohaline circulation derived by density variations throughout the remaining water column (Marshall and Plumb, 2007).

As far as in known, no previous studies have investigated Taylor columns, using Ro, over an island system they have recorded similar results over seamounts. Owens and Hogg (1980) recorded a Ro value of 0.09 near a seamount in the western North Atlantic, a much smaller Ro of 0.008 was recorded by Haidvogel et al. (1993) over the Fieberling Guyot seamount. The current study observed Ro values within the same range between 0 and 0.07 (*Figure 4.42; Figure 4.43*). White et al. (2007) confirmed an upper threshold of Ro ~ 1.5 to 2.0, above which the formation of a Taylor column would not occur. This suggests that conditions observed by both satellite and GLORYS are suitable to support the formation and existence of a Taylor column at the PEIs.

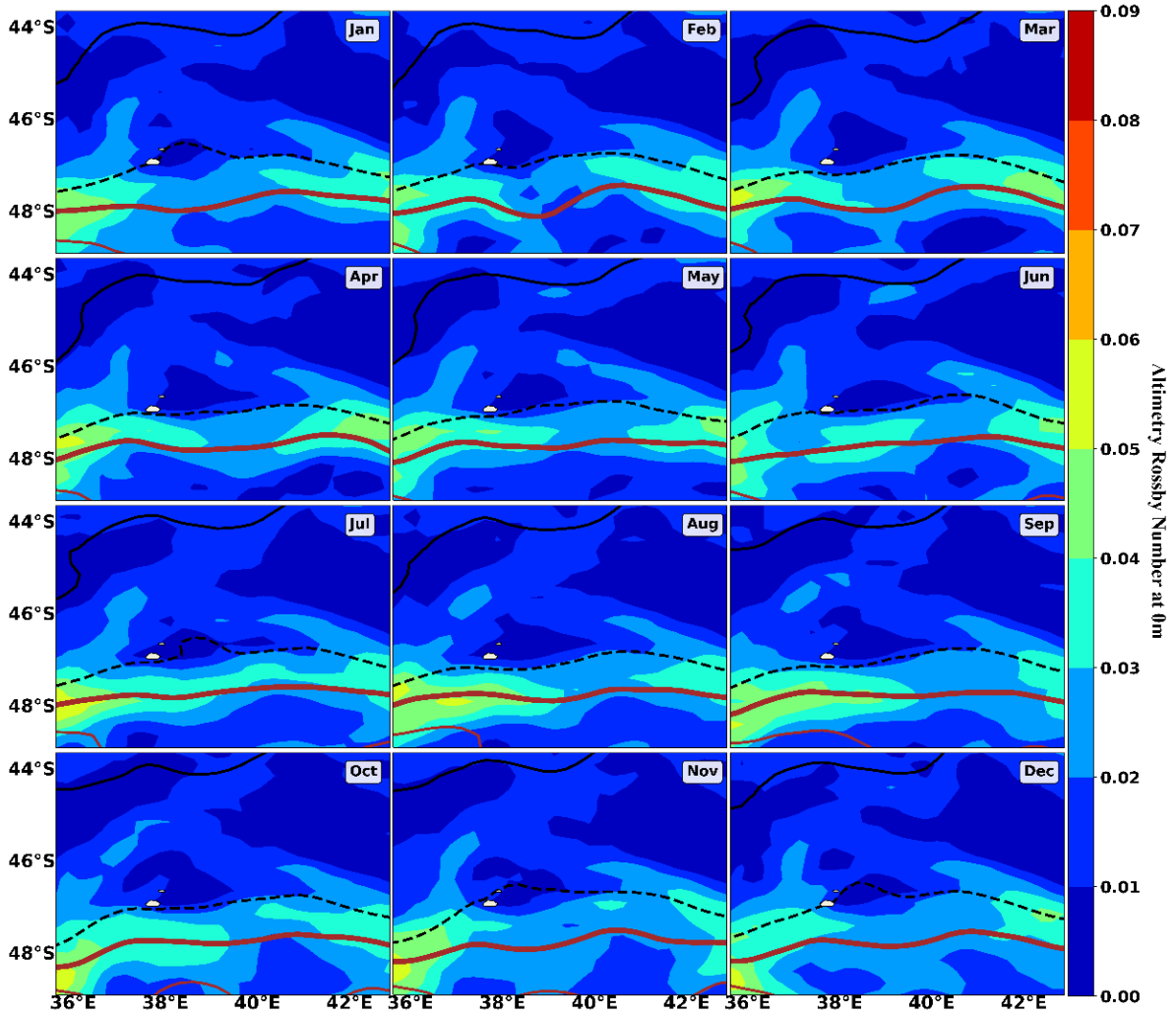

Figure 4.42: The monthly climatology of Rossby Number (Ro) calculated using geostrophic current velocity at the surface (0 m), from January (Jan) to December (Dec) around the Prince Edward Islands from 1993 to 2022 using the daily reprocessed ADT satellite data. The black solid and dashed lines represent the M-SAF and S-SAF, respectively. The solid thick and thinner brown lines represent the N-APF and M-APF, respectively. These front positions were identified from satellite altimetry using ADT according to the process described by Sokolov and Rintoul (2002).

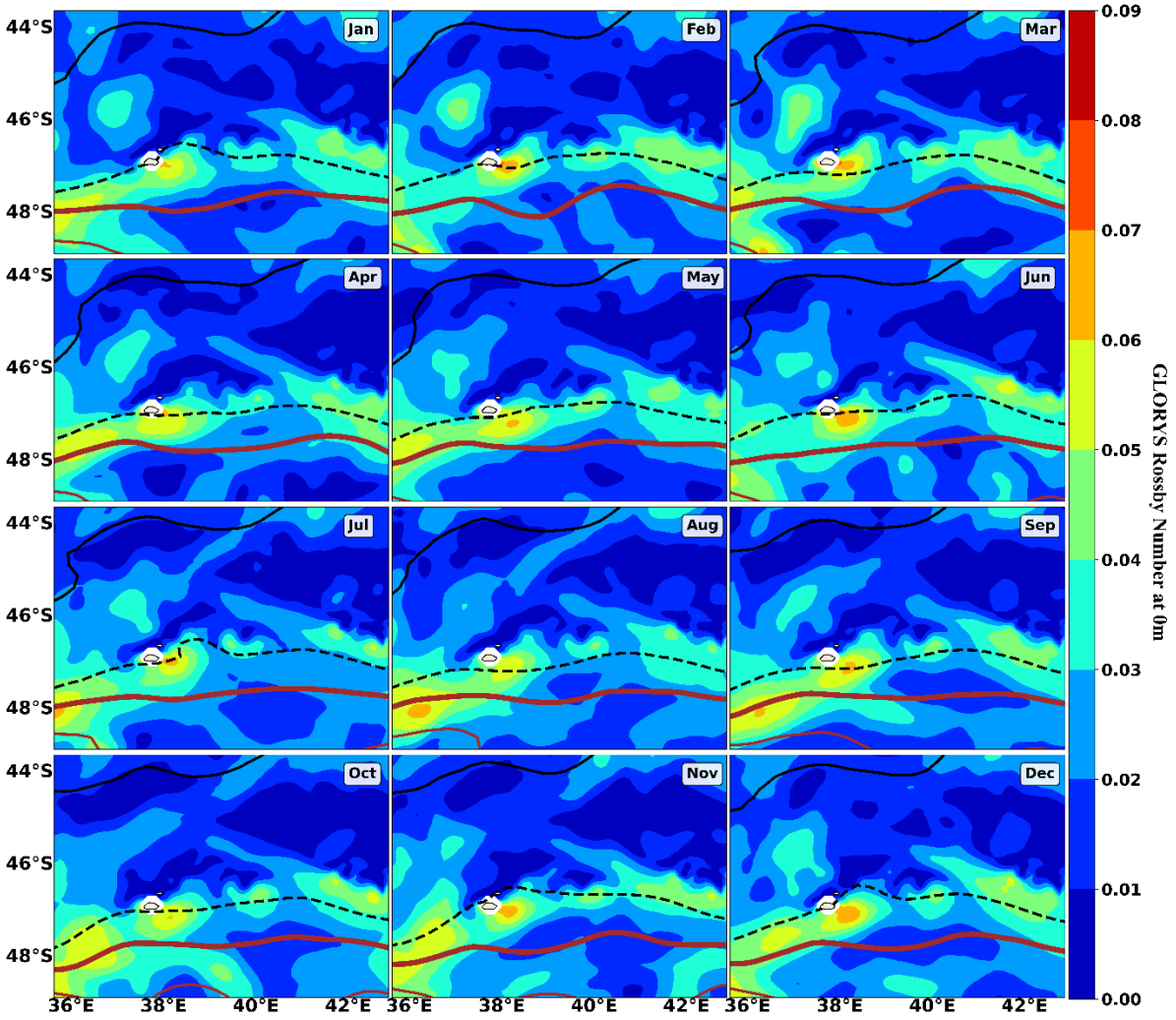

Figure 4.43 The monthly climatology of Rossby Number (Ro) calculated using geostrophic current velocity at the surface (0 m), from January (Jan) to December (Dec) around the Prince Edward Islands from 1993 to 2020 using the GLORYS model output. The black solid and dashed lines represent the M-SAF and S-SAF, respectively. The solid thick and thinner brown lines represent the N-APF and M-APF, respectively. Areas shaded white denote regions of no data. These front positions were identified from satellite altimetry using ADT according to the process described by Sokolov and Rintoul (2002).

4.2.2 Reynolds Number

Reynolds number (Re) is used to characterize the effect of viscosity in controlling the circulation patterns and velocity of a fluid, in this case specifically around an obstacle within the ocean (Rehm et al. 2008). The overall Re patterns observed in the satellite data (*Figure 4.44*) and GLORYS output (*Figure 4.45*) were a near perfect match to the respective satellite and GLORYS Ro patterns (see Section 4.2.1), with a band of higher Re at approximately 48 ^{o}S. Similarly, GLORYS generally also simulated higher Re values than what satellite captured. The reasons for these patterns are suggested to be the same as those posed for Ro (in Section 4.2.1), whereby the bifurcation of ACC resulted in accelerated flow of the current to the right

(facing downstream) inferring that the increased and concentrated current speed would have produced the band of higher Re values (*Figure 4.44; Figure 4.45*). GLORYS produced very similar findings of Re values at 200 m (see Appendix *Figure A17*), when compared to the Ro values at the same depth (see Appendix *Figure A16*), with lower Re values observed at 200 m than those at the surface. Reasoning for this is suggested to be the same as that inferred for Ro values, where wind forcing is the main driver of surface currents, while more sluggish thermohaline circulation governs the currents at depth (Marshall and Plumb, 2007). Since Re is the ratio of viscosity forces to inertial forces, it can be used to deduce whether a fluid is in laminar or turbulent flow (Mininni et al. 2009). As defined by Rehm et al. (2008) a Re $\leq$ 2100 is considered to show laminar flow and a Re > 2100 is indicative of turbulent flow. However, since the Rehm et al. (2008) Re threshold values were specifically recommended from the API 13D recommendations for fluid and oil drilling, these values do not appear to be good approximations for the oceanic environment of our study area. Rajani et al. (2009) observed in laboratory simulations that for two- and three-dimensional flows past a circular cylinder, different flow regimes existed. The most extreme Re values recorded were for Re > 48 for laminar flow with regular vortex shedding in the wake of the obstacle and Re > 180 for the formation of a streamwise vortex structure, representative of a turbulent flow. Since our Re values are much higher than the Rajani et al. (2009) thresholds, it suggests that *in situ* and model conditions indicate turbulent, unsteady flow around the PEIs.

Both the satellite data (*Figure 4.44*) and GLORYS (*Figure 4.45*) showed Re values higher than 2100, localised around the PEIs, indicating turbulent flow. The satellite data illustrated laminar flow downstream of the islands (Re < 2000). GLORYS simulated a similar decrease in Re values, they were however indicative of turbulent flow (Re < 10 000).

To the best of our knowledge no previous publications have been done which documented using Re values around island systems, to categorise the flow state around islands, which could be compared to this study's' Re values (Perissinotto and Duncombe Rae, 1990). Perfect et al. (2018) did use ocean modeling to investigate the effects of the Earth's rotation and stratification on ocean circulation patterns past a seamount. Perfect et al. (2018) recorded an effective Re value of approximately 2000 at the seamount, similar to the Re values observed at the PEIs in this study. White et al. (2007) descibed the formation process of turbulent flow patterns around a seamount, for the Northern hemisphere, which results in the formation of Taylor columns. As the water column moves, over a seamount, its height is decreased causing the water to acquire a negative relative vorticity, as the column moves past the seamount, its height

increases resulting in a positive relative vorticity (White et al. 2007). It is these opposing signs of relative vorticity which result in an anticyclonic spin of the water column above the seamount and a cyclonic rotation downstream of the seamount, driving a turbulent wake downstream. This turbulence, localised around the PEIs, was clearly evident in both GLORYS (*Figure 4.45*) and the satellite data (*Figure 4.44*), inferring that a Taylor column could form and persist within the region.

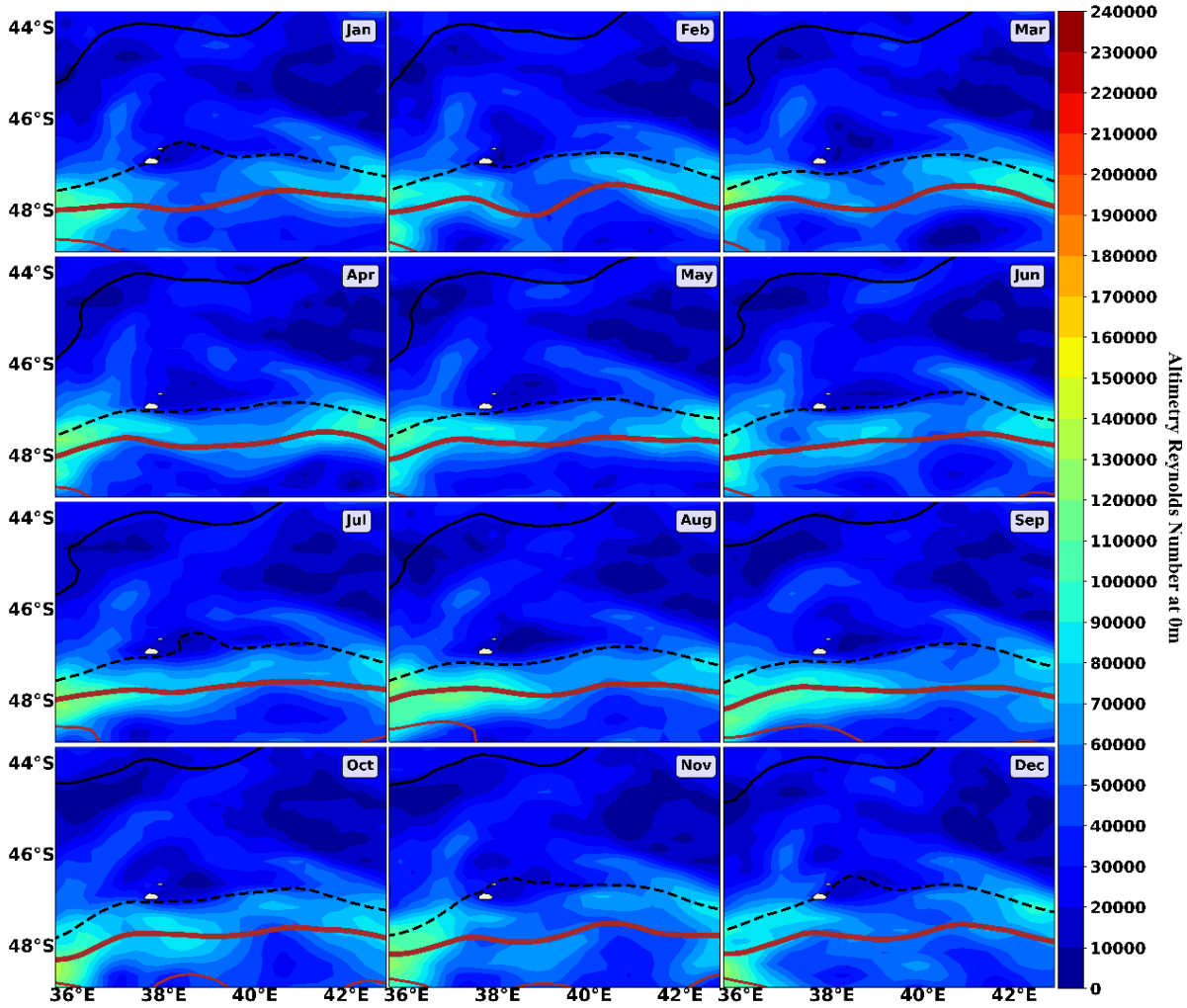

Figure 4.44: The monthly climatology of Reynolds Number (Re) calculated using geostrophic current vectors at the surface (0 m), from January (Jan) to December (Dec) around the Prince Edward Islands from 1993 to 2022 using the daily reprocessed ADT satellite data. The black solid and dashed lines represent the M-SAF and S-SAF, respectively. The solid thick and thinner brown lines represent the N-APF and M-APF, respectively. These front positions were identified from satellite altimetry using ADT according to the process described by Sokolov and Rintoul (2002).

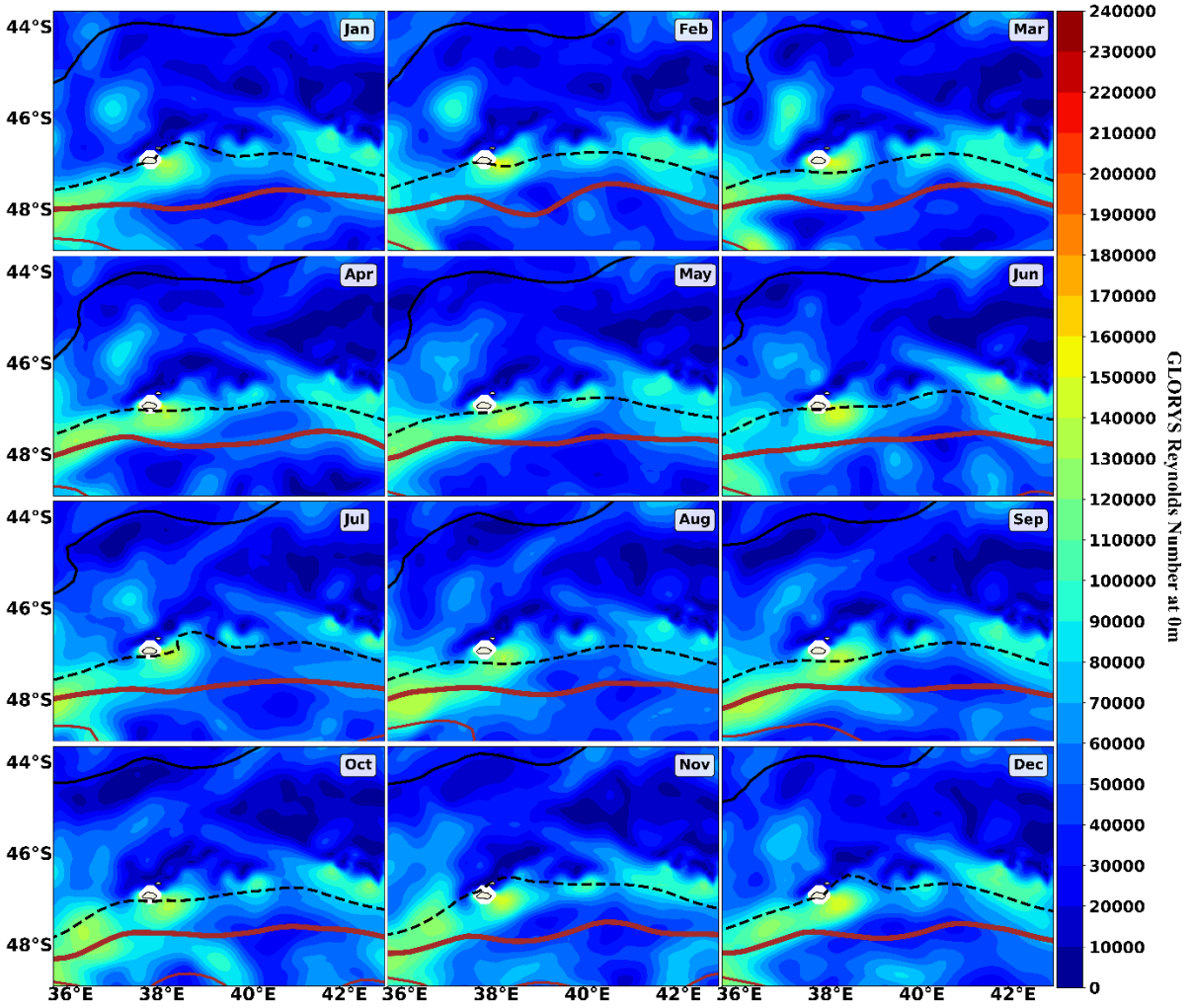

Figure 4.45: The monthly climatology of Reynolds Number (Re) calculated using geostrophic current vectors at the surface (0 m), from January (Jan) to December (Dec) around the Prince Edward Islands from 1993 to 2020 using the GLORYS model output. The black solid and dashed lines represent the M-SAF and S-SAF, respectively. The solid thick and thinner brown lines represent the N-APF and M-APF, respectively. Areas shaded white denote regions of no data. These front positions were identified from satellite altimetry using ADT according to the process described by Sokolov and Rintoul (2002).

4.2.3 Blocking Parameter

The ocean is stratified, and thus an insufficient amount of energy is available to support a Taylor column extending to the ocean's surface, instead a "Taylor cone" of a specific height may form, which would not extend to the surface (White et al. 2007). The Blocking parameter (Bl) governs the Taylor column or Taylor cone formation and circulation behaviour (White et al. 2007). It is the ratio of Ro to $\propto$ (see equations 12 and 13 in Section 3.4.7). Three total water depths were considered for the calculation of $\propto$. These were, the median depth of 3027.2 m simulated by GLORYS (*Figure 4.46; Figure 4.47*), the localised deepest depth of 2000 m

within the PEI vicinity (*Figure 4.48; Figure 4.49*), and the median depth of 2921.3 m simulated by GEBCO (see Appendix *Figure A18; Figure A19*).

While there was good agreement between the Bl values of the satellite data (*Figure 4.46; Figure 4.48)* and GLORYS (*Figure 4.47; Figure 4.49*), the values using the 2000 m total water depth were comparatively higher than those which made use of the median depth simulated by GLORYS. This is consistent with the equation used to calculate Bl, whereby a shallower total depth would produce a higher Bl value and vice versa. Notably the Bl observed in GLORYS (*Figure 4.47; Figure 4.49*), was higher directly to the north of the PEIs, whereas the satellite Bl (*Figure 4.46; Figure 4.48)* illustrated the higher values much further north of the islands. While these higher Bl values were present within the region, the localised area around the islands presented low Bl values (approximately < 0.2) (*Figure 4.47 to Figure 4.49*). These same observations were shown in the satellite and GLORYS Bl which made use of the GEBCO median depth (see Appendix *Figure A18; Figure A19*). A possible explanation for the increased Bl values, to the north of the PEIs, is proposed to be the result of GLORYS simulating a shallower bathymetry since the model uses ETOPO1 bathymetry model data for the open ocean and GEBCO bathymetry for the coastal regions (Drévillon et al. 2021b).

Several previous studies have investigated the formation of Taylor columns or Taylor cones under the condition of Bl values over seamounts, and there appears to be two main thresholds proposed, above which neither a Taylor column nor a Taylor cone could form. Some authors have proposed a critical value for Taylor cone formation of Bl $\geq$ ~ 1 (Huppert, 1975; Roden, 1987; Owens and Hogg, 1980; Martin and Drucker, 1997). While others have suggested a Bl threshold of $\geq$ ~ 2, this was specified to be the case with gaussian shaped seamount and moderately stratified water columns (Chapman and Haidvogel, 1992; Hogg, 1973). The current study presented a range of Bl values from 0 to 4 but within the vicinity of the PEIs, Bl values did not exceed 0.2, which is much lower than either of the thresholds previously put forward, indicating that the formation and persistence of either a Taylor column or Taylor cone would be likely within the PEIs region.

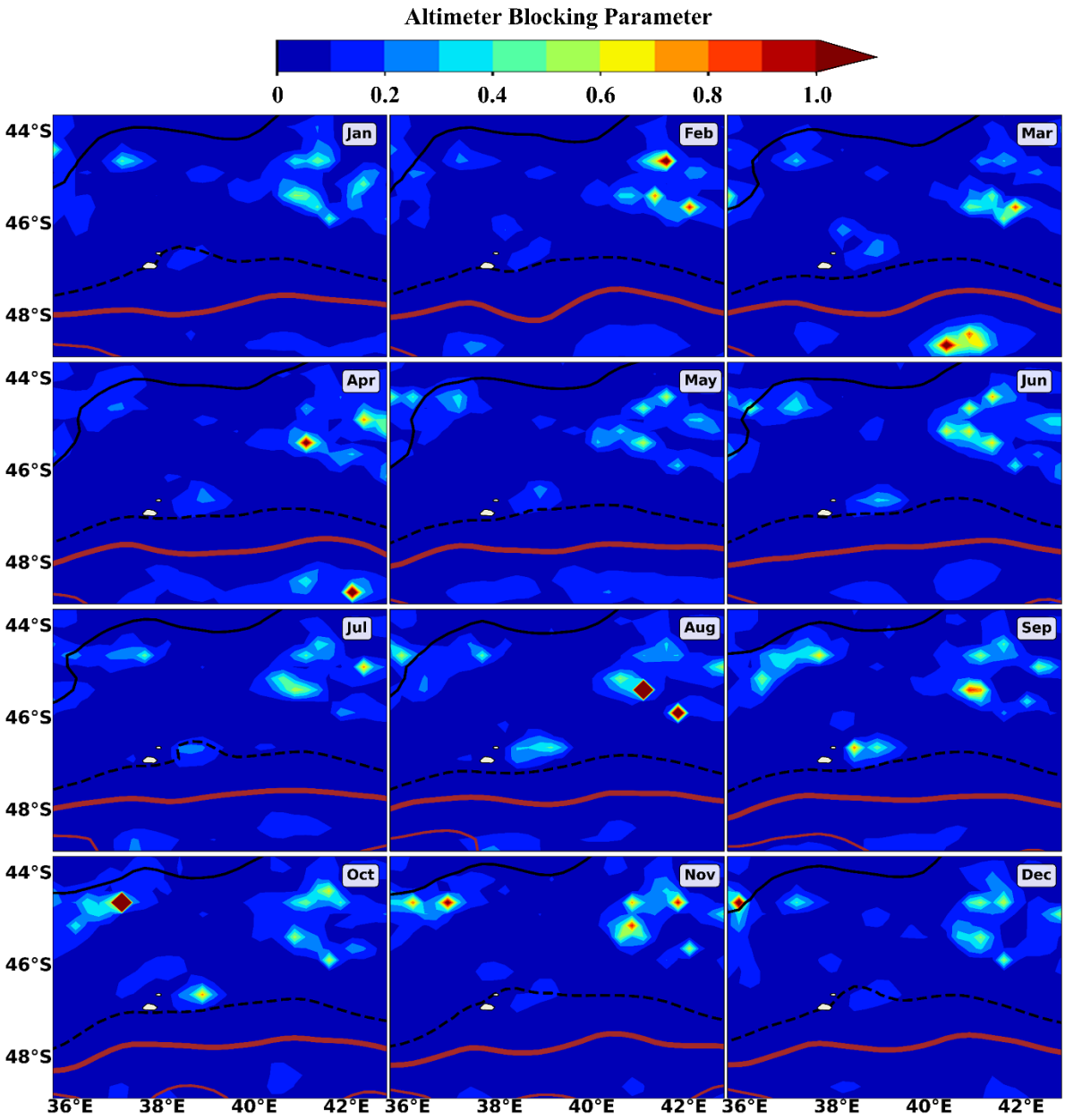

Figure 4.46: The monthly climatology of Blocking parameter (BI) calculated using GLORYS median water depth of 3027.2 m, from January (Jan) to December (Dec) around the Prince Edward Islands from 1993 to 2022 using the daily reprocessed ADT satellite data and the GEBCO 2022 bathymetry data. The black solid and dashed lines represent the M-SAF and S-SAF, respectively. The solid thick and thinner brown lines represent the N-APF and M-APF, respectively. These front positions were identified from satellite altimetry using ADT according to the process described by by Sokolov and Rintoul (2002).

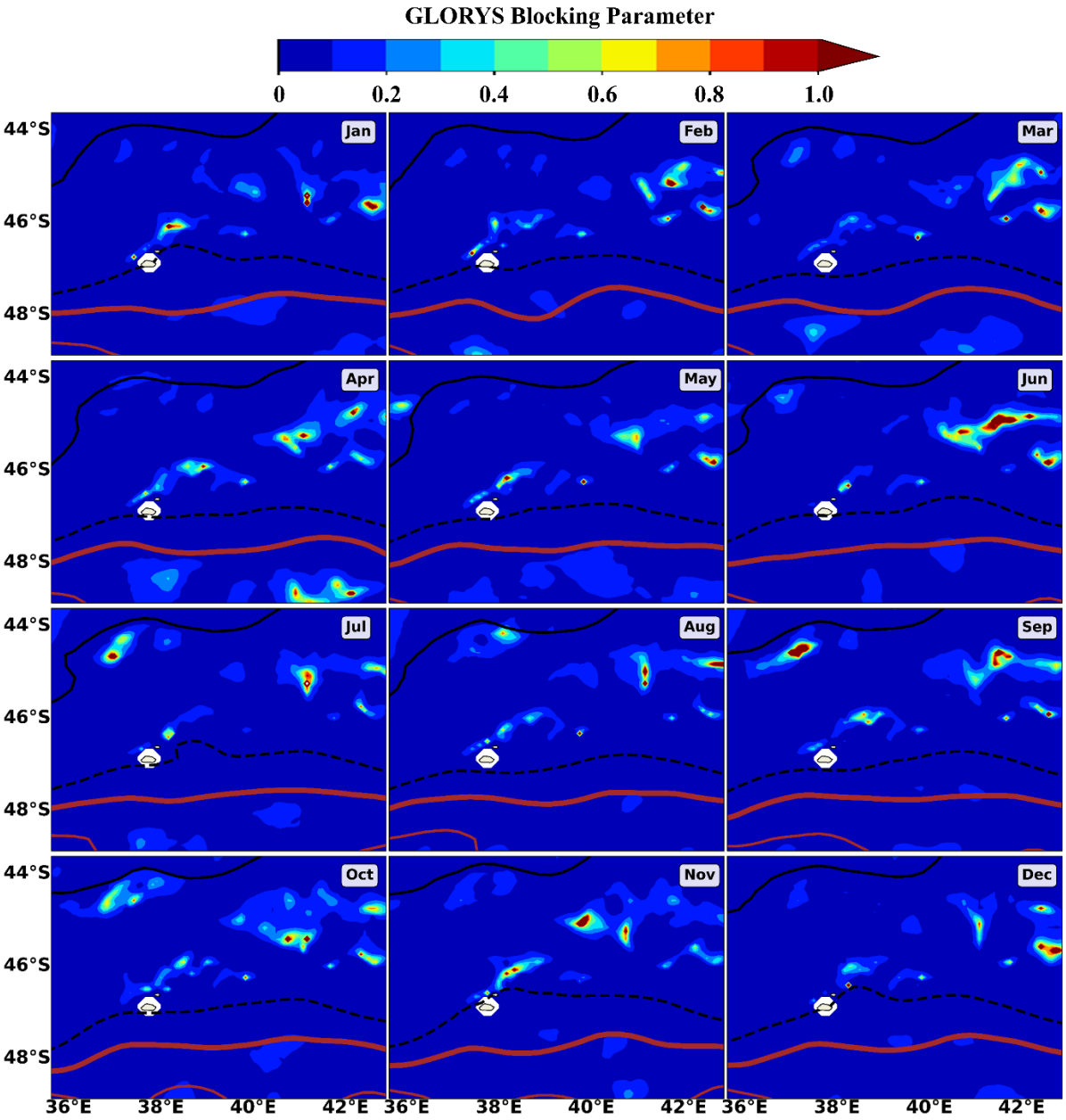

Figure 4.47: The monthly climatology of Blocking parameter (Bl) calculated using GLORYS median water depth of 3027.2 m, from January (Jan) to December (Dec) around the Prince Edward Islands from 1993 to 2020 using the GLORYS model output. The black solid and dashed lines represent the M-SAF and S-SAF, respectively. The solid thick and thinner brown lines represent the N-APF and M-APF, respectively. Areas shaded white denote regions of no data. These front positions were identified from satellite altimetry using ADT according to the process described by Sokolov and Rintoul (2002).

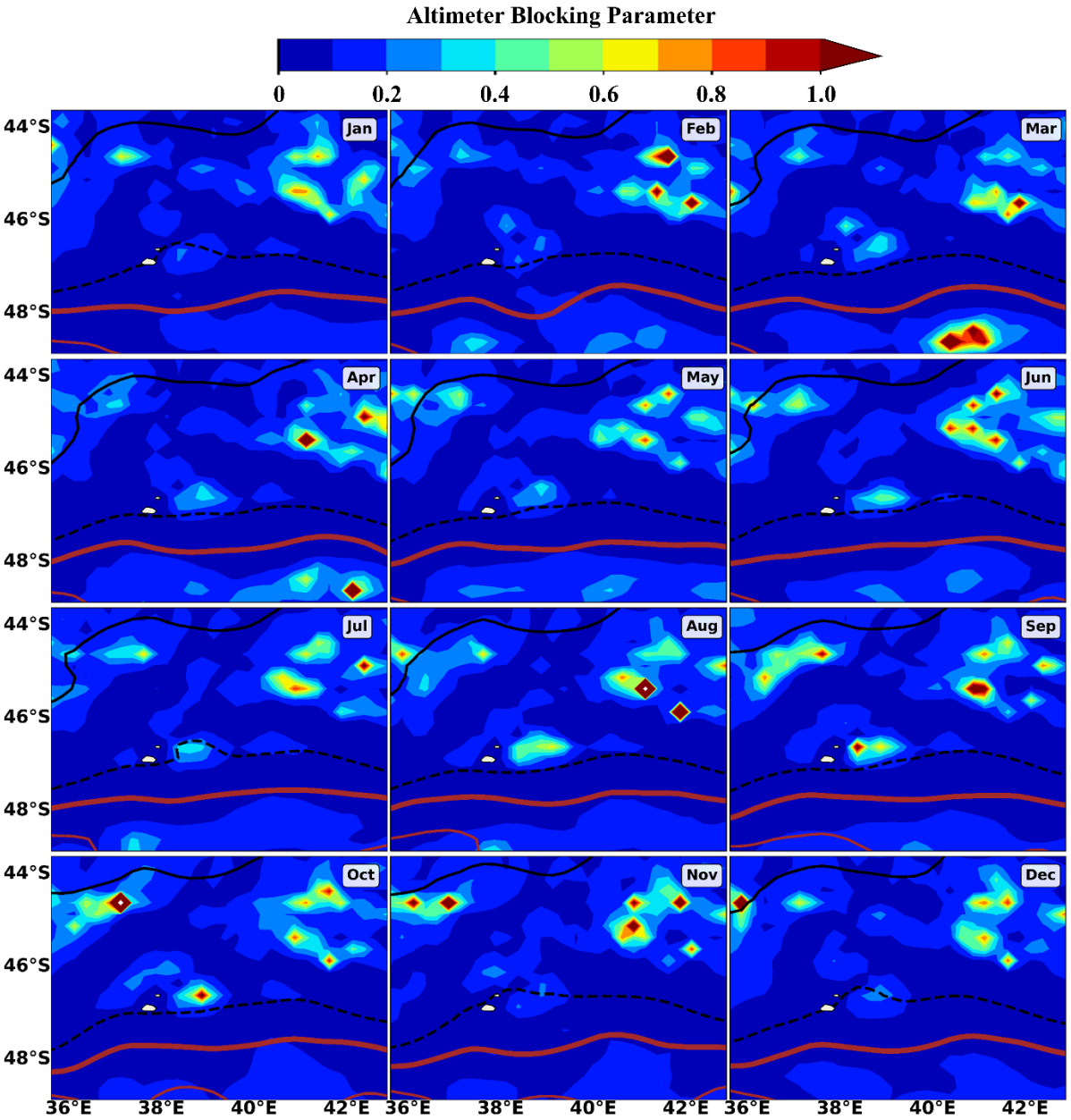

Figure 4.48: The monthly climatology of Blocking parameter (Bl) calculated using an average water depth of 2000 m, from January (Jan) to December (Dec) around the Prince Edward Islands from 1993 to 2022 using the daily reprocessed ADT satellite data and the GEBCO 2022 bathymetry data. The black solid and dashed lines represent the M-SAF and S-SAF, respectively. The solid thick and thinner brown lines represent the N-APF and M-APF, respectively. These front positions were identified from satellite altimetry using ADT according to the process described by Sokolov and Rintoul (2002).

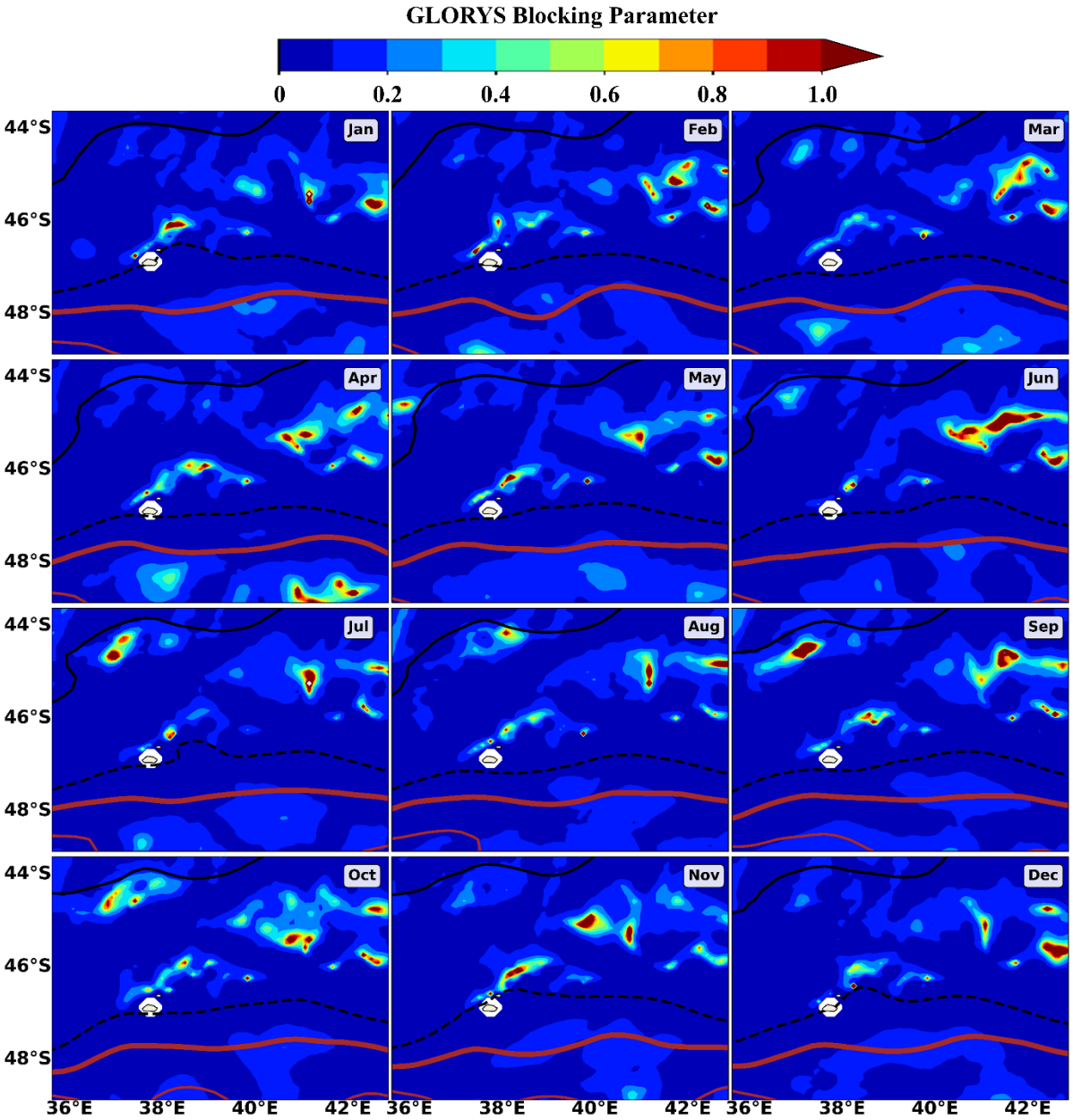

Figure 4.49: The monthly climatology of Blocking parameter (BI) calculated using an average water depth of 2000 m, from January (Jan) to December (Dec) around the Prince Edward Islands from 1993 to 2020 using the GLORYS model output. The black solid and dashed lines represent the M-SAF and S-SAF, respectively. The solid thick and thinner brown lines represent the N-APF and M-APF, respectively. Areas shaded white denote regions of no data. These front positions were identified from satellite altimetry using the ADT according to the process described by Sokolov and Rintoul (2002).

4.2.4 Rossby Radius of Deformation

The Rossby radius of deformation is used to indicate at which length scale Coriolis forces become as important as buoyancy forces (Gill, 1982). The Rossby radius was initially calculated for a barotropic ocean using GEBCO (*Figure 4.50*) and GLORYS (*Figure 4.51*) bathymetry data to describe to which degree the model could simulate the spatial variability of

the radii values. A very clear resemblance was observed between the two, with higher Rossby radii observed south of the PEIs and lower values to the north (*Figure 4.50; Figure 4.51*). This could be explained by the fact that south of the PEIs, the bottom depth is on average deeper (> 4000 m), while north of the PEIs, the bottom depth is on average much shallower (< 3000 m) (see the bathymetry map in Section 3.4; *Figure 3.7*). Prominent low Rossby radii were observed at three main sites; (1) in the localised region around the PEIs, (2) over a shallow bathymetric feature downstream of the PEIs, and (3) at the Del Cano Rise (*Figure 4.50; Figure 4.51*).

A barotropic ocean, is one in which density and pressure are solely dependent on depth, producing an approximately steady density flow throughout the water column (Marghany, 2021). Instead, a baroclinic ocean's density and pressure are impacted by several other factors such as wind stress, temperature and salinity changes, among other factors. The Rossby radius for a baroclinic ocean was investigated using the ATLAS data (see Section 3.4.7). These radii values were observed to be much lower (between 12 and 24 km) (*Figure 4.52*), than those observed for a barotropic ocean (*Figure 4.50; Figure 4.51*). Specifically, around the PEIs, the baroclinic Rossby radii values did not exceed 16 km (*Figure 4.52*). This is in agreement with Chelton et al. (1998) whereby the Rossby radius for a baroclinic ocean was described as having a large amount of latitudinal variabily, with values exceeding 200 km near the equator and those at higher latitudes measuring less than 10 km. These overall low radii values were suggested to be the primary result of the shallowed water depth due to the fact that the rossby radius of deformation claculation makes use of the Brunt–Väisälä frequency or buoyancy force (N(z)) which accounts for water depth (see Section 3.4.7).

As explained above, the low Rossby radii (barotropic and baroclinic), observed at the PEIs, both suggest that Coriolis forces become more important than buoyancy forces (Gill, 1982), which is the condition necessary for the formation and evolution of a Taylor column (White et al. 2007).

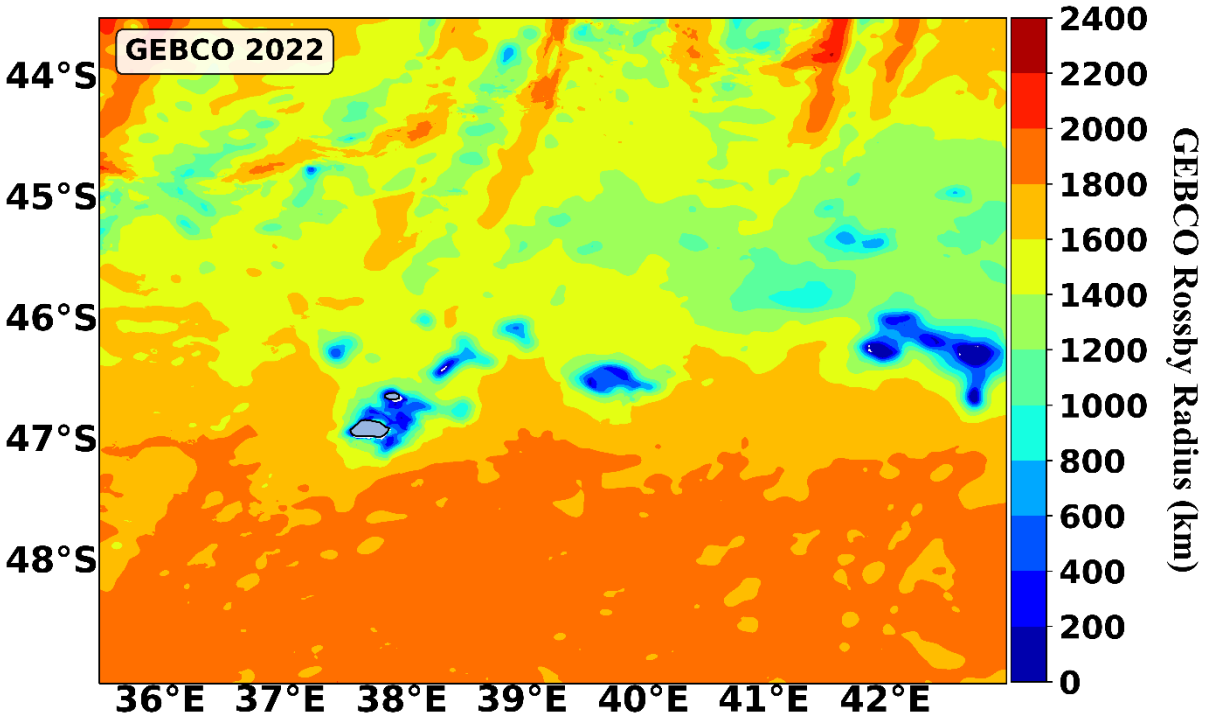

Figure 4.50: Rossby radius of deformation (km) for a barotropic ocean using the GEBCO 2022 bathymetry data around the Prince Edward Islands.

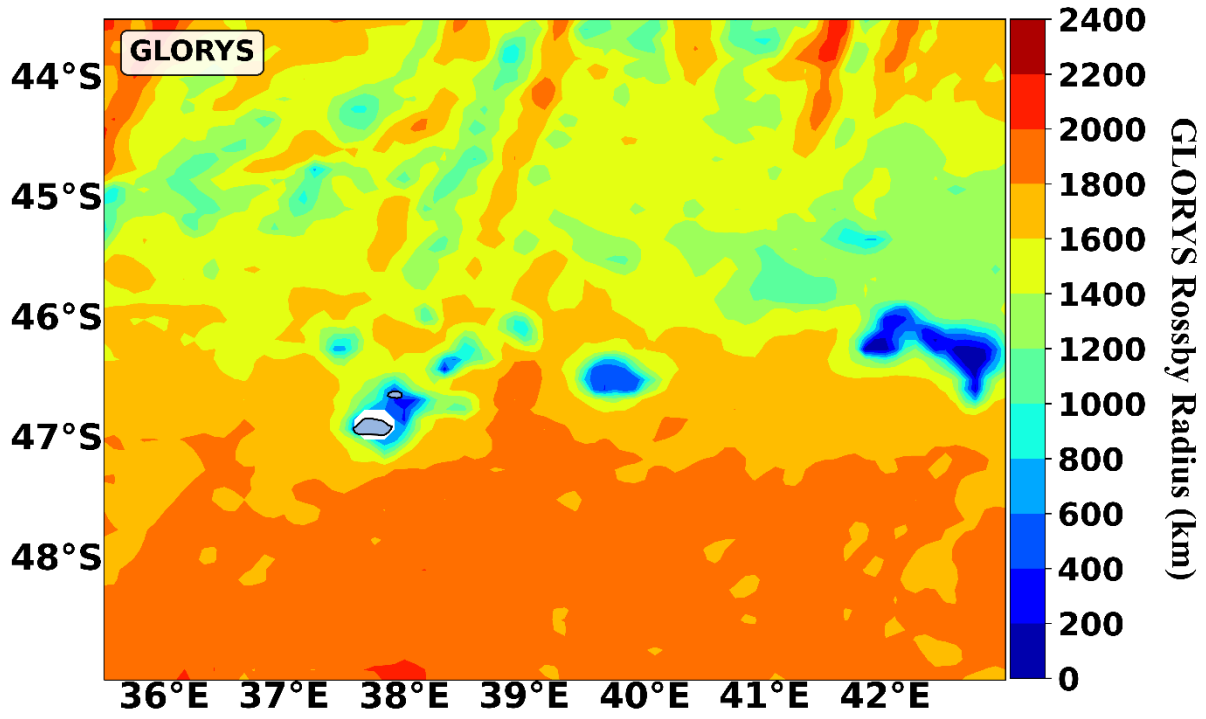

Figure 4.51: Rossby radius of deformation (km) for a barotropic ocean using the GLORYS bathymetry model output around the Prince Edward Islands. Areas shaded white denote regions of no data.

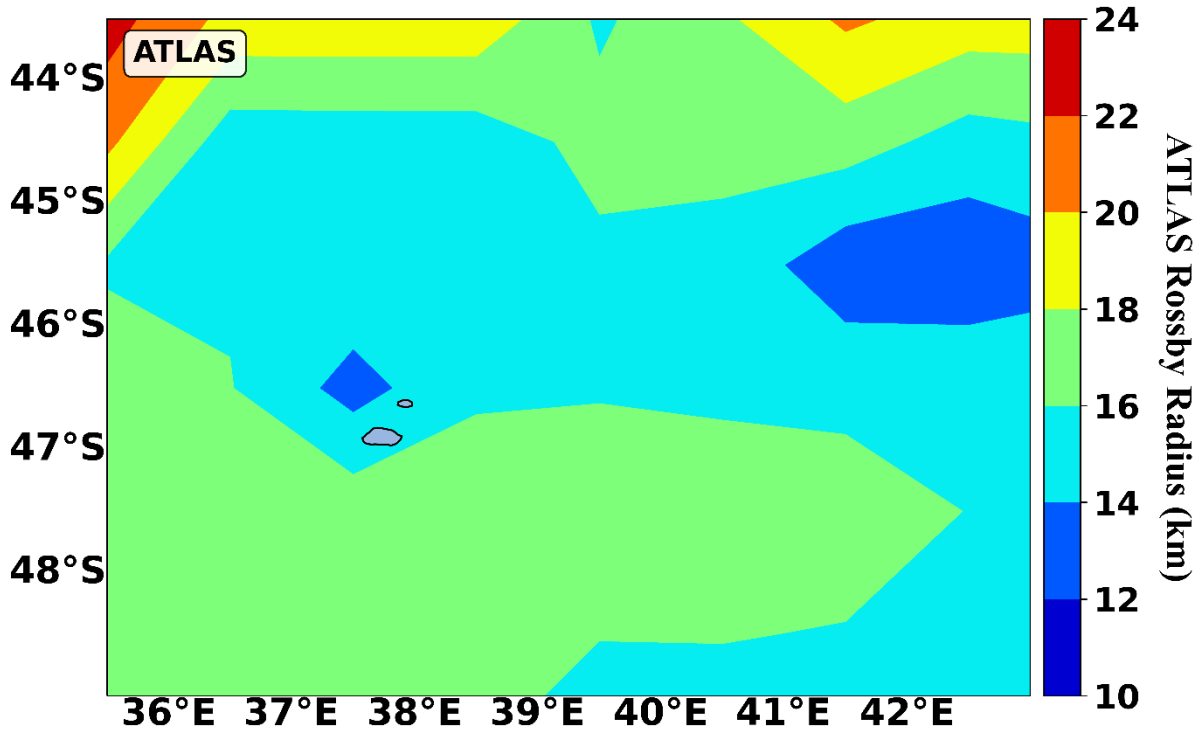

Figure 4.52 Rossby radius of deformation (km) for a baroclinic ocean using the radii values in the ATLAS dataset as described in (Chelton et al. 1998) around the Prince Edward Islands.

4.2.5 Meridional and Zonal Current Speed Climatologies

The meridional and zonal monthly climatologies of current speed, extracted along 37.90 ºE, (*Figure 5.53; Figure 5.54*) revealed southwestward flow directly north of the PEIs, while south of the Islands northeastward flow was observed (*Figure 5.54; Figure 5.53*). This is indicative of an anticyclonic flow pattern around the PEI plateau, which would agree with the circulation patterns that are typical of Taylor columns (White et al. 2007). However, as previously described in Section 4.2.3, in a strafied ocean a Taylor column may not extend to the ocean surface and instead form a "Taylor cone" (White et al. 2007). This may be the case for this study due to the fact that the anticlockwise flow pattern did not have a surface expression, instead it only extended to ~ 4 m below the surface with the GLORYS dataset (*Figure 5.53; Figure 5.54*). Additionally, the frontal identification in the meridional and zonal monthly climatologies (*Figure 5.53; Figure 5.54*) came from altimetry data, which was much coarser (~ 28 km) (Taburet et al. 2021) than GLORYS, suggesting that the altimetry fronts may not have coincided with the model's simulated fronts. This could imply that the strong eastward velocity signal, to the south of PEI, (*Figure 5.54*) may have been the presence of the S-SAF at the PEIs.

While the northward flow directly south of the PEI was stronger in the upper 300 meters of the water column from April to July, the southward flow, north of the island, was strongest from January to May and weakest between June and December (*Figure 4.53*). Additionally, there appears to be a region of southward flow, south of the islands (~ 49 °S) which was not observed to have any clear seasonal signal. The eastward flow, south of PEI, had a larger southward extension between July and October, whereas the westward flow, north of the island, was strongest from December until May, and weakest between June and November (*Figure 4.54*). The overlap between the strong westward and southward flow, north of the PEI, was indicative that the anticyclonic circulation around the PEI plateau was strongest during the late summer and autumn periods (January to May). This suggests that it would be during this period (January to May) that the signature of a possible Taylor column/Taylor cone would be most prominent.

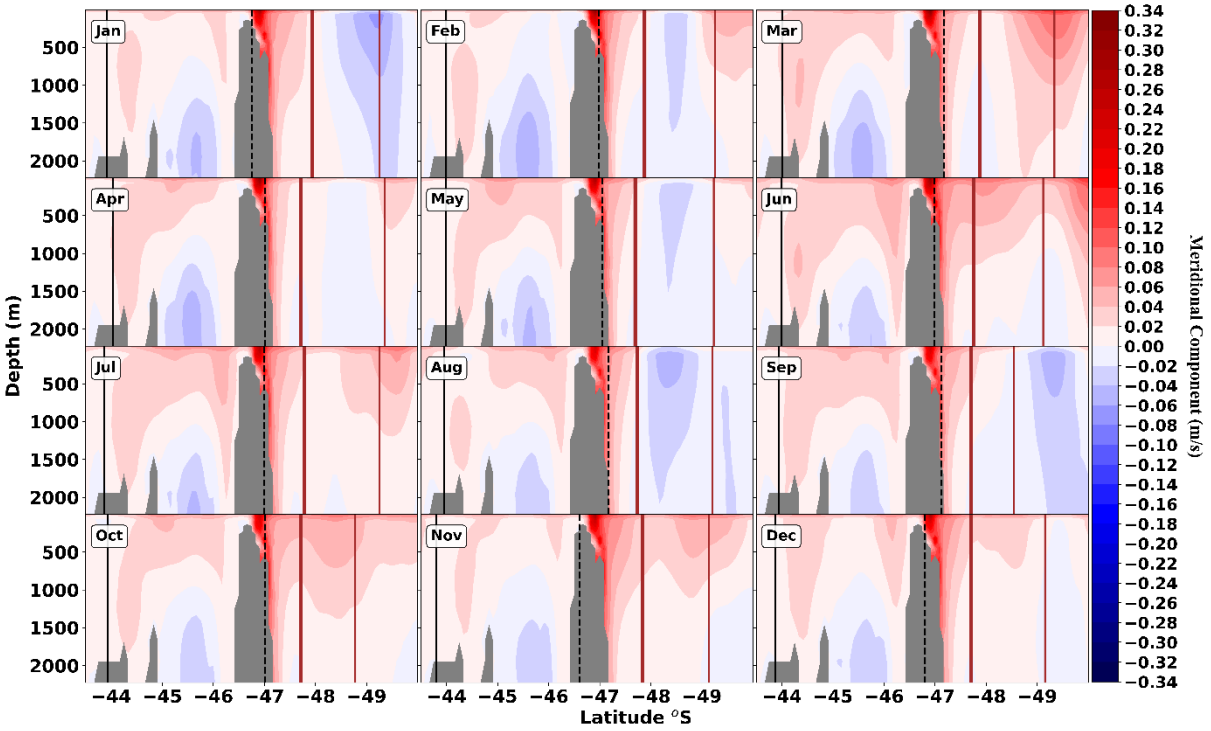

Figure 5.53: The monthly climatology of the meridional velocity component (m s^{-1}), extracted along the longitudinal position of 37.90 °E, from January (Jan) to December (Dec) between 1993 and 2020 using the GLORYS model output. The black solid and dashed vertical lines represent the M-SAF and S-SAF, respectively. The solid thick and thinner brown vertical lines represent the N-APF and M-APF, respectively. Areas shaded grey denote the bathymetry. These front positions were identified from satellite altimetry using ADT according to the process described by Sokolov and Rintoul (2002).

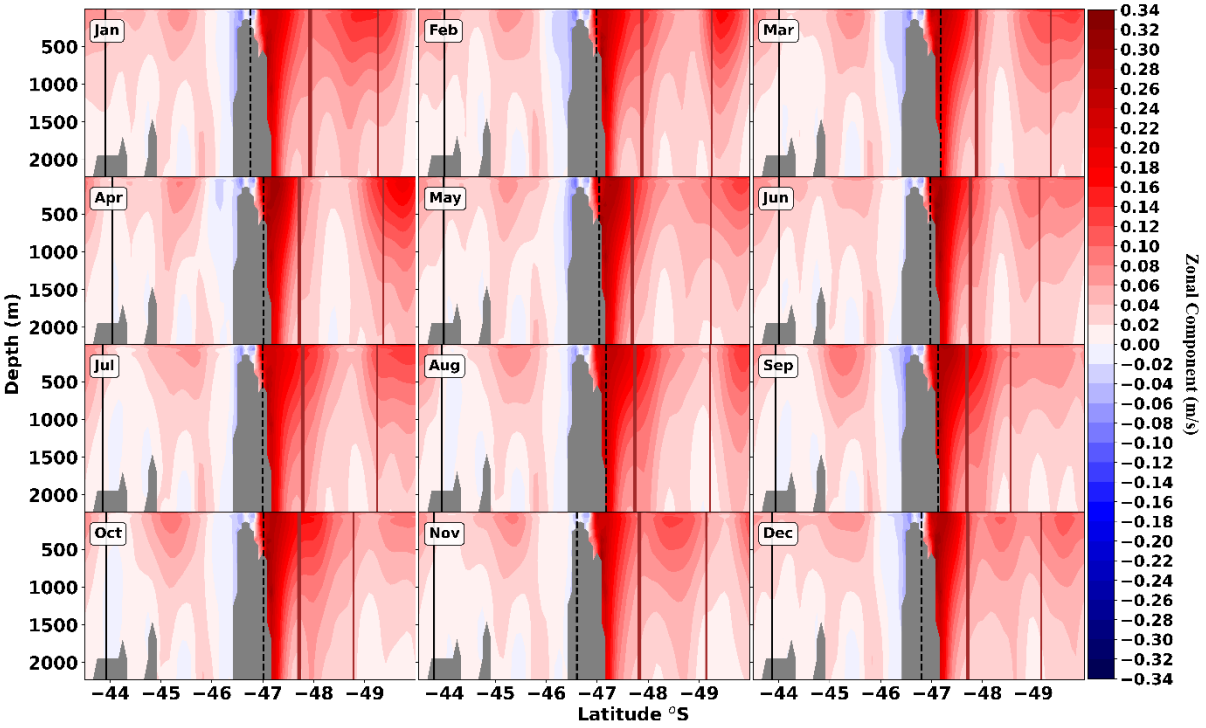

Figure 5.54: The monthly climatology of the meridional velocity component (m s^{-1}), extracted along the longitudinal position of 37.90 °E from January (Jan) to December (Dec) between 1993 and 2020 using the GLORYS model output. The black solid and dashed vertical lines represent the M-SAF and S-SAF, respectively. The solid thick and thinner brown vertical lines represent the N-APF and M-APF, respectively. Areas shaded grey denote the bathymetry. These front positions were identified from satellite altimetry using ADT according to the process described by Sokolov and Rintoul (2002).

Chapter 5. Conclusion and Future Recommendations

The objectives of this study were to analyse the various surface and sub-surface hydrographic parameters around the PEIs and the drivers thereof, using *in situ* data, satellite data, reanalysis data and the high resolution GLORYS model. The purpose of this was to establish the degree of accuracy to which the model could reproduce known oceanographic variability around the Islands, as well as its ability to simulate the possible existence of a Taylor column at the Islands.

The mean ocean surface currents simulated by GLORYS around the PEIs were in good agreement with the flow patterns observed by satellite, with both providing a good representation of the known mean eastward flow in the region surrounding the PEIs, throughout the year. The bifurcation of the ACC upon approaching the shallowing bathymetry of the Islands (Ansorge et al. 2010), was overestimated by GLORYS resulting in the simulation of faster current speeds downstream of the Islands. SSH was largely underestimated by GLORYS owing to the fact that GLORYS and satellite data made use of different MDT datasets for the calculation of SSH.

On a climatological scale, GLORYS captured both the large-scale temperature and salinity variations, and their respective seasonal cycles throughout the water column, reasonably well. The temperature biases were, however, larger than the salinity biases, suggesting either GLORYS is more capable of reproducing the salinity variability than temperature variability, or the less available *in situ* salinity data misconstrues the supposed 'true' salinity patterns being observed, resulting in a better agreement between the *in situ* and model data. Additionally, the sub-surface biases were greater than those at the surface for both temperature and salinity, inferring that GLORYS performed better at the surface (biases were smaller) because there was more surface data (*in situ*, satellite and reanalysis) available for assimilation into the model (Russo et al. 2022; Drévillon et al. 2021a) as opposed to the fewer *in situ* data points and lack of satellite data at 200 m. These large-scale patterns and biases captured by GLORYS were not isolated to just the PEIs (see Appendix Figures), suggesting that GLORYS could likely be suitable for long-term time series studies across the entire Southern Ocean.

GLORYS simulated all five water masses throughout time. These water masses are described as sub-Antarctic Surface Water (SASW), Antarctic Surface Water (AASW), Antarctic Intermediate Water (AAIW), Circumpolar Deep Water (CDW) and Antarctic Bottom Water

(AABW) (van den Berg et al. 2021; Lamont et al. 2019). Thus, due to GLORYS's capability of reproducing the structure of the water column fairly well, the model can now be used alongside satellite and *in situ* data, for the PEI surrounding region, resulting in the enhancement of our ability to investigate the hydrographic variability of the entire water column.

GLORYS at event-scale, generally captured the water column structure reasonably well, but sub-surface temperatures were overall higher and sub-surface salinities were overall lower than those observed by *in situ* CTD data. The 2013, 2014 and 2015 cyclonic and anticyclonic eddies, were simulated by GLORYS, however the model failed to accurately reproduce the mesoscale features in terms of location, size and intensity. However, care should be taken when using GLORYS for event-scale investigations since the model appears to struggle in simulating smaller scale variability, as similarly observed by Russo et al. (2022). This is suggested to be due to the fact that the model, although forced atmospherically (ECMWF ERA-Interim reanalysis and ERA5, see Section 3.3.2), may not have a feedback mechanism to consistently update and simulate the interaction between the atmosphere and the ocean's surface.

Perissinotto and Duncombe Rae (1990) performed a dimensional analysis and proposed that a Taylor column could exist for majority of the flow conditions at the islands. The use of the GLORYS model allowed for the calculation of several non-dimensional numbers (Rossby number, Reynolds number, Blocking parameter and Rossby radius of deformation), which aided in assessing whether the flow conditions were suitable for the formation of a Taylor column/Taylor cone at the PEIs. Each of these numbers were within the respective thresholds presented across multiple studies, indicative that a stationary anticyclonic eddy, associated with the Taylor column/Taylor cone, could be situated in the inter-island region over Prince Edward Island, while a cyclonic eddy is proposed to be advected downstream of the Islands. Other parameters (Brunt–Väisälä frequency and Burger number) could have also been used to investigate Taylor column formation, however they were not calculated in the current study because it would have only been possible to produce these using GLORYS, therefore not allowing for an *in situ* comparison. A future study is planned to further this investigation using these parameters when more *in situ* data with a higher spatial resolution becomes available within the PEI vicinity.

A recommendation for future studies is to perform an analysis using shorter timescales and smaller spatial scales on surface and sub-surface oceanographic data around the PEIs, which could help improve our understanding of the exact formation location and evolution of a Taylor

column/Taylor cone. One of the major limitations faced by the current study was the complete misrepresentation of bathymetry simulated by GLORYS. The use of a regional ocean model which assimilates and simulates accurate and higher resolution bathymetry for the surrounding PEI region, could result in the improvement of the simulated hydrographic parameters and a more accurate simulation of current flow patterns which would allow for a more definitive answer on the existence and location of a Taylor column/Taylor cone at the PEIs.

References

Alpert, P., Osetinsky, I., Ziv, B. and Shafir, H., **2004**. A new seasons definition based on classified daily synoptic systems: an example for the eastern Mediterranean. International Journal of Climatology: A Journal of the Royal Meteorological Society, 24(8), pp.1013-1021.

Amante, C. and Eakins, B., **2009**. ETOPO1 1 Arc-Minute Global Relief Model: Procedures, Data Sources and Analysis. NOAA Technical Memorandum NESDIS NGDC, pp. 1-19.

Anderson, R.F., Chase, Z., Fleisher, M.Q. and Sachs, J., **2002**. The Southern Ocean's biological pump during the last glacial maximum. Deep Sea Research Part II: Topical Studies in Oceanography, 49(9-10), pp.1909-1938.

Anon., 2022. The GEBCO_2022 Grid. [Online] Available at: https://www.gebco.net/data_and_products/gridded_bathymetry_data/gebco_2022/

Ansorge, I.J. and Lutjeharms, J.R., **2005**. Direct observations of eddy turbulence at a ridge in the Southern Ocean. Geophysical Research Letters, 32(14).

Ansorge, I.J., Durgadoo, J.V. and Treasure, A.M., **2014**. Sentinels to climate change. The need for monitoring at South Africa's Subantarctic laboratory. South African Journal of Science, 110(1-2), pp.1-4.

Ansorge, IJ and Lutjeharms, J.R.E., **2000**. Twenty-five years of physical oceanographic research at the Prince Edward Islands. South African Journal of Science, 96(11-12), pp.557-566.

Ansorge, I.J. and Lutjeharms, J.R.E., **2002**. The hydrography and dynamics of the ocean environment of the Prince Edward Islands (Southern Ocean). Journal of Marine Systems, 37(1-3), pp.107-127.

Ansorge, I.J., Pakhomov, E.A., Kaehler, S., Lutjeharms, J.R. and Durgadoo, J.V., **2010**. Physical and biological coupling in eddies in the lee of the South-West Indian Ridge. Polar Biology, 33, pp.747-759.

Armitage, T.W., Kwok, R., Thompson, A.F. and Cunningham, G., **2018**. Dynamic topography and sea level anomalies of the Southern Ocean: Variability and teleconnections. Journal of Geophysical Research: Oceans, 123(1), pp.613-630.

Atkinson, C.P., Rayner, N.A., Kennedy, J.J. and Good, S.A., **2014**. An integrated database of ocean temperature and salinity observations. Journal of Geophysical Research: Oceans, 119(10), pp.7139-7163.

Chapman, C.C., Lea, M.A., Meyer, A., Sallée, J.B. and Hindell, M., **2020**. Defining Southern Ocean fronts and their influence on biological and physical processes in a changing climate. Nature Climate Change, 10(3), pp.209-219.

Chapman, D.C. and Haidvogel, D.B., **1992**. Formation of Taylor caps over a tall isolated seamount in a stratified ocean. Geophysical & Astrophysical Fluid Dynamics, 64(1-4), pp.31-65.

Chelton, D.B., DeSzoeke, R.A., Schlax, M.G., El Naggar, K. and Siwertz, N., **1998**. Geographical variability of the first baroclinic Rossby radius of deformation. Journal of Physical Oceanography, 28(3), pp.433-460.

Cherel, Y., **2020**. A review of Southern Ocean squids using nets and beaks. Marine Biodiversity, 50(6), p.98.

Chown, S. and Froneman, P.W. eds., **2008**. The Prince Edward Islands: land-sea interactions in a changing ecosystem. African Sun Media.

Cunningham, S.A., **2005**. Southern ocean circulation. Archives of natural history, 32(2), pp.265-280.

de Boyer Montégut, C., Madec, G., Fischer, A.S., Lazar, A. and Iudicone, D., **2004**. Mixed layer depth over the global ocean: An examination of profile data and a profile-based climatology. Journal of Geophysical Research: Oceans, 109(C12).

Deacon, G.E.R., **1937**. The hydrology of the Southern Ocean. Discovery Rep., 15, pp.3-122.

Derkani, M.H., Alberello, A., Nelli, F., Bennetts, L.G., Hessner, K.G., MacHutchon, K., Reichert, K., Aouf, L., Khan, S. and Toffoli, A., **2021**. Wind, waves, and surface currents in the Southern Ocean: observations from the Antarctic Circumnavigation Expedition. Earth System Science Data, 13(3), pp.1189-1209.

Drévillon, M., Fernandez, E. and Lellouche, J.M, **2021a**. PRODUCT USER MANUAL: For the Global Ocean Physical Multi Year Product. [Online] Available at: https://catalogue.marine.copernicus.eu/documents/PUM/CMEMS-GLO-PUM-001-030.pdf

Drévillon, M., Lellouche, J.M, Régnier, C., Garric, G., Bricaud, C., Hernandez, O. and Bourdallé-Badie, R., **2021b**. QUALITY INFORMATION DOCUMENT: For Global Ocean Reanalysis Products. [Online] Available at: https://catalogue.marine.copernicus.eu/documents/QUID/CMEMS-GLO-QUID-001-030.pdf

Dunn, J., **2014**. CSIRO. [Online] Available at: https://www.marine.csiro.au/~dunn/cars2009/index.html

Froneman, P.W., Ansorge, I.J., Vumazonke, L., Gulekana, K., Bernard, K., Webb, A.M., Leukes, W., Risien, C.M., Thomalla, S., Hermes, J. and Knott, M., **2002**. Physical and biological variability in the Antarctic Polar Frontal Zone: report on research cruise 103 of the MV SA Agulhas: news & views. South African Journal of Science, 98(11), pp.534-536.

Fuentes, O.V., **2009**. Kelvin's discovery of Taylor columns. European Journal of Mechanics-B/Fluids, 28(3), pp.469-472.

Gill, A.E., **1982**. Atmosphere-ocean dynamics (Vol. 30). Academic press.

Gille, S.T., **1994**. Mean sea surface height of the Antarctic Circumpolar Current from Geosat data: Method and application. Journal of Geophysical Research: Oceans, 99(C9), pp.18255-18273.

Gille, S.T., **2008**. Decadal-scale temperature trends in the Southern Hemisphere ocean. Journal of Climate, 21(18), pp.4749-4765.

Gille, S.T., **2014**. Meridional displacement of the Antarctic circumpolar current. Philosophical Transactions of the Royal Society A: Mathematical, Physical and Engineering Sciences, 372(2019), p.20130273.

Grid, T. G., **2022**. [Online] Available at: https://www.gebco.net/data_and_products/gridded_bathymetry_data/gebco_2022/documents/GEBCO_2022_Grid.pdf

Haidvogel, D.B., Beckmann, A., Chapman, D.C. and Lin, R.Q., **1993**. Numerical simulation of flow around a tall isolated seamount. Part II: Resonant generation of trapped waves. Journal of physical oceanography, 23(11), pp.2373-2391.

Helmenstine, A., **2019**. Convert Temperature from Kelvin to Celsius and Back. [Online] Available at: https://www.thoughtco.com/convert-kelvin-to-celsius-609233

Hogg, N.G., **1973**. On the stratified Taylor column. Journal of Fluid Mechanics, 58(3), pp.517-537.

Hogg R. V., McKean J. and Craig A. T. **2014**. Introduction to mathematical statistics (7th Edition). Harlow, Essex: Pearson Education

Hughes, C.W., **2005**. Nonlinear vorticity balance of the Antarctic Circumpolar Current. Journal of geophysical research: Oceans, 110(C11).

Huppert, H.E., **1975**. Some remarks on the initiation of inertial Taylor columns. Journal of Fluid Mechanics, 67(2), pp.397-412.

Jousset, S. and Mulet, S., **2020**. New Mean Dynamic Topography of the Black Sea and Mediterranean Sea from altimetry, gravity and in-situ data. Presentation Ocean Surface Topography Science Team (OSTST). [Online] Available at: https://meetings.aviso.altimetry.fr/fileadmin/user_upload/tx_ausyclsseminar/files/OSTST2020_JOUSSET_MULET_MDT.pdf

Karas, C., Goldstein, S.L. and deMenocal, P.B., **2019**. Evolution of Antarctic Intermediate Water during the Plio-Pleistocene and implications for global climate: Evidence from the South Atlantic. Quaternary Science Reviews, 223, p.105945.

Klemas, V., **2011**. Remote sensing of sea surface salinity: an overview with case studies. Journal of Coastal Research, 27(5), pp.830-838.

Lamont, T. and Toolsee, T., **2022**. Spatial and Seasonal Variations of the Island Mass Effect at the Sub-Antarctic Prince Edward Islands Archipelago. Remote Sensing, 14(9), p.2140.

Lamont, T., van den Berg, M.A., Tutt, G.C.O. and Ansorge, I.J., **2019**. Impact of deep-ocean eddies and fronts on the shelf seas of a sub-Antarctic Archipelago: The Prince Edward Islands. Continental Shelf Research, 177, pp.1-14.

Legeais, J.F., **2021**. Algorithm Theoretical Basis Document. [Online]. Available at: https://datastore.copernicus-climate.eu/documents/satellite-sea-level/vDT2021/D1.SL.2-v2.0_ATBD_of_v2DT2021_SeaLevel_products_v1.1_APPROVED_Ver1.pdf

Lenton, A. and Matear, R.J., **2007**. Role of the southern annular mode (SAM) in Southern Ocean CO2 uptake. Global Biogeochemical Cycles, 21(2).

Li, S., Cai, W. and Wu, L., **2021**. Weakened Antarctic dipole under global warming in CMIP6 models. Geophysical Research Letters, 48(16), p.e2021GL094863.

Locarnini, M.M., Mishonov, A.V., Baranova, O.K., Boyer, T.P., Zweng, M.M., Garcia, H.E., Seidov, D., Weathers, K., Paver, C. and Smolyar, I., **2019**. World ocean atlas 2018, volume 1: Temperature. A. Mishonov, Technical Editor. NOAA Atlas NESDIS 81, pp.52.

Louise Allan, E., William Froneman, P., Durgadoo, J.V., McQuaid, C.D., Ansorge, I.J. and Richoux, N.B., **2013**. Critical indirect effects of climate change on sub-Antarctic ecosystem functioning. Ecology and Evolution, 3(9), pp.2994-3004.

Madec, G., **2016**. NEMO ocean engine, version 3.6 stable. Note du Pole de modelisation de l'Institut Pierre-Simon Laplace, 27.

Ma, J., Song, J., Li, X., Wang, Q. and Zhong, G., **2021**. Multidisciplinary indicators for confirming the existence and ecological effects of a Taylor column in the Tropical Western Pacific Ocean. Ecological Indicators, 127, p.107777.

Marghany, M., **2021**. Chapter 2 - Quantization of ocean dynamics. Nonlinear Ocean Dynamics: Synthetic aperture radar. Elsevier, pp. 45-84.

Marshall, J. and Plumb, R.A., **2013**. Atmosphere, ocean and climate dynamics: an introductory text. Academic Press.

Marshall, J. and Speer, K., **2012**. Closure of the meridional overturning circulation through Southern Ocean upwelling. Nature geoscience, 5(3), pp.171-180.

Martin, S. and Drucker, R., **1997**. The effect of possible Taylor columns on the summer ice retreat in the Chukchi Sea. Journal of Geophysical Research: Oceans, 102(C5), pp.10473-10482.

Mayeweski, P.A., Bracegirdle, T., Goodwin, I., Schneider, D., Bertler, N.A.N., Birkel, S., Carleton, A., England, M.H., Kang, J.H., Khan, A. and Russell, J., **2015**. Potential for Southern Hemisphere climate surprises. Journal of Quaternary Science, 30(5), pp.391-395.

McKenna, S., Santoso, A., Gupta, A.S., Taschetto, A.S. and Cai, W., **2020**. Indian Ocean Dipole in CMIP5 and CMIP6: characteristics, biases, and links to ENSO. Scientific reports, 10(1), pp.1-13.

Mélice, J.L., Lutjeharms, J.R., Goosse, H., Fichefet, T. and Reason, C.J., **2005**. Evidence for the Antarctic circumpolar wave in the sub-Antarctic during the past 50 years. Geophysical research letters, 32(14).

Mélice, J.L., Lutjeharms, J.R.E., Rouault, M. and Ansorge, I.J., **2003**. Sea-surface temperatures at the sub-Antarctic islands Marion and Gough during the past 50 years. South African Journal of Science, 99(7), pp.363-366.

Merchant, C.J., Embury, O., Bulgin, C.E., Block, T., Corlett, G.K., Fiedler, E., Good, S.A., Mittaz, J., Rayner, N.A., Berry, D. and Eastwood, S., **2019**. Satellite-based time-series of sea-surface temperature since 1981 for climate applications. Scientific data, 6(1), p.223.

Mininni, P.D., Alexakis, A. and Pouquet, A., **2009**. Scale interactions and scaling laws in rotating flows at moderate Rossby numbers and large Reynolds numbers. Physics of Fluids, 21(1), p.015108.

Morrison, A.K., Frölicher, T.L. and Sarmiento, J.L, **2015**. Upwelling in the Southern Ocean. Physics Today, 68(1), pp. 27-32.

Morrow, R., Ward, M.L., Hogg, A.M. and Pasquet, S., **2010**. Eddy response to Southern Ocean climate modes. Journal of Geophysical Research: Oceans, 115(C10).

Nardelli, B.B., Pisano, A. and Sammartino, M., **2021**. QUALITY INFORMATION DOCUMENT: For Multi Observation Global Ocean Sea Surface Salinity and Sea Surface Density Product. [Online] Available at: https://catalogue.marine.copernicus.eu/documents/QUID/CMEMS-MOB-QUID-015-013.pdf

Nigam, S. and Baxter, S., **2015**., Teleconnections. In: Encyclopedia of Atmospheric Sciences (2nd Editions). Vol 3, pp. 90–109. Academic Press.

NOAA, **2021**. How is bathymetric data used? National Ocean Service website: https://oceanservice.noaa.gov/facts/bathyuses.html#:~:text=Bathymetric%20maps%20can%20help%20scientists,assist%20in%20conservation%20and%20monitoring.

Owens, W.B. and Hogg, N.G., **1980**. Oceanic observations of stratified Taylor columns near a bump. Deep Sea Research Part A. Oceanographic Research Papers, 27(12), pp.1029-1045.

Pardo, P.C., Pérez, F.F., Velo, A. and Gilcoto, M., **2012**. Water masses distribution in the Southern Ocean: Improvement of an extended OMP (eOMP) analysis. Progress in Oceanography, 103, pp.92-105.

Pearson, K., **1895**. VII. Note on regression and inheritance in the case of two parents. proceedings of the royal society of London, 58(347-352), pp.240-242.

Perfect, B., Kumar, N. and Riley, J.J., **2018**. Vortex structures in the wake of an idealized seamount in rotating, stratified flow. Geophysical Research Letters, 45(17), pp.9098-9105.

Perissinotto, R. and Rae, C.D., **1990**. Occurrence of anticyclonic eddies on the Prince Edward Plateau (Southern Ocean): effects on phytoplankton biomass and production. Deep Sea Research Part A. Oceanographic Research Papers, 37(5), pp.777-793.

Perissinotto, R., Rae, C.D., Boden, B.P. and Allanson, B.R., **1990**. Vertical stability as a controlling factor of the marine phytoplankton production at the Prince Edward Archipelago (Southern Ocean). Marine Ecology Progress Series, pp.205-209.

Proudman, J., **1916**. On the motion of solids in a liquid possessing vorticity. Proceedings of the Royal Society of London. Series A, Containing Papers of a Mathematical and Physical Character, 92(642), pp.408-424.

Quilty, P.G., **2007**. Origin and evolution of the sub-Antarctic islands: the foundation. In Papers and Proceedings of the Royal Society of Tasmania, 141(1), pp. 35-58.

Rajani, B., Kandasamy, A. & Majumdar, S., **2009**. Numerical simulation of laminar flow past a circular cylinder. Applied Mathematical Modelling, 33(3), pp. 1228-1247.

Rehm, B., Haghshenas, A., Paknejad, A.S. and Schubert, J., **2008**. Situational problems in MPD. In Managed Pressure Drilling, pp. 39-80. Gulf Publishing Company.

Rintoul, S.R., Chown, S.L., DeConto, R.M., England, M.H., Fricker, H.A., Masson-Delmotte, V., Naish, T.R., Siegert, M.J. and Xavier, J.C., **2018**. Choosing the future of Antarctica. Nature, 558(7709), pp.233-241.

Rintoul, S.R., Hughes, C.W. and Olbers, D., **2001**. The Antarctic circumpolar current system. In International Geophysics, 77, pp. 271-302. Academic Press.

Rintoul, S.R. and Garabato, A.C.N., **2013**. Dynamics of the Southern Ocean circulation. In International geophysics, 103, pp. 471-492. Academic Press.

Roden, G.I., **1987**. Effect of seamounts and seamount chains on ocean circulation and thermohaline structure. Seamounts, islands, and atolls, 43, pp.335-354.

Rouault, M., Mélice, J.L., Reason, C.J. and Lutjeharms, J.R., **2005**. Climate variability at Marion Island, Southern Ocean, since 1960. Journal of Geophysical Research: Oceans, 110(C5).

RSA, S. A., **2013**. Government Notice 426. Declaration of the Prince Edward Islands Marine Protected Area in terms of section 43(1) of the Marine Living Resources Act, 1998 (Act No. 18 of 1998). South Africa.

Rudolph, E.M., Hedding, D.W., De Bruyn, P.J. and Nel, W., **2022**. An open access geospatial database for the sub-Antarctic Prince Edward Islands. South African Journal of Science, 118(9-10), pp.1-8.

Russo, C.S., Veitch, J., Carr, M., Fearon, G. and Whittle, C., **2022**. An intercomparison of global reanalysis products for Southern Africa's major oceanographic features. Frontiers in Marine Science, 9, p.284.

Shangheta, A., **2020**. Long-term climate variability at the Prince Edward Islands in the Southern Ocean. Masters. Thesis. University of Cape Town.

Shi, J.R., Xie, S.P. and Talley, L.D., **2018**. Evolving relative importance of the Southern Ocean and North Atlantic in anthropogenic ocean heat uptake. Journal of Climate, 31(18), pp.7459-7479.

Sigman, D.M. and Boyle, E.A., **2000**. Glacial/interglacial variations in atmospheric carbon dioxide. Nature, 407(6806), pp.859-869.

Smith, V.R., **2002**. Climate change in the sub-Antarctic: an illustration from Marion Island. Climatic Change, 52(3), pp.345-357.

Sokolov, S. and Rintoul, S.R., **2002**. Structure of Southern Ocean fronts at 140 E. Journal of Marine Systems, 37(1-3), pp.151-184.

Sokolov, S. and Rintoul, S.R., **2009**. Circumpolar structure and distribution of the Antarctic Circumpolar Current fronts: 1. Mean circumpolar paths. Journal of Geophysical Research: Oceans, 114(C11).

Sumner, P.D., Meiklejohn, K.I., Boelhouwers, J.C. and Hedding, D.W., **2004**. Climate change melts Marion Island's snow and ice. South African Journal of Science, 100(7), pp.395-398.

Taburet, G., Mertz, F. and Legeais, J.F., 2021. Product User Guide and Specification. [Online] Available at: https://www.cen.uni-hamburg.de/en/icdc/data/ocean/docs-ocean/sea-level-aviso-cmems-product-users-guide-for-dt2021.pdf

Taschetto, A.S. and Wainer, I., **2006**. Proceedings of 8 ICSHMO: HAS SAO BEEN DECREASING OVER THE SOUTHERN OCEAN? p. 635-638. Available at: http://mtc-m16b.sid.inpe.br/col/cptec.inpe.br/adm_conf/2005/10.31.17.38/doc/635-638.pdf

Taylor, G.I., **1917**. Motion of solids in fluids when the flow is not irrotational. Proceedings of the Royal Society of London. Series A, Containing Papers of a Mathematical and Physical Character, 93(648), pp.99-113.

Taylor, G.I., **1923**. Experiments on the motion of solid bodies in rotating fluids. Proceedings of the Royal Society of London. Series A, Containing Papers of a Mathematical and Physical Character, 104(725), pp.213-218.

Toolsee, **2021**. Interannual variability and long-term trends of surface hydrography around the Prince Edward Island Archipelago, Southern Ocean. Masters. Thesis. University of Cape Town.

Toolsee, T. and Lamont, T., **2022**. Long-Term Trends and Interannual Variability of Wind Forcing, Surface Circulation, and Temperature around the Sub-Antarctic Prince Edward Islands. Remote Sensing, 14(6), p.1318.

Toolsee, T., Lamont, T., Rouault, M. and Ansorge, I., **2021**. Characterising the seasonal cycle of wind forcing, surface circulation and temperature around the sub-Antarctic Prince Edward Islands. African Journal of Marine Science, 43(1), pp.61-76.

Tozer, B., Sandwell, D.T., Smith, W.H., Olson, C., Beale, J.R. and Wessel, P., **2019**. Global bathymetry and topography at 15 arc sec: SRTM15+. Earth and Space Science, 6(10), pp.1847-1864.

van den Berg, M., Jacobs, L., Marco, A., Toolsee, T., Mambaso, M. and Fourie, C., **2021**. Marion Relief Voyage 045 on SA Agulhas II. Cruise Report: Ship-based Oceanographic Research. Department of Forestry, Fisheries and the Environment, Republic of South Africa.

van den Broeke, M., **2000**. The semi-annual oscillation and Antarctic climate. Part 3: The role of near-surface wind speed and cloudiness. International Journal of Climatology: A Journal of the Royal Meteorological Society, 20(2), pp.117-130.

Veitch, J., Penven, P. and Shillington, F., **2009**. The Benguela: A laboratory for comparative modeling studies. Progress in Oceanography, 83(1-4), pp.296-302.

Volkov, D.L., Fu, L.L. and Lee, T., **2010**. Mechanisms of the meridional heat transport in the Southern Ocean. Ocean Dynamics, 60, pp.791-801.

Ward, S., Bowers, D., Green, M. and Wilmes, S.B., **2023**. Chapter 4 – Why is there a tide? A Journey Through Tides. pp.81-113. Elsevier.

White, M., Bashmachnikov, I., Arístegui, J. and Martins, A., **2007**. Physical processes and seamount productivity. Seamounts: Ecology, fisheries & conservation, pp.62-84.

White, W.B., Chen, S.C., Allan, R.J. and Stone, R.C., **2002**. Positive feedbacks between the Antarctic Circumpolar Wave and the global El Niño-Southern Oscillation Wave. Journal of Geophysical Research: Oceans, 107(C10), pp.29-1.

White, W.B. and Peterson, R.G., **1996**. An Antarctic circumpolar wave in surface pressure, wind, temperature and sea-ice extent. Nature, 380(6576), pp.699-702.

Wilks, D.S., **2011**. Statistical methods in the atmospheric sciences, 100. Academic press.

Worsfold, M., Good, S., Martin, M., McLaren, A., Roberts-Jones, J., Fiedler, E. and Met Office, UK, **2022**. PRODUCT USER MANUAL: Global Ocean OSTIA Sea Surface Temperature. [Online] Available at: https://catalogue.marine.copernicus.eu/documents/PUM/CMEMS-SST-PUM-010-011.pdf

Yuan, X., **2004**. ENSO-related impacts on Antarctic Sea ice: a synthesis of phenomenon and mechanisms. Antarctic Science, 16(4), pp.415-425.

Zanna, L., Khatiwala, S., Gregory, J.M., Ison, J. and Heimbach, P., **2019**. Global reconstruction of historical ocean heat storage and transport. Proceedings of the National Academy of Sciences, 116(4), pp.1126-1131.

Zweng, M. et al., 2019. World Ocean Atlas 2018, 2: Salinity. A. Mishonov, Technical Editor. NOAA Atlas NESDIS 81, pp. 50.

Zweng, M.M, J.R. Reagan, D. Seidov, T.P. Boyer, R.A. Locarnini, H.E. Garcia, A.V. Mishonov,O.K. Baranova, K.W. Weathers, C.R. Paver, and I.V. Smolyar (2019). World Ocean Atlas 2018, Volume 2: Salinity. A. Mishonov, Technical Editor, NOAA Atlas NESDIS 82, pp.50.

Appendix

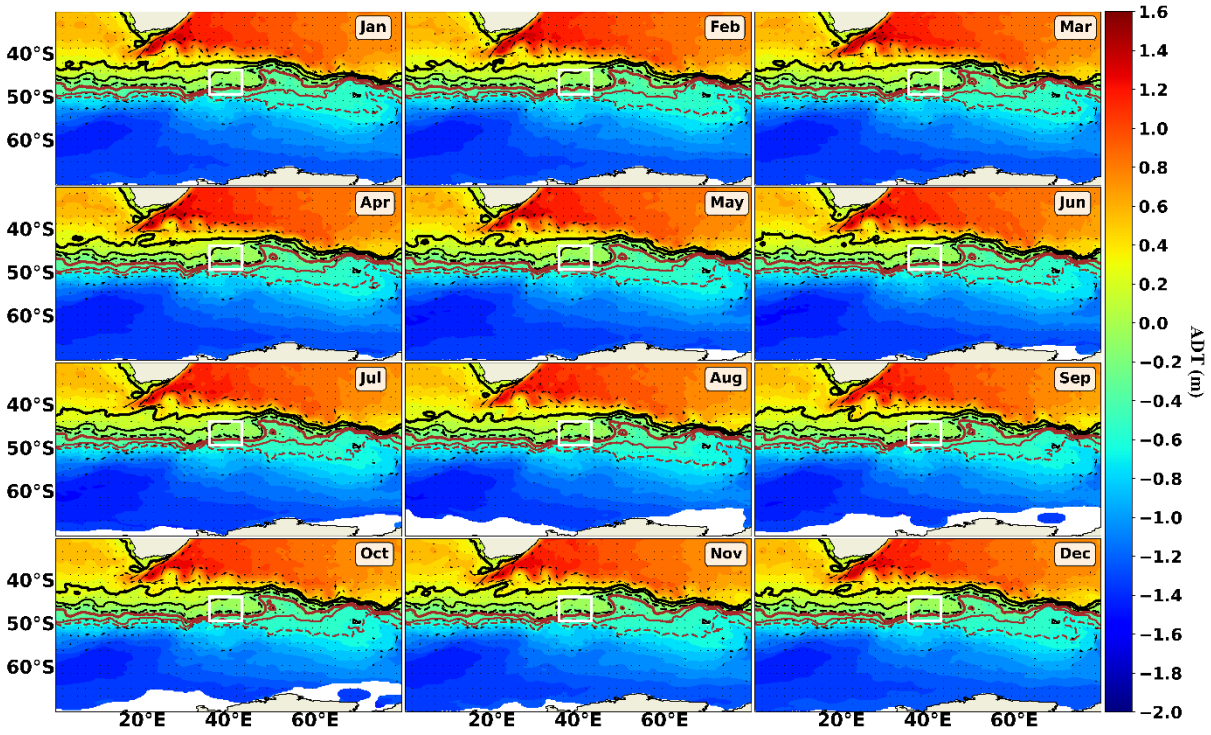

Figure A1: The monthly climatology of absolute dynamic topography (ADT) (m) with geostrophic current direction R_{geos}; (vectors) overlaid from January (Jan) to December (Dec) around the Prince Edward Islands from 1993 to 2022 using the daily reprocessed ADT satellite data. The black solid thick, thin and dashed lines represent the N-SAF, M-SAF and S-SAF, respectively. The solid thick, thin and dashed brown lines represent the N-APF, M-APF and S-APF, respectively. The white box denotes the study region. These front positions were identified from satellite altimetry using ADT according to the process described by Sokolov and Rintoul (2002).

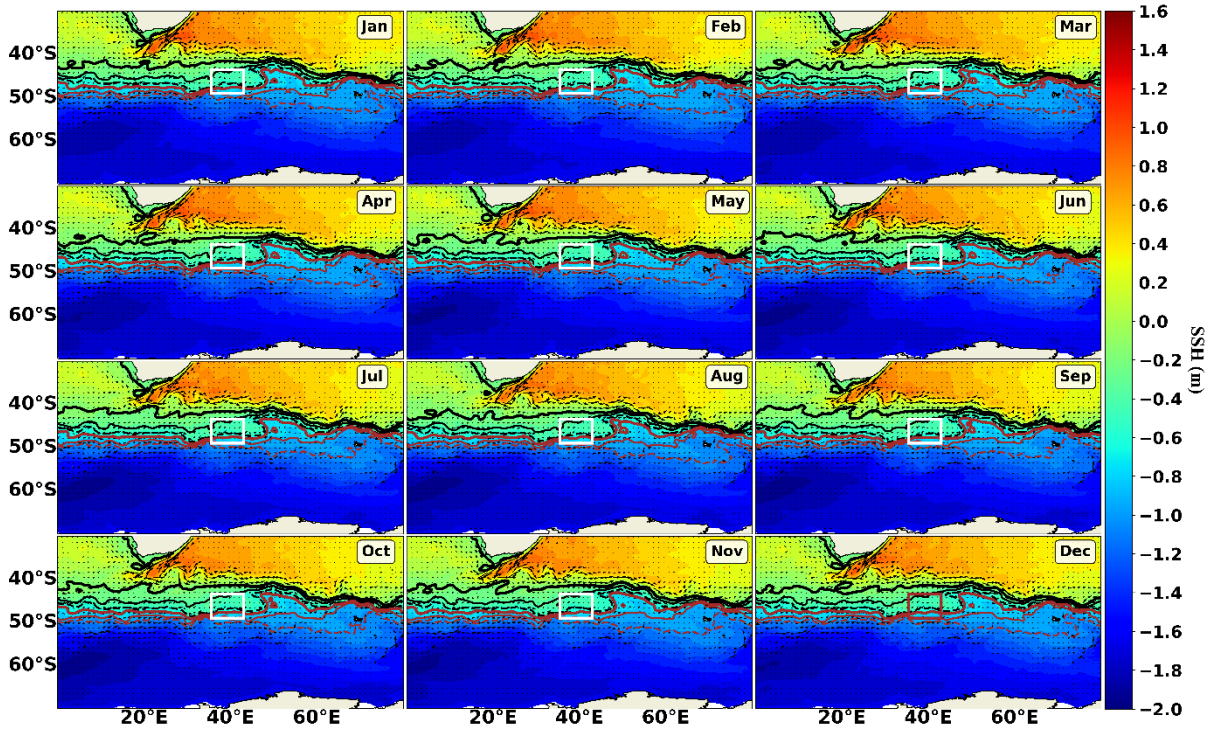

Figure A2: The monthly climatology of sea surface height (SSH) (m) with geostrophic current direction R_{geos}; (vectors) overlaid from January (Jan) to December (Dec) around the Prince Edward Islands from 1993 to 2020 using the GLORYS model output. The black solid thick, thin and dashed lines represent the N-SAF, M-SAF and S-SAF, respectively. The solid thick, thin and dashed brown lines represent the N-APF, M-APF and S-APF, respectively. The white box denotes the study region. These front positions were identified from satellite altimetry using ADT according to the process described by Sokolov and Rintoul (2002).

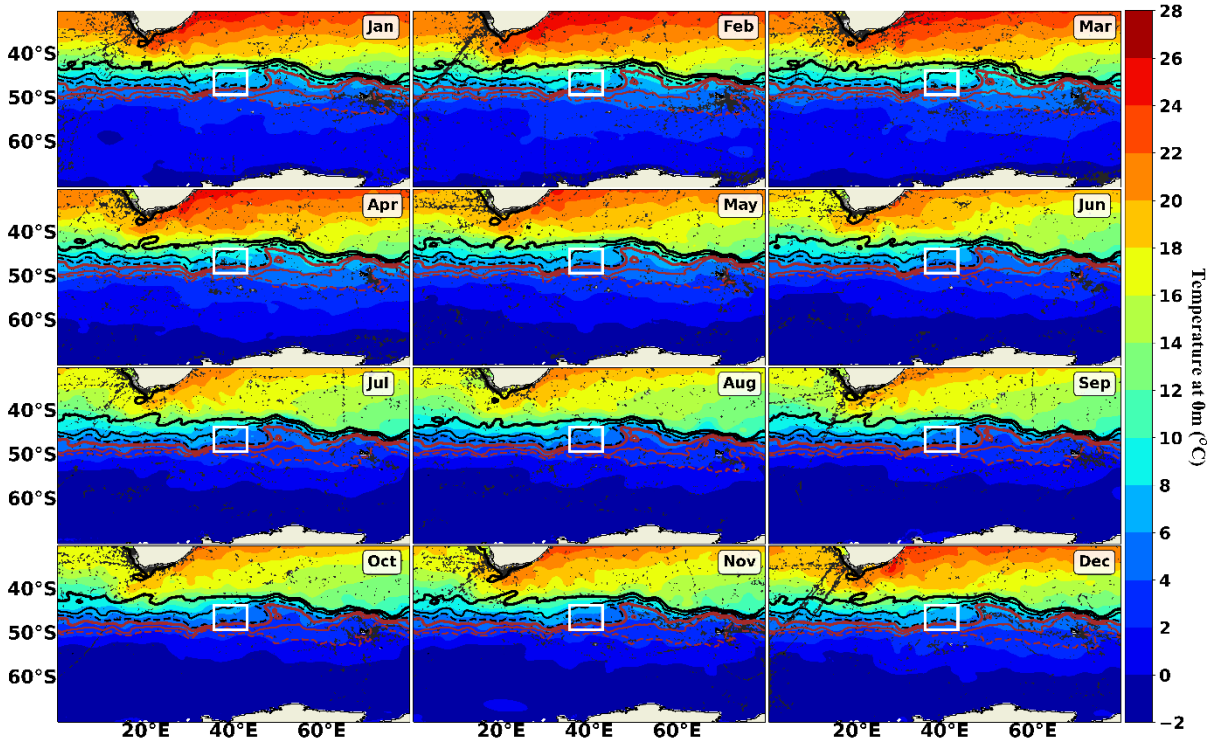

Figure A3: The monthly climatology of sea surface temperature (SST) (°C) from January (Jan) to December (Dec) around the Prince Edward Islands from 1955 to 2017 using the WOA18 data. The black solid thick, thin and dashed lines represent the N-SAF, M-SAF and S-SAF, respectively. The solid thick, thin and dashed brown lines represent the N-APF, M-APF and S-APF, respectively. The white box denotes the study region. These front positions were identified from satellite altimetry using ADT according to the process described by Sokolov and Rintoul (2002).

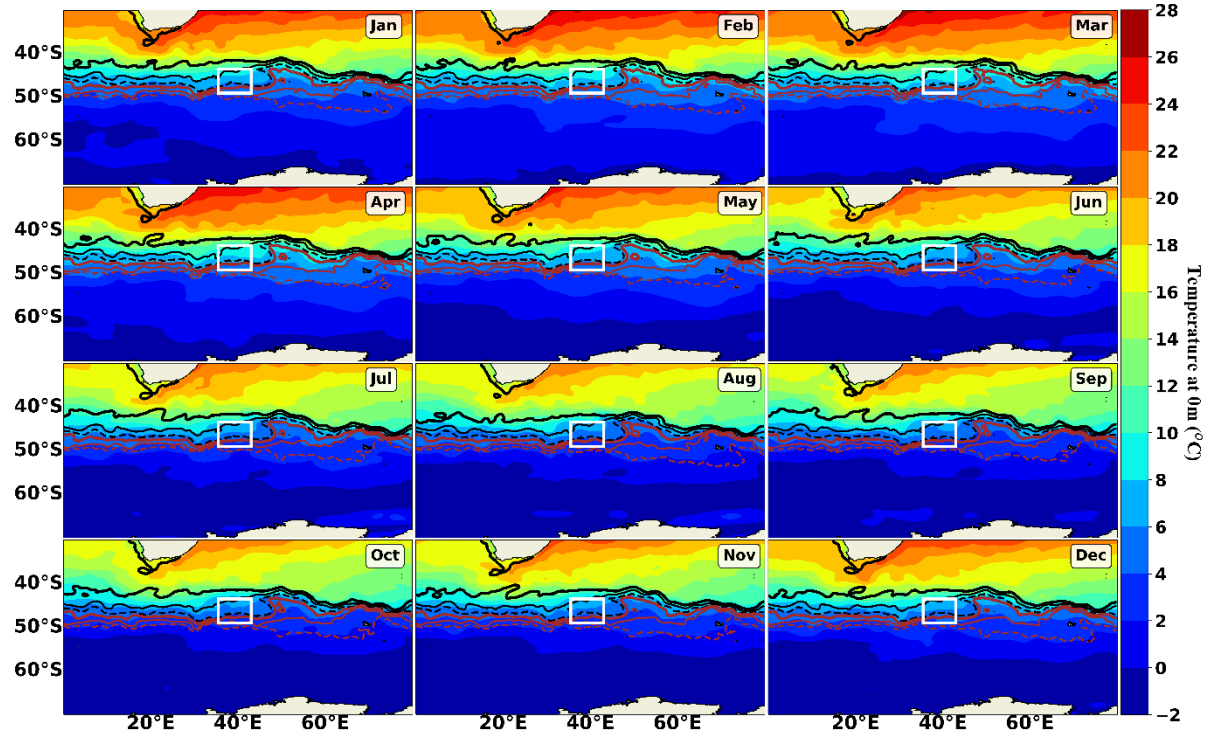

Figure A4: The monthly climatology of sea surface temperature (SST) (°C) from January (Jan) to December (Dec) around the Prince Edward Islands from1985 to 2009 using the CARS09 data. The black solid thick, thin and dashed lines represent the N-SAF, M-SAF and S-SAF, respectively. The solid thick, thin and dashed brown lines represent the N-APF, M-APF and S-APF, respectively. The white box denotes the study region. These front positions were identified from satellite altimetry using ADT according to the process described by Sokolov and Rintoul (2002).

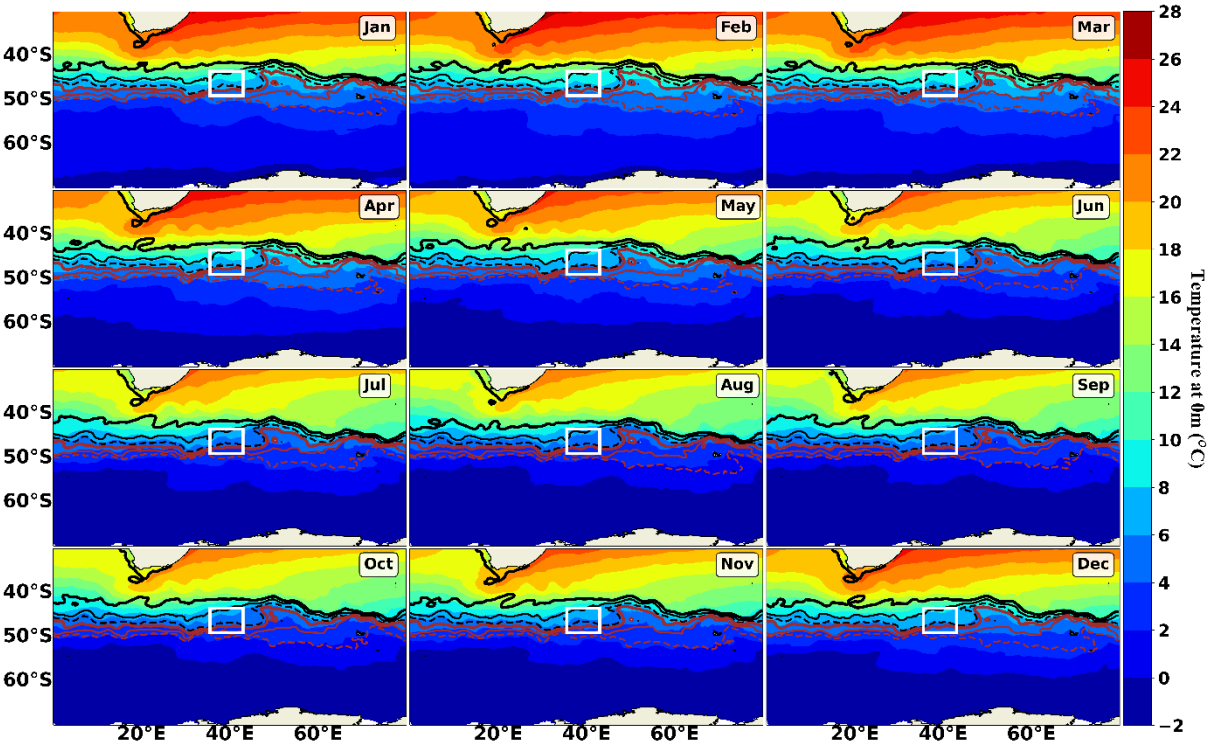

Figure A5: The monthly climatology of sea surface temperature (SST) (°C) from January (Jan) to December (Dec) around the Prince Edward Islands from 1981 to 2021 using the OSTIA dataset. The black solid thick, thin and dashed lines represent the N-SAF, M-SAF and S-SAF, respectively. The solid thick, thin and dashed brown lines represent the N-APF, M-APF and S-APF, respectively. The white box denotes the study region. These front positions were identified from satellite altimetry using ADT according to the process described by Sokolov and Rintoul (2002).

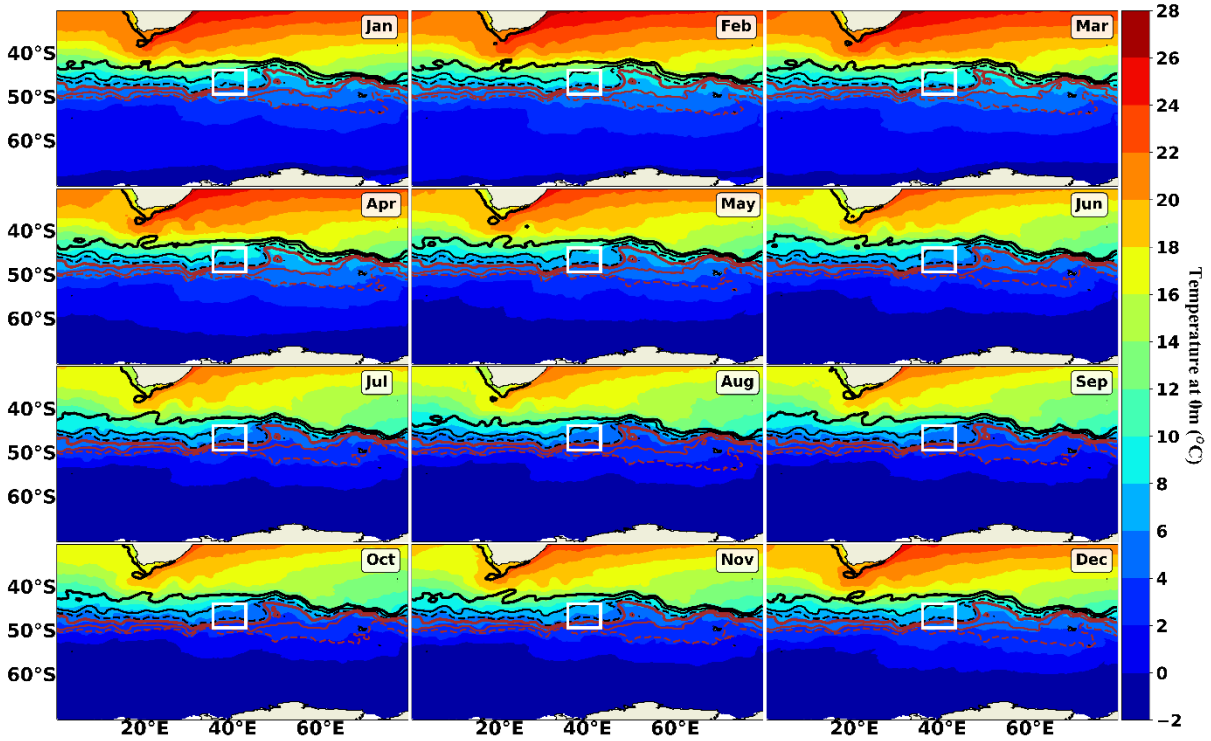

Figure A6: The monthly climatology of sea surface temperature (SST) (°C) from January (Jan) to December (Dec) around the Prince Edward Islands from 1993 to 2020 using the GLORYS model output. The black solid thick, thin and dashed lines represent the N-SAF, M-SAF and S-SAF, respectively. The solid thick, thin and dashed brown lines represent the N-APF, M-APF and S-APF, respectively. The white box denotes the study region. These front positions were identified from satellite altimetry using ADT according to the process described by Sokolov and Rintoul (2002).

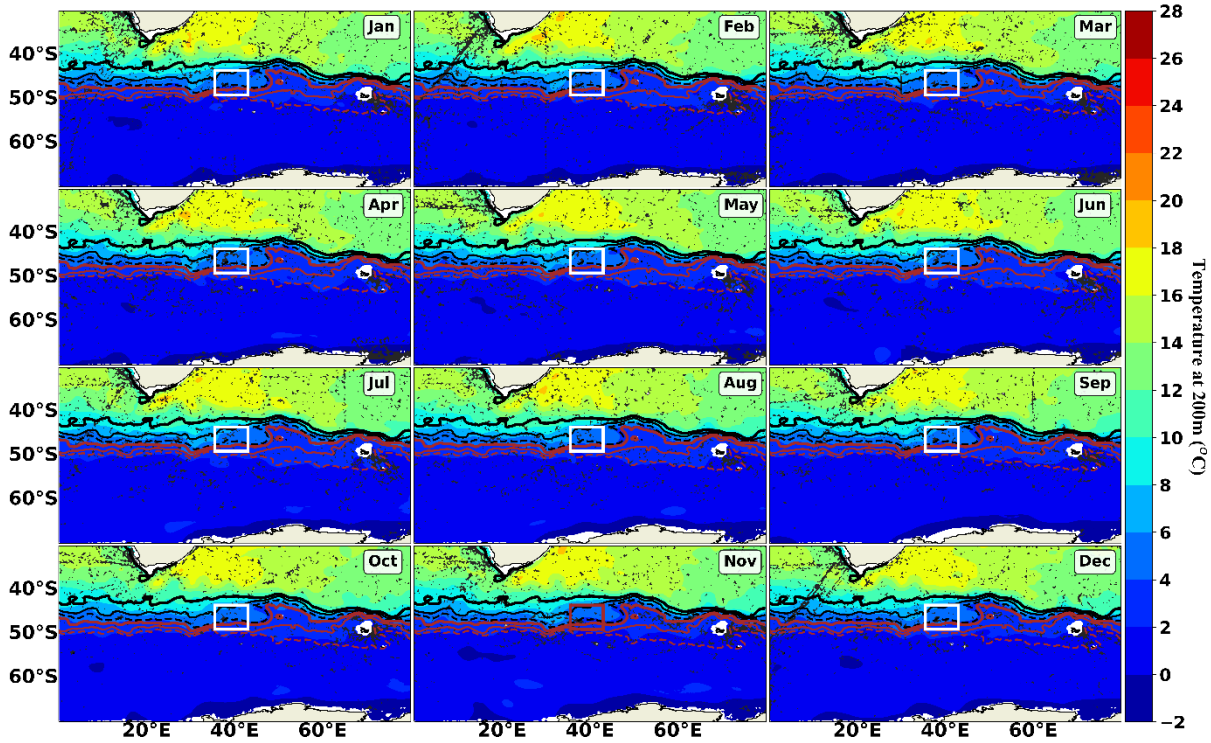

Figure A7: The monthly climatology of temperature at 200 m, from January (Jan) to December (Dec) around the Prince Edward Islands from 1955 to 2017 using the WOA18 data. The black solid thick, thin and dashed lines represent the N-SAF, M-SAF and S-SAF, respectively. The solid thick, thin and dashed brown lines represent the N-APF, M-APF and S-APF, respectively. The white box denotes the study region. These front positions were identified from satellite altimetry using ADT according to the process described by Sokolov and Rintoul (2002).

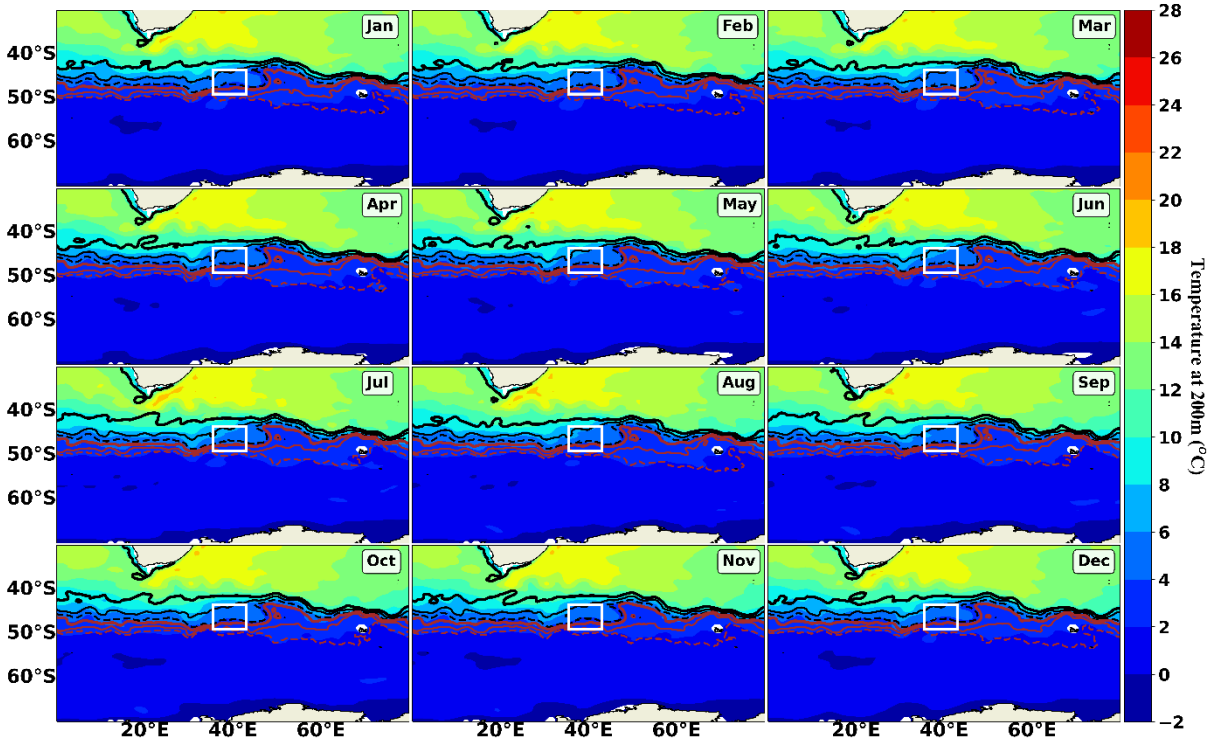

Figure A8: The monthly climatology of temperature at 200 m, from January (Jan) to December (Dec) around the Prince Edward Islands from 1985 to 2009 using the CARS09 data. The black solid thick, thin and dashed lines represent the N-SAF, M-SAF and S-SAF, respectively. The solid thick, thin and dashed brown lines represent the N-APF, M-APF and S-APF, respectively. The white box denotes the study region. These front positions were identified from satellite altimetry using ADT according to the process described by Sokolov and Rintoul (2002).

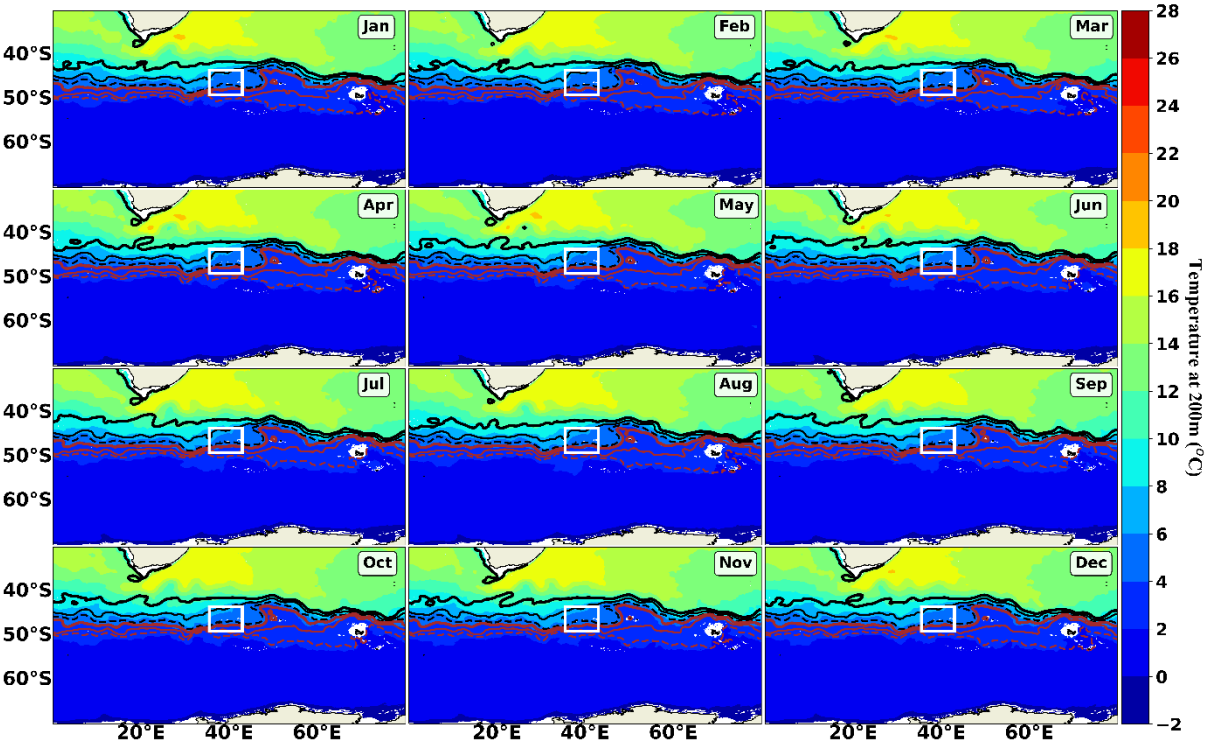

Figure A9: The monthly climatology of temperature at 200m, from January (Jan) to December (Dec) around the Prince Edward Islands from 1993 to 2020 using the GLORYS model output. The black solid thick, thin and dashed lines represent the N-SAF, M-SAF and S-SAF, respectively. The solid thick, thin and dashed brown lines represent the N-APF, M-APF and S-APF, respectively. The white box denotes the study region. These front positions were identified from satellite altimetry using ADT according to the process described by Sokolov and Rintoul (2002).

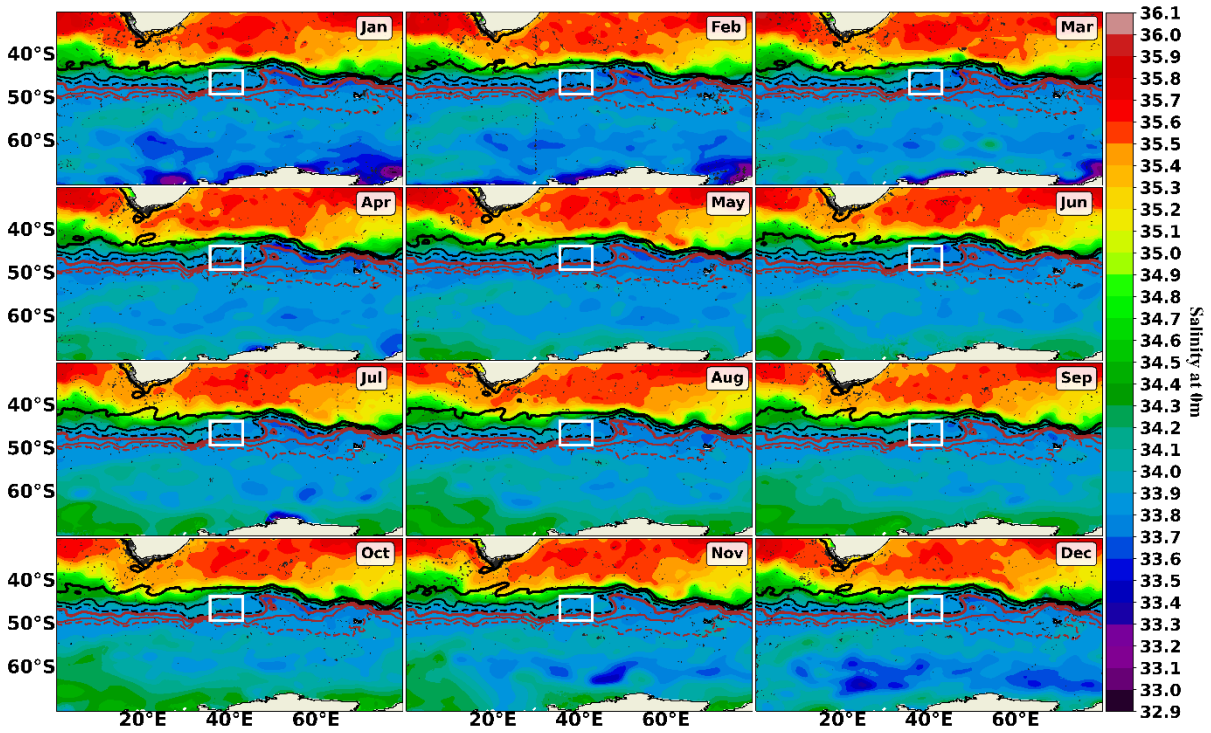

Figure A10: The monthly climatology of sea surface salinity (SSS) from January (Jan) to December (Dec) around the Prince Edward Islands from 1955 to 2017 using the WOA18 data. The black solid thick, thin and dashed lines represent the N-SAF, M-SAF and S-SAF, respectively. The solid thick, thin and dashed brown lines represent the N-APF, M-APF and S-APF, respectively. The white box denotes the study region. These front positions were identified from satellite altimetry using ADT according to the process described by Sokolov and Rintoul (2002).

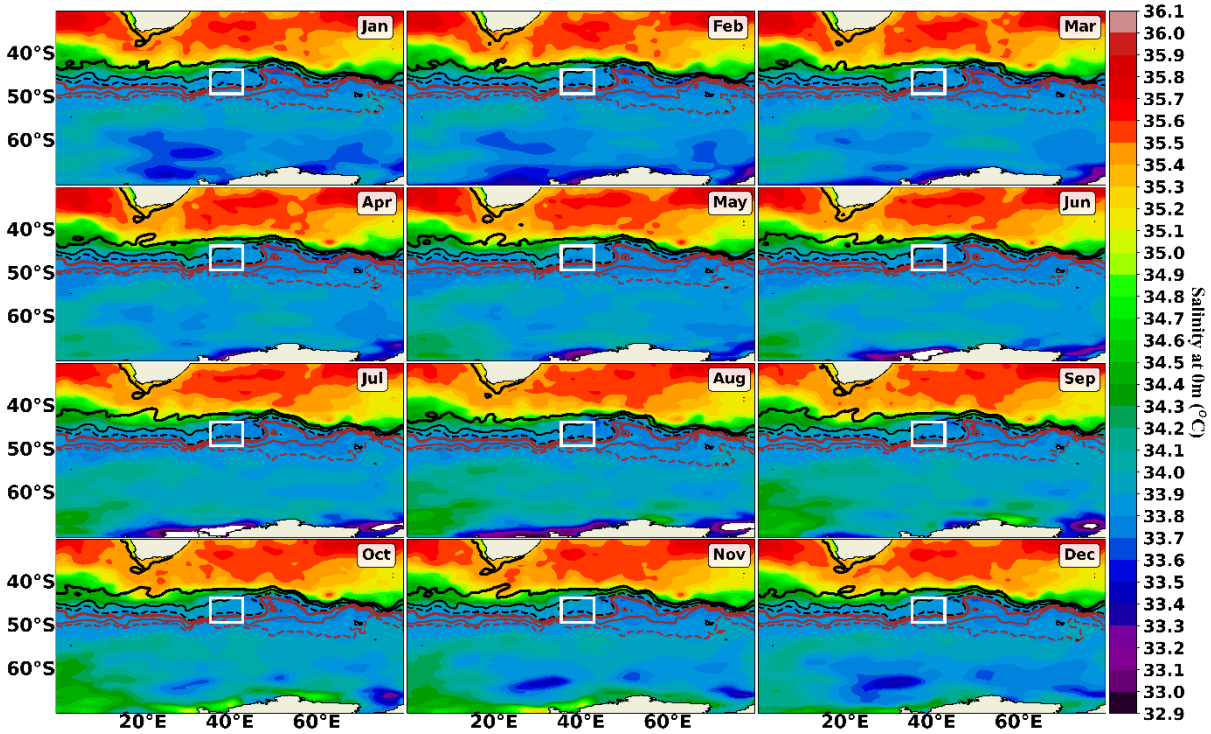

Figure A11: The monthly climatology of sea surface salinity (SSS) from January (Jan) to December (Dec) around the Prince Edward Islands from1985 to 2009 using the CARS09 data. The black solid thick, thin and dashed lines represent the N-SAF, M-SAF and S-SAF, respectively. The solid thick, thin and dashed brown lines represent the N-APF, M-APF and S-APF, respectively. The white box denotes the study region. These front positions were identified from satellite altimetry using ADT according to the process described by Sokolov and Rintoul (2002).

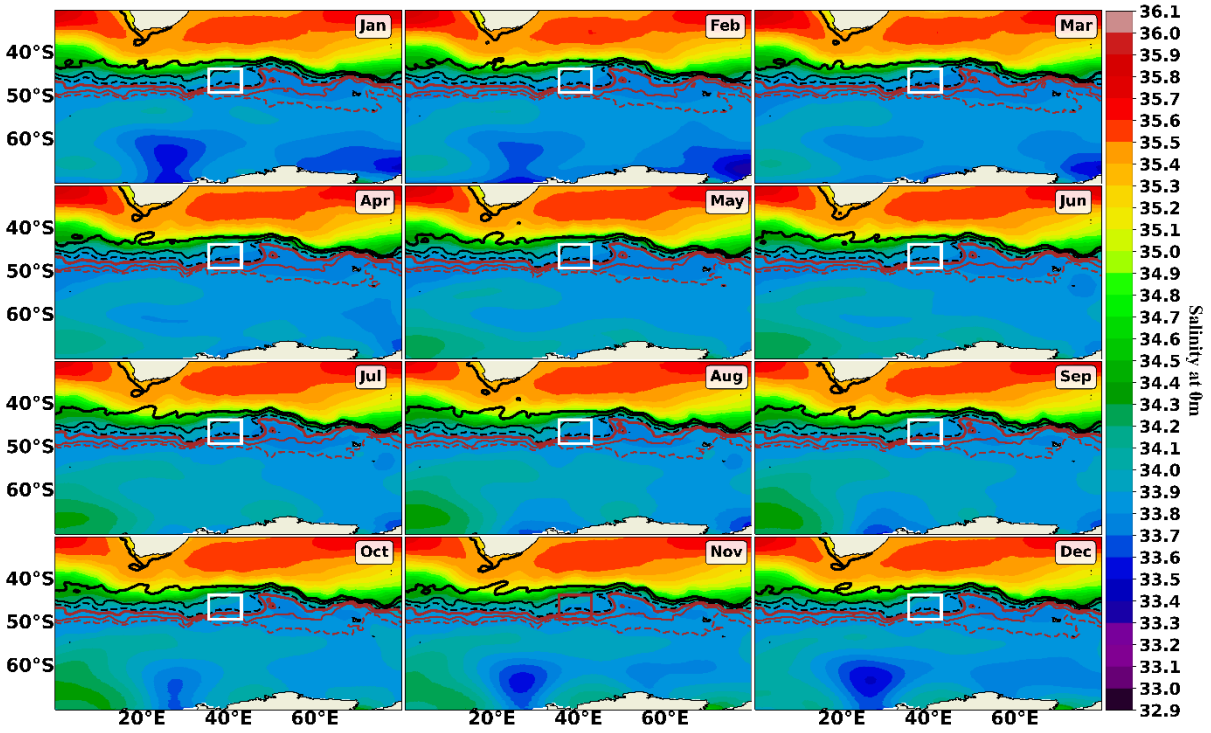

Figure A12: The monthly climatology of sea surface salinity (SSS) from January (Jan) to December (Dec) around the Prince Edward Islands from1993 to 2021 using the CNR data. The black solid thick, thin and dashed lines represent the N-SAF, M-SAF and S-SAF, respectively. The solid thick, thin and dashed brown lines represent the N-APF, M-APF and S-APF, respectively. The white box denotes the study region. These front positions were identified from satellite altimetry using ADT according to the process described by Sokolov and Rintoul (2002).

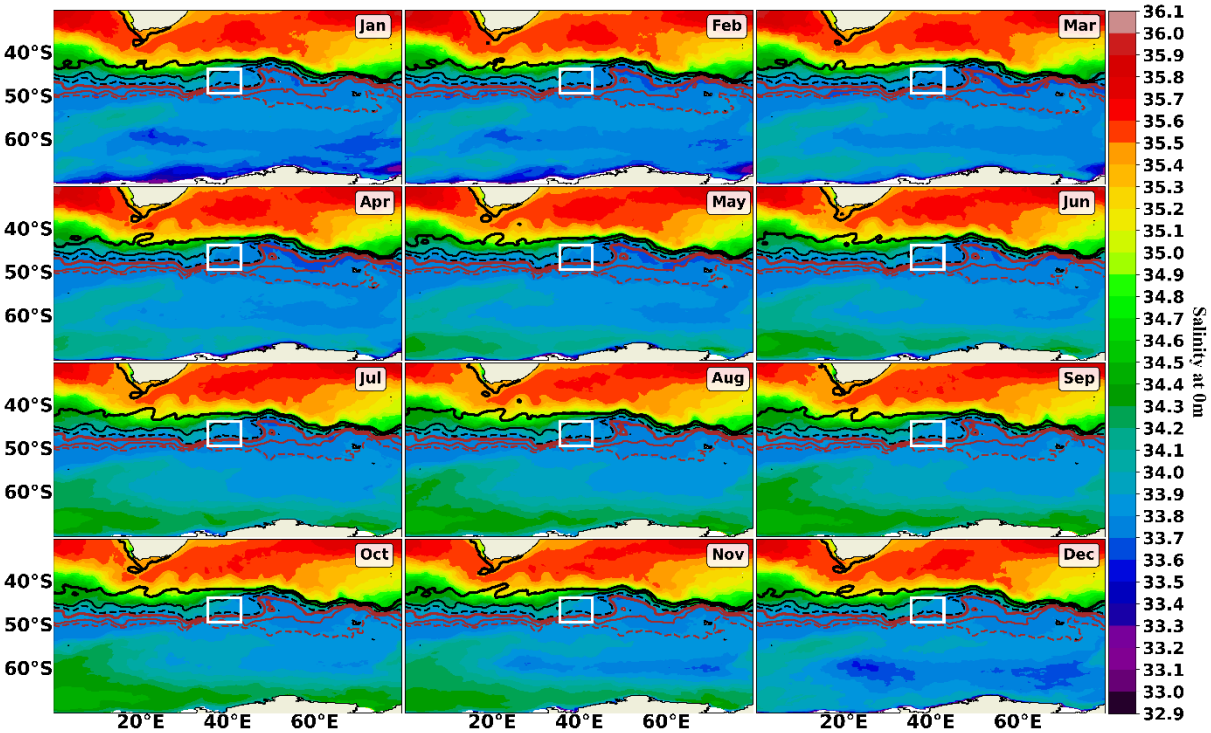

Figure A13: The monthly climatology of sea surface salinity (SSS) from January (Jan) to December (Dec) around the Prince Edward Islands from 1993 to 2020 using the GLORYS model output. The black solid thick, thin and dashed lines represent the N-SAF, M-SAF and S-SAF, respectively. The solid thick, thin and dashed brown lines represent the N-APF, M-APF and S-APF, respectively. The white box denotes the study region. These front positions were identified from satellite altimetry using ADT according to the process described by Sokolov and Rintoul (2002).

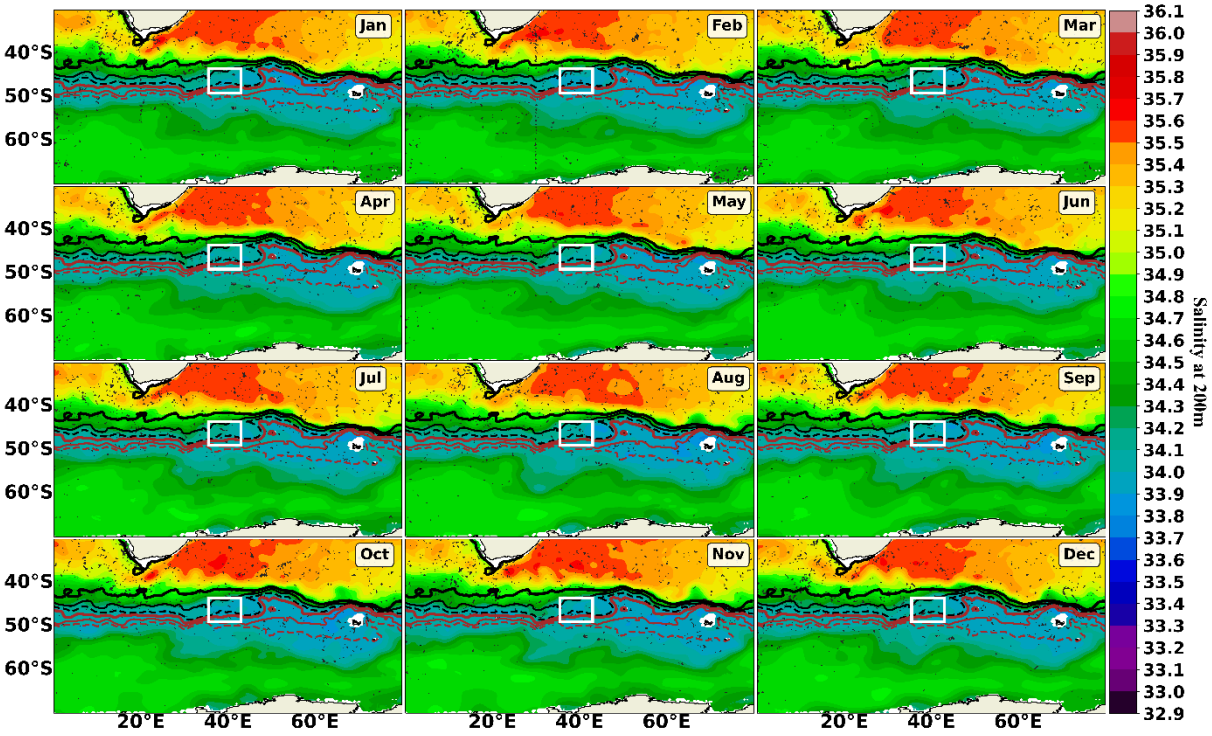

Figure A14: The monthly climatology of salinity at 200m, from January (Jan) to December (Dec) around the Prince Edward Islands from 1955 to 2017 using the WOA18 data. The black solid thick, thin and dashed lines represent the N-SAF, M-SAF and S-SAF, respectively. The solid thick, thin and dashed brown lines represent the N-APF, M-APF and S-APF, respectively. The white box denotes the study region. These front positions were identified from satellite altimetry using ADT according to the process described by Sokolov and Rintoul (2002).

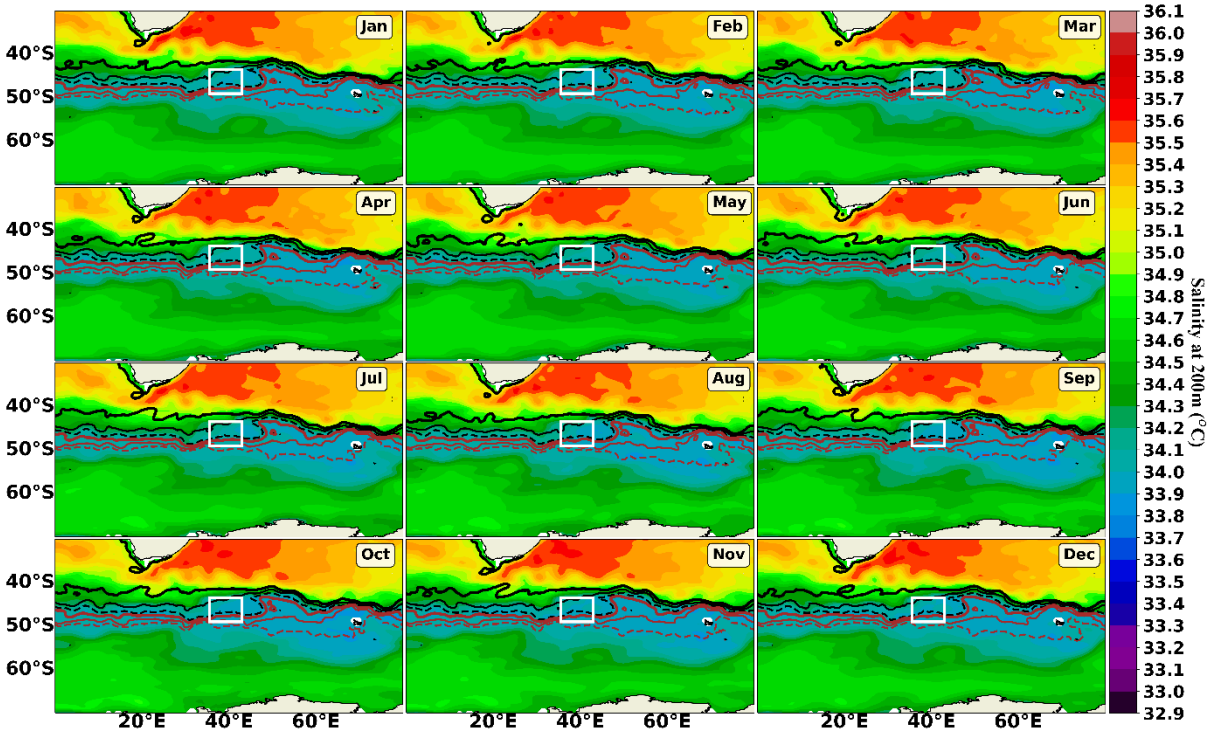

Figure A15: The monthly climatology of salinity at 200m, from January (Jan) to December (Dec) around the Prince Edward Islands from1985 to 2009 using the CARS09 data. The black solid thick, thin and dashed lines represent the N-SAF, M-SAF and S-SAF, respectively. The solid thick, thin and dashed brown lines represent the N-APF, M-APF and S-APF, respectively. The white box denotes the study region. These front positions were identified from satellite altimetry using ADT according to the process described by Sokolov and Rintoul (2002).

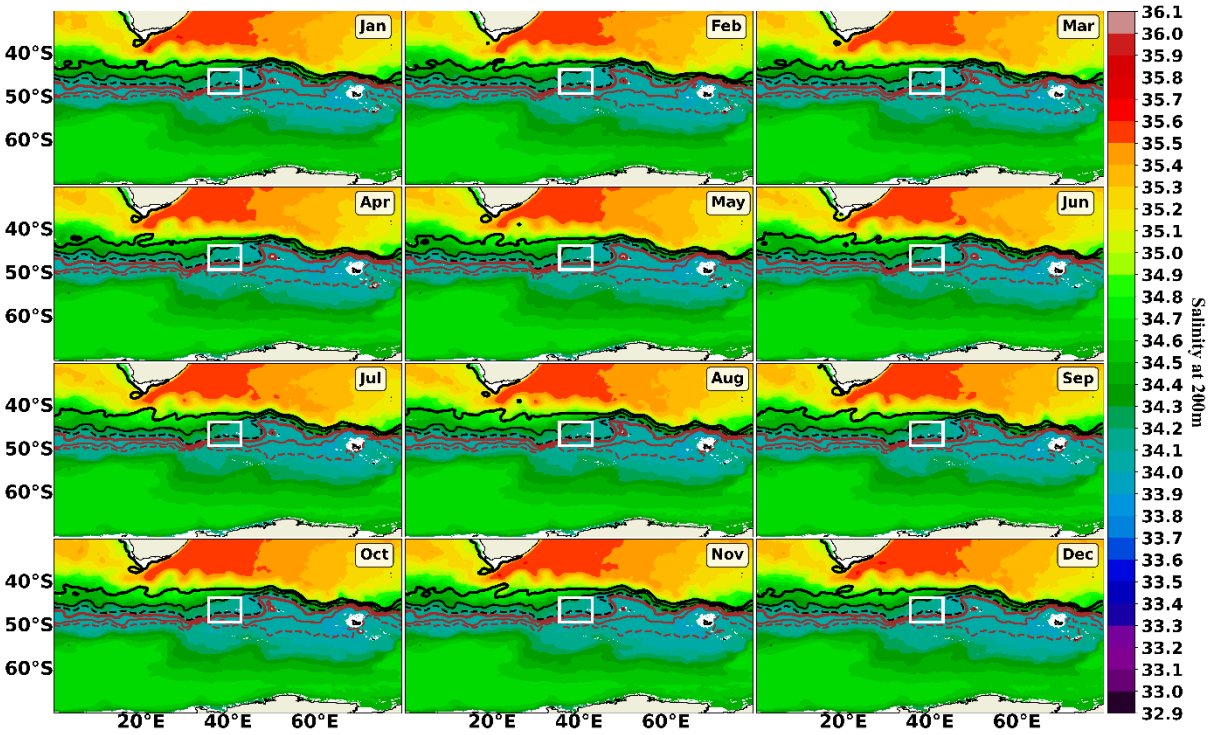

Figure A15: The monthly climatology of salinity at 200m, from January (Jan) to December (Dec) around the Prince Edward Islands from 1993 to 2020 using the GLORYS model output. The black solid thick, thin and dashed lines represent the N-SAF, M-SAF and S-SAF, respectively. The solid thick, thin and dashed brown lines represent the N-APF, M-APF and S-APF, respectively. The white box denotes the study region. These front positions were identified from satellite altimetry using ADT according to the process described by Sokolov and Rintoul (2002).

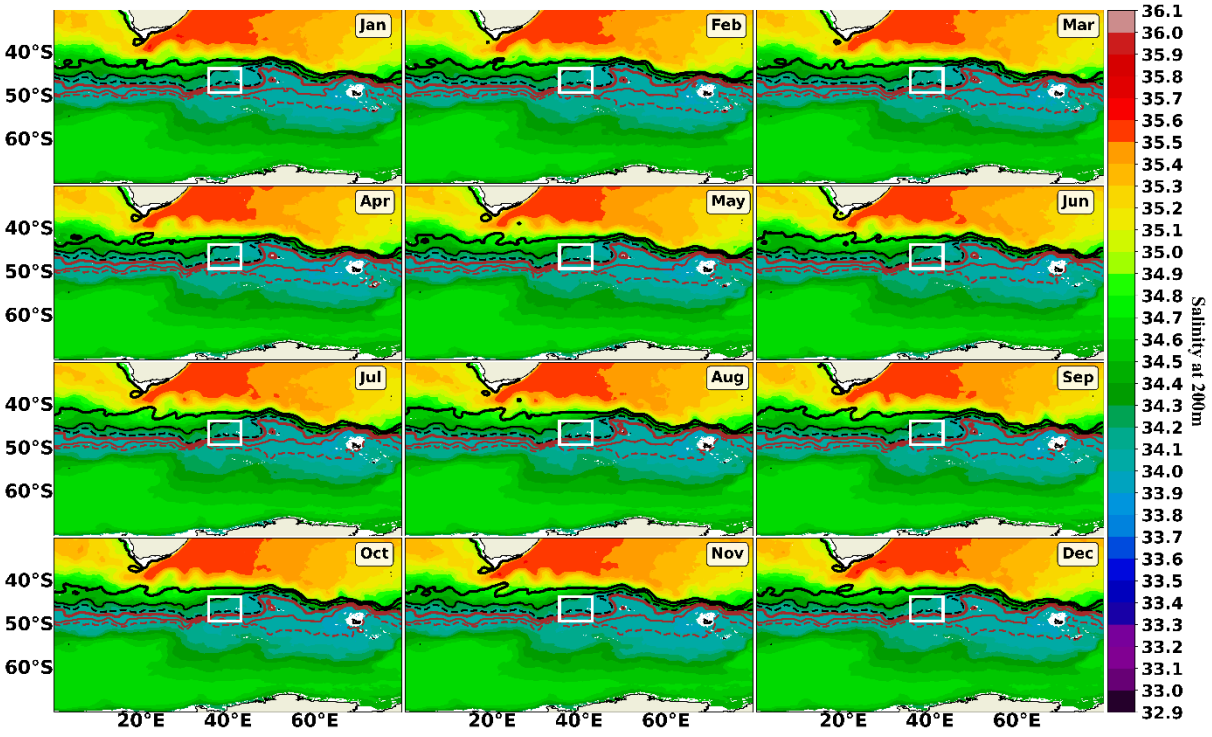

Figure A15: The monthly climatology of salinity at 200m, from January (Jan) to December (Dec) around the Prince Edward Islands from 1993 to 2020 using the GLORYS model output. The black solid thick, thin and dashed lines represent the N-SAF, M-SAF and S-SAF respectively. The solid thick, thin and dashed brown lines represent the N-APF, M-APF and S-APF respectively. The white box denotes the study region. These front positions were identified from satellite altimetry using ADT according to the process described by Sokolov and Rintoul (2002).

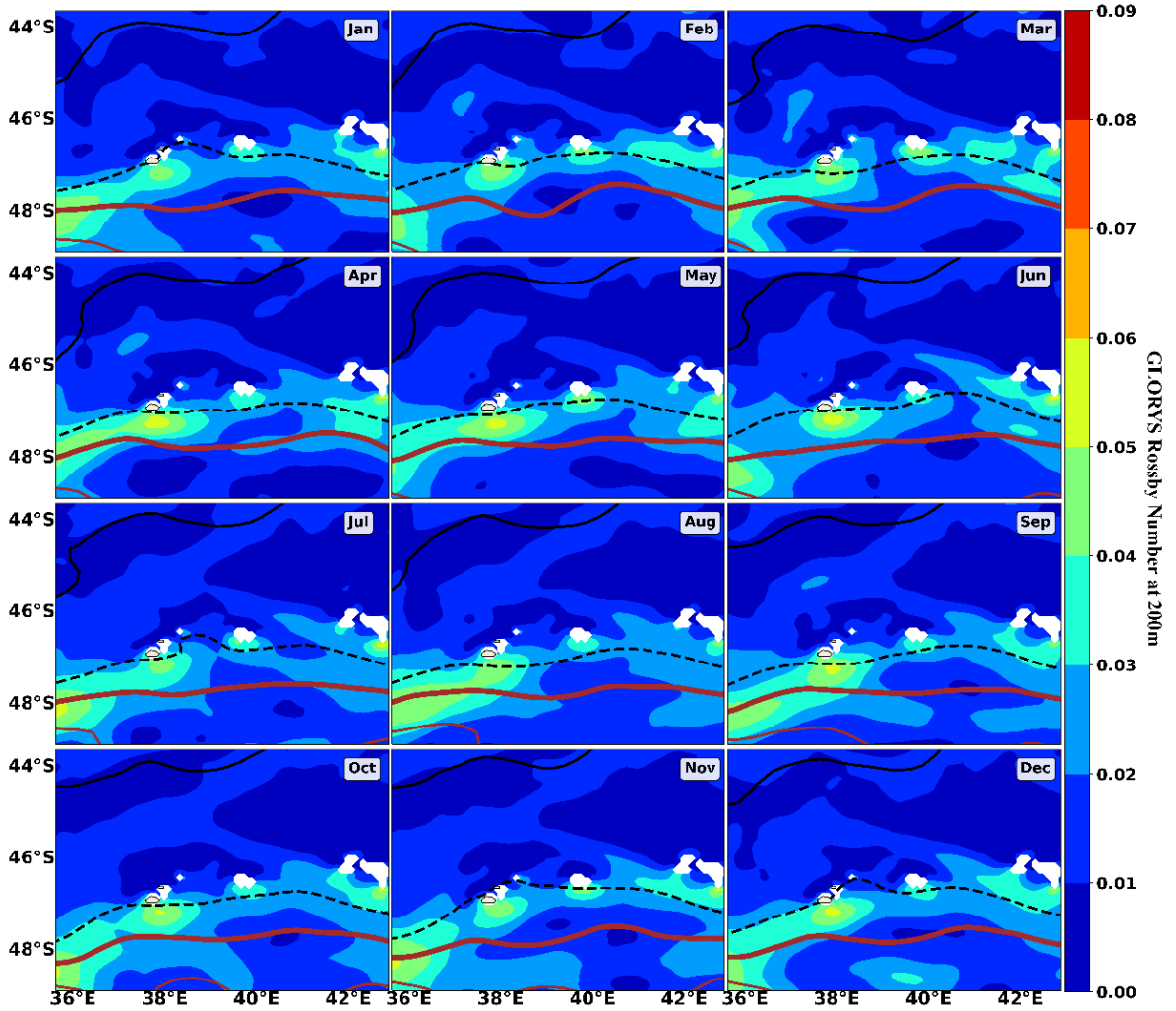

Figure A16: The monthly climatology of Rossby numbers (Ro) calculated using total current vectors at a depth of 200 m, from January (Jan) to December (Dec) around the Prince Edward Islands from 1993 to 2020 using the GLORYS model output. The black solid and dashed lines represent the M-SAF and S-SAF respectively. The solid thick and thinner brown lines represent the N-APF and M-APF respectively. Areas shaded white denote regions of no data. These front positions were identified from satellite altimetry using ADT according to the process described by Sokolov and Rintoul (2002).

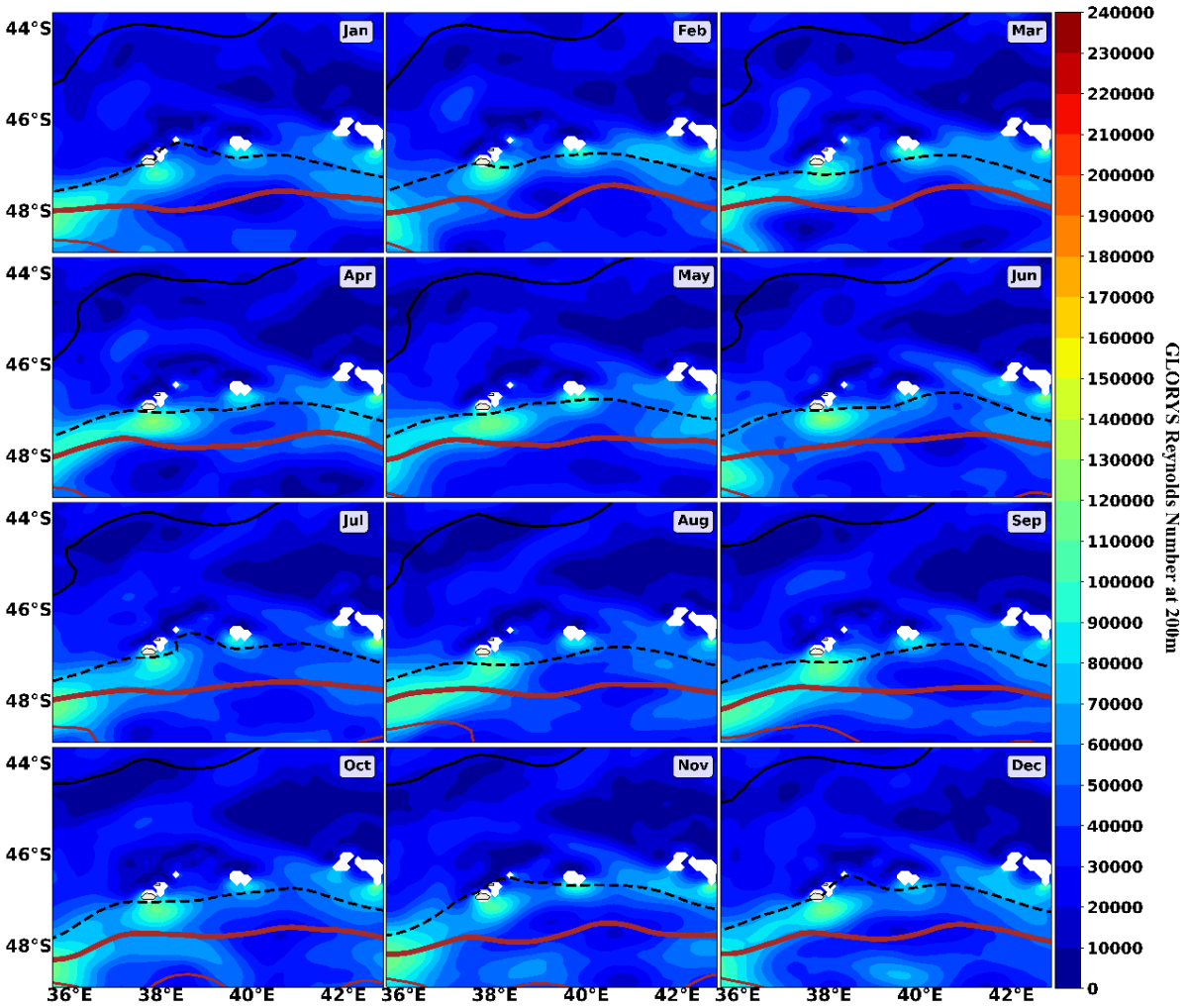

Figure A17: The monthly climatology of Reynolds numbers (Re) calculated using total current vectors at a depth of 200 m, from January (Jan) to December (Dec) around the Prince Edward Islands from 1993 to 2020 using the GLORYS model output. The black solid and dashed lines represent the M-SAF and S-SAF respectively. The solid thick and thinner brown lines represent the N-APF and M-APF respectively. Areas shaded white denote regions of no data. These front positions were identified from satellite altimetry using ADT according to the process described by Sokolov and Rintoul (2002).

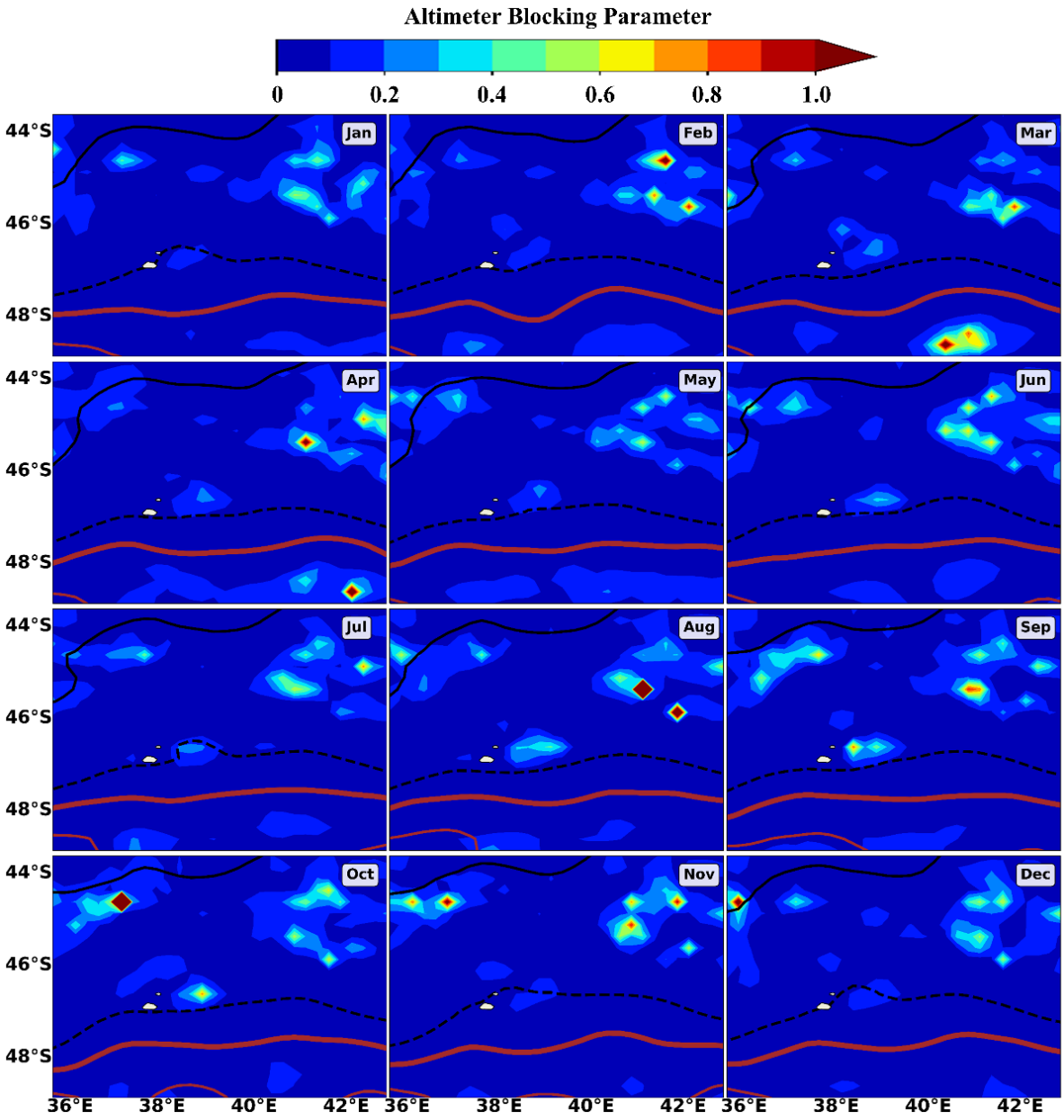

Figure A18: The monthly climatology of Blocking parameter (Bl) calculated using GEBCO median water depth of 2921.3 m, from January (Jan) to December (Dec) around the Prince Edward Islands from 1993 to 2022 using the daily reprocessed ADT satellite data and the GEBCO 2022 bathymetry data. The black solid and dashed lines represent the M-SAF and S-SAF, respectively. The solid thick and thinner brown lines represent the N-APF and M-APF, respectively. These front positions were identified from satellite altimetry using ADT according to the process described by Sokolov and Rintoul (2002).

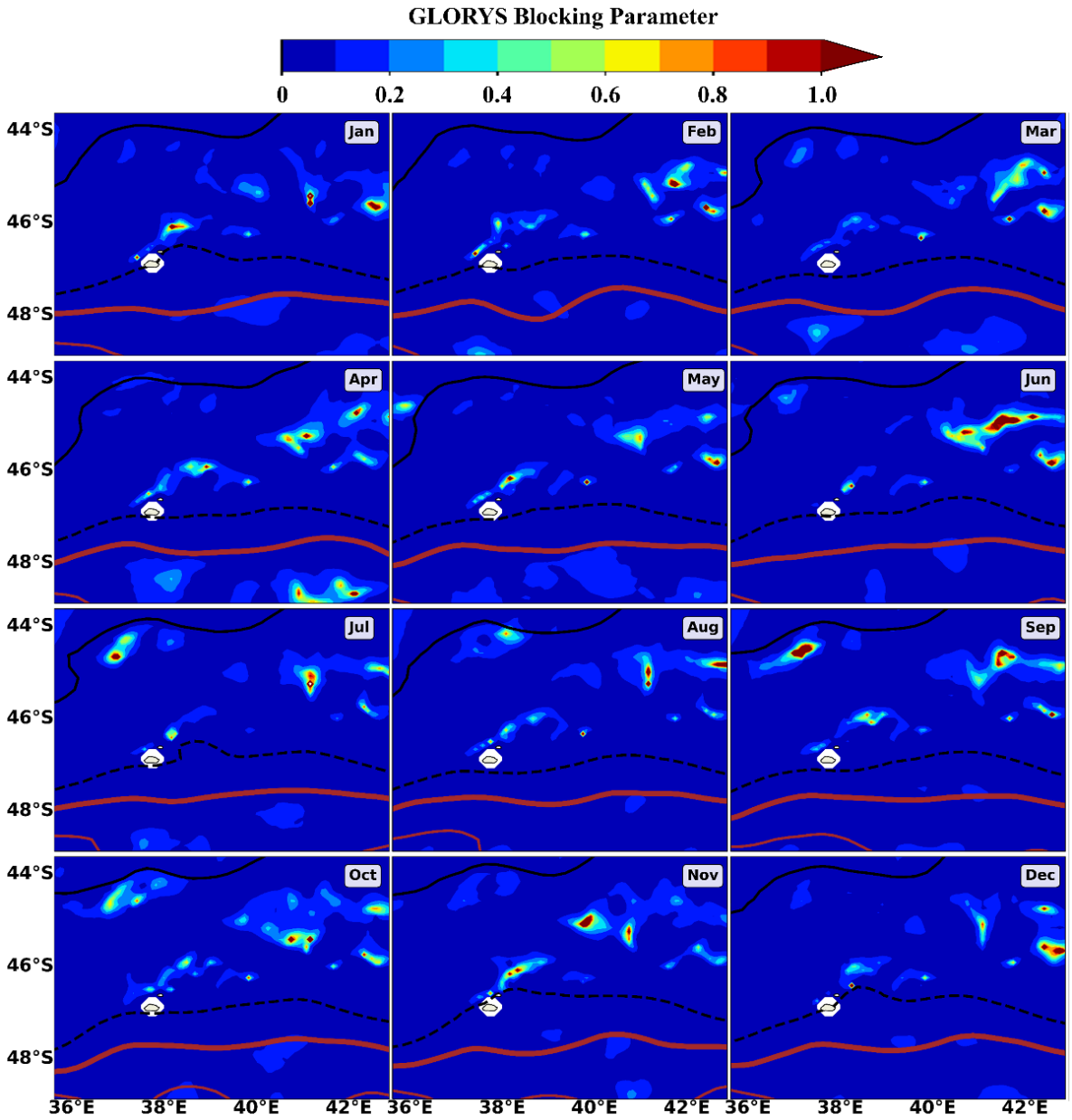

Figure A19: The monthly climatology of Blocking parameter (Bl) calculated using GEBCO median water depth of 2921.3 m, from January (Jan) to December (Dec) around the Prince Edward Islands from 1993 to 2020 using the GLORYS model output. The black solid and dashed lines represent the M-SAF and S-SAF, respectively. The solid thick and thinner brown lines represent the N-APF and M-APF, respectively. These front positions were identified from satellite altimetry using ADT according to the process described by Sokolov and Rintoul (2002).